The Design and Development of an Intelligent Atraumatic Laparoscopic Grasper

Submitted in Accordance with the Requirements for the Degree of
Doctor of Philosophy

The University of Leeds
Institute of Functional Surfaces
School of Mechanical Engineering

Louise Russell

April 2015

The candidate confirms that the work submitted is her own and that appropriate credit has been given where reference has been made to the work of others

Acknowledgements

I would firstly like express a huge thanks to Prof. Anne Neville, for her tireless support and encouragement throughout the project. Her enthusiasm and patience has helped me to maintain a positive outlook. I am also immensely grateful to Dr. Peter Culmer for his endless advise and knowledge of the different areas of my project. It has been a fantastic opportunity and would not have been possible without them.

I would also like to show my respect and appreciation to Jenifer Barrie for being hard working and committed to her profession while working with me to progress in our individual projects. Her collaboration has added a lot to my work and it has been a pleasure to work with her.

Thank you to Surgical Innovations Ltd. and Mike White, director of product development, for providing essential industrial knowledge.

I wish to extend my gratitude to Prof. David Jayne and Adrian Hood for their expertise and advise throughout the project, and enabling many aspects of the project to be carried out.

The Mechanical Engineering technicians and staff have proved invaluable, for their advise and help through the different stages of the project. Thank you.

A big thanks to my fellow colleagues, the surgical technologies group and my colleges in office 2.47. It has been a fun four years, in which I have gained new friends, many of whom will remain as friends for the years to come.

Thank you to my Mum, Dad and sister Joanne for all their encouragement and reassurance. I would also like to thank my grandparents who, even though they were unable to see me complete my PhD, always encouraged me to work hard in whatever area of life I pursued.

Finally I would like to thank my husband Christopher Russell who has been my biggest support throughout my academic studies. He is an inspiration to me and gave me a huge amount of motivation when things got tough.

Abstract

A key tool in laparoscopic surgery is the grasper, which is the surgeon's main means of manipulating tissue within the body. However inappropriate use may lead to tissue damage and poor surgical outcomes. This thesis presents a novel approach to the assessment and prevention of tissue damage caused by laparoscopic graspers. The research focusses on establishing typical grasping characteristics used in surgery and thus developing a model of mechanically induced tissue trauma. A review explored the state-of-the-art in devices for measuring surgical grasping, tissue mechanics, and damage quantification to inform the research.

An instrumented grasper was developed to characterise typical surgical tasks, enabling the grasping force and jaw displacement to be measured. This device was then used to quantitatively characterise grasper use in an *in-vivo* porcine model where the device was used to perform organ retraction and manipulation tasks. From this work, the range of forces and the grasping times used in certain tasks were determined and this information was used to guide the rest of the study. The *in-vivo* investigation highlighted a need for grasping in a controlled environment where the tissue's mechanical properties could be studied.

A grasper test rig was designed and developed to provide automated controlled grasping of *ex-vivo* tissue. This allowed the mechanical properties of tissue to be determined and analysed for indications of tissue damage. A series of experimental studies were conducted with this system which showed how the mechanical response of tissue varies depending on the applied grasping force characteristics, and how this is indicative of tissue damage through comparison to histological analysis. These data were then used to develop a model which predicts the likelihood and severity of tissue damage during grasping, based on the input conditions of grasping force and time. The model was integrated into the instrumented grasper system to provide a tool which could enable real-time grading and feedback of grasping during surgery, or be used to inform best practice in training scenarios.

Table of Contents

List of Figures

List of Abbreviations

(Alphabetical Order)

ASCII - American Standard Code for Information Interchange

CAD - Computer Aided Design

DAQ - Data Acquisition

DOF - Degrees of Freedom

DP - Decimal Point

FBD - Free Body Diagram

GUI - Graphical User Interface

HALS - Hand Assisted Laparoscopic Surgery

MAGS - Magnetic Guidance Anchoring System

MEG - Motorized Endoscopic Grasper

MIS - Minimally Invasive Surgery

MRI - Magnetic Resonance Imaging

NOTES - Natural Orifice Transluminal Endoscopic Surgery

OR - Operating Room

PC - Personal Computer

PDMS - Polydimethylsiloxane

PID - Proportional Integral Derivative

RMS - Root Mean Square

S/s - Samples per second

SILS - Single Incision Laparoscopic Surgery

SMA - Shape Memory Alloy

USB - Universal Serial Bus

VR - Virtual Reality

Chapter 1

Introduction

Surgical techniques have been developing for around two hundred years and still a large amount of research is being done into improving these methods to make them safer and more efficient. A major development of surgical techniques is in the field of Minimally Invasive Surgery (MIS), which aims to limit the size of the access wound, resulting in reduced pain and faster recovery time.

1.1 Motivation for the Project

Besides these benefits, there are however a number of disadvantages such as reduced haptic feedback, lack of depth perception, a longer time spent in the operating room and a fulcrum effect experienced on the tools, where the motions of the tool tips are the reverse to that of the surgeons hands. The disadvantages associated with MIS can result in higher forces used during tasks which leads to tissue damage, and in turn can increase the risk of perforation, tissue necrosis, and infection, especially in abdominal surgery if the bowel was to be damaged. Often this damage is undetected during the procedure and so there is a need for more surgery to correct the issue, increasing the patients recovery time, but the symptoms may not be spotted until there are serious complications. In the case of tumour resections for bowel cancer, slight damage to the delicate membranes, because of inappropriate grasping, can increase the risk of recurrence by spreading cancer cells during grasping [1, 2]. This project aims to develop a method of reducing the chance bowel injury by assessing, in real-time and post-operatively, the likelihood of damage occurring and to what degree. The improved surgical outcomes which will be brought about by this have the potential to hasten patient recovery, reduce the length of required post-operative care and improve the learning curve of trainee surgeons.

During the development of laparoscopic graspers, very little has been done to investigate the tool's interaction with tissue. The usual approach taken by the manufacturers is to manually grasp and manipulate samples such as cow tongue or chicken breast, to check that they can be retracted with limited slip [3], all of which is subjective to the individual user, and without consideration for the actual forces being applied to the sample. This has prompted investigation into the functionality of the laparoscopic grasping tools, focussing on the main grasping forces used in abdominal surgery and how these forces affect the induced tissue trauma.

1.2 Aims and Objectives

1.2.1 Aims

The aim of the project is to develop instrumentation for an atraumatic laparoscopic grasper which is capable of determining if tissue damage has been induced during use. The grasper will monitor the laparoscopic grasping forces which are applied to the tissue, and highlight when an excessive force is being used, and to what degree of severity.

1.2.2 Objectives

To achieve these aims the following objectives will be met:

i. Perform a literature review of the current state-of-the-art of MIS methods and technological development.

ii. Design and develop an instrumented laparoscopic grasper to measure *in-vivo* grasping forces; this provides the ability to highlight when excessive forces are being used.

iii. Perform *in-vivo* testing using the instrumented grasper to establish the typical task forces and characteristics in abdominal surgery.

iv. Design and develop a laparoscopic grasper test rig which can replicate the forces used in surgery in a controlled laboratory environment.

v. Use the test rig to grasp tissue samples with varying grasping parameters, advised from previous *in-vivo* testing.

vi. Develop a model of tissue damage characteristics from tissue mechanics analysis, supported by histological analysis.

1.3 Contributions of the Work

This work links measurements characterising *in-vivo* grasper use in MIS with a detailed study of the resulting tissue response and trauma. Other research has investigated either measuring *in-vivo* surgical task parameters, and how these differ between surgeons, or *ex-vivo* tissue characteristics, without a link between the two. The test rig uses laparoscopic graspers typically used in surgery to allow for comparable measurements to the *in-vivo* testing, again developing the link between *in-vivo* and *ex-vivo* testing. It provides an accurate and repeatable measure of the mechanical properties of tissue under varying forces, linking to a mechanical and histological measure of tissue damage for laparoscopic tools, which has not been currently

shown in this area of research. Using these findings, the intelligent grasper damage model assesses grasping force and duration from the instrumented grasper, to give a grading of the expected level of induced damage. While previous research has shown *in-vivo* task performance data, the intelligent grasper is unique in that it gives the surgeon an expected damage grade, advised from *ex-vivo* findings, instead of simply numerical data.

1.4 Thesis Structure

Chapter 2 covers the review of current literature on MIS, laparoscopic grasper design, tissue analysis (tissue properties and measurements of tissue damage), current MIS devices to measure surgical task performance and tissue characteristics. The development and testing of an instrumented grasper, used to measure *in-vivo* grasping profiles and typical surgical manipulations is discussed in Chapter 3. Chapter 4 describes the design of a test rig for laparoscopic grasping, demonstrating its capabilities for use with porcine tissue. Chapter 5 investigates the tissue's mechanical response to applied forces, supported by histological analysis, over the range of *in-vivo* grasping forces using the previously developed test rig, and Chapter 6 combines the findings from the instrumented grasper and rig chapters to provide a model to predict the likelihood of tissue damage. Chapter 7 presents a discussion of the research results and their implications for improvements to surgery, together with recommendations for future work.

Chapter 2

Literature Review: Minimally Invasive Surgery Techniques, Bio-Mechanical Tissue Characteristics and State of the Art Grasper Designs and Developments

2.1 Background to Minimally Invasive Surgery

As life expectancy rates rise with an ever-increasing population, new surgical techniques are being developed to tackle the higher demand and complexity of procedures. Minimally Invasive Surgery (MIS) was first introduced in 1983 as a therapeutic tool to perform an appendectomy (appendix removal), whereas previously it had just been used as a diagnostic aid. By 1993 MIS was recognised by surgeons as the preferred method of choice for simple procedures such as appendectomies and cholecystectomies (gallbladder removal), and is now the leader in abdominal surgery, due to aesthetic and trauma reduction benefits [4]. In the 1990's a small number of surgeons developed an experimental procedure for laparoscopic resection of colorectal cancer and has now been established worldwide as a mainstream treatment, which is as safe as previous methods both in the short and long term [5]. To perform MIS, several incisions (typically 3-5), each approximately 20 mm long (depending on the port size) are made to the patients abdomen using a scalpel, often including the navel for improved aesthetics. Through these incisions, trocars (tool ports) are advanced through the abdominal wall so as to enter the intra-peritoneal cavity, taking care not to injure the intra-abdominal viscera [6]. The trocar provides a sterile and sealable internal access, reducing the risk of infection to exposed organs and limiting irritation to the wound. A laparoscope, a camera consisting of a light source and optical cable, is inserted down the navel trocar to provide a live video feed of the surgery, which is displayed on a screen in the Operating Room (OR), and is subsequently used to guide further trocars through the abdomen walls, preventing the bowel from being punctured (Figure 2.1a) [7]. The abdomen is then insufflated using CO_2 to allow the surgeon room to manoeuvre the laparoscopic tools (typically 230 - 350 mm long) and to provide a clearer view of the surgical procedure (Figure 2.1b).

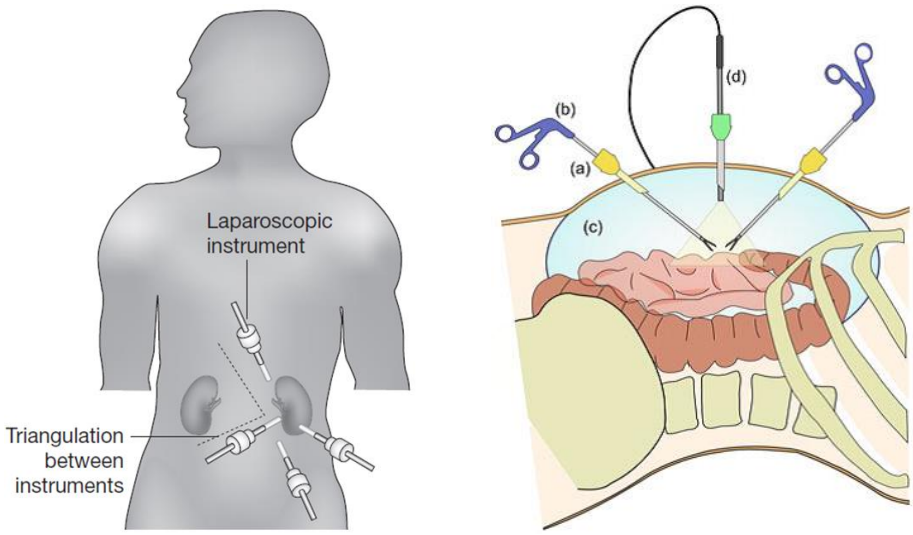

(a) (b)

Figure 2.1: Example of MIS port set-up highlighting (a) the location and triangulation of the trocars (nephrectomy), including the navel, down which the laparoscope is typically placed [8], and (b) the typical layout of a, the trocars, b, the laparoscopic tools, c, the insufflated abdominal cavity, and d, the laparoscope (appendectomy) [9].

There are a number of benefits to performing MIS over open surgery, such as a faster recovery, reduced access trauma and smaller scars which result in less pain and a better cosmetic result [10]. By reducing the size of the wound and using several smaller incisions, fewer stitches are needed for each opening, therefore causing less strain on the wound after surgery and limiting the risk of broken stitches. The wounds can therefore heal faster with a reduced chance of infection, minimizing time spent in hospital and allowing for a faster return to normal function [11]. MIS also decreases the amount of adhesion formation between the viscera and peritoneum, reducing the potential for complications in future surgery [12, 13]. With cosmetic outcome becoming an ever increasing factor, the ability of the surgeon to be able to perform complex procedures while keeping visible scarring to a minimum provides a highly desirable option for patients, as growing numbers are now opting for this type of surgery [14]. Even though initial costs for MIS can be considered as quite large, the overall cost is generally lower when considering patient aftercare. Research into the cost-effectiveness of MIS describes how overall there was a £300 increase in surgery cost per patient and that in terms of long term results, both open surgery and MIS were the same (as of 2001). It states that a judgement is required as to whether the short-term benefits are worth this extra cost. However due to a lack of long-term MIS patients (when compared to open surgery), there is insufficient data for this to be fully concluded [15].

Besides these advantages, there are however a number of disadvantages accompanying MIS [14, 16]. Laparoscopy-induced bowel injury, although rare, can have devastating consequences, so avoiding this requires meticulous surgical technique and experience by

the surgeon [17]. This type of injury can be caused when the trocars enter the abdominal cavity and accidentally puncture the internal viscera, by a coagulator (a device used to sever and cauterise tissue) or by the tools used during manipulations. It has a potential mortality rate of 3.6% if left undetected, with typically 66.8% of cases being recognised during the procedure [1]. In open surgery the surgeon is fully able to palpate organs and decipher whether it is healthy or diseased. This allows for a relatively small margin of error when removing tissue. Using MIS, the surgeon's hand does not come into physical contact with the tissue, so any direct sensory feedback is lost [18]. This prevents the surgeon from fully knowing the magnitude of force they are exerting on the tissue, preventing the capability to palpate and determine the thickness, density or texture of the tissue [1, 19, 20]. A variety of surgical tools have been designed to return dexterity to the surgeon and so the ability to carry out certain tasks, such as grasping, retracting and organ manipulation, however this means that the surgeon is required to switch tools between different tasks, increasing the length of time spent in the operating room [21]. The only image seen by the surgeon is from the laparoscope monitor, often at a different angle to that of the surgeons point of view of the procedure, affecting manoeuvrability and depth perception. As both the surgeons hands are holding the surgical tools, an assistant is also required to manoeuvre the laparoscope which often results in the image displayed on the screen not being entirely what the surgeon requires and again increasing the time spent in the OR. A fulcrum effect is also experienced from the laparoscopic tools where they are inserted into the body, thus inverting the surgeons hand motions (to move the tool tip *'up and left'* the surgeon must move the handle *'down and right'*) [22]. These issues can make manoeuvrability difficult and increase the likelihood of excessive forces being used to prevent tissue from slipping. As a result unnecessary tissue damage can occur which the surgeon may not realise until after the surgery has been completed [14, 17]. If a procedure is deemed too difficult, or a serious complication arises, the surgeon can opt to convert to open surgery, whereby the tools and ports are removed, and a single, large incision is made. This is often a last resort due to the traumatic nature of open surgery, but usually chosen when the seriousness of the complication outweighs this. However, there are novel intermediate states where single finger access is made to assist the laparoscopic procedure [23], in an attempt to avoid open surgery where possible.

2.1.1 Current MIS Technology

The latest developments in MIS aim to either build on the current advantages and designs or reduce the significance of the previously discussed disadvantages, covering a large range of techniques and tools [24]. The *da Vinci*® robot is one example of robotic assisted surgery or tele-operated surgery, where the surgeon remotely controls the laparoscopic tools and camera (Figure 2.2) [25]. Robotic surgery is quickly becoming the preferred method of choice for

performing highly technical surgeries, requiring higher dexterity than previously possible in MIS [26]. Robotic tele-operated surgery was originally developed to allow remote access to the patients, such as in war zones or isolated locations, where the surgeon does not need to be present in the operating room. However this has recently become popular in everyday procedures due to benefits such as reduced hand tremors using filtering software, motion control of the laparoscope and continuation of the desired point of view (the position is maintained by the robot which will not slip or suffer from fatigue, unlike a human user), and the *da Vinci*® 3D imaging, which provides the surgeon with improved depth perception, allowing for more control over movements [27]. The *da Vinci*® system has the disadvantage of zero feedback on the tools (more so than conventional MIS), preventing the surgeon from knowing the pressures they are applying to the grasped surface, therefore intense training and technical knowledge are required to use these types of system effectively [28], with further research providing an understanding of these forces, and how they translate to the tissue-tool interface [29].

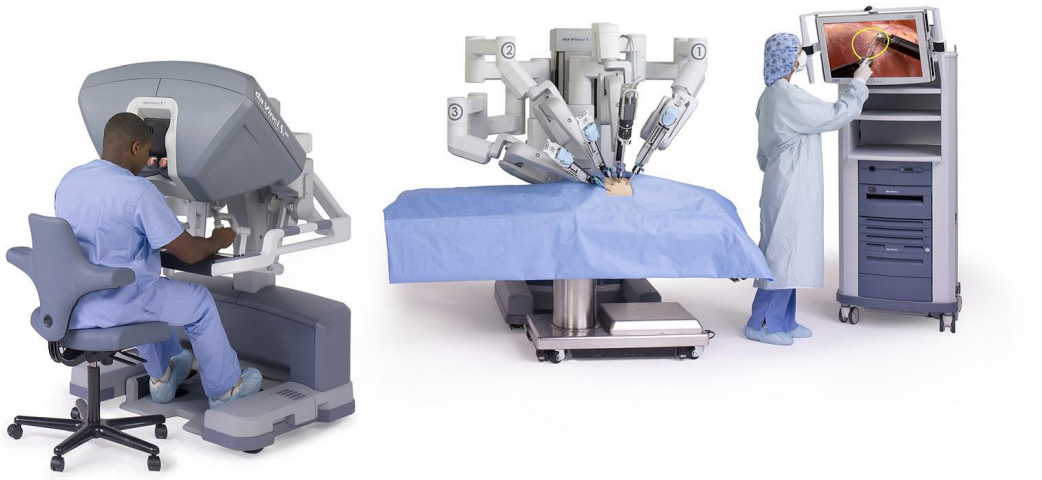

Figure 2.2: The *da Vinci*® Surgical System robotic platform for teleoperated MIS comprising of the control console (left), where the seated surgeon has a magnified 3D image of the surgery, and the patient cart (right) with up to three instruments and the 3D laparoscope [28].

Advancements in software used alongside robotic surgery, combined with pre-operative assessment, can define a *'safe'* working area in which the surgeon can move unrestricted. Upon manoeuvring the tool-tip outside of this area active constraints are applied, where an incrementing resistive force is experienced with relative magnitude to the distance from the *'safe'* zone, until the outer boundaries are reached and the tool-tip cannot move further away. This prevents the surgeon accidentally moving into a potentially dangerous region, but does require advanced planning and would be difficult to implement if complications arise [30]. Further advancements on this have allowed for deformable motion tracking of

the heart surface, allowing the surgeon to operate on a seemingly motionless subject, while the positional control software of the laparoscope and tools compensates for the patient's heartbeat and breathing [31], allowing for much safer surgery as the heart does not need to be stopped.

2.1.2 Developments of Future MIS Technology

Advancements in MIS have lead to developments in Single Incision Laparoscopic Surgery (SILS) (Figure 2.3a), where tools are passed through a single larger incision, often utilising umbilical access for improved aesthetic results, which is still considerably smaller when compared to open surgery [32]. Benefits also include reduced pain and lower port site complications such as infections and hernias, and typically costing less than conventional laparoscopy [33]. This method has been shown to be equally as safe as traditional methods for a number of procedures including the treatment of uncomplicated gallstone disease [34], and lymphadenectomies [35]. However there are still issues with manoeuvrability and the tools clashing due to the arched instruments required to pass through the same port, and can therefore affect task motions and increase the time spent in the OR [36, 37]. Further research and advanced training of SILS provides the surgeon with skills to overcome these problems, such as optimum placement of the endoscope, and novel tools designed to provide the greatest dexterity, while still passing through a single port (Figure 2.3a) [38]. SILS techniques have been shown as a suitable and safe method for performing colorectal resections when compared to conventional laparoscopy when considering operating time, conversion to open laparotomies and patient outcome [39], although this should only be performed by surgeons with high laparoscopic skills [40].

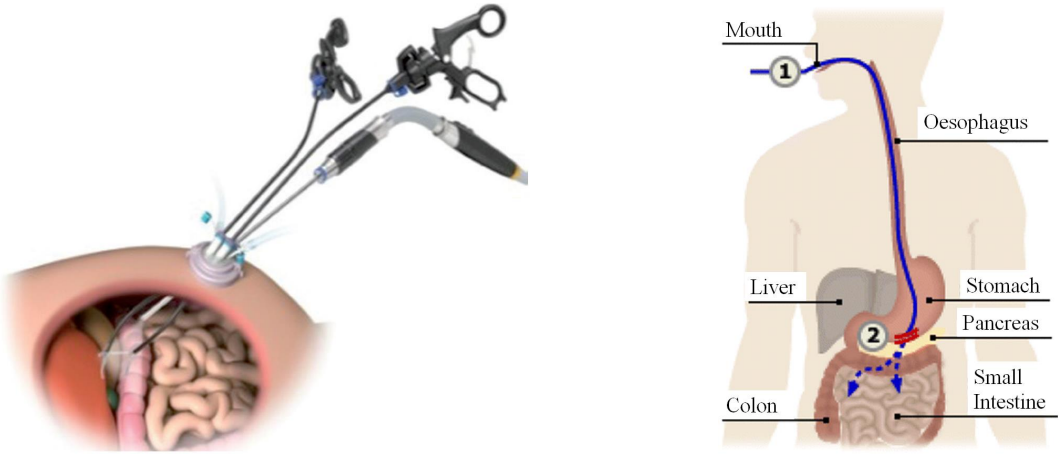

(a) (b)

Figure 2.3: Examples of novel access techniques in MIS; (a) SILS highlighting the single required port and modified/bent tools [41], and (b) NOTES showing an example of oral access through the base of the stomach [42].

Another novel aspect of MIS currently being developed is Natural Orifice Transluminal Endoscopic Surgery (NOTES), in which access to the surgical site is gained by entering the body through a natural opening, either orally, or via the anus or vagina, further reducing visible scarring (Figure2.3b) [43]. As with the SILS technique, there is an improved aesthetic outcome and reduced pain, but this method also prevents the potential for hernias occuring during the recovery process due to the abdominal wall remaining intact [32]. From this further developments have combined endoscopes with conventional MIS tools, miniature graspers and biopsy devices with the aim of reducing the number of requred ports [42, 44]. These give back dexterity to the surgeon and allow difficult areas to be reached without the need to add extra access ports [45]. However there are still difficulties with the tools as greater skill is required above SILS to control the steerable endoscopes, which are used to navigate through the access channel.

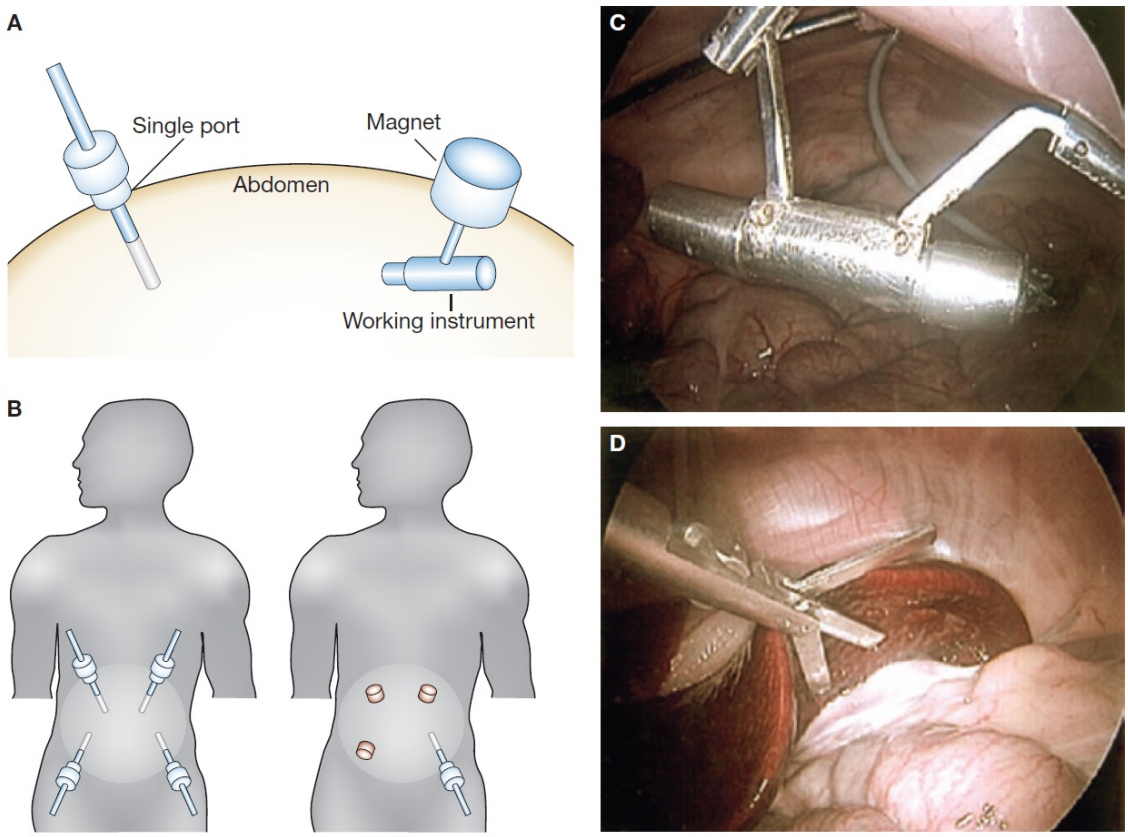

Figure 2.4: An example of the MAGS device, showing (A) a schematic of the MAGS positioning relative to an instrument port, (B) the potential port reduction, requiring a single access to insert the tools and multiple locations possible, (C) the MAGS device in place, secured to the abdomen wall, and (D) a cutting tool attachment in use while held by the MAGS [8].

Instead of performing a purely NOTES procedure, often it is combined with conventional laparoscopic techniques which assist in some of the more technical aspects of surgery,

including mini-laparoscopic surgery which uses tools of diameter 3 - 5 mm, thus reducing the incision length and maintaining the aesthetic benefits [46]. New devices are also used to assist the surgeon while keeping the number of incisions to a minimum. The Magnetic Anchoring and Guidance System (MAGS) (Figure 2.4) can be used to secure either an internal camera, a tissue retractor or a robotic cauterizer, and can be used alongside SILS or NOTES, removing the need to add extra ports and allowing easier access by reducing the number of port tools required [8, 41]. However this system is still in early development and can often be difficult to control or secure in position, with future designs looking to address these issues.

(a) (b)

Figure 2.5: Miniature MIS robotic cameras; (a) a wheeled camera for traversing the internal environment [47] and (b) a stationary camera which is placed internally and can then rotate the camera module for the optimum view [48].

Miniature robotic devices are also currently in the early stages of development to be used in conjunction with SILS and NOTES techniques, with the aim of reducing the number of required ports while maintaining the dexterity and abilities of the surgeon [49]. The devices include miniature cameras (Figure 2.5) for alternative views of the surgery [48], and also biopsy robots (Figure 2.6) which are able to traverse the abdomen or colon, extend a biopsy tool to remove a sample, then return to the port site [50]. Other miniature robots may act as an extra laparoscopic tool, with the capability of grasping and cutting [47]. Various locomotion techniques have been developed to tackle the issue encountered when trying to remotely navigate *in-vivo*, such as traction wheels, vacuum suction to pull the device, and Shape Memory Alloy (SMA) transducers which extend and retract, creating a pulsating motion to carry the device along [51, 52]. There are still a number of issues to overcome before a fully versatile design is created, therefore due to the non-uniform nature of the viscera and the difficult environment, medical robotics is still not fully dependable.

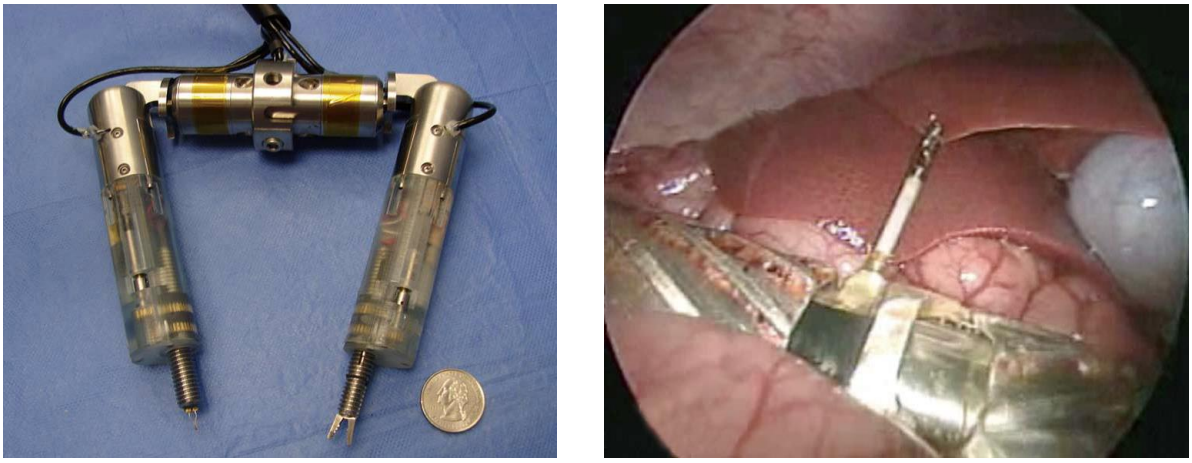

(a) (b)

Figure 2.6: Miniature MIS biopsy robots; (a) an armed device for improved manoeuvrability and access [47], and (b) a wheeled device with biopsy attachment [48].

Previous advancements in MIS technology, techniques and tool design have aimed to address difficulties experienced during procedures by the surgeon and post-operatively by the patient. However with such a large area of potential research, current techniques are being investigated to determine what needs to be understood and developed until these novel tools are commonplace. One key area of this is understanding the design and functionality of commonly used laparoscopic graspers, what their limitations are and what improvements can be quickly and easily implemented. Current MIS tools will be around for the foreseeable future and there is significant potential for improvement through optimising these.

2.2 Minimally Invasive Surgical Graspers

One significant disadvantage in MIS experienced by the surgeon is the unavoidable use of small tools, as opposed to their hands, in the manipulation of organs and performance of the different tasks required. The severely reduced haptic feedback and complete loss of the surgeon's ability to palpate organs have lead to further advancements by the manufacturers in the tool development to ensure a reliable design to reduce slipping, improve ergonomics and to simplify tasks such as suturing, cauterising and stapling.

2.2.1 Grasper Designs

By interviewing a number of experienced surgeons it has been understood that the main role of surgical graspers is for tissue manipulation and organ retraction, which involves grasping the organ and pulling, typically to hold the tissue out of the view of the laparoscope and stretch out organs for dissection (Figure 2.7), the second of which requires the largest

retraction force to be placed on the organ by the grasper to ensure the task is carried out safely [53].

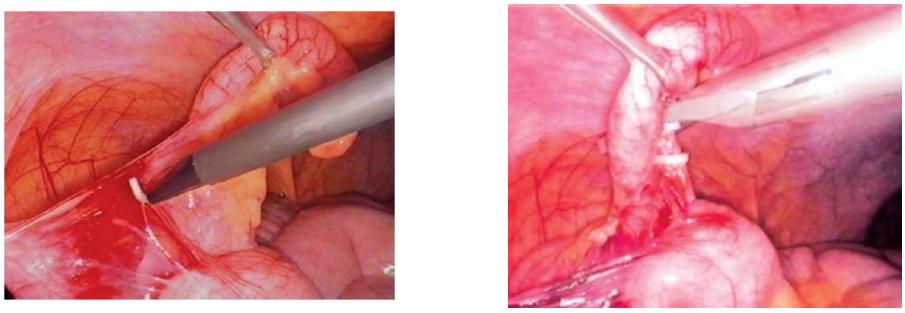

(a) (b)

Figure 2.7: Examples of abdominal MIS tissue manipulation with graspers; (a) *in-vivo* manipulation to expose tissue, (b) stretched tissue suspended during stapling dissection.

Laparoscopic grasper manufacturers generally use similar grasper designs (Figure 2.9), and typically used the same rolling link mechanism (single action graspers) or scissor linkage mechanism (double action graspers) to convert the linear motion into a grasping action (Figure 2.8) [54].

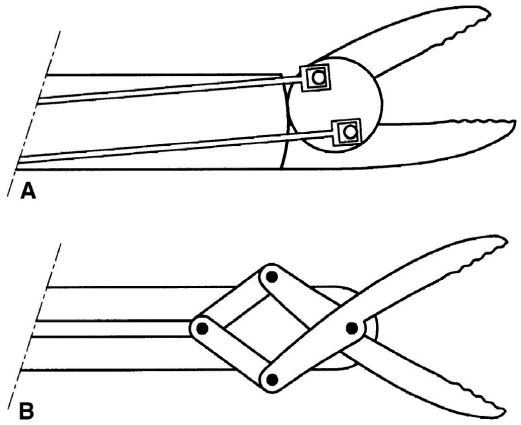

Figure 2.8: Two examples of grasper mechanism design; (A) a rolling link mechanism (single action), and (B) a scissor link mechanism (double action) [55].

When manufacturing laparoscopic graspers, several design parameters firstly need to be considered [56]. With regards to the type of material, if a tool is designed for multiple uses, then the material should be able to withstand sterilisation and still function reliably afterwards, typically stainless steel is used. Single use items however are designed to be disposed of. The design should also consider if it is to be atraumatic, as the manipulation of delicate tissue using traumatic graspers (Figure 2.9a) will cause serious trauma. Fenestrations are usually added to prevent this (Figure 2.9b). For some tools it is necessary to be traumatic (Figure 2.9c) to ensure non-biological items can be removed easily, e.g. to removed resected

tissue, it is placed inside a bag and drawn out through the laparoscope port, using a traumatic grasper to ensure it is not dropped, compared to graspers which are used to retract and hold organs or tissue (Figure 2.9d). They have been designed to allow the surgeon to grip tissue during surgery while attempting to reduce the amount of trauma caused as much as possible. A large variety of different graspers exist to provide the surgeon with as much choice as possible to perform each surgical task.

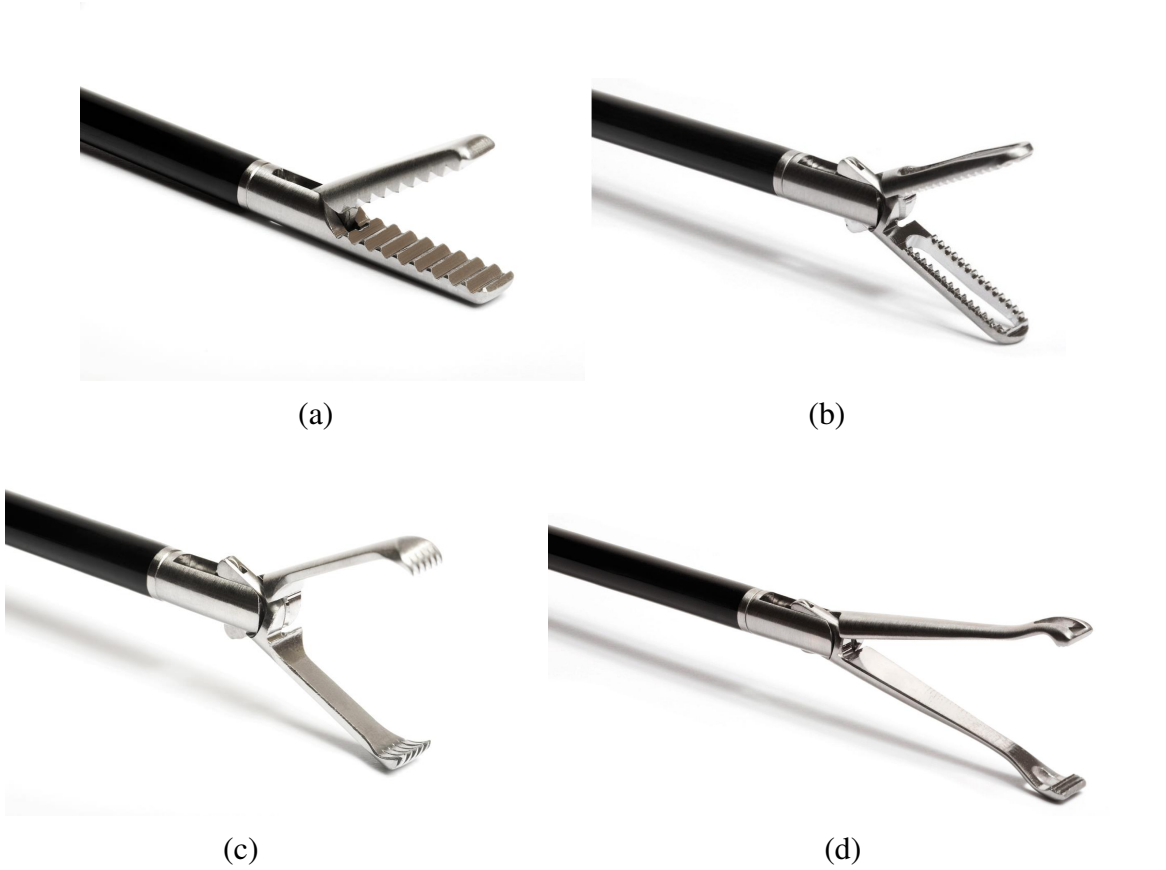

(a) (b)

(c) (d)

Figure 2.9: Surgical Innovations Ltd. reusable laparoscopic grasper examples; (a) crocodile forceps (traumtic), (b) short fenestrated (atraumatic), (c) fine toothed forceps (traumatic), and (d) babcock (atraumatic).

The reusable tools are designed as individual modules which can be separated for cleaning and the resposable tools (reusable handle with disposable tool-tip) again allow the reusable parts to be disconnected and cleaned. Other commonly used grasper designs have slight variations in the shape, length and diameter (5 mm and 10mm, and new 3 mm) and whether they are single or double action. It can be seen that there are significant differences in grasper designs, such as tooth profile, shape and scale. Careful consideration should be made when selecting a tool as these different factors will greatly influence how damage is caused and how the force is transferred from the handle to the tool tip.

(a) (b)

Figure 2.10: Surgical Innovations Ltd. laparoscopic grasper handles; (a) pistol grip and (b) horizontal handle.

The traditional design for laparoscopic handles (Figure 2.10a) has faced much criticism over the poor ergonomic design, causing discomfort for the surgeon after prolonged use. New ergonomic designs (Figure 2.10b) are becoming increasingly popular due to the more natural hand position. Both types also include a ratcheted version to allow an area to be clamped and held, without requiring the surgeon to maintain this force.

2.2.2 Grasper Mechanism Analysis

To provide surgeons with a better understanding of how the handle movements and forces relate to the tool tips, mathematical modelling and kinematic analysis of graspers under different conditions have been investigated. A grasper's performance can affect the user's gripping ability when manipulating tissue, as well as the likelihood of the tissue slipping, often resulting in the surgeon overcompensating and increasing the potential for trauma [57]. By investigating the relation of the handle motions and forces to the tip parameters, research has highlighted previously unknown issues with laparoscopic graspers. Mathematical models have been developed [58], to benefit the optimisation of MIS tools as well as analysis of the forces involved during tasks [59]. When compared to open surgery, surgeons have a tendency to apply too much force for too long during MIS, to be certain the tissue will not slip. This is due to the fact that the geometry of the tool and transmitted forces differ to that of the surgeon's hand, and even though it is still possible to differentiate between objects of varying hardness certain techniques need to be re-learnt [60]. The effect of this has been explored by asking 10 novices to perform barehanded and laparoscopic lifts, while the grasping and pulling forces were monitored by the artificial tissue, using a force sensing lining and loadcell, which generated a random resisting force. The results showed that all participants could perform a safe lift when barehanded, as they were able to compensate during the grasp. However the laparoscopic data showed that 38 % resulted in slippage, with frequent high forces of up to 7.9 N at the tip (compared to 2.5 N for a barehanded grasp) [61].

One analysis shows an experimentally determined relationship between the handle angular movement (β) and the grasper jaw angular movement (θ) for a scissor linkage (double action) mechanism (Equation 2.1) [62]. This suggests a linear relationship between both parameters, but a relationship that the surgeon can only appreciate after practise.

$$\theta = -12.55\beta + 41.70 \tag{2.1}$$

However it has also been shown that there is a non-linear relationship between the inner shaft forces and the output forces for various jaw opening angles [63], suggesting that different handles and grasper geometries will not always provide a linear relation between the handle and tip [64, 65]. In a situation where infrequent grasping is needed, tools with low mechanical efficiency (high hysteresis) are suitable, but for repeated opening and closing, a high mechanical efficiency (low hysteresis) is better [66]. It is key to understand the force transmission relation in scissor linkage tools [67], but for a fully defined system the response of the material is also required [68].

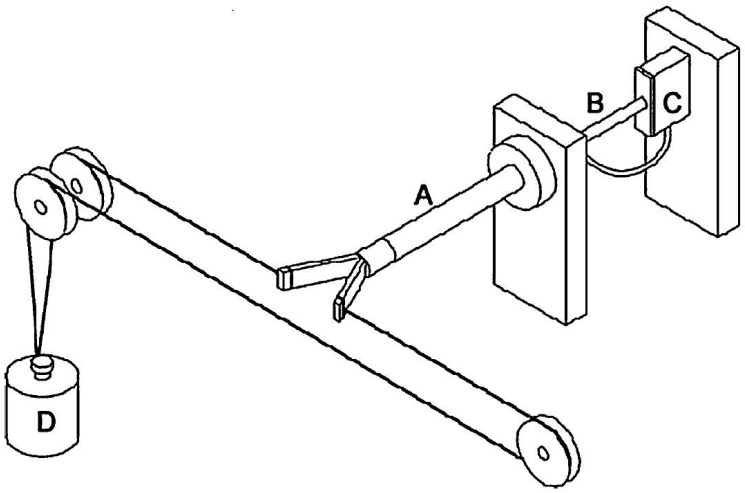

Figure 2.11: Laparoscopic grasper force transmission rig, highlighting the locations of (A) the grasper, (B) the connecting rod, (C) a linear force sensor, and (D) the applied weight [63].

One research group sought to experimentally characterise the relationship between input and output forces of laparoscopic graspers. The tool was held in a rig, with a force sensor along the internal linkage and a pulley weight system to apply force directly to the grasper tip (Figure 2.11) [63]. However this set-up does not consider the angle of the jaws which are likely to affect the transmitted force. Altering the fenestration design can affect the retraction force and tip pressures [69], and by varying the meshing abilities of the fenestrations, the slip properties have been investigated [57]. Pressure distribution differences for grasper profiles have shown the patterns of failure for varying fenestration designs [53, 70]. By increasing

the number of fenestrations, the potential damage can be reduced [71], and by altering the profile of the fenestrations to hemispheres rather than teeth, again the pressures on the grasped area can be limited [58]. Also depending on the angle at which the grasping plane is to the tissue surface, the pressure generated can spike to over three time greater than average possible pressure between a surgeons index finger and thumb (for an angle up to 135° from parallel) [72]. Another comparison describes differences between laparoscopic tools and surgical forceps [73]. Even though the use of surgical forceps differ from hand palpation, there is still a considerably larger force being used with laparoscopic tools. Key features of typical laparoscopic graspers have been investigated to provide surgeons with a further understanding of their functionality. From this analysis improvements can be made to the designs to overcome issues such as non-linearity and mechanical efficiency.

2.2.3 Laparoscopic Grasper Design Improvements

To improve some of the apparent issues with laparoscopic grasper designs, a variety of different mechanisms and materials have been investigated. Improvements of the grasper tip mechanics allow for more precise movements (Figure 2.12), but this will again require the surgeon to relearn manipulation forces and limitations of the design, potentially leading to further overcompensation [74].

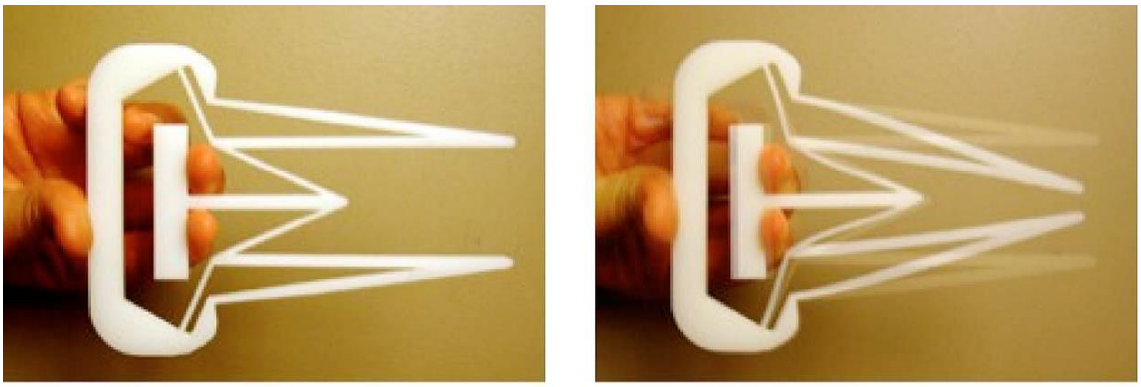

Figure 2.12: Design and grasping function of a compliant mechanism for surgical tools; open (left), closing action (right) [75].

Some designs have attempted to mimic the human hand, known as Hand Assisted Laparoscopic Surgery (HALS) (Figure 2.13), which is then assembled internally to retain the small incision size. These typically consist of three appendages allowing for tasks such as grasping, pushing organs aside, pinching, and opening [76, 77]. The tools used during HALS need to be assemblable to maintain the size of the port holes, however this increases the time spent in the OR [78].

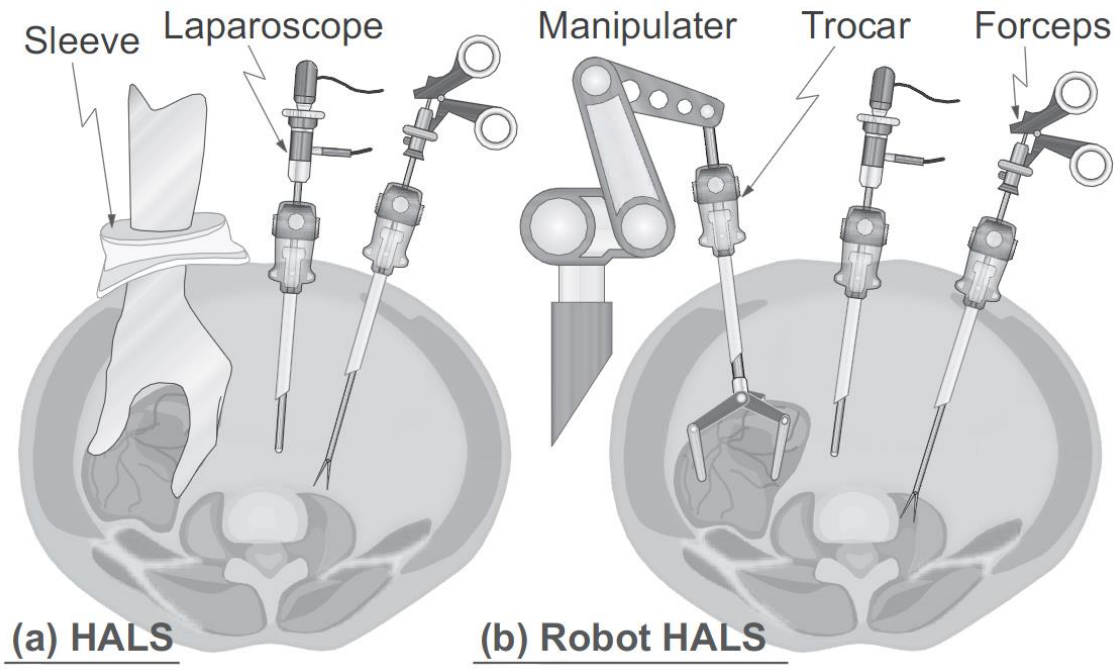

Figure 2.13: The comparison between (a) conventional HALS, and (b) robotic HALS [76].

Multi Degree Of Freedom (DOF) designs allow for access to larger areas and improve dexterity through typical sized incisions [79]. These types of graspers still require advanced training by the surgeon to fully benefit, and often require an external power supply. For a reliable substitution, a secure fail safe is needed in case of power or mechanism failure. Multifunctional devices combine the functionality of different tools, such as cutting and grasping devices, potentially reducing the number of ports needed as well as limiting the time spent switching between tools [80]. These devices, like the traditional designs, still need refinement and could potentially complicate the force transmission relation further [81]. Modifications to the grasper materials show a reduction in stresses and improved contact area, making manipulation safer and more reliable [75, 82, 83]. Considerations for the ergonomics of the handles have led to new designs to improve the efficiency and comfort in prolonged procedures but can often greatly change the functionality and motions related to grasping, requiring the surgeon to relearn these tasks [84].

While many advancements have been made in the manufacture of conventional laparoscopic tools there are still many unknown factors which can affect surgical performance. Modifications to traditional graspers still require an understanding by the surgeon as to the force propagations. Investigation of the tissue/tool interface and identifying how the tissue responds under grasping conditions is key to determining the magnitude of damage and how this can be reduced.

2.3 Abdominal Tissue Analysis

By analysing the grasped tissue as opposed to the tools, models can be made to provide better information to designers, surgeons and researchers. One major issue to consider is how the tissue will react when forces are applied. In abdominal surgery there are different organs with varying stiffness and damage thresholds, and for organs like the colon, there are numerous layers to the tissue which will respond differently to manipulation forces (Figure 2.14).

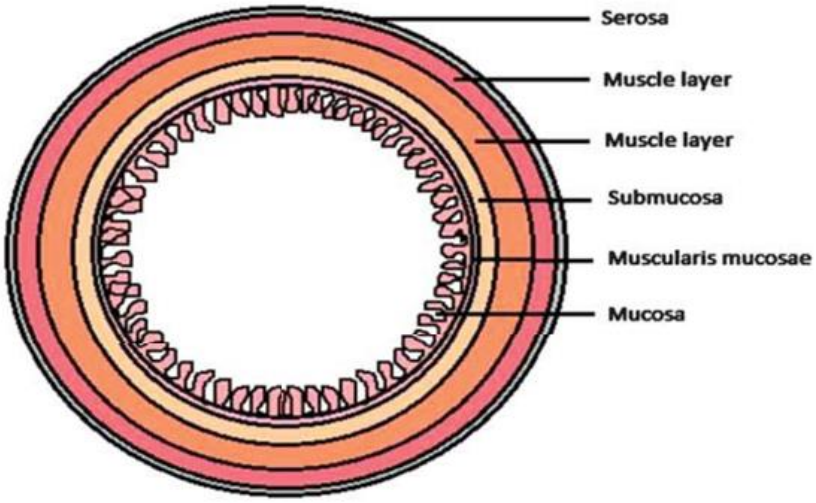

Figure 2.14: The cross section of a colon sample showing the connective tissue, muscular layers, submucosa, and mucosa [85].

2.3.1 Rig Designs Used to Investigate Tissue Characteristics

A number of tissue rigs have been developed to investigate tissue characteristics and understand the underlying mechanics at the tissue-tool interface. A typical indenter rig requires the tissue sample to be placed under an indenting arm with an attached force sensor. As the arm is extended into the sample, the force response of the tissue is measured (Figure 2.15). A test rig has been developed for *in-vivo* indentation testing, allowing tissue characteristic measurements to be measured during surgery [86]. This can provide results closer to *'true'* values, as there is greater control of the indentation motion, compared to that of a surgeon. Reliability of the results however, could be compromised by effects from other organs surrounding test site, if they were to move during the indentation, affecting instrument measurments. Typical rigs are uniaxial, i.e. they have only one DOF. However those with multiaxial designs allow for more parameters to be measured with a single device [87]. Where indenter rigs tend to measure compressive responses of tissue for scenarios such as grasping, tensile rigs aim to measure the tissue's response to being pulled or stretched, typically during

dissection or when inserting a tool. Other rigs also allow for a combinations of compression, sliding and rolling over the tissue using different test surfaces.

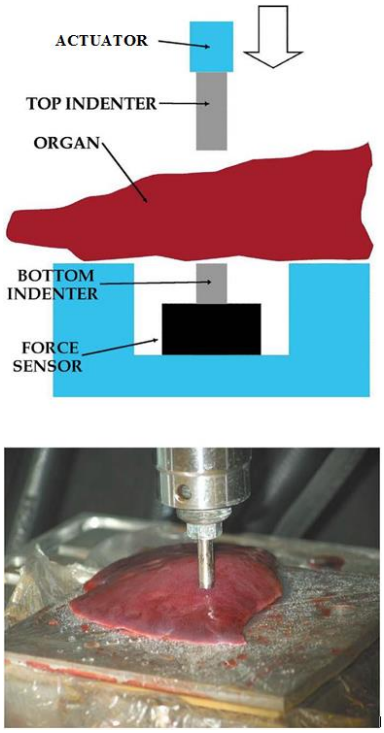

Figure 2.15: Single DOF tissue indentation rig to measure tissue response; schematic (top), indentation test on liver sample (bottom) [88].

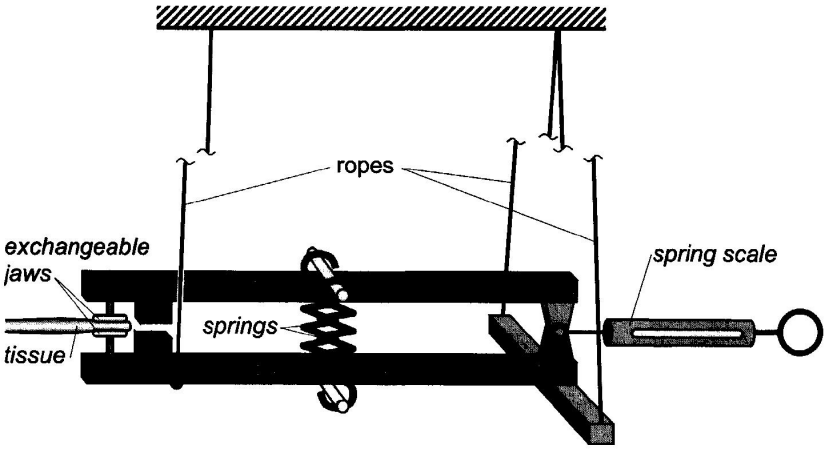

Figure 2.16: Test rig to measure the grasping properties of fenestrations on tissue [53].

Current *ex-vivo* test rigs can be used to simulate typical *in-vivo* scenarios, to analyse the tissue mechanics and damage, as well as investigating the implications of particular surgical tools. This *ex-vivo* approach is beneficial as it can provide a controlled set-up, for higher reliability of results, when compared to *in-vivo* testing [63]. Other test equipment has been designed to incorporate different grasper profiles to apply to tissue samples. This can

include various types of fenestration designs to advise design improvements to manufacturers (Figure 2.16) [53]. Tests have been designed to measure the various properties of tissue, but understanding what this data is showing will allow for improved grasping ergonomics and identification of tissue damage.

2.3.2 Modelling the Mechanical Properties of Tissue

Due to the complexity of biological structures, it can often be difficult to model their mechanical characteristics, but it is essential to understand how the tissue will respond during procedures [89]. It is crucial to understand how biological structures behave under different conditions, as this can indicate anomalies such as tumours or ruptured tissue. Analysis has been carried out on modelling tissue response from force data collected. This is particularly useful for Virtual Reality (VR) simulators, to ensure simulated organs will respond in the same way as actual tissue, giving a more realistic simulation, and improving a surgeon's ability to learn [90, 91]. Modelling the mechanics is made especially difficult as the tissue samples are usually made of several different layers, each typically with their own mechanical properties [92]. Researchers have attempted to model fibrous tissue and incorporate a more complex system into the models [93]. Work has also been carried out to observe the different properties of the intestine, showing the mechanical properties of the muscle layers and mucosa [94]. This work highlights the variation in each and how the different cellular structures give rise to particular attributes, namely the structure of the collagen in the mesocolon which contributes to an increased rigidity.

Various methods are being developed to determine the mechanical properties of tissue. This is a difficult task because, unlike silicone for example, tissue does not have predictable, uniform properties. Over a small area of tissue, there can be different blood vessels, glands, and fatty deposits, which are distributed unevenly. Researchers have attempted to model factors such as elastic modulus [95, 96], shear modulus [97, 98], and stress and strain properties [99, 100]. The Young's Modulus of tissue was investigated by using electron microscopy and confocal microscopy to analyse the microscopic structure of the tissue [101]. From this, the cell structure behaviour and the different stresses involved are estimated to determine when the tissue will be damaged. To analyse the tissue properties, the samples are sometimes preconditioned where repeated stress-relaxation cycles are performed on the samples. This is believed to affect the mechanical properties of tissue by stretching the fibres, gradually breaking down the cellular structures, and as a result reducing how much stress the sample can endure [102]. By performing different types of preconditioning methods, it was observed that there are slight changes in the tissue's stress-strain response. Typical values of the Young's Modulus for soft tissue have been measured and shown to range from approximately 1 kPa [101] up to 6.7 kPa for relatively low strain rates ($\dot{\varepsilon} = 0.002s^{-1}$).

However by increasing the strain rate to the order of $\dot{\varepsilon} = 1000s^{-1}$ the modulus increases by more than three orders of magnitude to 3 MPa [101].

However elastic modulus calculations show a maximum measurement error of 14 percent, again highlighting the variability when using tissue [95]. Calculations of the shear modulus of tissue have been performed to estimate how the tissue will respond to a compression [97]. Physical measurements have also been taken, and by applying a compressive load to the tissue and observing the visual deformation, it was concluded that cell deformation played an important factor in cell damage, with length of compression also attributing to the level of trauma [103, 104].

Lumped parameter models are often used to describe the behaviours of different types of tissue. Although physically they do not represent the tissue structure, when a force is applied, the element can mimic certain properties.

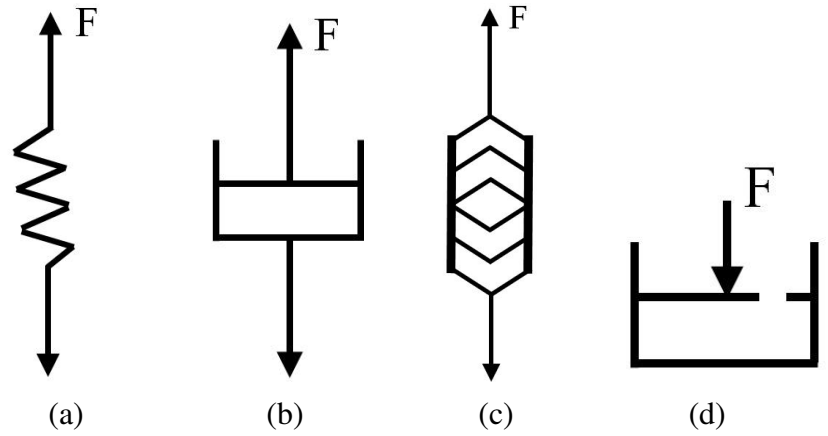

Figure 2.17: The four typical lumped parameter models; (a) a Hookian spring element, (b) a damping element, otherwise known as a viscous dashpot, (c) a contractile element, and (d) a Darcy or permeability element [92].

A tissue's elastic response is represented as a spring element (Figure 2.17a), where an applied force F, results in an instant deformation, proportional to F [92, 105]. The viscosity of a tissue uses the dashpot element (Figure 2.17b), where the applied force results in constant velocity dependant on the magnitude of F [92, 105]. Other designs include the contractile element (Figure 2.17c) which mimic muscle response, where the element contraction results in an applied force. This is observed when the muscle nerve is stimulated, and the resulting force is measured as the muscle contracts and relaxes (Figure 2.18). The Darcy element (Figure 2.17d) simulates when an applied force results in a pressure difference in the chamber, pushing the fluid out, usually used to represent single fluid filled cells, or the movement of fluid. The two latter elements will not be further considered in this work as they are not typically used to describe tissue responses of those observed in abdominal surgery.

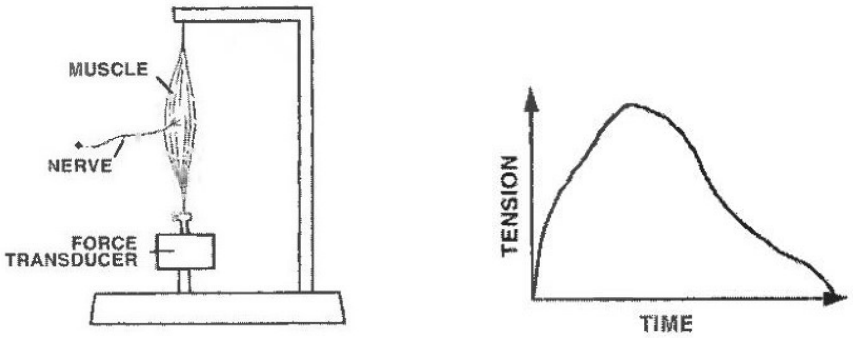

Figure 2.18: A muscle excitation experiment, showing (a) the diagram of the set-up, and (b) the resulting tension over time [92].

The spring and dashpot elements are usually combined in various configurations to show different attributes of tissues [105]. The Maxwell model (Figure 2.19a) uses a single spring and dashpot element placed in series, to simulate a material with an initial elastic response, followed by gradual motion with no final limit, typically for very soft tissues such as brain matter. The Voigt model consists of a single spring dashpot in parallel, where the motion of the spring is restricted by the rate at which the dashpot moves, and the final extension of the model is limited by the spring, typically used to describe higher resistant materials such as bone or cartilage [106, 107].

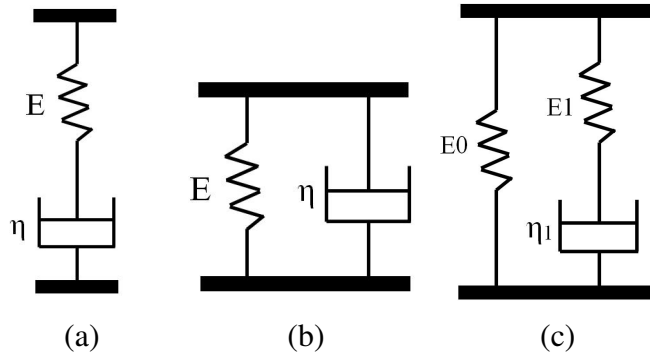

Figure 2.19: Tissue mechanics model configurations using the spring-damper elements, showing (a) the Maxwell model, (b) Voigt model, and (c) the Kelvin model [92, 105].

A Kelvin model (also known as the standard linear model) uses a second spring in parallel with the Maxwell model (Figure 2.19c). This gives a similar response to the Maxwell model, but the full extension is limited by the spring element, as with the Voigt. This design is typically used to describe viscoelastic materials such as abdominal organs, with soft or stiff organs such as colon or lung, respectively, modelled by varying the parameter values.

By analysing these models under various circumstances, their properties can be observed. By applying a constant force the models continue to deform. This shows the creep associated

with it. In the Maxwell model (Figure 2.20a), an immediate deflection can be seen as a result of the spring element, followed by the steady motion of the dashpot. This deflection is seen again as the force is immediately reduced. The resultant deformation from the motion of the dashpot is permanent, as there is no returning force. For the Voigt model (Figure 2.20b), after the force is applied there is no immediate motion, as this is restricted by the dashpot. The rate of deformation will gradually reduce however, as the spring element takes an increasing amount of the load, giving the limit of the deformation. Once the force is removed, the model will return to its original position, as the retracting force from the spring, moves the dashpot. For the Kelvin model (Figure 2.20c), a similar result is observed, with an initial deflection from the single spring element, followed by the exponential response from the spring-dashpot series. The maximum deflection of this model is also limited by the single spring element, which also returns it to the start position once the force has been removed, also with a sudden response from the spring [105]. This type of test can be performed typically using an indenter rig, or similar, and by observing characteristics such as the initial gradient after release, factors such as the material hardness can be found (Figure 2.21) [108].

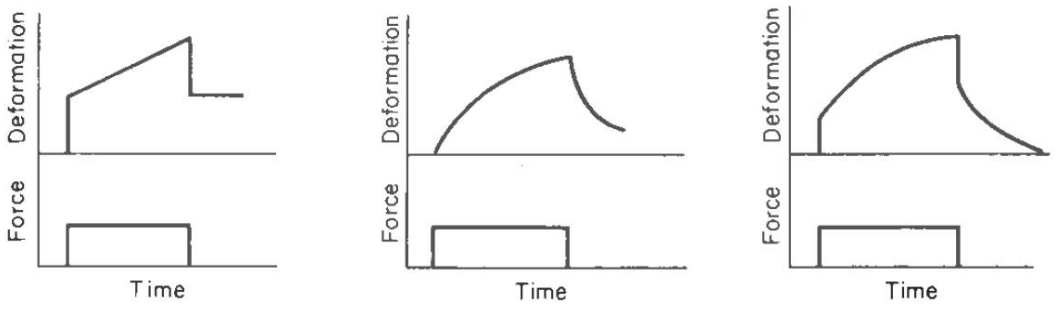

Figure 2.20: The creep functions, for loading and unloading, of (a) the Maxwell, (b) the Voigt, and (c) the Kelvin model [105].

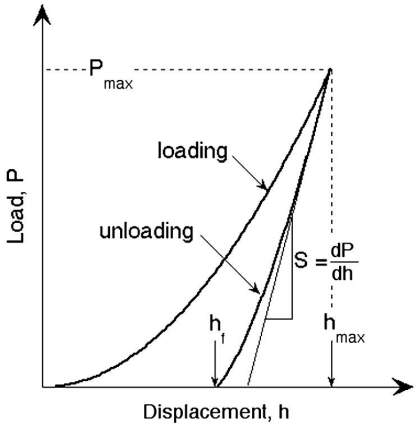

Figure 2.21: A typical indentation profile showing how the hardness, *S*, is found from the initial gradient of the unloading curve [108].

By applying a constant deformation, the corresponding force induced in the models decrease with time, showing the associated relaxation. In the Maxwell model (Figure 2.22a) the sudden deformation causes an increase in force from the dashpot, resulting in an immediate reaction from the spring element, followed by the exponential response from the dashpot. The force tends to zero as the dashpot moves. For the Voigt model (Figure 2.22b) a sudden deformation results in a very large force as there is no inital movement, due to the dashpot. This is theoretically infinite, for a step deformation. The overall force will decay exponentially until the spring reaches its limit giving the resultant force, which is then maintained. For the Kelvin model (Figure 2.22c), as with the Maxwell model, an initial increase in force is observed due to the dashpot. The relaxation is similar to the Maxwell model, except that the resultant force does not tend to zero. Instead it reaches the limit of the single parallel spring element, ending with a resultant force, which is then maintained, as with the Voigt model [105].

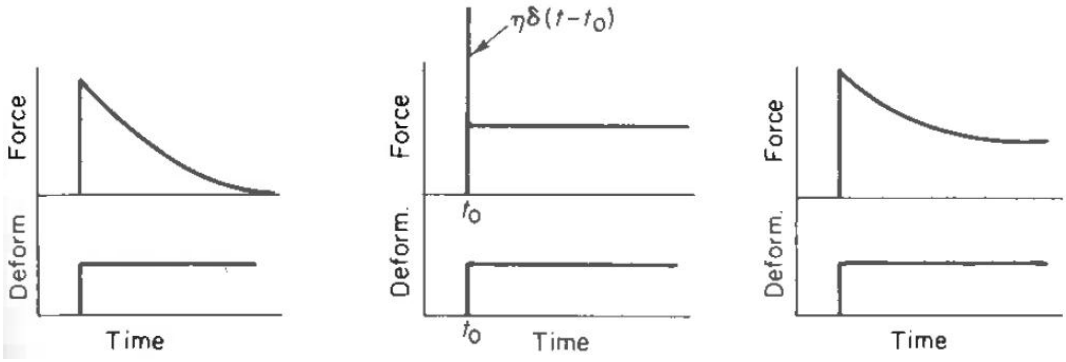

Figure 2.22: The relaxation functions, of (a) the Maxwell, (b) the Voigt, and (c) the Kelvin model [105].

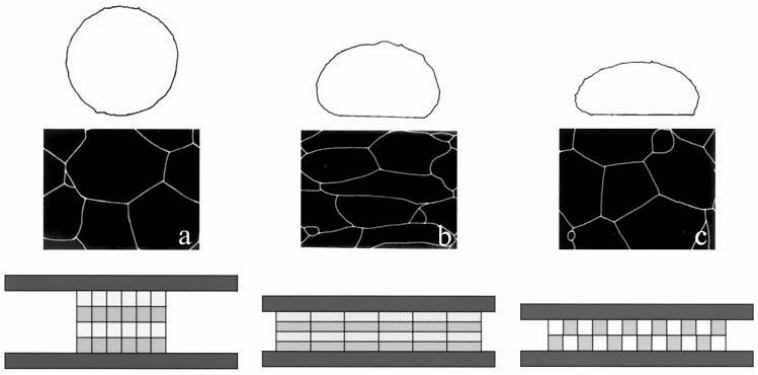

Figure 2.23: Tissue relaxation from top to bottom is the sample, the cell outlines, and the cell structure schematic, highlighting (a) the sample under no load, (b) the sample under 2000 $\times$ gravity applied over 5 minutes, and (c) the sample under 2000 $\times$ gravity applied over 36 hours [109].

Researchers have observed the cellular structure of tissue under different loads to further understand how they respond, and how this may affect mechanical measurements [109]. With an initial force applied, the cells are stretched, but given long enough to recover, the cells attempt to return to the original structure (Figure 2.23).

Another observation can be found using cyclic testing to show the hysteresis or energy loss of the tissue. Researchers varied the stimulation frequency to determine particular factors including time response [110]. By stimulating tissue *in-vivo*, the forces and motions present in typical MIS were replicated to generate stress/strain graphs of different organs, such as the liver, bowel, spleen, and stomach [88]. Other research into organ tissue properties involved stimulating the tissue under different circumstances. Finite element models were then made to show varying stresses and contact pressures [71]. A viscoelastic model was used to characterise the tissue, and then using a micro-machined piezoelectric sensor the tissue properties could be measured [111]. From this, approximations could be made about the mechanics of the tissue; however this is only generalized and assumes uniformity throughout [112].

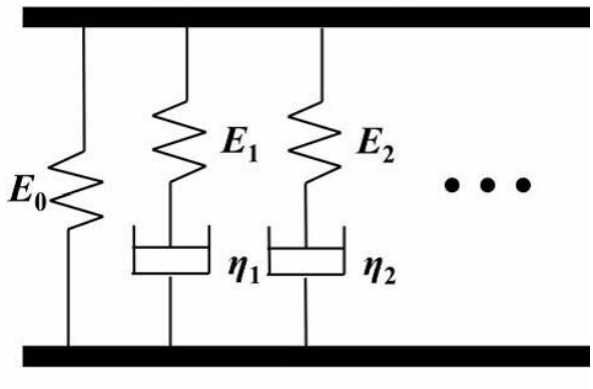

Figure 2.24: The Wiechert model typically used to model viscoelastic tissue properties, comprised of a single spring element E_0 in parallel with i number of Maxwell models (a spring E_i in series with a dashpot η_i) [113].

Typically force relaxation observations lie closer to *in-vivo* scenarios as the surgeon would grasp the tissue and maintain the position using a ratchet, therefore this will be the focus of this work. Developments in soft biological tissue modelling have led to advancements into the most suitable model configurations [92], and have given rise to the use of a five element model known as the Wiechert viscoelastic model (Figure 2.24). This uses five parameters to define the stress relaxation in the samples response. The E_0, E_1 and E_2 parameters show the elastic elements of the samples, with η_1 and η_2 giving the viscous elements. This model allows for the fact that tissue relaxation does not occur at the same time, but over a period of time. Additional Maxwell configurations can be added in series with the Wiechert design to give increasingly complex models. Typically the Wiechert model is the most suitable

for modelling viscoelastic materials such as abdominal tissues, as previous research has shown this provides the closest response fit, when compared to the Maxwell, Voigt, or Kelvin models, yet has the least complexity over 7, and above, element models [113] [114].

The Wiechert model can be represented as an equation (Equation 2.2) where the values of the time constant τ_i are found from the stiffness E_i and viscosity η_i (Equation 2.3) [114].

$$E(t) = E_0 + E_1 e^{-t/\tau_1} + E_2 e^{-t/\tau_2} \tag{2.2}$$

$$\tau_i = \eta_i / E_i \tag{2.3}$$

The single spring element E_0 describes the initial instant relaxation observed in the response curve, demonstrating the tissue's elastic response, as this has no viscous element, and hence no time coefficient. The spring-dashpot combinations, E_1, η_1 and E_2, η_2 represent the middle and final stage of relaxation. Typically E_1 should be greater than E_2 as the middle stage is still exhibiting elastic behaviour, but with an increasingly apparent viscous component. Also η_2 should be greater than η_1 leading to a greater time constant τ_2 which is the remaining component of relaxation over the final stage of the response [109]. The value of $E(t - \tau)$ physically represents the decaying effect of the strain at a time τ before the current time t on the current stress [115]. This is typically used to determine soft tissue characteristics with the model parameters being investigated for various organs (Table 2.1) [109]. To extract additional information from the viscoelastic response, such as the Young's Modulus or hardness, the stress-strain curve must be analysed, and the relaxation gradient typically used. This can often give large discrepancies when using materials like tissue.

Cell Type	E_0	E_1	E_2	μ_1	μ_2
Neural retina	1.6 ± 0.5	3.4 ± 0.5	2.1 ± 0.3	7.3 ± 1.0	55.2 ± 9.5
Liver	4.6 ± 0.1	4.0 ± 0.6	2.3 ± 0.4	7.6 ± 1.5	49.6 ± 13
Heart	8.5 ± 0.2	5.1 ± 0.6	2.5 ± 0.3	9.5 ± 1.2	66.0 ± 17
Limb	20.1 ± 0.5	8.6 ± 1.3	7.7 ± 2.6	23.5 ± 4.4	341 ± 116

Table 2.1: Values of the model parameters for varying organs [109]

Often human cadaver tissue is used for investigating tissue properties, to give biologically accurate measurements, but properties such as viscosity and hardness are greatly affected by how fresh the tissue is and the method, if any, of preservation [99, 116]. Analysed tissue types include the small intestine [117, 118], colon [119], liver [120] and the rectal wall [121]. Due to the large variations in abdominal organ properties, each needs to be understood. Methods for investigating tissue properties include contact analysis, where a known surface

is brought into contact with the sample for a predetermined time and/or at a certain pressure [58], and similarly soft indentation where the known profile of an object is used to indent the sample, and the response is measured [122]. Properties which have been investigated include the elastic modulus of tissue, or the samples resistance to deformation [96, 123, 124], surface deformation for varying forces [125], the friction of the sample surface, particularly useful for retraction [126], and cell mechanics which considers all the previously listed characteristics, but on the microscopic scale, with the intention of extrapolating to a full model [127]. Analysis of animal models allow for easier testing and control over subjects, in particular porcine tissue which shares some similarities to human tissue, in that they exhibit a biological visco-elastic material, with typical similar deformations [66, 128]. Animals include porcine and rat models to have been investigated, with the larger sized porcine model often used to train surgeons [129, 130]. One benefit of modelling is the ability to show tissue abnormalities [98] such as cancerous tissue, as despite being able to determine the exact characteristics of cancers, they are different enough to be detected. Other aspects include cancer cell nanomechanical analysis, again drawing from typical cell mechanics, and extrapolating to full scale [131]. Tissue response analysis has allowed the development of synthetic materials to mimic certain properties, again allowing easier access for testing and training [132, 133].

Initial investigations have aimed to model the properties of varying organs when damage has been induced. This is often done using appropriate simulations of the tissue, but could lead to potential significant errors, as these assume an ideal tissue structure [134]. Another investigation has looked as the response of liver samples, as a needle is passed into it, to validate a modelling simulation [91]. This showed the need to use an increased complexity of model, as the response is not linear. Finally *in-vivo* measurements of the stress-strain curves of damage induced in the tissue have been measured [100]. The results have been compared to other means of damage, but still work is needed in identifying what is classed as damage. By investigating these properties and how tissue should behave under normal circumstances, advances can be made in determining the conditions for trauma to occur.

2.3.3 The Measurement of Tissue Damage

There are many parameters which can affect the likelihood of tissue being damaged even after taking preventative steps to avoid it [135]. Complications from severe tissue damage, although rare, can be life threatening [1]. To try and quantify the damage that has been induced in tissue samples by laparoscopic graspers (either *in-vivo* or *ex-vivo*), different methods of measuring damage have been found. Perforation forces of large pig bowel and human small bowel have been investigated using a similar parallel set-up to the work carried out on the fenestration investigation (Figure 2.16). The force is applied direct to the tissue

surface, with a system to measure the electrical continuity between each side of device. This indicates when both indenters (located at opposing sides of the sample) touch, to indicate tissue perforation [2]. This however does not show damage which occurs before perforation, which can still be of serious concern. The results showed that for large bowel (Figure 2.25), the average perforation force was 13.5±3.7 N, with a minimum force needed to perforate the tissue at approximately 8 N.

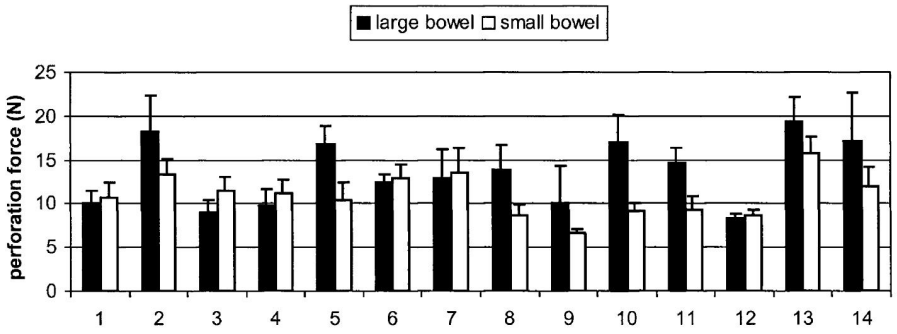

Figure 2.25: Comparison of the forces required to perforate both large and small porcine bowel tissue [2].

It was observed that there was initial superficial damage, and also damage at a cellular level, which was shown using histological techniques (studying the tissue at a microscopic level) [136]. Generally histological methods are more precise than macroscopic analysis as the sample is observed at a much smaller scale, however both techniques require human judgement as to the classification of damage. Physical discolouration can be analysed to give an indication of the damage (Figure 2.26), but can also be subject to individual interpretation or image properties (contrast, brightness, quality, etc).

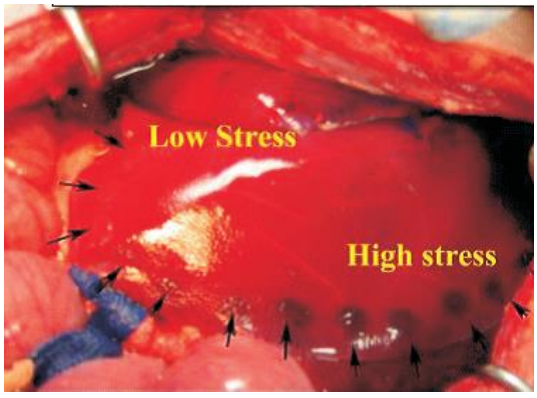

Figure 2.26: Example of local discolouration observed after increasing degrees of applied stress to show tissue damage [100].

Macroscopic analysis provides an indication of the severity of the damage and also the location. Bruising suggests damage to the blood vessels whereas bleeding would indicate

more severe structural damage. However it is difficult to accurately determine the cellular damage without performing a histological or microscopic analysis. Histological methods highlight various tissue structures that could potentially be damaged. By using a microscope, these structures can clearly be seen along with damage caused. Another method that has been introduced uses semi-quantitative image analysis so the amount of damage can be quantified in various terms, for example by counting the number of ruptured blood vessels, damaged cells, misshaped glands etc. Once the software has been taught what constitutes as damage, it will count objects which fit the criteria for each tissue sample.

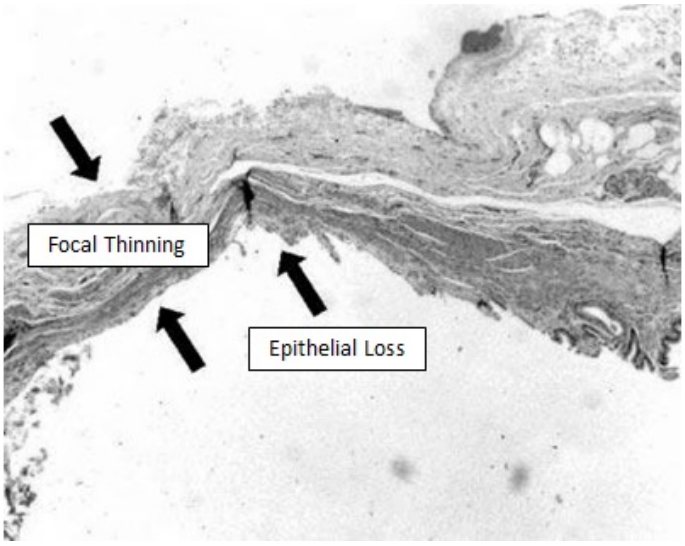

Figure 2.27: Focal thinning of the tissue sample, and epithelial loss (cell destruction) of the tissue layers [19].

Fast unloading can help to reduce the amount of trauma [71]. Different forces may cause damage to the tissue by rupturing the cells, damaging the mucosa and other structures, depending on the tissue type (Figure 2.27) [100]. By analysing the likelihood of a sample tearing, graspers can be optimised to try and prevent this. Such work has been carried out by testing different grasper jaw profiles when pulling tissue at varying forces [19]. However this will be highly dependent on the type of tissue used, for example colon samples can undergo larger stresses before tearing, when compared to delicate tissue such as mesocolon [66]. The application for tissue damage analysis can then be transferred to a surgical situation to try to improve results [137]. Research has been conducted into the amount of trauma experienced by patients undergoing either open surgery or MIS [138]. This is done by analysing four different chemicals (interleukin-6, interleukin-10, C-reactive protein and granulocyte elastase) present in blood before the surgery, and then six hours, one day and 2 days after surgery, to observe the body's response. After trauma to the body, these chemicals increase relative to the amount of trauma experienced. Also there have been investigations into the metabolic and inflammatory response [139]. The research shows that MIS, when compared to open

surgery, induces significantly less trauma. To ensure accurate results, human and pig tissue was also compared [2], with simulations carried out over the tissues failure points to highlight patterns of failure [134]. Investigations into tissue structure and response from grasping have shown that often tissue trauma is unavoidable and can be difficult to detect. By incorporating sensors into conventional laparoscopic devices, grasping forces and tissue responses can be investigated.

2.4 Current Research Developments in MIS Devices

One area of research which is still in it's infancy is the development and modification of the laparoscopic tools used for measuring various *in-vivo* parameters. This is most likely due to a number of factors, including difficulty to manufacture designs on a large scale, issues concerning safety regulation in the OR, and even the slow uptake from surgeons who are comfortable with their current methods. These developments span from the design of new transducers to convert the data from one form to another, to the instrumentation of traditional MIS devices. They aim to further understand the mechanics of surgery, as well as return information to the surgeon which would otherwise be lost from the conversion from open to closed surgery, known as haptic feedback [140]. An investigation into the benefits of haptic feedback highlighted that without it, the magnitude of the average force and peak force applied to tissue during a blunt dissection task increased by at least 50% and 100% respectively, and the number of errors to cause tissue damage increase by over a factor of 3 [141]. The result of providing the surgeon with extra information when asked to perform a blunt dissection showed that without force feedback, surgeons are much more likely to apply a higher force to the tissue and also are more likely to make mistakes as they will have to concentrate more on gripping [138]. The research assumes that the difference between the different tissues makes force feedback more beneficial, but may become redundant if used in an areas where all tissues have similar mechanical properties.

2.4.1 Force/Pressure Sensors

There are numerous designs for force/pressure sensors which allow an array of measurements to be taken over the surface of an object. These sensors aim to replicate the sensing ability of the surgeon's hand/fingers which is lost in MIS. There are several types of biological sensor mechanisms which combine to give tactile information to humans (Figure 2.28) [142]. A large variety of sensors have been developed to measure the applied forces and pressures over a surface to understand tactile feedback and the types of forces present for various tasks [143, 144]. In particular these have been integrated with surgical tools to begin to understand what is happening at the tissue tool interface. As well as

providing numerical feedback of forces, some sensors are used to monitor wounds after surgery to ensure the patient does not exert too high a force on it [145]. Bio-compatable sensors are being developed for full *in-vivo* measurements to be taken in humans [146], with fibre optical sensors under developement for use in Magnetic Resonance Imaging (MRI) machines [147].

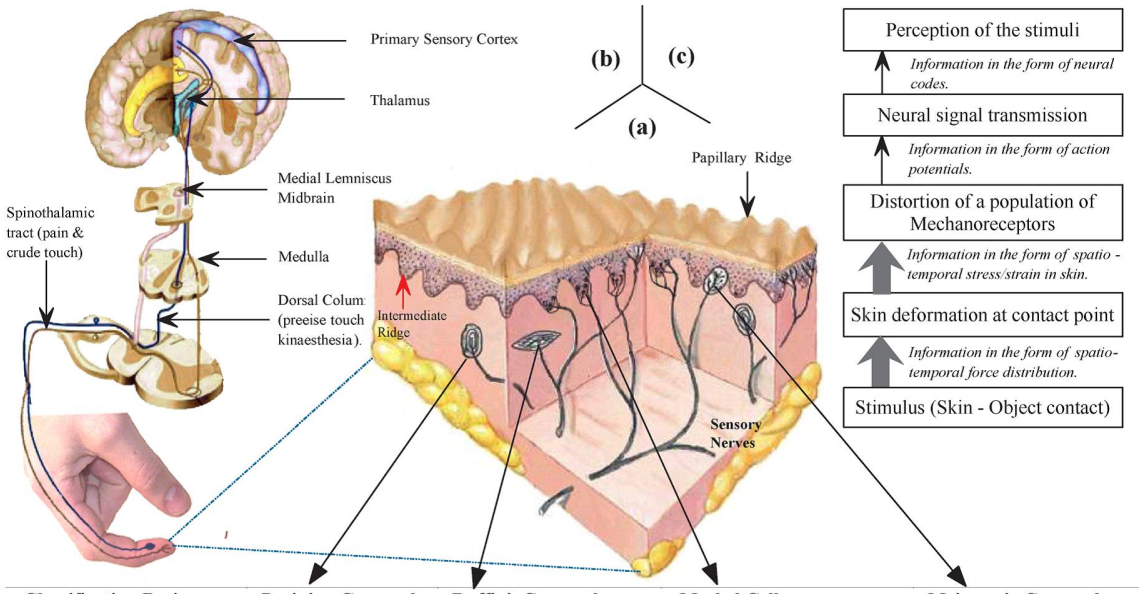

Classification Basis		Pacinian Corpuscle	Ruffini Corpuscle	Merkel Cells	Meissner's Corpuscle
Type		FA II	SA II	SA I	FA I
Adaptation Rate		Fast	Slow	Slow	Fast
Spatial Acuity (mm)		10+	7+	0.5	3-4
Vibration/rapid indent. threshold	Best(μm)	0.01	40	8	2
	Mean(μm)	0.08	300	30	6
Stimuli Frequency (Hz)		40-500+	100-500+	0.4-3	3-40
Conduction Velocity (m/s)		35-70	35-70	40-65	35-70
Effective Stimuli		Temporal changes in the skin deformation	Sustained downward Pressure; Lateral skin stretch; Skin slip.	Spatial deformation; Sustained pressure; Curvature, edge, corners.	Temporal changes in skin deformation
Sensory Function		High frequency vibration detection; Tool use.	Finger position; Stable grasp; Tangential Force; Motion direction	Pattern/form detection; texture perception; Tactile flow perception.	Low frequency vibration & motion detection; Grip control; Tactile flow perception.

Figure 2.28: The five sensing mechanics of human fingertips [142].

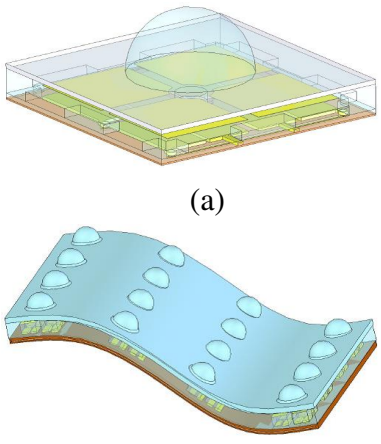

(a)

(b)

Figure 2.29: Capacitive normal and sheer force sensor showing (a) single sensor and (b) sensing array [148].

Sensor designs also include semiconductors, piezo electric and air cushioned [111, 149–151]. Capacitive sensors (Figure 2.29) have been designed to allow compressive and shear forces to be measured, potentially allowing for a single sensor to measure both grasping and retraction force. Novel pressure sensing skins are being used to detect tissue damage during surgery but are still at the prototype stage of developement [152]. Piezoelectric oxide semiconductor field effect transistor device based tactile sensing is another alternative as the designs can be small to give a higher resolution [153, 154]. One key focus of sensor developers is to create a design which is compatible with the human body, therefore it needs to be waterproof and flexible. Using Polydimethylsiloxane (PDMS), devices can be set in a waterproof housing which also gives flexible design (Figure 2.30).

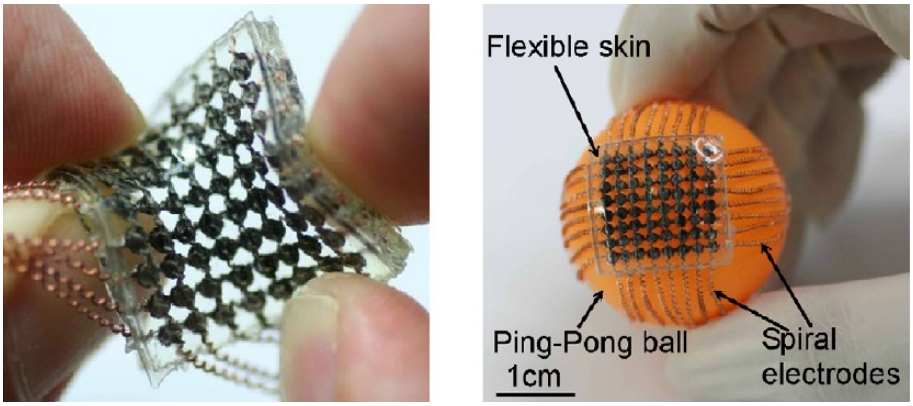

Figure 2.30: Flexible and stretchable tactile sensing array consisting of helical electrodes embedded in PDMS [155].

Soft compliant sensors are developed alongside compliant grasper designs for improved manipulation and reduced forces [156, 157]. By using microfluidics, changes in the internal pressure can be calibrated to give an external applied force. Designing the fluid channels in a grid can also give a location of the applied force (Figure 2.31).

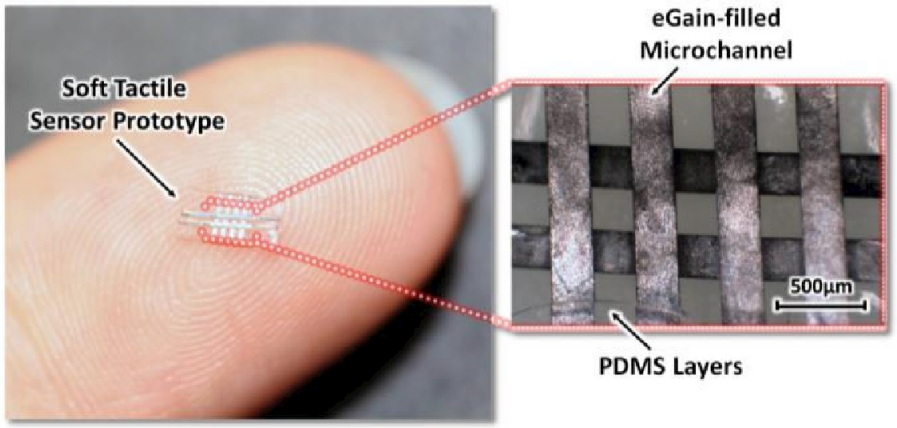

Figure 2.31: Soft tactile sensing array with conductive microfluidic channels set in PDMS [156].

When developing the sensors, considerations need to be made as to how they can be integrated with different laparoscopic tools (Figure 2.32). Either the sensor is fabricated independently of the tool, leaving the potentially difficult task of securing it later, or the sensor is fabricated around the tool, ensuring the design will fit securely, although this method means the sensor cannot be used with any other tool, and if the tool is damaged, the sensor is rendered useless.

Figure 2.32: Pressure array sensor embedded in a laparoscopic grasper; the full construction (top-left), a schematic showing the array location (top-right), and the scale of the array (bottom) [9].

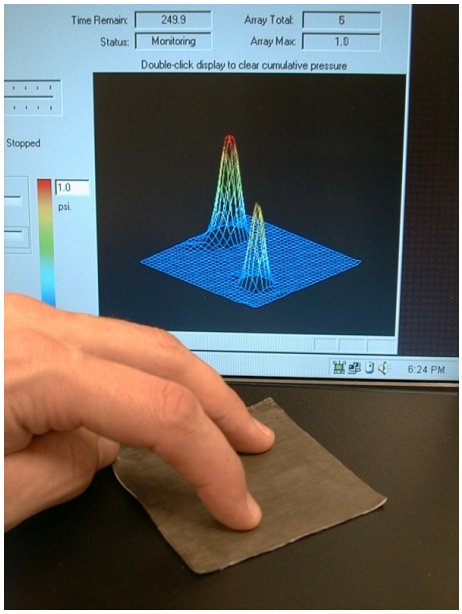

Figure 2.33: Pressure Profiling Systems Inc. TactArray pressure sensor.

One other aspect of force profile sensors is the development of an appropriate output, to indicate what is happening to the user. A number of companies have developed different

sensors and means of displaying the data, typically user friendly graphical interfaces, although the higher resolution and reliable devices come at increasingly higher costs.

A main focus of current research is around the types of forces present during surgery. A survey into the application of force sensing in MIS compares the various current techniques of force sensing in order to find the areas that are missing [158]. The research suggests that more research needs to be done into more accurate, non-electrical sensors. However a large assumption is made by assuming the sensors are able to be inserted into the body. While this may provide good data, it would be very difficult to pass the stringent health and safety checks, such as those required when inserting electrical devices into the body. It is also important to consider if the device is sterilizable, reusable and how the electronics are protected.

2.4.2 Devices to Measure MIS *In-vivo* Task Parameters

In-vivo procedural parameters can highlight potential issues in surgical procedures and training, however as well as the full 7 DOF of the applied forces, there is also internal friction in the graspers, trocars and from nearby organs (Figure 2.34).

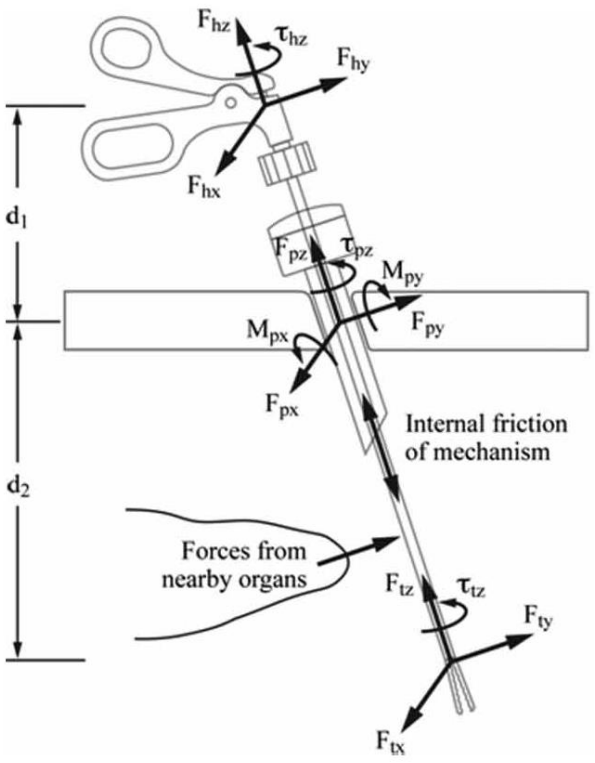

Figure 2.34: The typical forces present in MIS, occurring at the handle, trocar entry site and tool-tip [22].

Research developments have allowed for multi DOF systems [159, 160], with force

sensing robotic surgery proving popular due to the complete lack of force feedback when compared to conventional laparoscopic surgery [161–164], and bespoke designs to aid the surgeon [68]. Alternative information, other than force, can be passed back to the surgeon in an aim to compensate for the lost sensory information [165], along with robotic force control, which can limit the grasping force exerted by the surgeon [162]. Measuring surgical gestures allows for the study of quantitative data for surgical performance [166], and to understand expected forces in surgery to advise other aspects of research [167, 168]. The design of a device to measure *in-vivo* surgical gesture measurements (BlueDRAGON) provides a deeper insight into the technical aspects of different procedures (Figure 2.35) [169]. It provides a 7 DOF design to measure typical surgical manipulation data, which has been used to compare expert and novice surgeons, showing how expert surgeons are typically quicker at performing tasks, and generally used lower forces when manipulating.

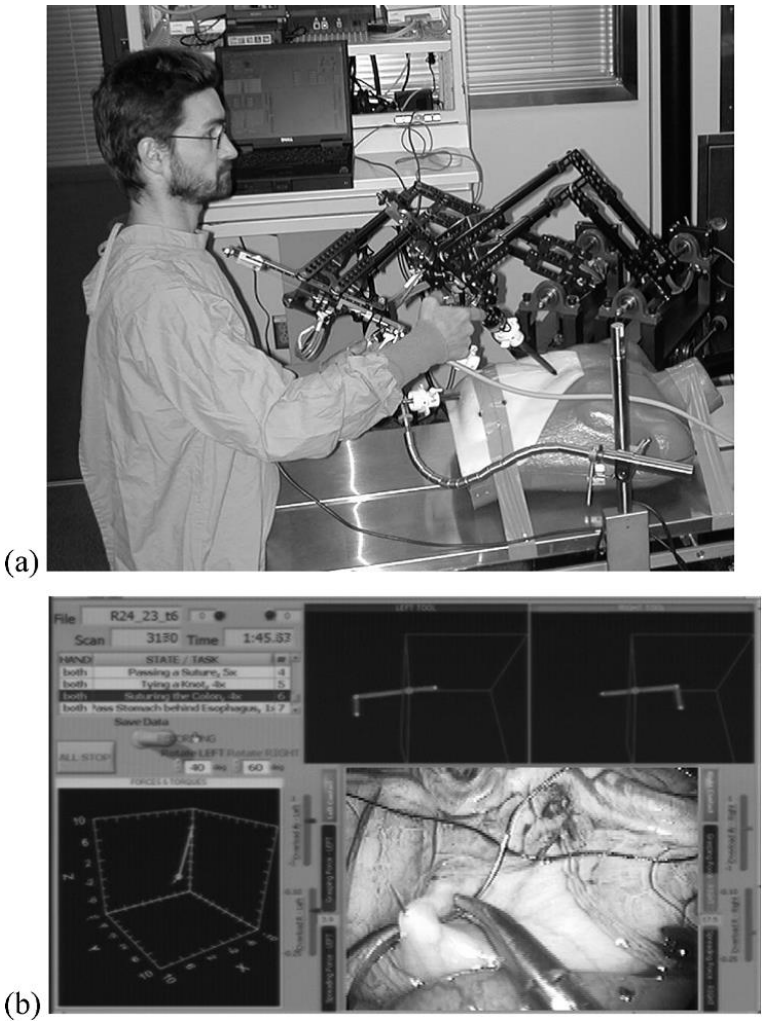

Figure 2.35: The Blue DRAGON system used to measure *in-vivo* surgery performance parameters, highlighting (a) the integrated user set-up, and (b) the graphical user interface [170].

One focus of current research has been put on developing devices which will allow a surgeon to palpate the tissue. This will allow them to distinguish between healthy and diseased tissue during MIS. Neural networks were used to process the information from the sensors [171]. The device can be *'taught'* what would be considered normal and what could be cancerous. This is a small step towards a fully automated system, and an idea which has recieved mixed opinions. It has also been investigated where the neural network uses visual and kinaesthetic information to perform tasks [172]. Initial designs of a palpation instrument showed that issues may arise when it is integrated with a laparoscopic tool, when considering size and usability [173]. A laparoscopic tool was developed to detect objects of different dimensions and stiffness. The design worked well but difficulties would arise in a practical situation when it needs to be sterilized [174]. A typical *in-vivo* grasping profile (Figure 2.36) showed peak forces of less than 25 N (measured at the handle) when running the bowel, but it is difficult to determine tissue characteristics from this data as the tissue relaxation is *'hidden'* by the potential vibrations from the surgeon's hand.

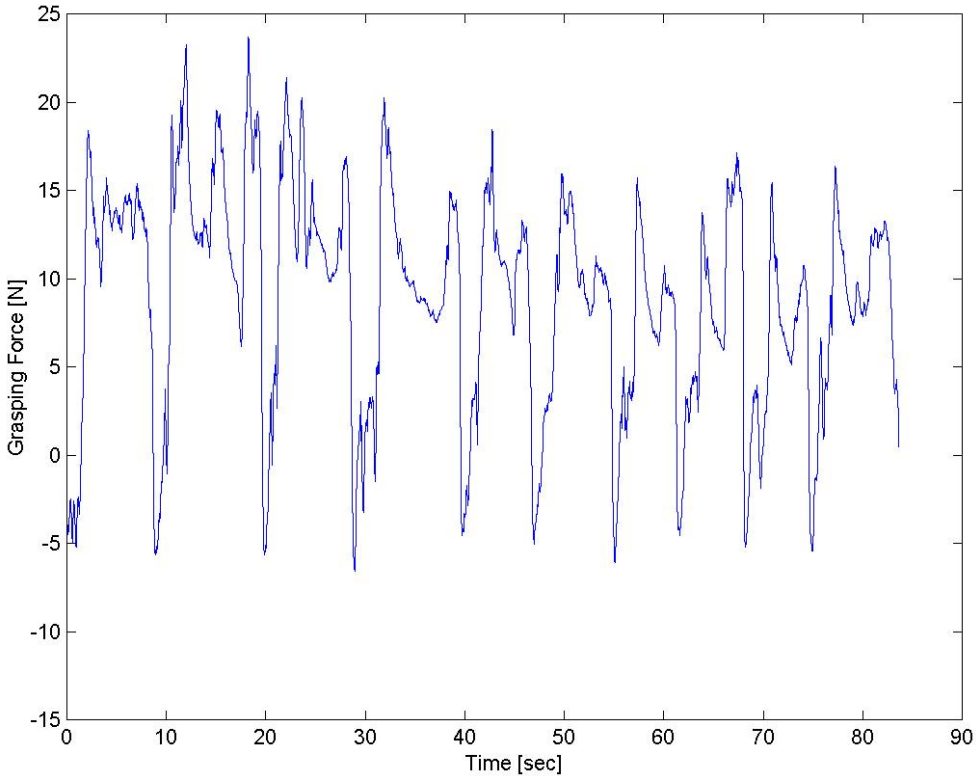

Figure 2.36: A typical *in-vivo* grasping profile when running the bowel for an instrumented tool (left hand) measured at the handle [175].

In tele-operated surgery there is no haptic feedback at all, therefore the right data needs to be sent to the user to prevent confusion, i.e. the forces received need to seem as natural to the surgeon as possible as they may not be able to quantify the magnitude of force by vision alone [176]. To allow a surgeon to palpate the tissue, algorithms have been developed from finite

element tissue models to ensure that detection of diseased tissue can be successful even deep inside the tissue [177]. The use of tele-operated systems can prove useful [178], but with force feedback the system needs to be thoroughly tested to ensure that it does not become unstable. It may be undesirable to output too great of a force to the surgeon. Researchers are focussing more on the ability to analyse all the DOF during surgery [161, 179]. This ensures that all aspects of the surgery are understood [180]. By using motion tracking through image processing, the optimal positioning of tools can be monitored [181].

2.4.3 Devices for Determining Tissue Characteristics

As discussed previously (section 2.3.2), the measurement of tissue characteristics can be useful for detecting anomalies in samples, from tumours to ruptured tissue. *Ex-vivo* test rigs have the disadvantage of not analysing living tissue. By instrumenting surgical tools, *in-vivo* tissue properties can be investigated. One such device is the Motorized Endoscopic Grasper (MEG) [182, 183]. Other devices have aimed to characterise tissue [184], and analyse an object's stiffness [185], by using sensors designed to measure soft tissue response attached to laparoscopic tools [111, 186].

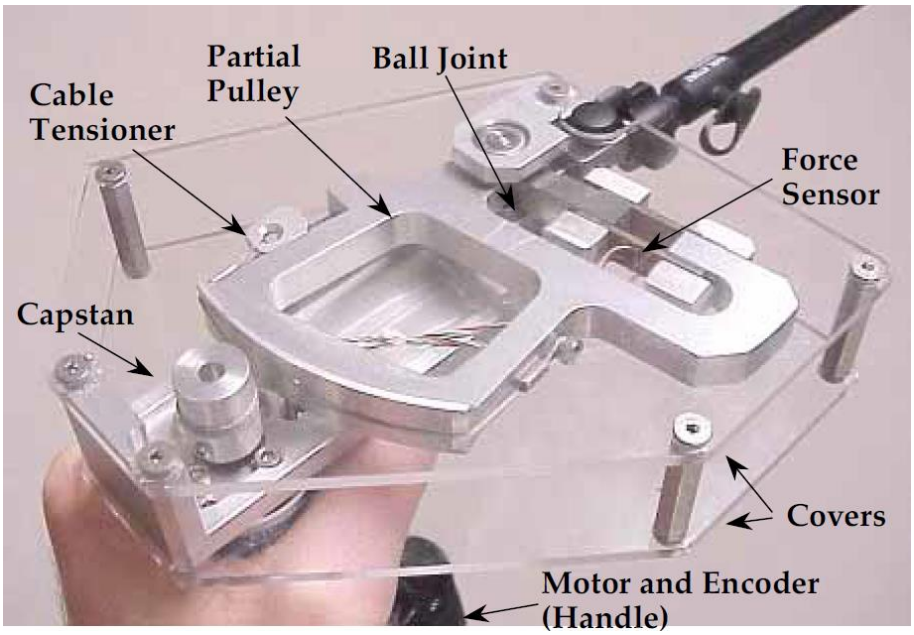

Figure 2.37: The instrumentation of the MEG used to measure *in-vivo* tissue response [183].

An MRI compatible loading device allows for tissue response analysis combined with response readings from the MRI scanner [187]. This is covered again [170], by looking at how to model MIS using the same model as before. Thirty surgeons were monitored as they tied an intercorporal knot. This data was then used in the Markov model to attempt

to produce the learning curve of the surgeons. The model is, however, unable to show the cognitive process of the surgery, but was able to output a similar learning curve to that of the surgeons performance. The BlueDRAGON, a device which measures the various forces that are seen during MIS, highlighted a maximum applied force of 68.17 N [175]. By testing on a selection of surgeons a comparison between left and right handed techniques could be made, showing no real difference, [170, 175]. Similarly a system was developed which monitors the force and position of the laparoscopic tools, allowing for postoperative data analysis to take place, and provides a more detailed analysis of how surgery is performed [188].

2.4.4 Tactile Feedback Transducers

In order to give the surgeon the perception of palpation, various tactile transducers have been developed [9]. A typical transducer uses pins or rods embedded in a surface which move in and out to generate the desired surface profile [189], typically controlled by electro-magnetic coils [190], radio-controlled servomotors [191], or SMA actuators [192, 193]. Other methods include varying the vibrating frequency to create a polarity effect [194]. By tuning the frequency of a plate, varying tactile sensations can be generated [195–197]. The current main area of focus for tactile transducer design is on making designs compact to fit inside commonly used surgical tools, and not add significant weight [9, 198]. Another need for the compact designs is to increase the resolution of the devices, improving the quality and amount of information which can be transferred to the surgeon (Figure 2.38).

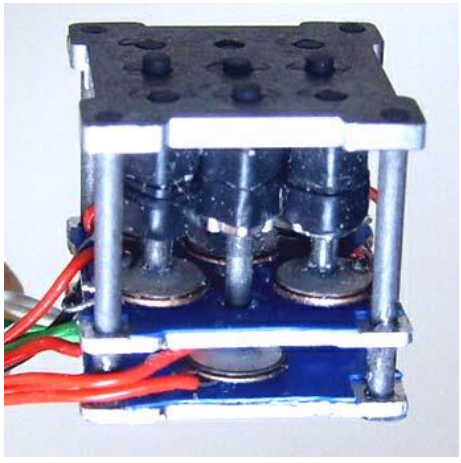

Figure 2.38: Actuator driven pins set in a tactile display [198] .

Other designs use comformable materials to fit against the surgeons skin, reducing the liklihood that an output will be missed (Figure 2.39).

Figure 2.39: Pneumatic actuated balloon tactile display [199] .

Readily available devices have been made which can give a resistive force in multi DOF [200]. Current devices are still either too large or do not have a high enough resolution to provide reliable information. Investigations have also highlighted that the user needs to prefer haptic feedback, as it could negatively affect their performance otherwise [201]. Further investigation is needed to understand how this type of tactile feedback is interpreted by the surgeon.

2.4.5 MIS Tissue Palpation Devices

Haptic feedback has been shown to help the surgeon understand the forces being applied in surgery [202, 203]. Tools have been made using a combination of both sensors and feedback transducers to give the surgeon the ability to virtually palpate tissue [204, 205]. These are usually integrated into commonly used tools, to make them more user friendly [206]. Also by incorporating the ability to palpate, tele-operated surgeries can greatly benefit from this [207]. By accurately varying the amount of force applied to the tissue, procedures can be completed quickly and cleanly as the amount of slip is reduced [208, 209]. It has also been shown that robotic palpation set-ups do not require as great an indentation as a human might use when detecting an anomaly [210]. By measuring the force and position, the surgeon will have a greater understanding of what is happening at the grasper/tissue interface [22]. The multi DOF system sends an output to the surgeon via a computer interface.

To make a device as generic as possible, a new grasper handle was developed for use on laparoscopic tools [61]. This allows for the measurements and feedback to be performed, and makes it easier to integrate with current devices in future testing. The novel design which differs from conventional laparoscopic tools has been implemented [68, 211, 212]. It uses an SMA actuator and a new grasper design to measure forces on the tissue. The suggested use would be as an end-effector on a micro-instrument to provide haptic feedback. The unique design of the device allows the user to grasp and feel the object of interest without inducing damage through pinching.

Similarly laparoscopic tools with increased DOF have been designed [79]. These allow

the surgeon to grasp and manipulate the tissue in a much more natural way, by mimicking the natural motion of a surgeon's wrist while still providing force feedback [213, 214]. The silicone-based balloon actuators apply a relative force, as measured via a force array sensor, to the surgeons hand [199]. Devices such as this show an improvement in identifying material stiffness but still needs refining [113]. When converting the force from the sensors to the tactile output there should be considerations for the magnitude and whether this relation is linear or not [60, 215].

Considerations need to be made for the type of task which will be carried out. Typically the tool handles are integrated with the tactile outputs to show the grasping forces currently being applied [216]. However further advancements have allowed tasks such as the application of pressure, lateral motion and a combination of these to be detected for different materials [217]. Investigations have shown that it must be a requirement of the surgeon to have force feedback, otherwise there is risk of added complexity and confusion, possibly hindering them [218]. To accompany the palpation devices, inclusion detection algorithms can be implemented to further aid the surgeons manipulation motions [219]. Using a neuro-fuzzy regulator, a grasping device with active control has been developed, which learns the minimum stresses which need to be applied to tissue to prevent it slipping, but which also allows for efficient grasping control [220]. A novel alternative to current palpation devices would be to use an external device which magnetically controls an opposing sensor, varying the magnetic field and measuring the force response of the tissue allowing for wireless palpation [221, 222].

Advancements in the design of new MIS devices has lead to improved sensing, manipulation and output of *in-vivo* grasping tasks, with miniaturisation and ergonomics driving the research. These new developments still currently require a steep learning process by the surgeon, and can be difficult to interpret the data effectively. By understanding the learning process and methods used, future developments can hope to build on this and incorporate this into designs.

2.4.6 MIS Training Techniques

To try and prevent excessive damage occurring, surgeons can be given extra training under a simulated laparoscopic surgery situation (Figure 2.40). This can include a VR simulation where a computer model of tissue is generated via a computer screen, and handles controlled by the surgeon are monitored by the computer program which controls the VR tools on screen [223]. The benefits of this are the ability to practice on lifelike situations and to highlight any problem the surgeon may encounter in actual surgery, without the risk. However there are also disadvantages. Due to the fact that the scenarios are computer generated, the response is an approximation and will not accurately reflect real surgery, and would be difficult to model every scenario encountered in an actual surgery.

Figure 2.40: VR training simulator, highlighting (a) user stations set-up, (b-c) VR display of different training tasks [224].

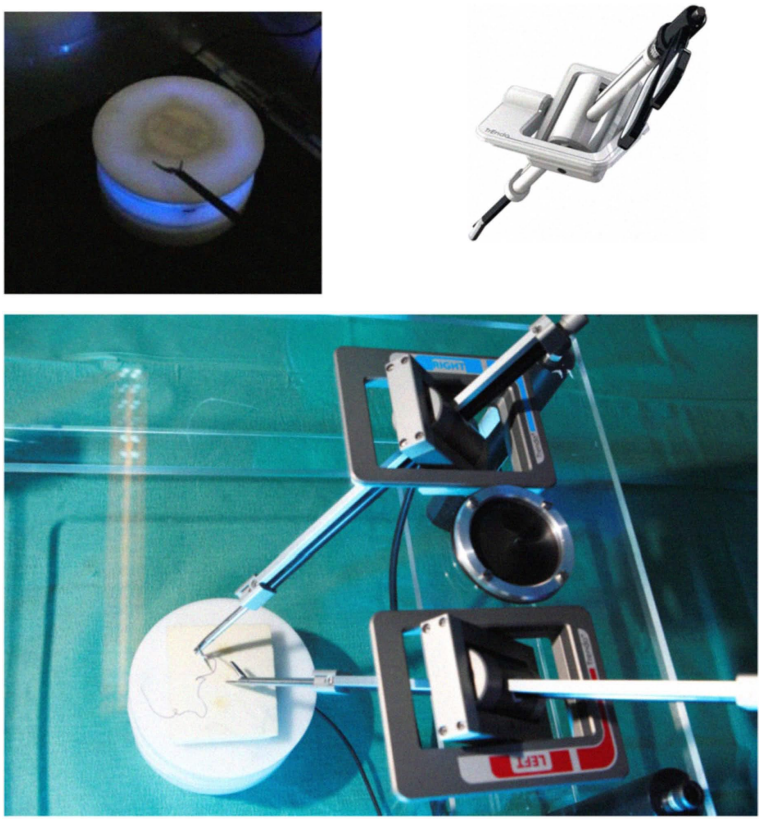

Figure 2.41: A MIS trainer device used to simulate *in-vivo* procedures and measure manipulation parameters [24].

Another outcome of force measurements during surgery is the ability to analyse the skill of the surgeon. Using a discrete Markov model, a surgeon's skill level has been assessed [225]. This is beneficial to surgeons as there is a very grey area on how best to teach surgery. Some believe that by simply observing an expert, the skills can be transferred. However others believe that in order to truly learn something, hands on experience is essential, if somewhat impractical, making laparoscopic trainers vital to surgical learning (Figure 2.41). By analysing these two methods the most suitable way of learning can be found [225]. The model still requires initial input by the expert surgeons in order to give a scale of expertise and this still requires a level of human judgement.

When designing devices which provide grasping feedback, considerations need to be made for the force propagation through the tools and how this can be modelled to ensure an accurate representation [223]. Previously developed palpation devices can also be used as a method of skills assessment, but require prior knowledge as to what is considered good or bad [226]. The role of tactile feedback in laparoscopic surgery training is to give the surgeon a better understanding when identifying tissue characteristics in order to increase the rate of learning [227]. New methods of laparoscopic training use high quality embalmed cadavers, with particular areas of interest permanently coloured, allowing for a more accurate model over animals, and clear distinction in areas of interest [228]. An alternative to this is to have a physical set-up with artificial tissue, to still allow for the task skills to be acquired, although issues such as tissue damage will not be accurately shown (Figure 2.42).

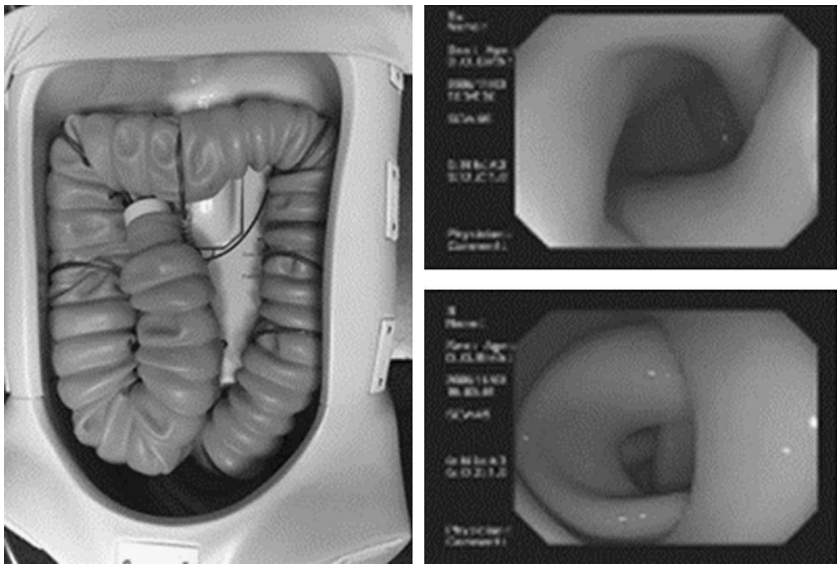

Figure 2.42: MIS artificial colon training device, showing external view of device (left), and internal views through a colonoscope (right) [229] .

Typical state-of-the-art trainers look at the force and motion characteristics of the trainee when compared to an expert [230, 231]. Different tasks can be assessed using different training setups such as a box trainer for generic MIS [232, 233], a palpation simulatior [234],

and a NOTES simulator [235]. There have been investigations into the learning curve of surgeons, and how quickly their particular skills can improve depending on the teaching method [236, 237]. Traditional methods involve simply watching an expert perform the tasks, but it has been shown that performing these skills themselves can improve the learning curve by increasing muscle memory. VR systems are becoming increasingly popular [224, 229], although more still needs to be understood about human perception of VR and how this compares to real surgery [238].

By incorporating the tissue properties into simulations, VR can be used as a diagnostic aid. One such example has allowed a virtual colon model, created from a CT scan, to be virtually *'unfolded'* with the aim of highlighting significantly sized polyps ($\geq$3 mm). This would allow future operations to be planned out thoroughly beforehand. However the methods are not perfect and the final result is still just an approximation, with higher accuracies being developed using advancing mathematical analysis [239].

Advances in MIS devices and training techniques are under constant development and improvement, with issues such a functionality as the main focus, so that these solutions can be implemented effectively.

2.5 Summary of Literature Review

The number of research papers that have been published on the topic of MIS shows a steady increase from 1990 to 2008, and again from 2009, with a steep jump between 2008 and 2009 (Figure 2.43).

This sharp rise can be attributed to the increasing popularity of the *da Vinci*® robot among surgeons in the three years leading up to 2008 (Figure 2.2), and its increased use in ever more complex procedures during this time [25]. With MIS becoming increasingly popular, it has become vital that the tools and techniques used are improved to help the surgeon perform tasks as efficiently as possible. Numerous areas are being researched to provide as much information to the surgeon while reducing the number of difficulties experienced during procedures. However there is much debate over how the surgery should be performed and exactly what will benefit the surgeon. With the benefits of MIS making it more appealing, more pressure is being placed on surgeons to perform more difficult tasks and at a higher standard. With an ever increasing range of laparoscopic tools becoming available, it has become more difficult to understand exactly what the most suitable options for particular surgical scenarios are. This usually falls down to the surgeon's particular preference and previous experience. Because these tools are attempting to replicate the many functions of the human hand, little is known about what the particular disadvantages associated with them are. The current models incorporate a very general description of the graspers, and even though there is currently a lot of research being done into the tool-tip forces present, it is still

very difficult to get a full understanding of the forces present.

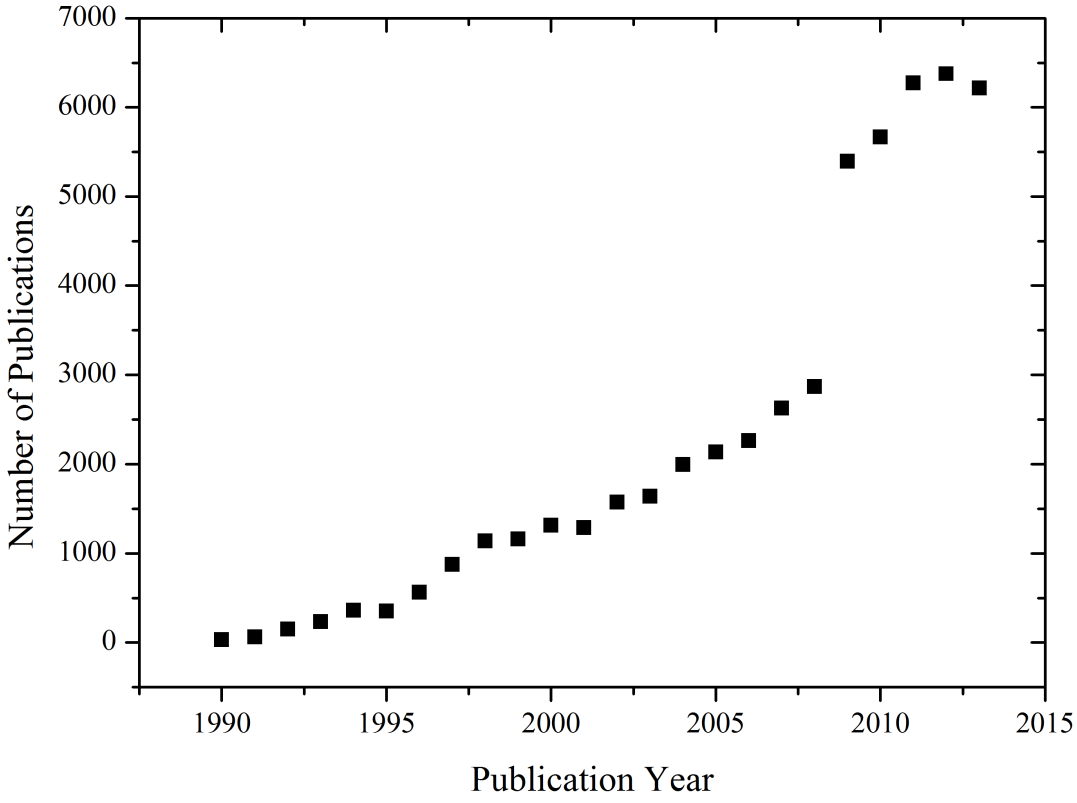

Figure 2.43: Number of publications on the topic of MIS per year from 1990 to 2013 (Web Of Science).

By observing the effect that laparoscopic surgery has on tissue, researchers are looking at new methods of optimising tools. VR simulations are becoming increasingly accurate to provide safe yet effective methods of teaching new surgeons the techniques needed to perform in the operating room. Research is being carried out to try and quantify the tissue properties; a task which has proved very difficult given the non-homogeneous structure of tissue and its sometimes unpredictable nature. Because MIS is a relatively new technique, there is a large amount of new technology being developed to try and aid the surgeon. These range from sensors which provide a detailed map of force distribution, to tactile displays integrated into laparoscopic tools, which attempt to provide some degree of haptic feedback to the surgeon which is otherwise lost through MIS. Laparoscopic tools are being developed and tested which have been instrumented with this new technology. With such a vast amount of choice available, lots of work must be put into working out exactly which devices will benefit the surgeon. Many of these new devices require a large amount of knowledge on the forces and DOF necessary to perform the various MIS tasks.

2.6 The Gaps in Knowledge

By conducting this literature review, it is apparent that there are a number of areas in the research which have yet to be investigated.

While work has been carried out to identify the forces transmitted through laparoscopic grasper mechanisms to the tip, there is still need for a generic method of determining this relationship for any sized grasper. This could then be used by manufacturers to understand the implications of varying the geometry. There is currently no obvious standard for tool development, as the design process is subject to the surgeon's requirements, and is often based on functionality, rather than typical engineering standards, such as efficiency, transmitted force, linearity, pressure grasping profile, etc. By providing the surgeon with a number of set parameters to describe the grasper design, a more informed choice could be made, potentially improving surgical performance and efficiency, and reducing the amount of unnecessary tissue damage, as each tool would be more suited to the task.

Current designs of instrumented grasper are typically *'single use'* as the design is integral to the grasper. An instrumented grasper design with reusable sensors would allow for reliable comparison between laparoscopic grasper designs and replacement of the grasper or handle, should they become damaged. Current research has shown that instrumented surgical graspers can reliably give comparative data on the performance of a skilled surgeon to that of a novice. However this data does not highlight to the surgeon how the tissue is responding, and if indeed damage has been caused. Also the designs can be quite restrictive and large, particularly those with high DOF measurements, leading to a difficulty in crossing over to full clinical use. The development of a modular design, to correspond to the grasper modules, could allow for future clinical use without hindering the surgeron. Current surgical training devices also provide comparative data between individual users, but do not indicate the effect of the surgeons grasp.

A number of tissue rigs have been developed to investigate different parameters involved during laparoscopic surgery. These include rigs to investigate how, by varying the surface geometry of laparoscopic graspers, the grasping and retraction efficiency may change. Another looked to measure the forces required to perforate the tissue samples, and an indentation rig was used to apply known forces to the tissue, using an *'idealised'* surface, to observe the how the tissue might respond. These designs have yet to incorporate actual surgical tools, which would give closer representation to actual *in-vivo* surgery and allow for typical *in-vivo* scenarios to be *'simulated'*. This would allow for a more direct comparison between *in-vivo* and *ex-vivo* results.

Current methods of measuring damage to tissue samples all require post analysis, either by taking samples for histological analysis, or blood samples to observe changes in particular chemicals. The closest method currently to *'real-time'* analysis observed the development of

bruises *in-vivo*, but this still requires time for the bruise to appear. By developing a method to determine damage immediately, the surgeon can act if necessary, reducing the likelihood for repeat procedures and improve survival rates.

The most widely used methods of surgical training are subjectively compared to that of an expert surgeon. While the expert may be able to perform tasks more efficiently, it is a combination of factors, such as time or grasping force, which may affect the results. Also even though the expert has had more experience than the trainee, the data will not show if they are grasping too hard, or even moving too fast. An improved method of training is needed which does not use an expert as a baseline, and also gives a grading of success rather than a simple pass or fail, i.e. even though the trainee may complete the task in the allotted time, showing how efficiently this was done would improve the learning rate.

There has not been an investigation of how the mechanical properties of tissue are affected when damage is induced. Current research shows how the tissue responds to relatively low forces, but does not consider how the tissue may respond differently after being damaged. Similarly tissue response modelling is typically performed using an *'ideal'* surface, so there is difficulty when comparing to *in-vivo* scenarios. By performing indentation tests on tissue using conventional grasper jaw surfaces, and inducing damage in the tissue, a greater understanding of the tissue mechanics and *in-vivo* tissue damage can be found.

This project therefore is essential to current laparoscopic techniques to try and reduce the amount of damaged caused, thus reducing one disadvantage of MIS. Current state of the art in new ergonomic grasper designs are still in the development stages, therefore this project should provide a solution to the current devices and also ensure that future designs will perform well.

Chapter 3

Design, Development, and Testing of the Instrumented Grasper

3.1 Introduction

During Minimally Invasive Surgery (MIS) procedures it can often be difficult for the surgeon to palpate organs and determine the magnitude of forces which are applied at the tissue-tool interface due to the limited haptic feedback which propagates through the device. This can often lead to excessive forces being exerted on the tissue, potentially causing damage. From the literature investigation (section 2.4), there are a number of instrumented graspers which have been designed, or are still currently under development, to provide surgeons with numerical information, such as forces, torques, and displacements, relating to surgical manipulation tasks. These devices can be categorised into those which measure the multiple Degrees Of Freedom (DOF) of the grasper movements for various grasping tasks (BlueDRAGON) [175, 181], and those which attempt to determine tissue characteristics for different organs and if they are healthy or diseased [88, 176]. However to fully understand how and to what degree tissue trauma is generated, before complexity can be added, a greater understanding is needed of how each individual parameter contributes to the overall task performance in typical MIS. The instrumented grasper presented in this work focusses solely on the grasping forces of organ manipulation tasks in MIS, with the development of a reliable system for measuring this, as this is the primary DOF of a laparoscopic grasper with all subsequent DOF relying on this.

3.2 Instrumented Grasper Design Specification

To aid in the design development, a specification for the instrumented grasper was established from the literature review, as follows:

1. The grasper instrumentation should measure the grasping force exerted over time (in real-time).

2. The instrumented grasper should be capable of measuring shaft forces up to 100 N, as this is greater that those demonstrated in previous research (68.17 N [175]).

3. The grasper and handle should be interchangeable to allow for future investigations of varying grasper designs, and to allow for damaged parts to be replaced.

4. The design should not impede movement through the trocar ports.

5. It should be easy to attach and remove, reducing potential impact on the time spent in the Operating Room (OR).

6. There should be little or no customisation required of the grasper or handle.

7. A computerised system should record the force, position, and time data for post-analysis of measurements.

8. The design should not affect the usability or grasper functionality.

9. The instrumentation should be housed/sealed to prevent unwanted external interference of sensors, incorrect measurements, or damage to components.

10. The device should be passive, i.e. if there is catastrophic damage to device (including the power supply), normal grasping function should still be possible.

3.3 Sensor Location Considerations

A reusable fenestrated atraumatic laparoscopic grasper, of length 305 mm and diameter 5 mm, with a horizontal handle (101-48020 and 101-41000 respectively, Surgical Innovations Ltd.) was selected as the base of the instrumented grasper (Figure 3.1), as this design is typical of the type used in MIS and the interchangeable parts allow for easy assembly and replacement. The non-ratcheting handle design was used to ensure that the surgeon has full control over the applied force and when it is released.

Figure 3.1: Surgical Innovations Ltd. Logic™(2010) fenestrated grasper full assembly (long fenestrated grasper and ratcheted horizontal handle shown).

Three options were considered regarding the location of the sensors which would require the minimum amount of customisation of the grasper. As highlighted in the literature review (section 2.4.4), recent developments in force array sensors have allowed for increasingly smaller pressure profile devices to be manufactured. However these still only have a relatively low resolution, around 2 mm^2 pixel area, which is larger than the grasper fenestration spacing (Figure 3.2a) of less than 1 mm, and of a similar scale as typical tissue features (3 - 5 mm) [239], meaning the data would be averaged across the elements. The sensors would also change the grasper surface chemistry and functionality, and as the instrumented grasper aimed to simulate as close as possible to typical MIS, changes to the tissue-tool interface would greatly impede this. Finally this location would require the sensors to be placed inside the patient with wiring passed through the trocars, increasing the risk of infection and creating extra friction in the ports.

(a) (b)

Figure 3.2: Surgical Innovations Ltd. (2010) selected design of (a) the fenestrated atraumatic grasper, and (b) the horizontal handle without ratchet.

One alternative was to mount sensors on the handle, (Figure 3.2b), removing the need to insert electronic devices into the patient and maintaining the grasper surface. However the handle has a sizeable degree of backlash in the mechanisms which even though comparatively small considering the expected force measurements (68.17 N [175]), would result in an unknown degree of error in the data readings. Measuring the forces applied to the handle would be relatively simple, but finding a reliably accurate method of determining the the position of the handle would be difficult to measure without it becoming cumbersome.

The final choice was to locate the sensors at the connection between the handle and grasper linkage, where the cone nut is located (Figure 3.3). This removes the need to insert sensors into the patient, while still allowing for accurate readings to be taken relative to the expected grasping forces [175]. This would also not limit the normal insertion depth of the tool during surgery as the outer shaft and cone nut would remain unaltered.

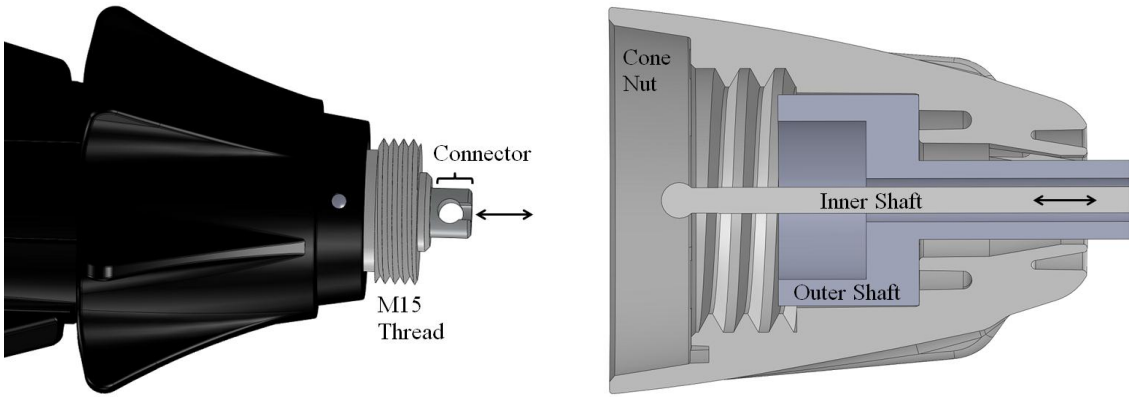

(a) (b)

Figure 3.3: The CAD of the grasper components, showing (a) the handle connector with threaded element, and (b) cone nut inner and outer shaft set-up.

The handle section (Figure 3.3a) highlights the modular design of the grasper. As the handle is actuated by a user, this movement is transferred into linear motion of the connector, and by inserting the end of the inner shaft (Figure 3.3b) into the connector's slot, this motion continues down the full length of the grasper. This then controls the opening and closing of the grasper jaws. By extending the inner shaft, with respect to the outer shaft, the grasper jaws open (Figure 3.4a), and when retracting, the jaws are closed and the force increases (Figure 3.4b).

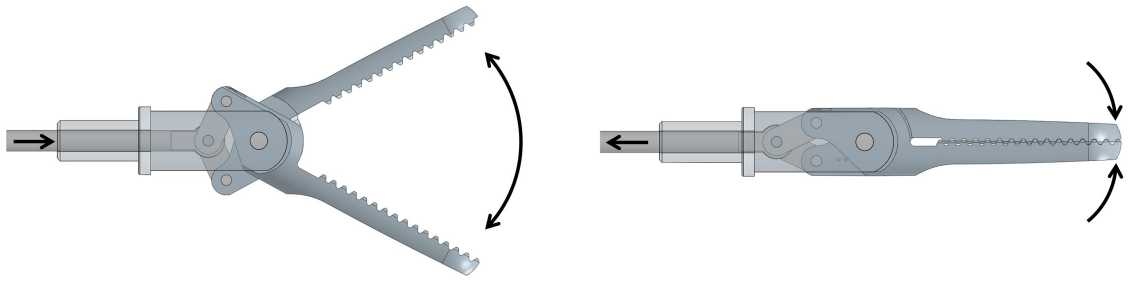

(a) (b)

Figure 3.4: CAD of the grasper scissor mechanism, highlighting (a) a linear extension to open the grasper jaws, and (b) a retraction to close and apply force.

To understand the forces at the tissue-tool interface, the relationship between the inner shaft force and the tool-tip force needed to be found for this configuration. This needed to consider the angle of the jaw when the force was being applied so it could be understood if this had an effect on the magnitude of force transmitted to the tip. If this was found to be true, then the instrumented module would also need to measure the displacement of the inner shaft and how this varied over the duration of the grasp.

3.4 Mathematical Modelling of Scissor Linkage Mechanism

To understand the relationship between the tool-tip force and the measured force along the grasper's inner shaft, the kinematic relation was investigated. The resulting mathematical model indicates how the variation in the jaw angle affects the magnitude of force transmitted from the shaft to the tip, thus advising the design of the grasper instrumentation. This also allows for an easier comparison of grasping forces with other research data [59]. The model is suitable for any grasper geometry with a scissor linkage, differing from previous work which limits the variation in grasper geometries to linkage ratios instead of actual lengths [65]. The handle is not included as the instrumented grasper measurements are taken from the linkage, and also due to the various handle designs available, the model would become less generalised and be susceptible to more error [176].

3.4.1 Free Body Diagram and Assumptions

To simplify the model, several assumptions were made about the system. It was assumed that the system would be static, to allow the model to be derived. This also relates to how a surgeon may typically grasp and hold tissue. The grasper mechanism design is symmetrical therefore it was assumed that the grasping force is equally distributed, i.e. halved, along each jaw linkage. Also any friction at the joints, pivots and between the inner and outer shaft was considered to be negligible when compared to the expected grasping forces in this work (from the literature review 68.17 N was found to be the maximum grasping force via the linkage [175]). Similarly the mass of the linkages were assumed to be negligible in relation to the applied forces and motions expected in this project (due to the potential unknown orientation of the grasper, the effect of gravity on its linkages cannot be determined). Finally due to the difficulties in determining how the force is distributed across the grasped area, especially when considering tissue, the force will be calculated to act perpendicular to the jaw tip, providing a consistent point of reference and making the work comparable to other research data [88].

Firstly a Free Body Diagram (FBD) was created from the original grasper mechanism, with the linkages and central pivot (Figure 3.5a). In the FBD (Figure 3.5b) only the lengths and connections of the linkages were required. By assuming the system is symmetrical (the linkages are identical on each side), only one side of the scissor mechanism needed to be modelled which will be used in the final model derivation (Figure 3.5c).

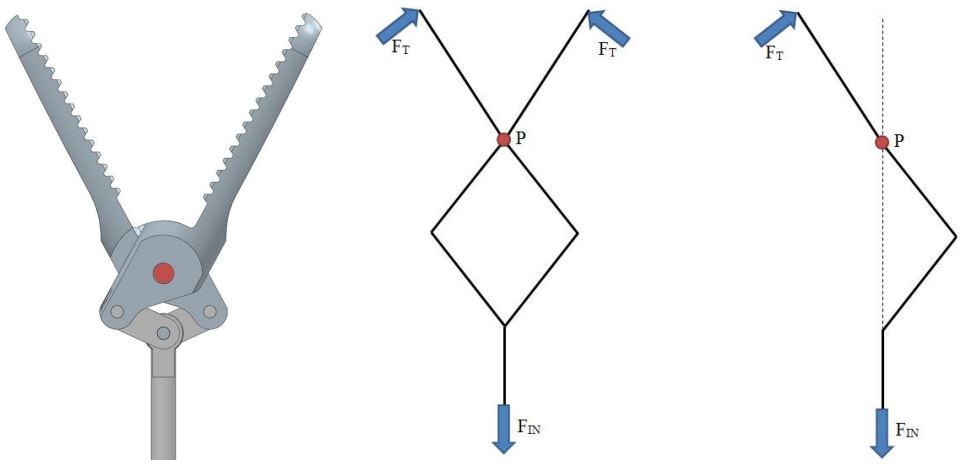

Figure 3.5: MIS grasper with fixed pivot (highlighted in red), showing (a) the scissor linkage mechanism, (b) a FBD highlighting input shaft force, F_{IN}, and output jaw tip forces,F_T, and (c) a half FBD including line of symmetry.

3.4.2 Force Propagation Model Derivation

Using the FBD of the grasper mechanism, the resultant forces on the individual linkages were added, along with the linkage lengths l_j, A, and B (Figure 3.6a). It was noted that the force acting upon each linkage would be comprised of two components in the x and y axis, which act along the linkage and perpendicular to it, respectively. However it was assumed that the force acting along linkage A, F_{AX}, would not contribute to any applied tip force or motion, due to the pivot, P, restricting it. Also the perpendicular force acting on linkage B, F_{BY}, would not contribute to the transmitted force or motion as this is restricted by the constraints on linkage L, which may only move in a single DOF.

The FBD was therefore simplified to only include the contributing force components, and the terms were simplified to F_A and F_B, which act on linkage A and B through angles α_A and α_B, respectively (Figure 3.6b).

After halving the input force F_{IN}, the force acting along link B could be calculated as,

$$F_B = \frac{1}{2} \times cos\alpha_B F_{IN} \tag{3.1}$$

Using F_B as the applied force to linkage A, the component force can be found,

$$F_A = F_B cos\alpha_A \tag{3.2}$$

Therefore,

$$F_A = \frac{1}{2} cos\alpha_A cos\alpha_B F_{IN} \tag{3.3}$$

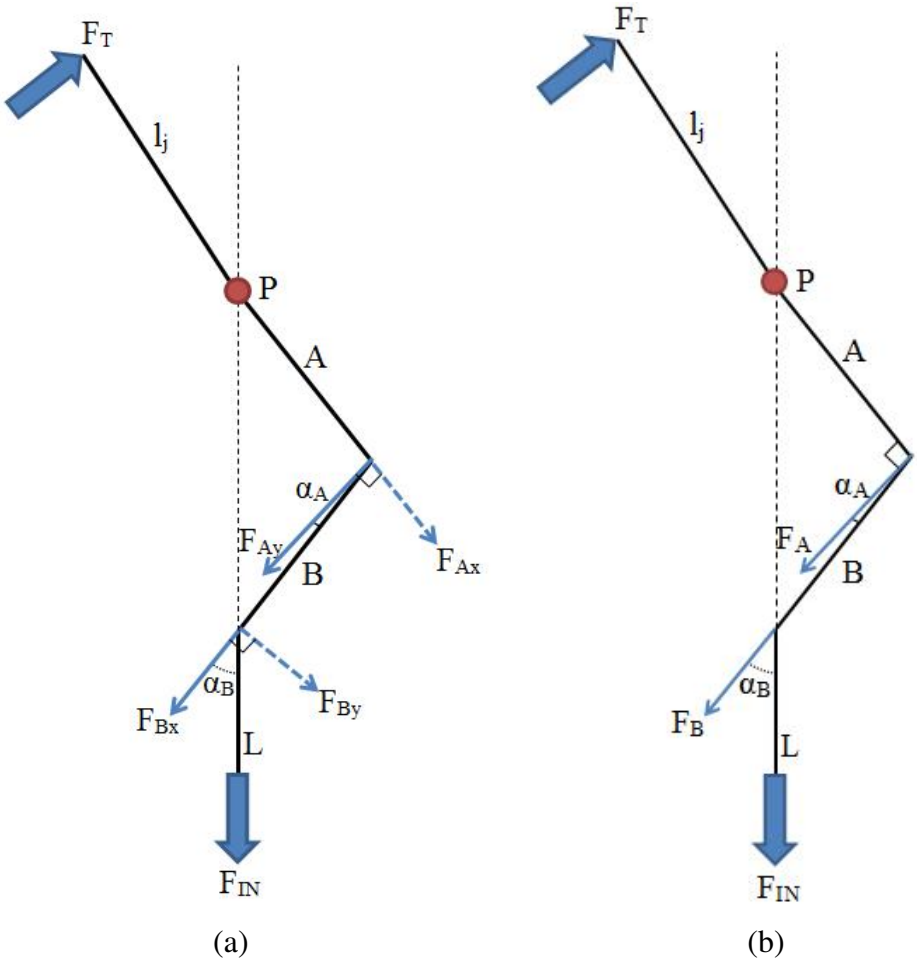

Figure 3.6: FBD of half grasper with pivot, P, input force, F_{IN}, and tip force, F_T, showing (a) force components acting on indiviual linkages, with non-contributing force components shown as dashed lines, and (b) resulting FBD showing only contributing force components.

Finally by taking moments about the pivot P, the final force F_T can be determined for the half jaw model. This is achieved by equating the sum of moments about the pivot to 0, due to the assumption of a static system.

$$\Sigma P_{Moment} = AF_A - l_j F_T = 0 \tag{3.4}$$

Rearranging gives,

$$F_T = \frac{A}{l_j} F_A = \frac{A}{2l_j} cos\alpha_A cos\alpha_B F_{IN} \tag{3.5}$$

This equation now allows the tip force, F_T, to be calculated from the input force, F_{IN}. However the values of α_A and α_B still need to be determined.

3.4.3 Jaw Angle Model Derivation

The relation between the input force, F_{IN}, and the tangential tip force, F_T, for each jaw, is still dependent on the internal angles α_A and α_B (Equation 3.5). Also the mathematical model requires the relationship between the linkage displacement and the jaw angle. The linkage displacement, Δ_L, and jaw angle, θ, were included in the FBD (Figure 3.7a). Also the jaw offset, θ_O, was included as the jaw and linkage A are not parallel.

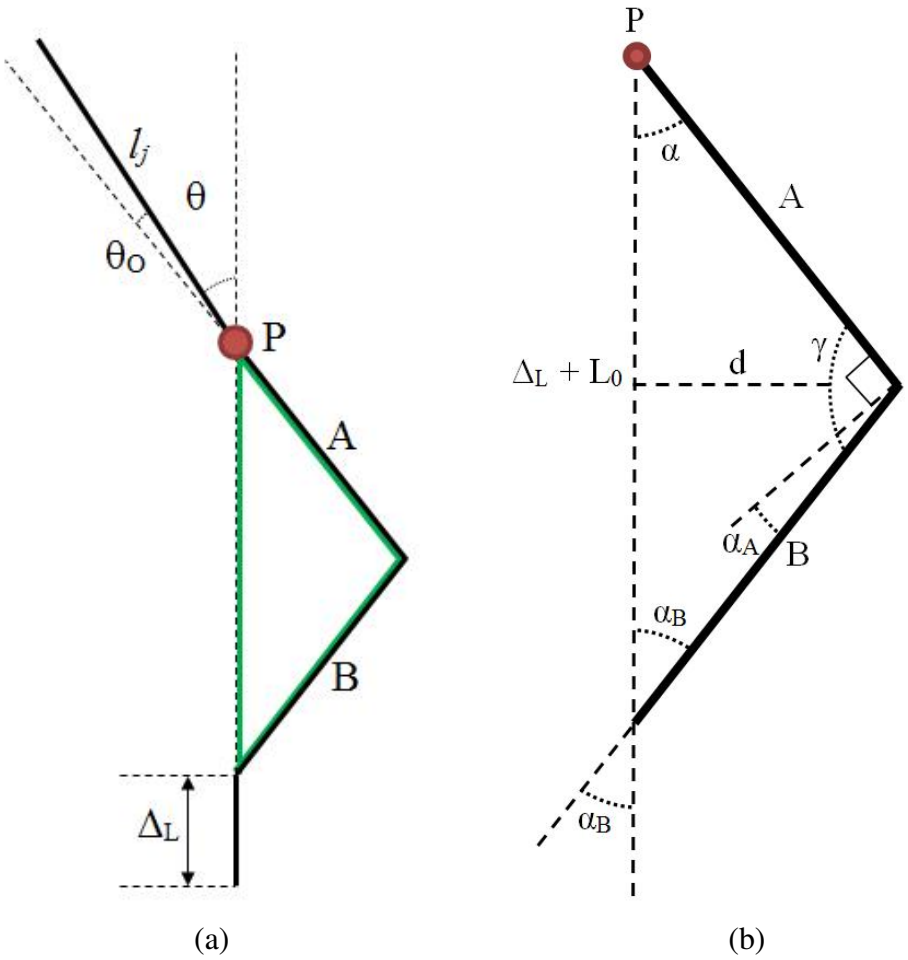

Figure 3.7: The half grasper FBD, showing (a) the grasper geometry, with internal triangle highlighted (green), and (b) the internal triangle parameters.

The internal geometry of the grasper linkages were then added (Figure 3.7b). This includes the angle, γ, between linkage A and B, the initial displacement offset (minimum value), L_0, the top angle, α, and the distance between the linkage joint and vertical, d. To determine these parameters, the cosine rule (Equation 3.10) was used.

$$a^2 = b^2 + c^2 - 2bc\cos(A) \tag{3.6}$$

Using the FBD triangle parameters (Figure 3.7b), the cosine equation was rewritten to determine α,

$$B^2 = A^2 + (\Delta_L + L_0)^2 - 2A(\Delta_L + L_0)\cos(\alpha) \tag{3.7}$$

Rearranging gives α in terms of the grasper geometry,

$$\alpha = \frac{\cos^{-1}(B^2 - A^2 - (\triangle_L + L_0)^2)}{-2A(\triangle_L + L_0)} \tag{3.8}$$

The internal angle α can now be determined from the known grasper geometry, and taking the angle offset θ_O of the jaw into consideration, the jaw angle θ can be shown in terms of the grasper geometry,

$$\theta = \alpha - \theta_O \tag{3.9}$$

Rewriting this gives,

$$\theta = \frac{\cos^{-1}(B^2 - A^2 - (\triangle_L + L_0)^2)}{-2A(\triangle_L + L_0)} - \theta_O \tag{3.10}$$

It is now possible to determine θ from Δ_L, but the internal angles α_A and α_B, are still needed for the force model (Equation 3.5). Using the FBD triangle (Figure 3.7b) α_B can be found,

$$\alpha_B = sin^{-1}\left(\frac{d}{B}\right) \tag{3.11}$$

Where the length of d can be shown as,

$$d = Asin\alpha \tag{3.12}$$

Combining these equations gives,

$$\alpha_B = sin^{-1}\left(\frac{Asin\alpha}{B}\right) \tag{3.13}$$

Again by observing the FBD internal geometry, α_A can be found,

$$\alpha_A = 90 - \gamma \tag{3.14}$$

Where γ can be shown as,

$$\gamma = (90 - \alpha) + (90 - \alpha_B) = 180 - \alpha - sin^{-1}\left(\frac{Asin\alpha}{B}\right) \tag{3.15}$$

Therefore α_A can be shown as,

$$\alpha_A = \alpha + sin^{-1}\left(\frac{Asin\alpha}{B}\right) - 90 \tag{3.16}$$

These equations for the internal grasper angles, α_A (Equation 3.16) and α_B (Equation 3.13), were then fed back into the original equation (Equation 3.5) to complete the mathematical model of the grasper's scissor linkage.

$$F_T = \frac{A}{2l_j} cos \left(\left(\frac{\cos^{-1}(B^2 - A^2 - (\triangle_L + L_0)^2)}{-2A(\triangle_L + L_0)} \right) \dots \right.$$

$$\dots + sin^{-1} \left(\frac{Asin \left(\frac{\cos^{-1}(B^2 - A^2 - (\triangle_L + L_0)^2)}{-2A(\triangle_L + L_0)} \right)}{B} \right) - 90 \Bigg) \dots$$

$$\left. \dots cos \left(sin^{-1} \left(\frac{Asin \left(\frac{\cos^{-1}(B^2 - A^2 - (\triangle_L + L_0)^2)}{-2A(\triangle_L + L_0)} \right)}{B} \right) \right) F_{IN} \right. \tag{3.17}$$

Where F_T is the resulting tip force output, the constants are A which is the length of linkage A, B is the length of linkage B, l_j is the length of the grasper jaw, L_0 is the initial value of the linkage displacement, and the variables are $\triangle_L$ which is the displacement of the linkage, and F_{IN} is the input force.

3.4.4 Modelling Results for the Specific Grasper Geometry

The mathematical grasper model allows the tip force and angle to be determined from the input force and internal linkage displacement. Using MATLAB (v.2011), a script was written to implement the previous model equations. The dimensions for the short fenestrated grasper were measured using Computer Aided Design (CAD) software (SolidWorks 2011) (Figure 3.8b).

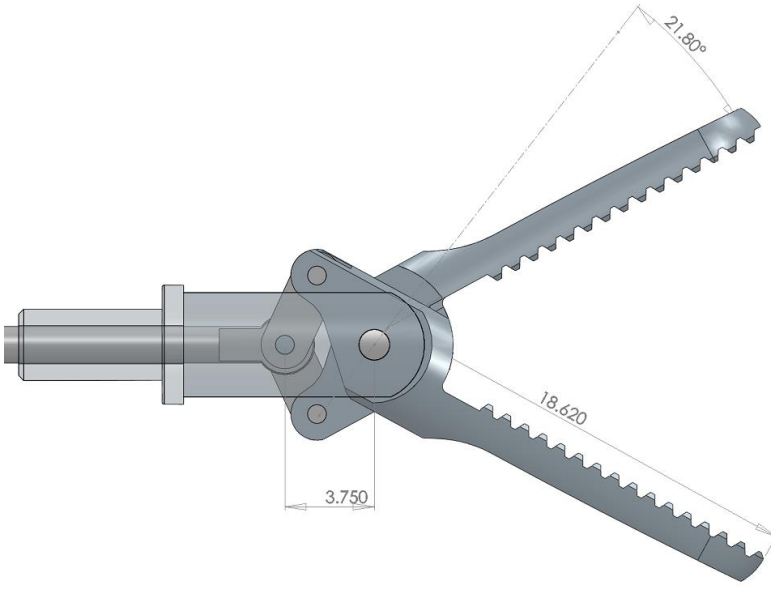

(a)

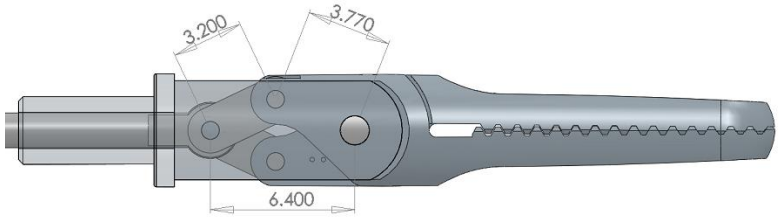

(b)

Figure 3.8: CAD of grasper measurements showing (a) jaw length, angle offset and minimum displacement, and (b) lengths of scissor linkages *a* and *b* and maximum displacement.

Parameter	Symbol	Value
Jaw length	l_j	18.620 mm
Linkage zero disp.	L_0	3.750 mm
Jaw offset angle	θ_O	21.80 °
Linkage 'A' length	A	3.770 mm
Linkage 'B' length	B	3.200 mm
Linkage disp.	Δ_L	0 – 2.650 mm max disp (6.400 mm) - L_0

Table 3.1: Measured characteristics of the laparoscopic grasper scissor mechanism.

The values of θ were calculated for the measured range of Δ_L, and from this α_A and α_B were determined. The relation between Δ_L and θ is shown in Figure 3.9a showing a non-linear relation between the linkage displacement and the jaw angle.

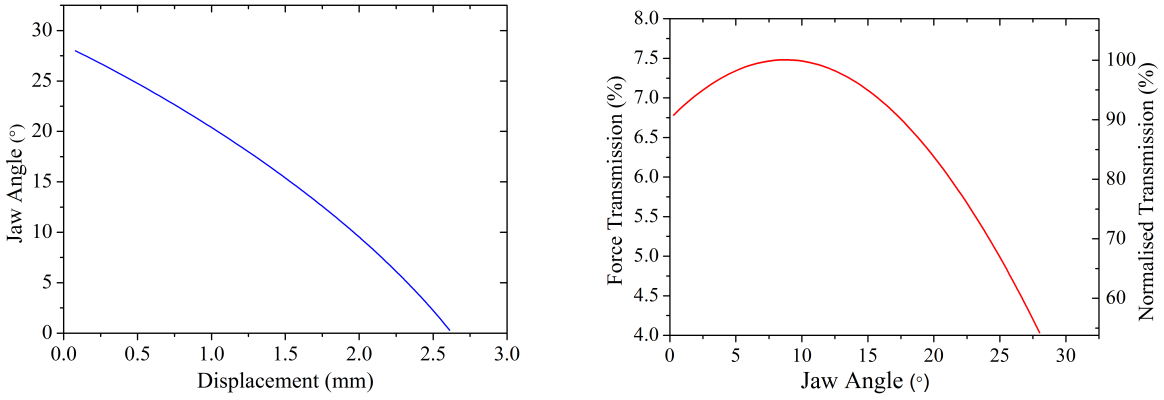

(a) (b)

Figure 3.9: Grasper jaw kinematics showing (a) the relation between linkage displacement and jaw angle, (b) the relation between jaw angle and the percentage of force transmitted to each jaw tip.

Finally, the values of α_A and α_B were used in the force equation (Equation 3.5), and the input force, F_L, and resulting tip force, F_T, were used to determine the percentage of force, $F\%$, transmitted over the displacement range (Figure 3.9b), using the equation,

$$F\% = \frac{F_T}{F_L} \times 100 \tag{3.18}$$

From the model results, it can be seen that there is an optimum point of force transmission for a jaw angle of 8.68 ° (linkage displacement of 2.06 mm), and that the percentage of force transmitted along the mechanism varies between 4.04% and 7.48% over the range of possible jaw opening angles. By normalizing the force transmission percentage, it can be seen that the transmitted force can vary by 54%, showing that it is vital that the displacement of the linkage is also measured to ensure valid tip force conversions. To summarise, the mathematical model allows for force readings from the inner grasper shaft, to be converted to a tangential tool-tip estimation. However the model also shows that the linkage displacement is required in determining the tool-tip force, therefore this will need to be incorporated into the grasper instrumentation. Further investigations may also need to take into consideration the fact that there is a distributed pressure over the grasped surface instead of a point force, however the current model still allows for comparison between different grasps, assuming similar grasping conditions.

3.5 Grasper Model Validation

The grasper mechanical model was validated to ensure that the linkage measurements were reliably converted to the tip forces for all possible jaw angles. Two methods of validation were considered. A force/pressure sensor could be placed between the grasper jaws during a grasp for varying force targets, while the linkage force was monitored. For the second method of validation, weights could be applied to the jaw to simulate a grasping force. The jaws could then be moved through the full range of motion, and the propagated force would be measured via the shaft loadcell. For either method, the jaw angle will also need to be determined.

3.5.1 Angle Validation

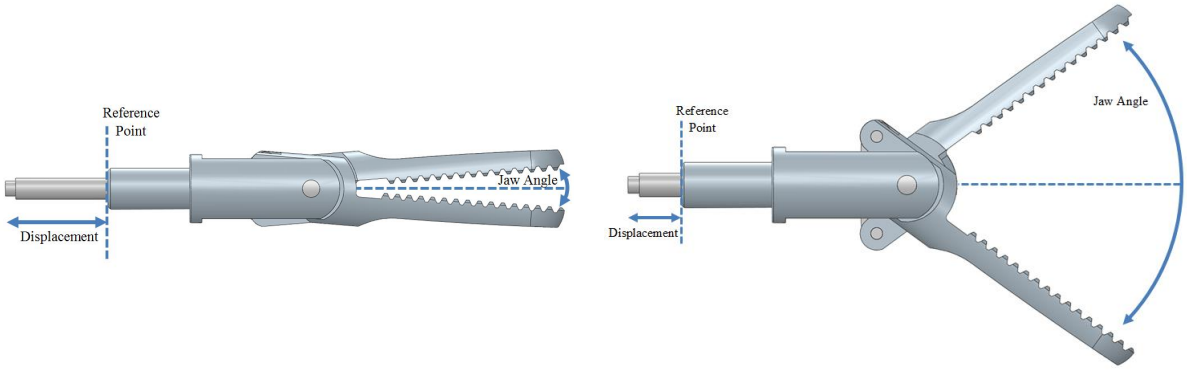

(a) (b)

Figure 3.10: CAD of grasper jaws used for the angle validation, showing the reference point and centre axis for (a) closed jaws, and (b) open jaws.

To validate the angle model the CAD of the grasper jaws was used, by measuring the linkage displacement compared to the jaw angle. This would ensure there is no error in the measurements as it will use an idealised system. The linkage was moved through 57 displacements to five approximate 0.5 degrees increments, then the actual displacement and jaw angle was measured (Figure 3.10). The displacement of the linkage was measure from a stationary reference point.

The measured results follow the predicted values from the model showing that the model can be used to reliably determine the jaw angle from the linkage displacement (Figure 3.11).

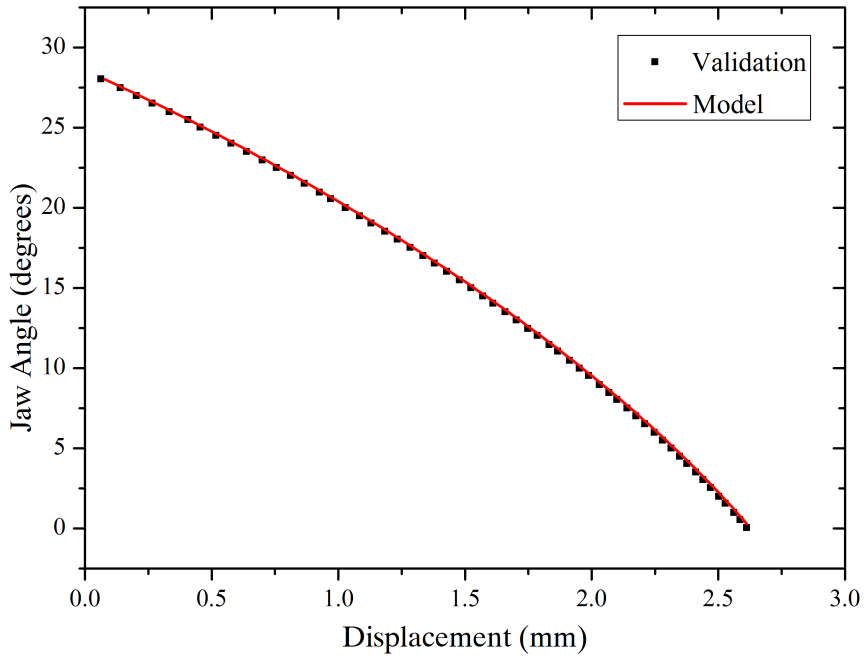

Figure 3.11: Graph of the angle validation measured results (black), and model (red).

The ideal model validated the mathematics but not the realities of the physical system. To account for any potential error in the physical mechanism (linkages or joints), the backlash in the grasper mechanism was measured at 0.13 mm (up to a maximum of 0.95 degrees), resulting in a potential error of ± 2.45 %. This was achieved by securing the actual grasper jaws together, then moving the actuator rod back and forth while logging the force. The range of motion was recorded where the force remained at zero (Figure 3.12).

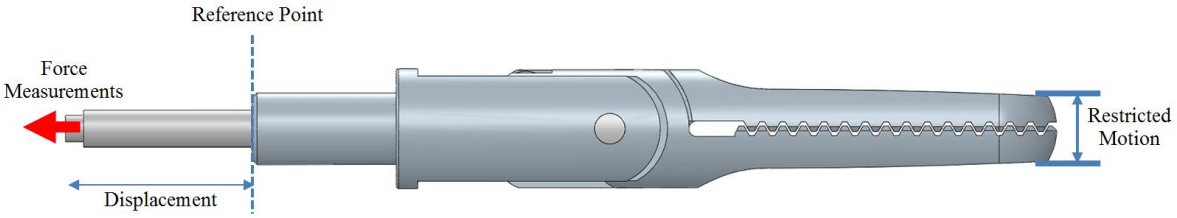

Figure 3.12: Mechanism backlash measurements set-up, showing the secured jaws and direction of motion (CAD shown for clarification).

3.5.2 Force Transmission Validation

To validate the force propagation model, weights were suspended from the grasper tips. This method would require the applied tip force to be normalised using trigonometry, to determine the tangential tip force. This method requires two 100 g weights suspended via a pulley at each side using lightweight thread (Figure 3.13). As the model was developed for a static system, any friction introduced from the pulleys would be kept to a minimum.

Measurements were taken over 11 positions, up and down for 3 repeats. During loading and unloading, the force was monitored and logged through a linkage loadcell (LCM703-25, Omegadyne Inc.) placed in series with the linkage, and the jaw angle was calculated using the previously validated angle model.

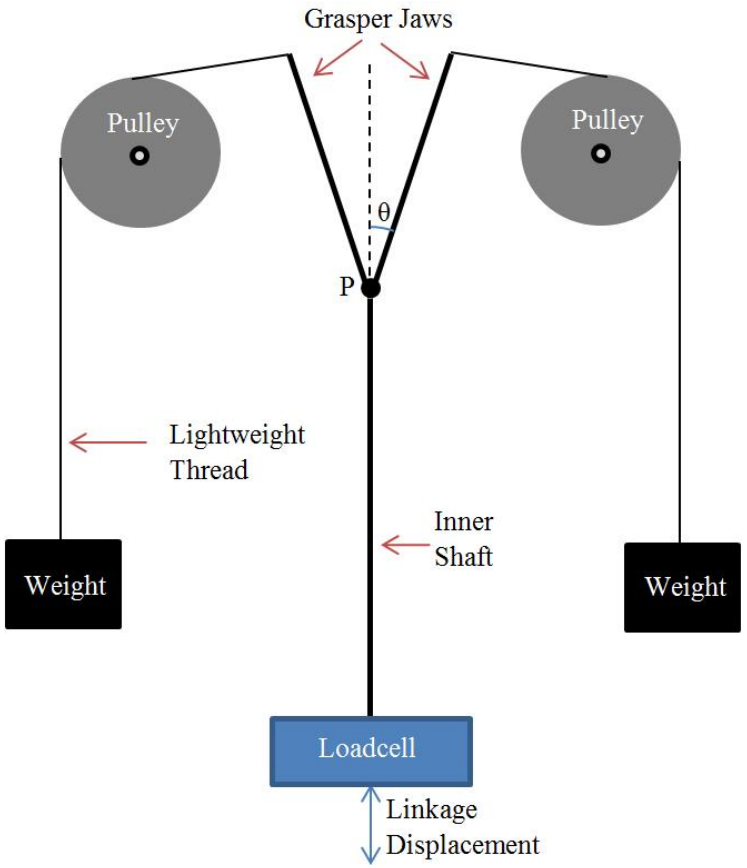

Figure 3.13: The force validation set-up showing the suspended weights via the pulleys with the loadcell and displacement measurements.

The tangential tip force was calculated, assuming an ideal pulley system i.e. no force is lost from friction (internal bearings in the pulley make this possible). Assuming the system is also symmetrical, one side of the system was observed, simplifying the overall model. The force acting on the tip from the applied weight, F_W, would have two components, one acting along the jaw, F_{TX}, and the second acting perpendicular to the jaw, F_{TY}, (Figure 3.14a). It has been assumed that the longitudinal force, F_{TX}, does not cause the grasper jaw to move, due to the fixed pivot, P, and therefore only the perpendicular force, F_{TY}, was calculated (for clarity the parameter term has been shortened to F_T). For a given jaw angle, θ, the tangential force, F_T, was found as the component of the applied weight, F_W, through the angle β (Figure 3.14a) with the following equation,

$$F_T = F_W cos\beta \tag{3.19}$$

From this FBD, additional parameters could be added to give the size and location of the pulley relative to the grasper (Figure 3.14b).

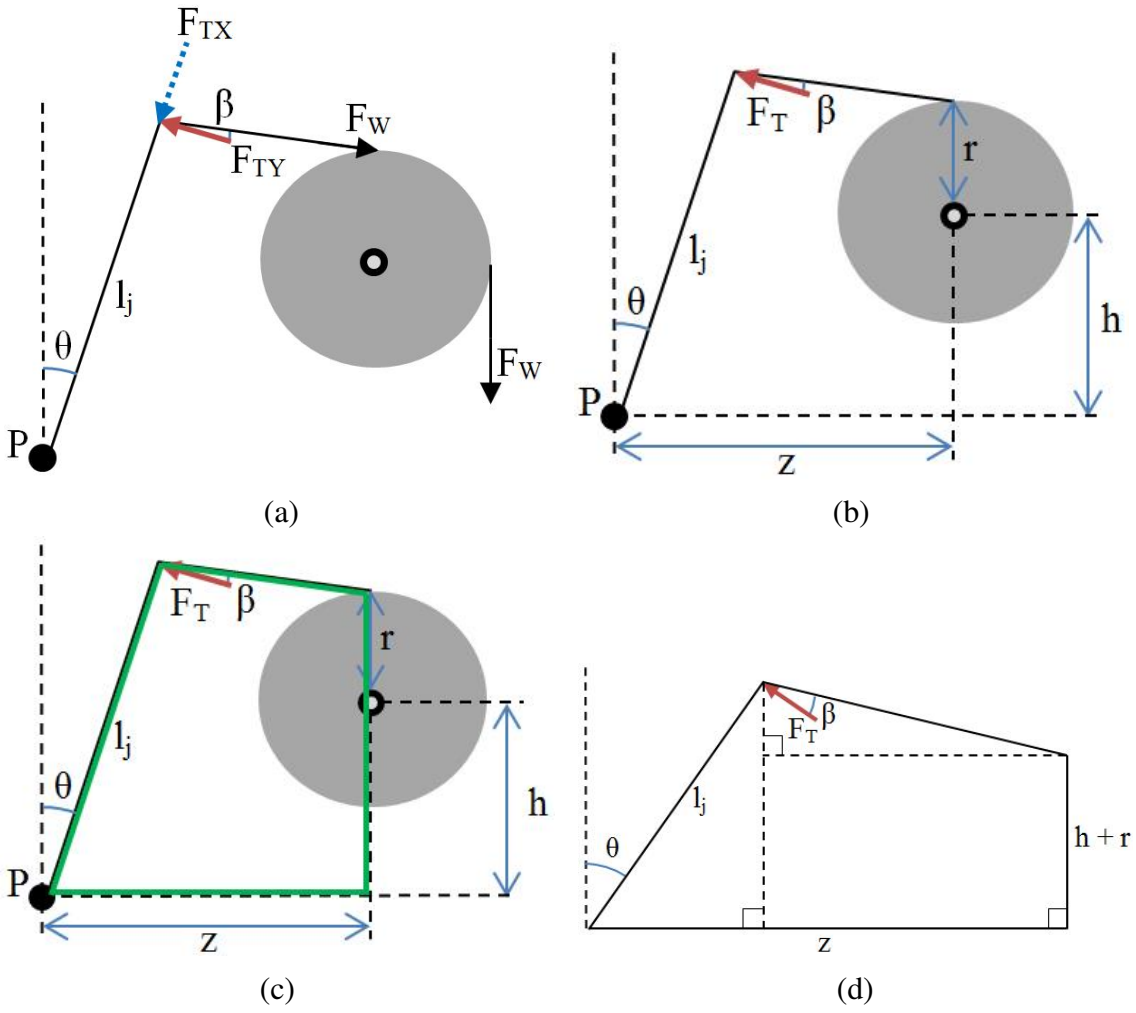

Figure 3.14: The pulley system diagram used to determine the tangential tip force, F_T, using β, highlighting (a) the initial system showing the applied weight F_W, and (b) the system with additional paramters, z and h, the pulley location and r, the pulley radius, with (c) the highlighted trapezium used, and (d) the exaggerated trapezium model.

The trapezium that was formed (Figure 3.14c) was then used to determine the value of β. The geometry of the trapezium has been exaggerated to clarify the internal angles and dimensions (Figure 3.14d). The parameters l_j, r, h, z, and F_W are all known, and in the case of θ, can be determined by the model. From this the trapezium was split into 2 triangles and a square, and parameters were added to allow β to be calculated (Figure 3.15).

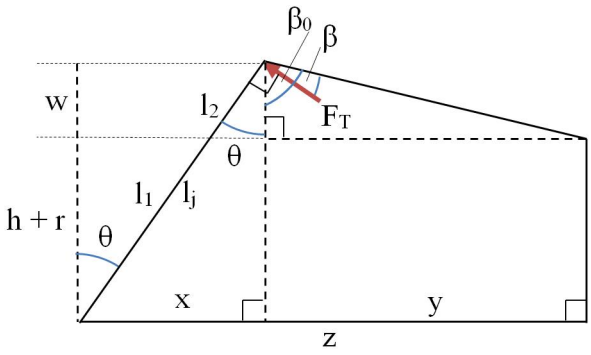

Figure 3.15: The trapezium model used to determine the tangential tip force, F_T.

From this, using trigonometry, it can be seen that,

$$x = l_j sin\theta \tag{3.20}$$

which then gives,

$$y = z - x \tag{3.21}$$

Additionally,

$$h + r = l_1 cos\theta \tag{3.22}$$

rearranging gives,

$$l_1 = \frac{h + r}{cos\theta} \tag{3.23}$$

which then gives,

$$l_2 = l_j - l_1 \tag{3.24}$$

and,

$$w = l_2 cos\theta \tag{3.25}$$

Using these parameters, the angle of β_0 is found as,

$$\beta_0 = tan^{-1}\left(\frac{y}{x}\right) \tag{3.26}$$

And finally the resulting angle, β, is found using,

$$\therefore \beta = \beta_0 + \theta - 90 \tag{3.27}$$

From this the applied weight via the pulley could be converted into a tangential tip force using β, for each value of θ, (Equation 3.19) (Figure 3.16a).

For each position the linkage force, F_L, was logged (Figure 3.16b), and used to determine the magnitude of force which is transmitted through the grasper mechanism, $F\%$ (Equation 3.18)

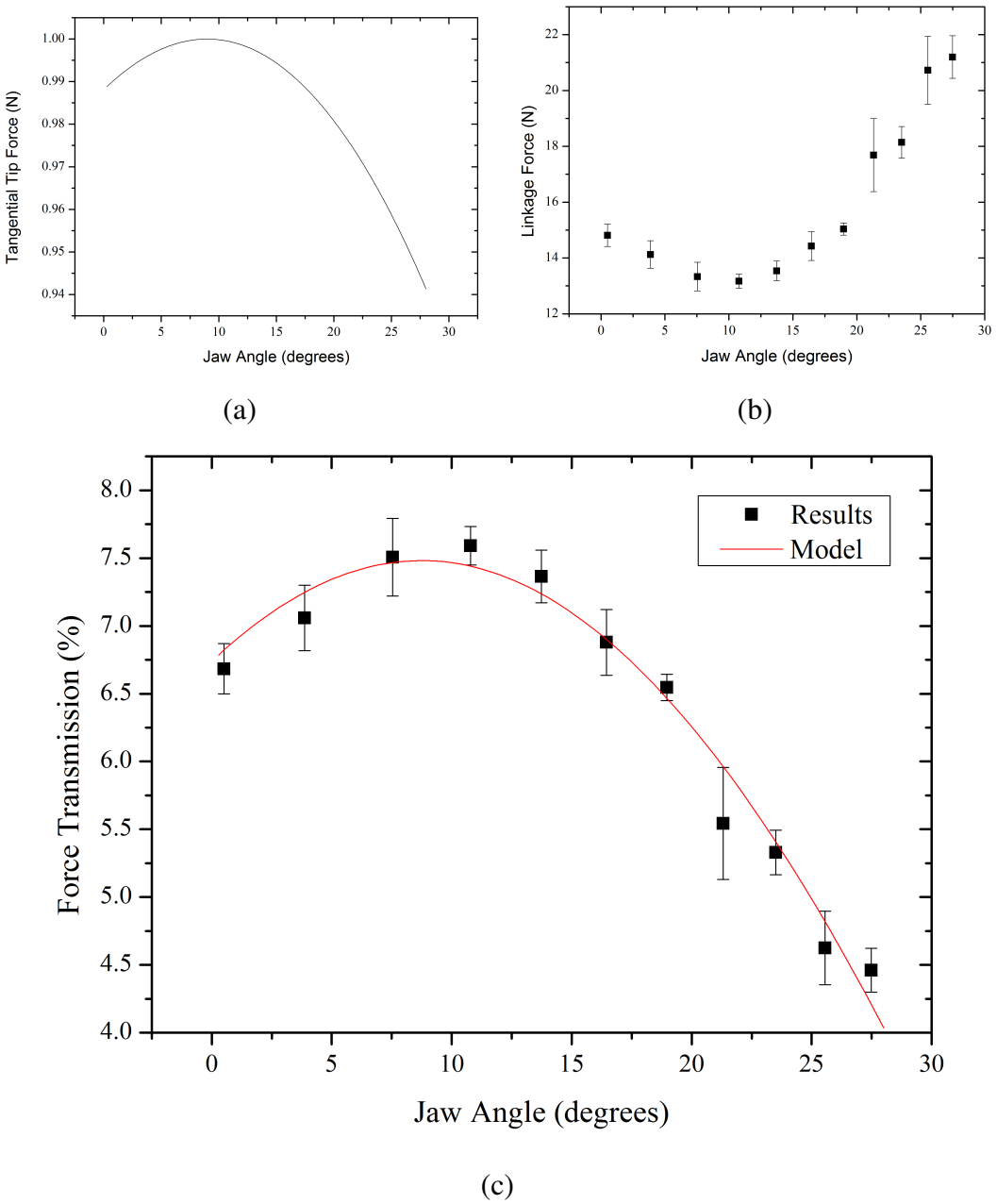

Figure 3.16: The validation results showing (a) the variation of the tangential tip force as the jaw angle changes, (b) the measured linkage forces, and (c) the resultant transmitted force through the grasper mechanism with measured data (black) and model (red), for three repeats during loading.

These results were then plotted against predicted values from the model to compare (Figure 3.16c).

3.5.3 Validation Conclusion

The results showed that the measurements collected from the grasper set-up show the same trend as those calculated using the mathematical model, with an associated error of

0.13 mm/0.95 degrees ($\pm 2.45\%$)for angle/displacement measurements, and $\pm 0.41\%$ absolute variance in the force (up to $\pm 5.47\%$ for the normalised variance) for the force readings. The force transmission results and tip forces are of a similar magnitude to those predicted by the model, therefore this was used to convert grasper linkage measurements to the jaw angle and tip forces. These results have potential implications on the resulting tip forces for small angle changes especially when the grasper is mostly open, however it is anticipated that the surgeon would generally use the grasper over the higher efficiency range, lowering the potential error. Also there would be implications for highly dynamic grasping but it is also expected that the grasper jaws will remain stationary for the majority of the time.

3.6 Development of the Instrumented Grasper Prototype

3.6.1 Designing the Instrumentation Module

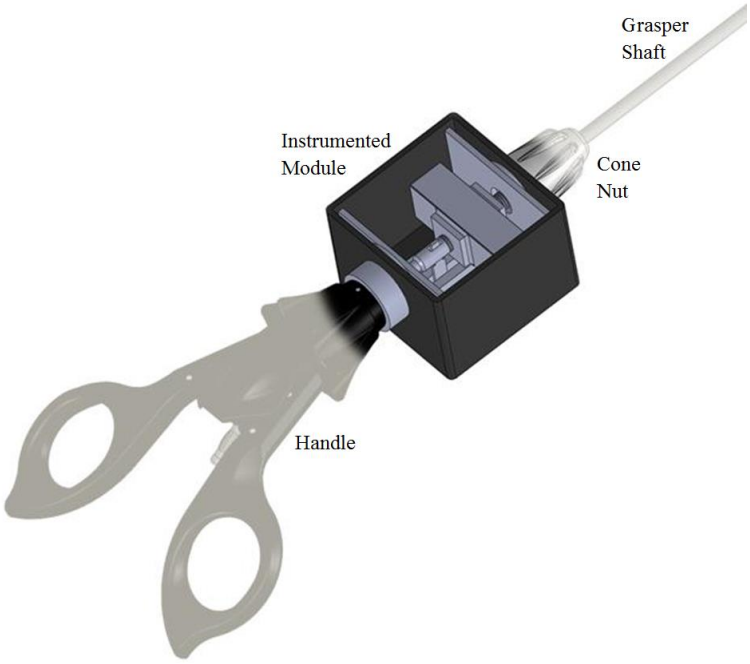

Figure 3.17: SolidWorks CAD of the first instrumented grasper prototype, highlighting the location of instrumented module.

The first design of the instrumented grasper was created using SolidWorks (Figure 3.17). The sensors are mounted in a polycarbonate housing which is secured between the handle and grasper linkage using M15×1.5 threaded hollow connectors. An M15×1.5 thread is used to secure both sections together while ensuring that the outer shaft of the grasper does not move while in use. The instrumentation is fixed between these two sections using the

same M15×1.5 threads, while a bespoke, free moving linkage was placed inside to rejoin the connector and inner shaft.

To measure the force along the inner shaft of the grasper, a miniature loadcell (dimensions 41×17×19 mm) with opposing M6×1.0 threaded holes has been used, to ensure the design is compact and is also capable of high force readings. Two bespoke connectors are fixed to each side of the loadcell to reconnect the handle to the inner shaft, which consist of an M6×1.0 threaded end to fit into the loadcell, and each one designed to match either the handle or shaft connection (Figure 3.3).

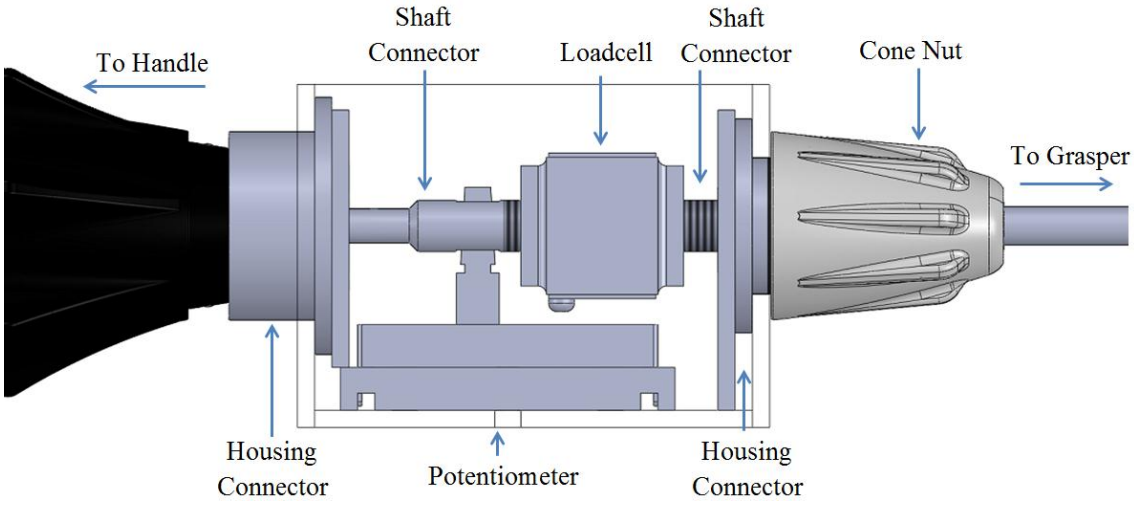

Figure 3.18: CAD (side view) of the first instrumented grasper module *in-situ* highlighting the suspended loadcell and potetiometer sweeper arm fixture, the housing connectors, and the inner shaft connectors.

To provide a simple and cost-effective method to measure the displacement of the inner shaft, a linear potentiometer (length 30 mm and travel 20 mm) was chosen. The potentiometer is fixed to the bottom of the housing and the loadcell is suspended between the handle and inner shaft. The sweeper arm of the potentiometer slots into the loadcell connector at the handle side (Figure 3.18) to prevent any unwanted friction interfering with the forces being measured by the loadcell. Wiring then passes from the housing to a Personal Computer (PC) via a Universal Serial Bus (USB) Data Acquisition (DAQ) device (described in section 3.6.2).

The shaft and housing connectors have been manufactured from stainless steel to improve rigidity when grasping and the housing connectors are secured into place using strips of aluminium, allowing if necessary for the module to be disassembled.

There were also considerations to implement a wireless system however this was dismissed for the following reasons:

- There would be a considerable amount of added weight from both the batteries and loadcell amplifier.

- The size of the housing would be much larger to incorporate this, along with extra space for the prototyping wireless module/antenna.
- There would be a limited amount of time the instrumented grasper could be used before the batteries were depleted.
- A tethered device would not add any extra restrictions as surgeons are trained to use cauterizing devices which require tethering to a power supply.

3.6.2 Instrumented Grasper Hardware

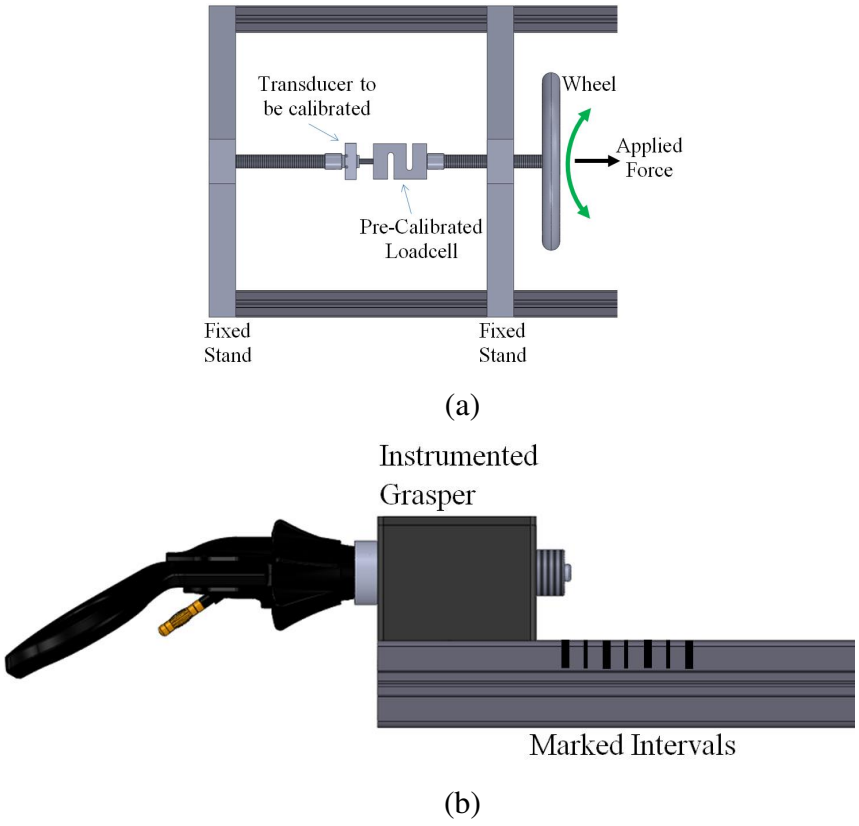

Figure 3.19: Calibration set-up of (a) the loadcell (top view) showing a pre-calibrated loadcell in series with the transducer to be calibrated along a threaded bar, and (b) the potentiometer showing the measured output voltage and marked intervals.

To measure the tensional forces along the grasper's inner shaft, the loadcell (LCM703-25, Omegadyne Inc. (Appendix A)) was chosen and is capable of $\pm$250 N, with a linear relation between the applied force and the output voltage. To amplify the loadcell output (2 mV/V), it is connected to a transducer amplifier (DR7DC, RDP Electronics Ltd. (Appendix A)) which uses a 15 V power supply and was adjusted to give a bridge supply of 10 V and an output of 0 - 10 V for a force of approximately 0 - 150 N. A calibration rig (see Figure 3.19a) with

a force accuracy of ±0.05 N was used to determine the force/voltage relation equation of the loadcell. As the wheel was rotated clockwise, the threaded bar was placed under tension simultaneously increasing the force applied across each loadcell.

The output voltage from the loadcell was plotted against the pre-calibrated force reading for three sweeps up and down the force range (0 - 150 N) (Figure 3.19b). The sweeps were split into approximately 15×10 N increments, with the exact force and voltage readings taken each time. A line fit equation was then used to determine the applied force for a given output voltage, where F is the force to be calculated, the line gradient is 14.94 (± 0.00), the intercept is 0.07 (±0.03) and V is the voltage variable (0 - 10 V). The lines intercept does not pass through the origin due to small errors when *'zeroing'* the system, but this is taken into account by the line equation.

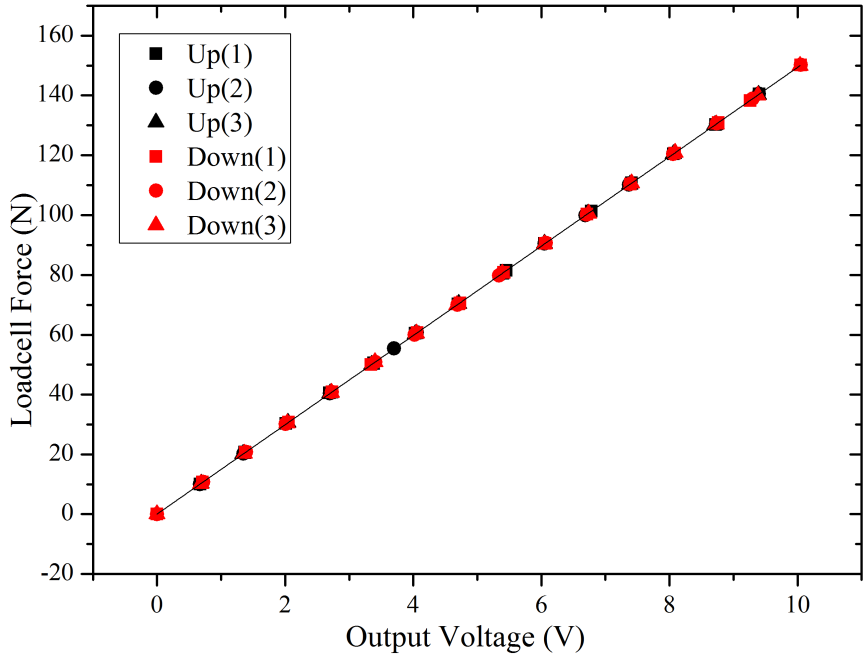

Figure 3.20: Loadcell (LCM703-25) calibration graph showing three continuous up/down sweeps and linear fit (fit; $F = 14.94V + 0.07 (R^2 = 1.00)$(F is force, V is voltage)).

The 10 kΩ potentiometer uses a 15 V supply and is placed in series with two 1 kΩ resistors to prevent the power supply from being overloaded, giving a normalised voltage range of approximately 0 - 12.5 V. To calibrate the potentiometer the sweeper arm was moved through 5 mm marked intervals in its stroke length (0 - 20 mm) using a linear scale with accuracy ±0.25 mm (Figure 3.19b). The output voltage was taken at each interval for three sweeps up and down the range. As with the loadcell calibration results, a linear fit can be used to determine the position of the potentiometer from the output voltage (Figure 3.21), where D is the displacement to be calculated, the line gradient is 1.62 (±0.02), the intercept is 0.51

($\pm$0.30) and V as the voltage variable (0 - 12.5 V).

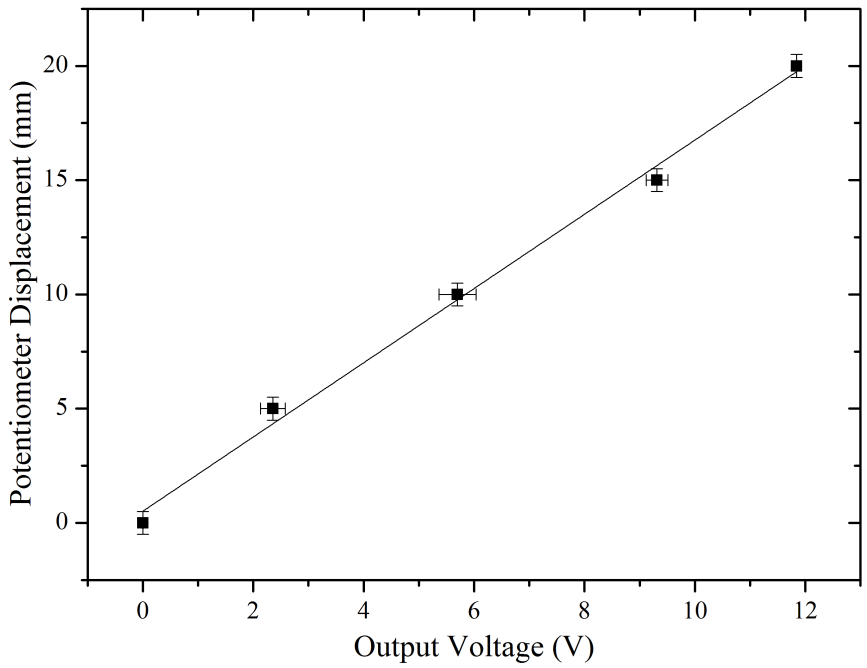

Figure 3.21: Linear potentiometer calibration graph showing the average of three up/down sweeps with vertical measurement error bars, horizontal error bars from positional accuracy, and the linear fit (fit; $D = 1.62V - 0.28$(D is displacement, V is voltage)).

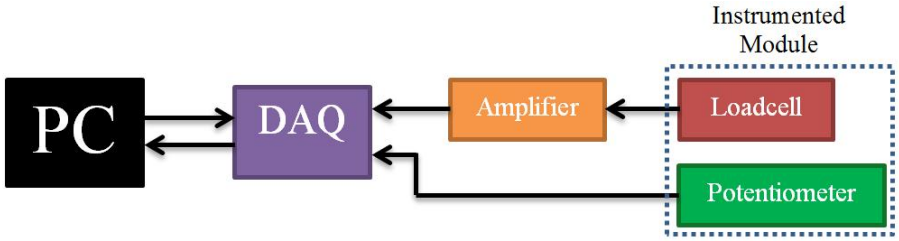

Figure 3.22: The instrumented grasper system diagram, showing the data connections between each hardware device and highlighting the components located in the instrumented module.

To interface between the PC and the rig, the DAQ USB device (National Instruments USB-6009, (Appendix A)) was chosen for fast reliable data collection, consisting of eight analogue inputs (14 bit, 48 k Samples/second (S/s)), two analogue outputs (12 bit, 150 S/s), 12 digital inputs/outputs, a 32-bit counter, and is compatible with the program development software LabVIEW. The outputs from both the loadcell amplifier and the potentiometer are connected to the two analogue inputs (Figure 3.22), with the components situated in the instrumented module.

The final instrumented grasper kit set-up (Figure 3.23) comprises of a regulated 15 V adapter to provide a stable DC power supply, a USB connection to interface the kit with a PC or laptop, the housed amplifier and DAQ device for easier transportation, and the complete instrumented grasper. The handle, shaft, and cone nut remain unmodified and a 5 m long flexible cable is used to prevent restriction on the user and provide ample access in surgery.

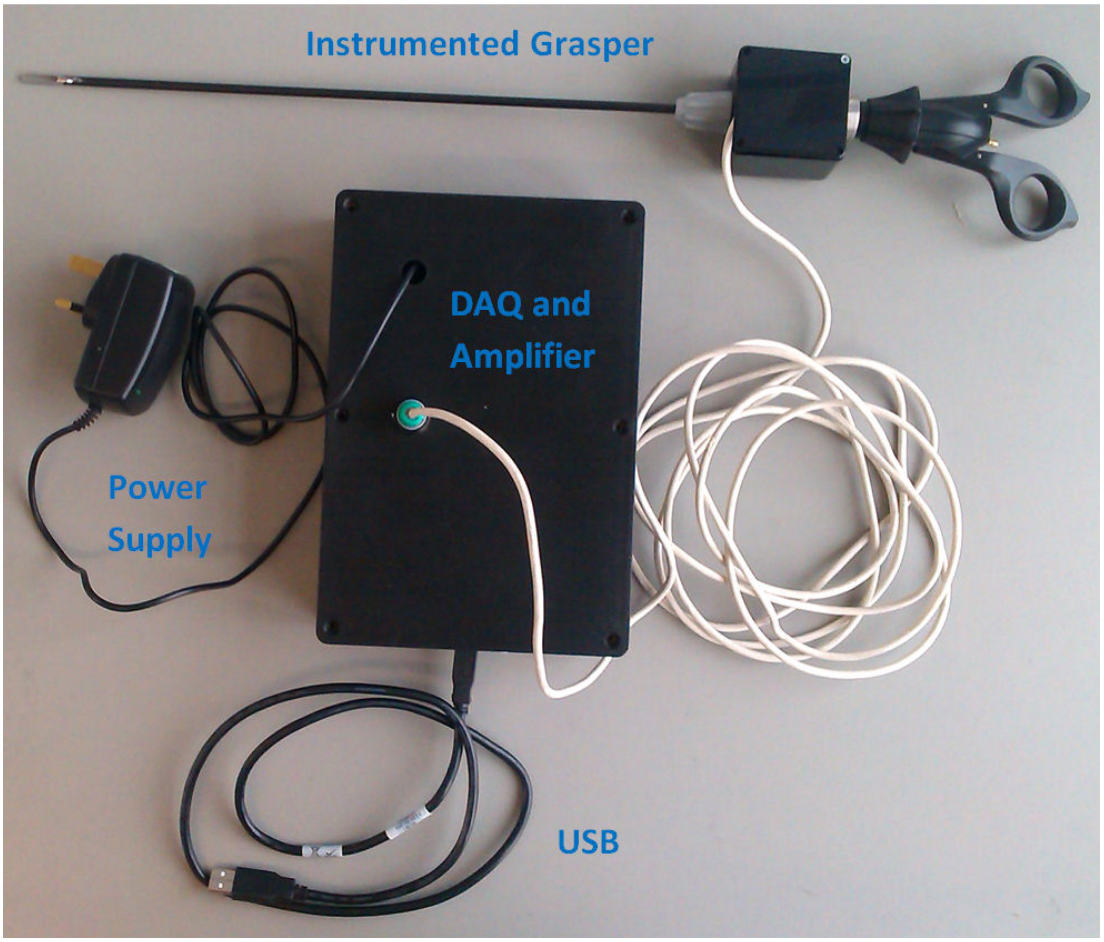

Figure 3.23: The complete instrumented grasper set-up showing power supply, USB connector, housed DAQ and amplifier and the assembled instrumented grasper.

3.6.3 Instrumented Grasper Data-Logging Program

To control the force-time and displacement-time DAQ of the instrumented grasper and to provide the simple user interface, a program (Figure 3.24) was implemented using LabVIEW (Appendix B). Forces up to 100 N were expected with potential logging time of up to 10 minutes for each, which was considered a suitable time in which to perform individual manipulation tasks.

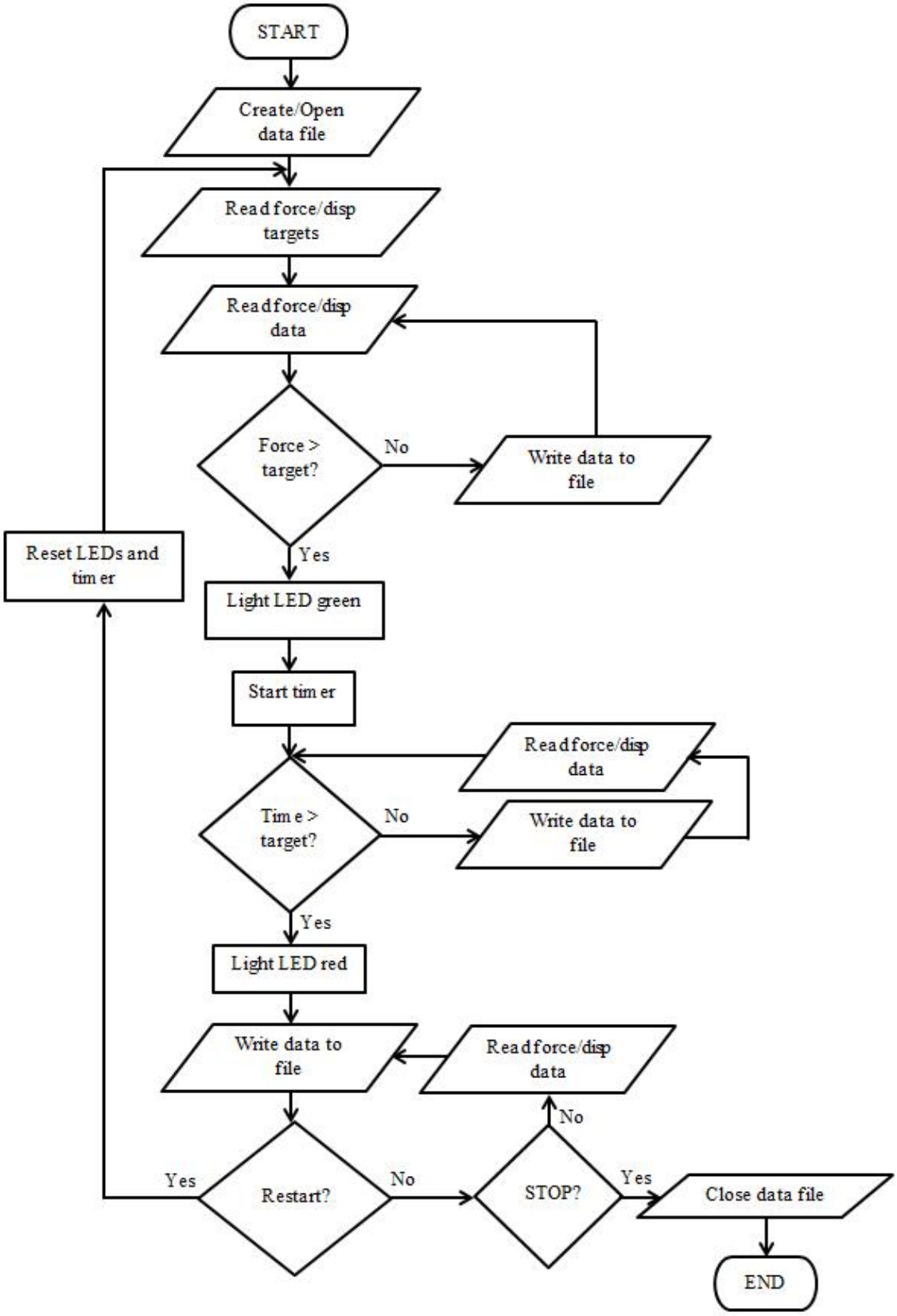

Figure 3.24: Instrumented grasper flow chart, showing the force and time target loops with force and displacement (disp) and restart/stop loop.

Simultaneous force and displacement readings are taken by a PC via the DAQ USB device and displayed on the programs Graphical User Interface (GUI) (Figure 3.25). When required, the GUI also allows the user to alter the force and time targets with the green and red lights used to indicate when the desired targets have been reached respectively. These can be reset using the *'restart'* button allowing for multiple cycles to be performed. The appropriate DAQ ports can be selected in *'set-up'* with the measurement data saved in the stated file, while the force waveform is used to show the surgeon the current grasping force profile if needed.

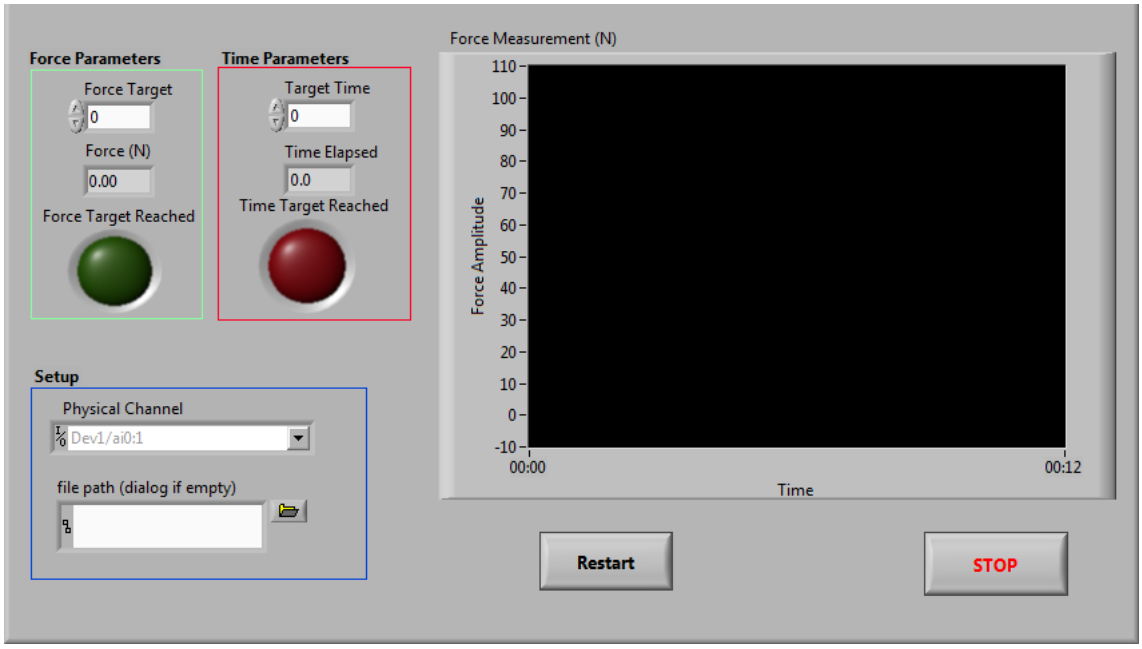

Figure 3.25: LabVIEW GUI for the instrumented grasper showing the force and time control parameters, the setup options and the graphical data display.

The programs sample rate was investigated to ensure accurate data is collected in a fast and consistent time, limiting the potential for missed readings. The program was run for ten seconds (to average any noise that might occur in the signal) while logging the force, position and time data with the grasper stationary, while the time between samples was monitored. This was performed over three repeats for each sample rate (500 Hertz (Hz) - 1k Hz). From this the average time between samples was found and used to calculated the standard deviation of the sample rate (Figure 3.26). For the optimum sample rate, a low standard deviation was required to show that the time between samples is repeatable.

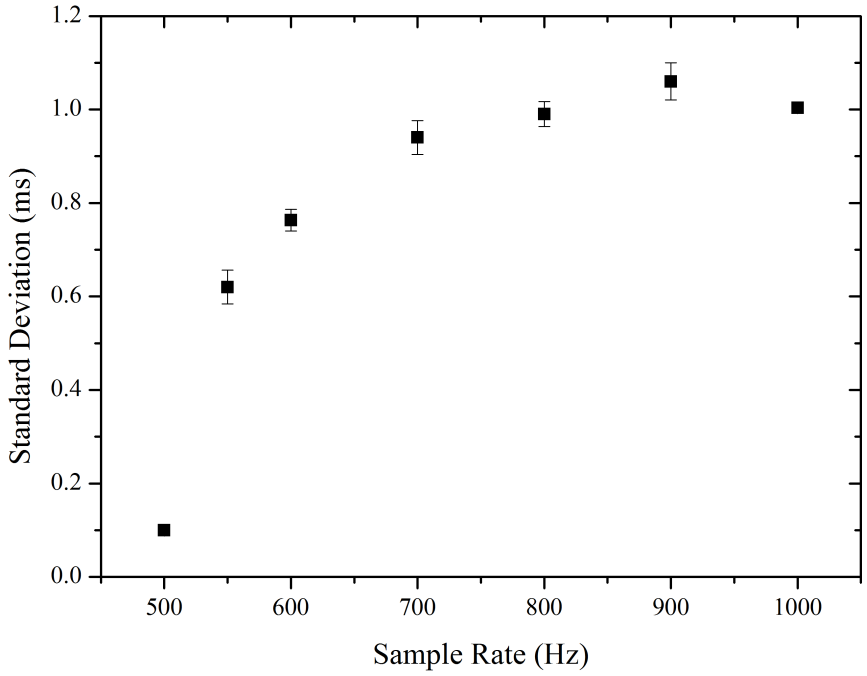

Figure 3.26: Sample time standard deviation for desired sample rates, for the first instrumented grasper LabVIEW program.

As the demanded sample rate increases, the time between samples becomes less reliable, so a sample rate of 500 Hz was chosen as this is significantly higher than the frequency response expected in typical surgical situations [182].

3.6.4 Validation of the Loadcell and Potentiometer Measurements

To ensure that the loadcell and potentiometer provide accurate and repeatable readings, both were validated *in-situ*. Firstly a series of 50 g weights were suspended from the loadcell connector up to 1 kg (Figure3.27). For each weight change the readings from the amplifier were sampled for three seconds then averaged to minimise the effect of error caused by any noise in the signal. The weight was incremented then decremented for three sweeps, and a linear fit found (Figure 3.28). The linear fit was used to determine the accuracy of the loadcell, where F_L is the loadcell force reading, the line gradient is 1.00 ($\pm$0.00), the intercept is 0.01 ($\pm$0.01) and F_A is the applied force (0 - 10 N).

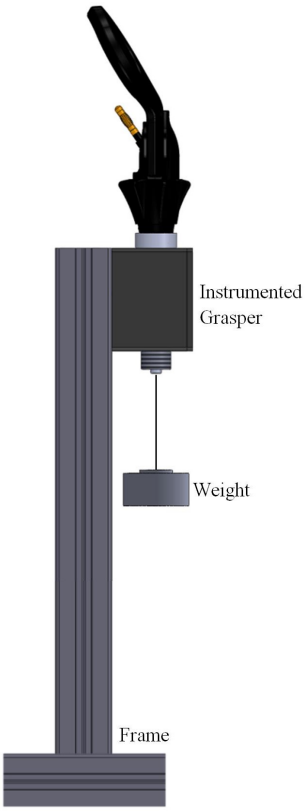

Figure 3.27: Loadcell force validation set-up for the instrumented grasper.

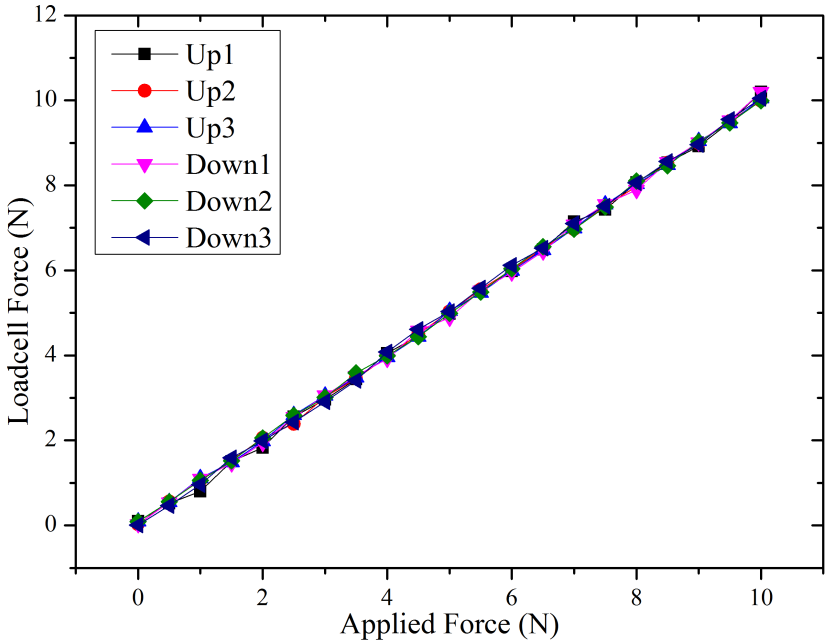

Figure 3.28: Loadcell force validation graph for three up/down sweeps with a linear fit (fit; $F_L = 1.00F_A + 0.01 (R^2 = 1.00)$).

The results show that the loadcell readings are accurate to 1 DP with maximum 0.02 N

error for each reading. This is a maximum error of 0.4 % for a force range of 5 - 70 N [175] and so can be considered as negligible. Due to the high accuracy of the system, the R^2 term was also included to highlight this. R^2 is a statistical measure to show how close the data lies to the linear fit, ranging from 0 to 1 (high to low variability respectively).

Using a pre-calibrated laser displacement sensor (accuracy $\pm$0.025 mm) (Appendix A), the potentiometer was moved using the handle through its full range (approximately 0 - 8 mm) (Figure 3.29). At each approximate 1 mm increment the laser position was measured and the potentiometer reading was sampled for three seconds then averaged, to account for any noise.

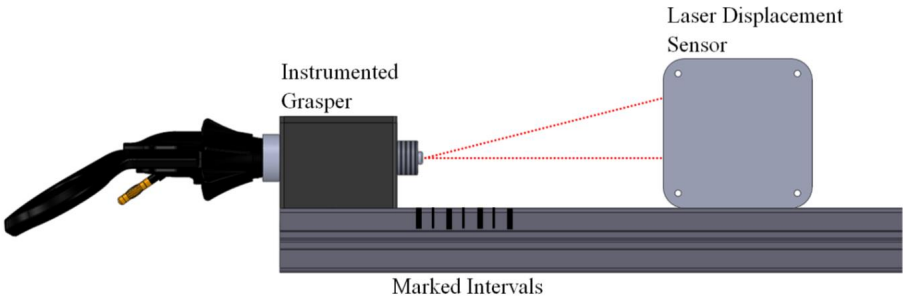

Figure 3.29: Potentiometer displacement validation set-up for the instrumented grasper (laser shown in red).

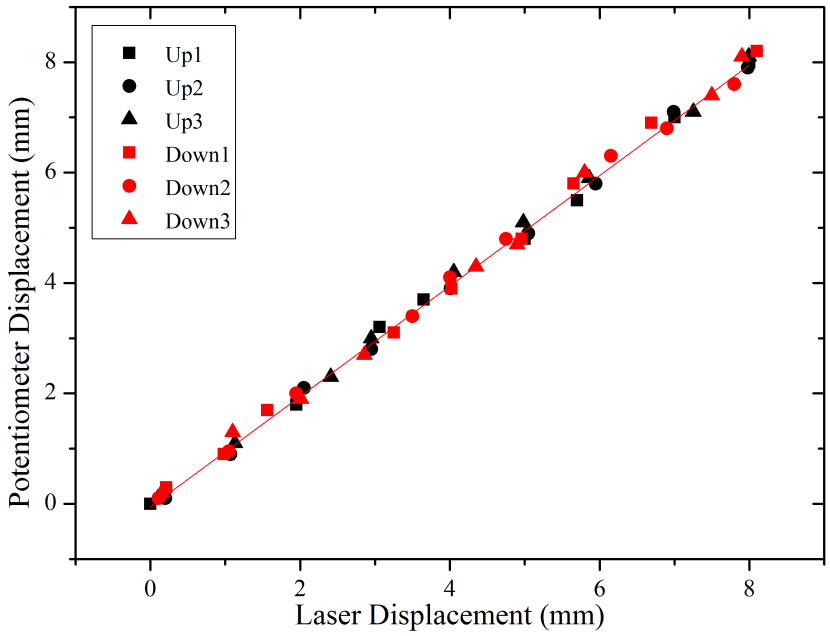

Figure 3.30: Potentiometer displacement validation graph for three up/down sweeps with a linear fit (fit; $D_P = 1.00D_L + 0.06$).

Three sweeps of up and down readings were taken of the laser sensor and potentiometer readings (Figure 3.30). The linear fit was used to determine the accuracy of the potentiometer,

where D_P is the potentiometer displacement reading, the line gradient is 1.00 ($\pm$0.08), the intercept is 0.06 ($\pm$0.02) and D_L is the actual displacement (0 - 8 mm). The results show that the potentiometer readings have a maximum possible error of 2 % for the highest readings.

3.7 *In-vivo* Testing with the Instrumented Grasper

Two testing methodologies were performed using the instrumented grasper to investigate what typical measurements are to be expected in surgery when performing tasks. This could then be used in further areas of the project, to advise the choices for test parameters. Secondly the grasper usability has been explored to show if the grasper could be used to apply precise forces for a given time by a user.

3.8 *In-vivo* Organ Manipulation Testing

For the *in-vivo* organ manipulations, the first instrumented grasper prototype was used alongside a non-instrumented grasper of the same design, to allow for easier manipulation and set-up during testing. This aimed to investigate the typical *in-vivo* grasping profiles and how tissue responds during grasping, i.e. how does tissue relaxation vary. Both these experiments were performed in the closed abdominal cavity insufflated with CO_2, while being viewed on a monitor through a laparoscope, to simulate typical MIS. For the *in-vivo* tissue testing, an anaesthetised 40 kg white pig was used due to the similarities to the human model, as discussed in the literature review (section 2.3).

3.8.1 Methodology of *In-vivo* Organ Manipulation

For the first part of the experiment, a trainee surgeon was asked to *'run the bowel'* whereby the colon is passed from grasper to grasper, progressing along the colon. Each run consisted of 10 grasps in total, 5 with each grasper, starting with the non-instrumented grasper. The force-time and displacement-time measurements were stored over five repeats for post-analysis.

Secondly the trainee surgeon was asked to grasp various abdominal organs and retract them for 30 seconds, with 5 repeats, on a fresh area of tissue. The retraction motion performed was that of typical MIS, whereby the surgeon would gain access under the organ by holding it out of the way. The organs which were grasped were the bladder, colon, gallbladder, rectum, and small intestine, as these represent those involved in typical abdominal surgery and the force-time and displacement-time measurements were stored for post-analysis.

It has been noted that the trainee surgeon would potentially perform tasks differently when compared to an experienced surgeon, but it is likely that the grasping forces would be

slightly larger and therefore this would provide a *'worst case scenario'*.

3.8.2 *In-vivo* Laparoscopic Testing Set-up

The *in-vivo* setup (Figure 3.31) comprised initially of three ports for the two graspers and laparoscope, with additional ports added as the operating region changed.

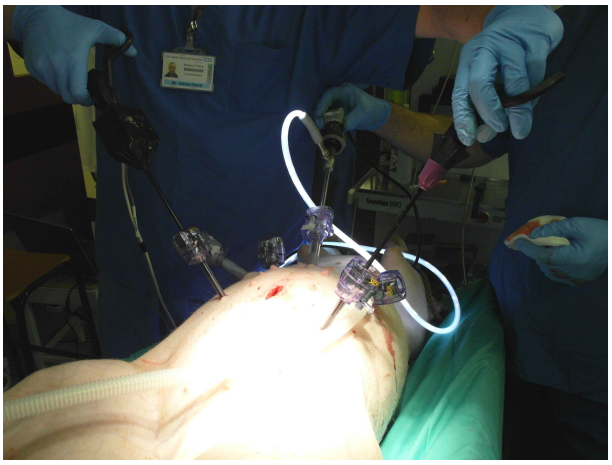

(a)

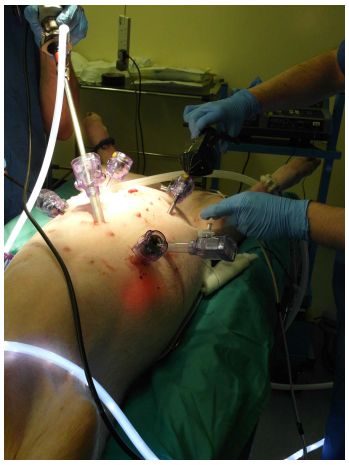

(b)

Figure 3.31: *In-vivo* laparoscopic surgery set-up showing (a) grasper setup with instrumented grasper on the left, unaltered grasper on the right and laparoscope in the middle, and (b) additional ports used for alternative access.

The images were displayed on a monitor for the surgeon to see the tasks being performed, simulating as close a possible to actual MIS (Figure 3.32).

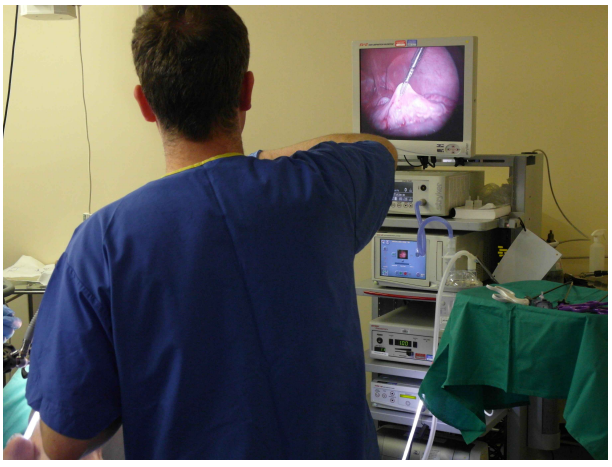

(a)

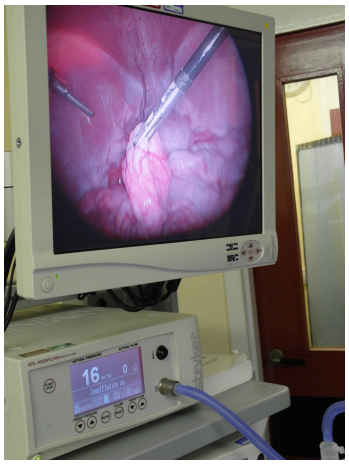

(b)

Figure 3.32: *In-vivo* laparoscopic testing, showing (a) the surgeon performing surgical task observed on a monitor, and (b) the monitor display of the view from the laparoscope.

3.8.3 *In-vivo* Organ Manipulation Results

For each set of data for the organ manipulation tests, the instrumented grasper linkage measurements were converted to tool-tip forces and jaw angles using the mathematical model (section 3.4). There were a number of differences in the types of grasping profile observed (Figure 3.33). Due to external factors such as hand vibrations and other organs moving around during grasping, it was often difficult to witness natural relaxation in the tissue. The maximum applied force and Root Mean Square (RMS) average of each grasp were found. Inclusion of the RMS average takes into consideration the full grasp profile so a truer average force can be observed, for example when grasping the rectum, one grasp has a higher maximum force of 2.74 N (Figure 3.33a), over a second grasp which has a maximum force of 2.28 N (Figure 3.33b), but due to the variations in grasping profile the RMS average forces are 1.13 N and 1.19 N respectively.

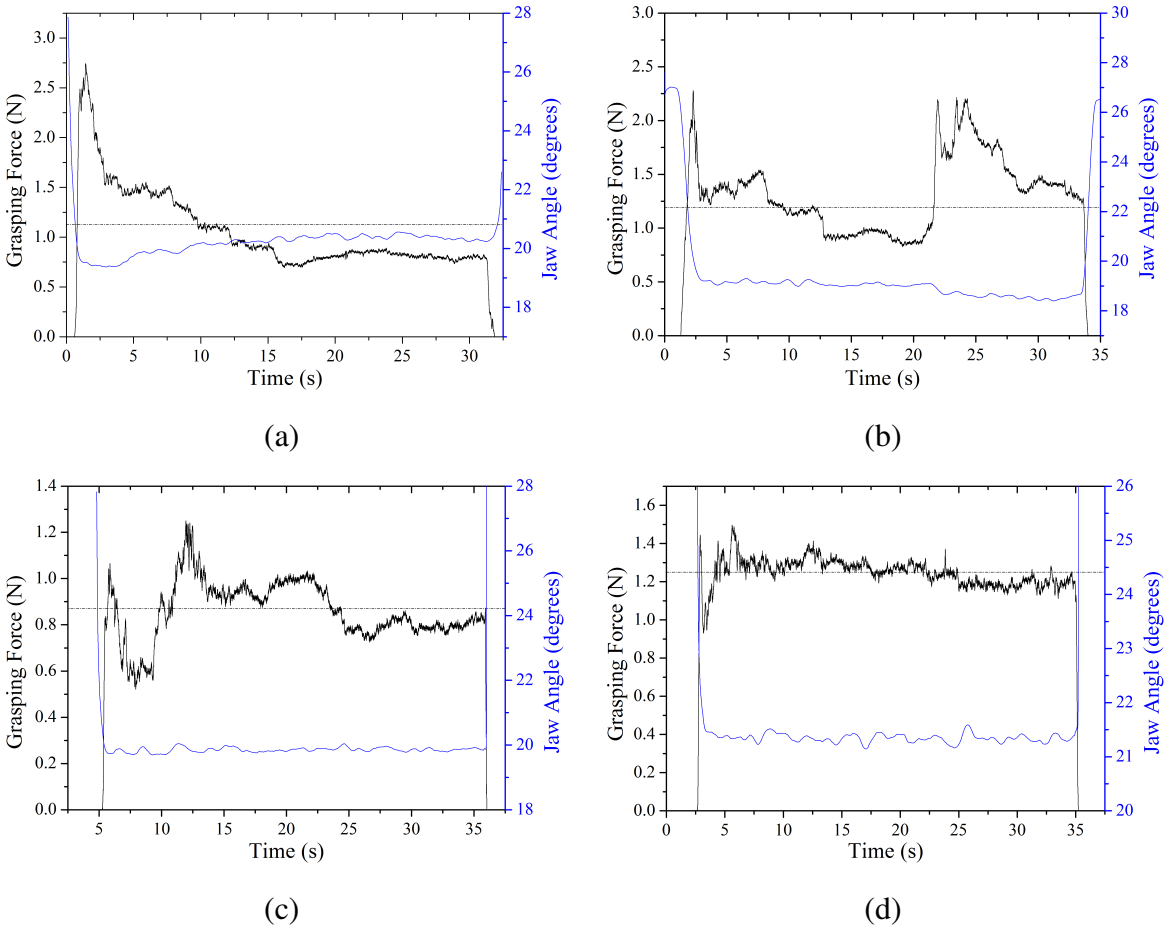

Figure 3.33: *In-vivo* grasping characteristics (RMS values shown as dotted line) representative of typical force-time profiles; (a) force peak is reached with some relaxation observed (rectum), (b) fluctuating grasp force (rectum), (c) maximum force occurs midway through grasp (bladder), and (d) little or no relaxation observed (bladder).

An ideal grasping force profile, for observing tissue response and ease of analysis, would show exponential decay as the grasped tissue relaxed, similar to the typical grasping observed in rectum (Figure 3.33a). However this profile is not ideal for tissue response analysis due to slight tremors throughout which has been shown in previous research (section 2.4.2). Other typical profiles include large force fluctuations (Figure 3.33b), those whose force peaks midway through the grasp (Figure 3.33c), and flat profiles showing little or no relaxation (Figure 3.33d). The maximum applied force and average applied force were plotted with standard deviation, to show the applied force to each abdominal organ over 5 repeats. This shows that the maximum tip forces on colon, rectum, and gallbladder are approximately double that of the bladder and small intestine (Figure 3.34). These higher force are likely a results of ensuring the heavier/larger organ can be retracted far enough, with less chance of the smaller or lighter organs slipping. However in the case of the gallbladder this may be due to the difficult accessibility of the location. By observing the variation in grasping angle it can be seen however that occasionally, slight changes in grasping can lead to larger fluctuations (Figure 3.33b), where a small reduction when grasping the rectum seems to lead to the secondary force peak. But this is not always the case, where a particularly stable force is not affected by angle fluctuations (Figure 3.33d).

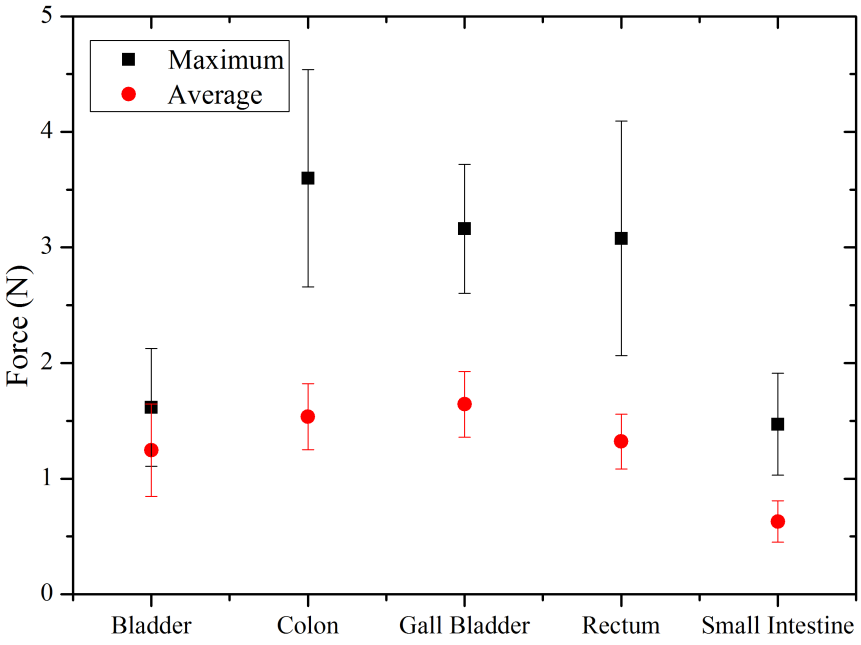

Figure 3.34: Maximum and average applied force during organ manipulation for the five repeats, including standard deviation (alphabetical order).

The average RMS force for the gallbladder manipulation is greater than the other organs. Similarly the RMS for the bladder is closer to its maximum applied force, compared to other

organs (Figure 3.34). This suggests that less relaxation occurs as the tissue structures are much thinner when compared to the colon, rectum, and small intestine.

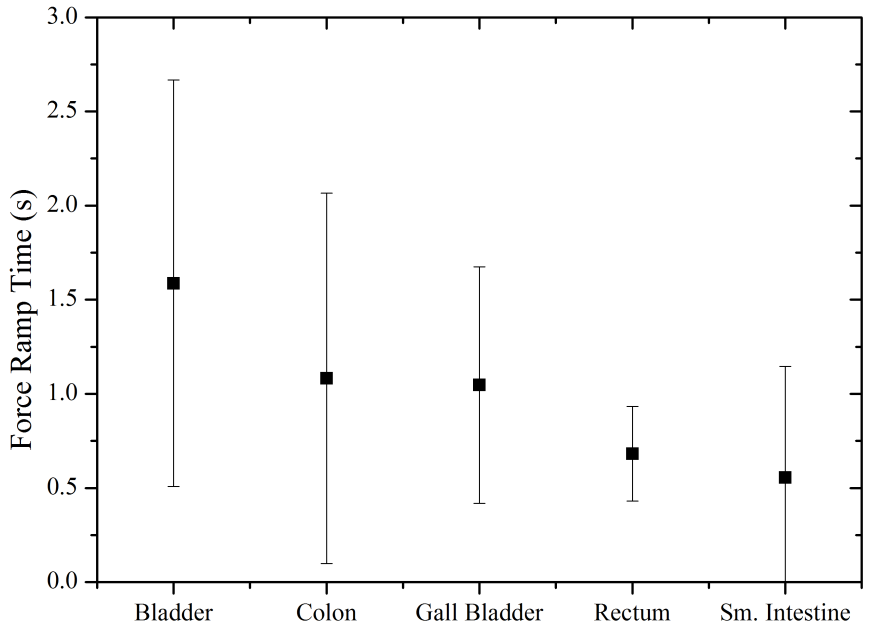

Figure 3.35: The average and standard deviation of time taken to reach the maximum applied force when grasping each organ.

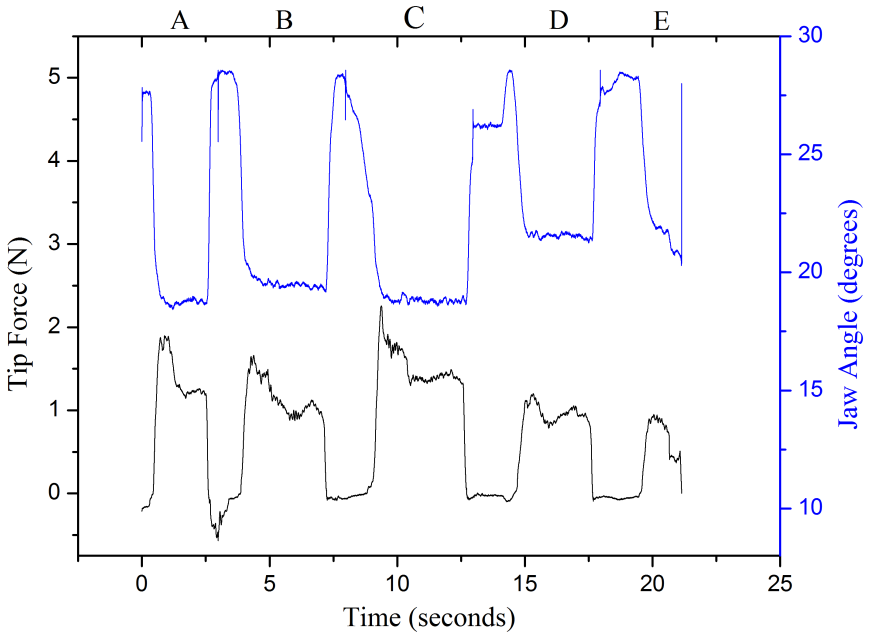

Figure 3.36: An example profile for the force (black) and jaw angle (blue) of a bowel run, with individual grasps, A-E.

The bowel run profiles typically showed that there was an initial peak force for each grasp (Figure 3.36), occasionally followed by a final increase as the surgeon switches hands (profiles B and D). Also for relatively stable jaw angle measurements, there are force fluctuations, suggesting that during a grasp, minor variations could affect the applied force.

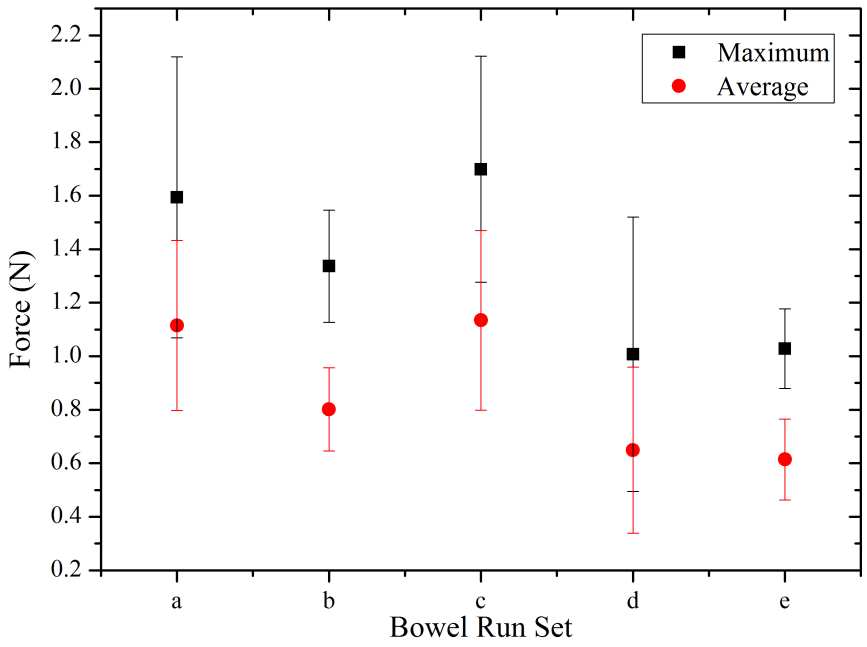

Figure 3.37: Maximum and average applied force during bowel run for the five repeats, including standard deviation (for each independent *'run'*, a-e).

The bowel run results highlight how maximum and average forces are generally lower for quick manipulations of the colon, compared to prolonged tasks (Figure 3.37). During retraction, the maximum and average grasping forces for colon were 3.60 N and 1.54 N respectively, whereas for the bowel run experiment, the combined maximum and average force was at 1.29 N and 0.83 N for the average force. This may be due to the fact that a firm hold is only required for prolonged periods of grasping, such as retraction, but when manipulating organs quickly, perhaps when locating a particular area, there is little consequence to the organ slipping out of the grasper.

There is also a correlation between the grasping forces and grasp time (Figure 3.38), as there is a larger spread of grasp time for a lower spread of grasping force. By multiplying the standard deviation (σ) of the average force, F_{AVE}, and σ of the grasp time, T_{GRASP}, for each bowel run an approximate relation in the variance can be shown (Equation 3.28).

$$\sigma_{F_{AVE}} \times \sigma_{T_{GRASP}} = 0.29(\pm 0.03) \tag{3.28}$$

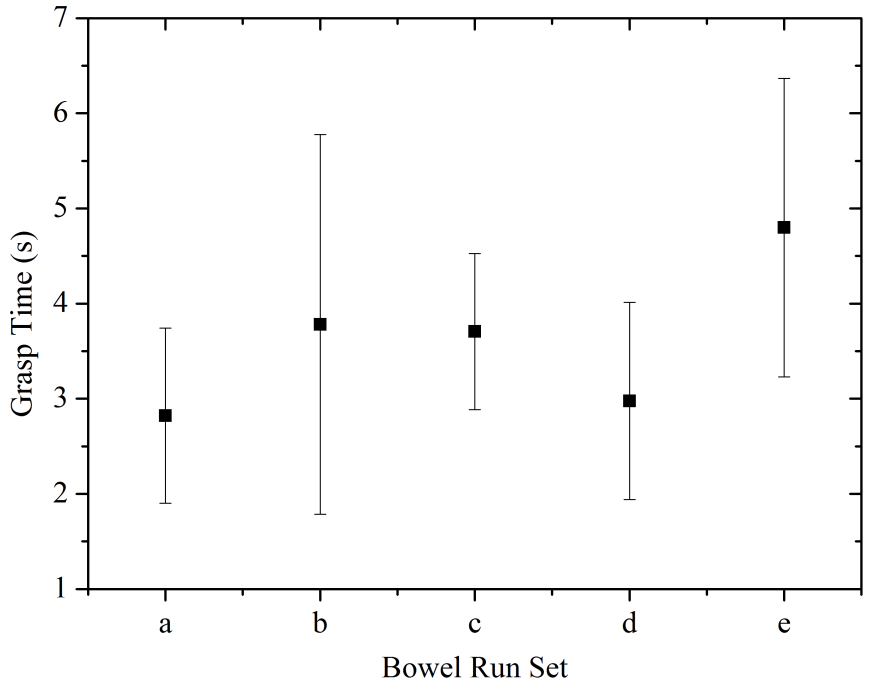

Figure 3.38: Grasping duration during bowel running for the five repeats, including standard deviation (for each independent 'run', a-e).

This suggests that if the surgeon takes longer between grasps when manipulating, they can achieve a higher consistency of grasping forces. The maximum force results were also considered in the analysis of the variance but showed a much larger spread (0.40 ± 0.12), indicating that there is a closer correlation between the average force and grasp time variance, which is to be expected as the average force considers the grasping profile for the full grasp.

3.9 *In-vivo* Colon Force Grasp Testing

The following experiment was performed to investigate the instrumented grasper's ability to measure tissue characteristics, such as the relaxation response from applied forces. This could potentially allow for further information to be found from grasping data, such as whether the sample was diseased or healthy. As with the *in-vivo* organ manipulation tests an anaesthetised 40 kg white pig was used.

3.9.1 Methodology of *In-vivo* Colon Grasping

A trainee surgeon was asked to grasp a fresh area of colon at pre-determined forces of 5, 10, 20, 40, 50 and 70 N, each for 5, 30 and 60 seconds without repetition (due to the limited colon length), and the grasper measurements were logged for post-analysis. The experiment

was carried out through open surgery, manually placing the colon in the full grasper jaw each time (Figure 3.39). This provided greater control over the grasps and would prevent other factors from affecting the results from the tissue analysis. Finally after all experiments had been completed the surgeon was asked to grasp the colon twice, at they highest force possible for 30 and 60 seconds, to establish the limits of the design.

3.9.2 *In-vivo* Open Surgery Grasping Set-up

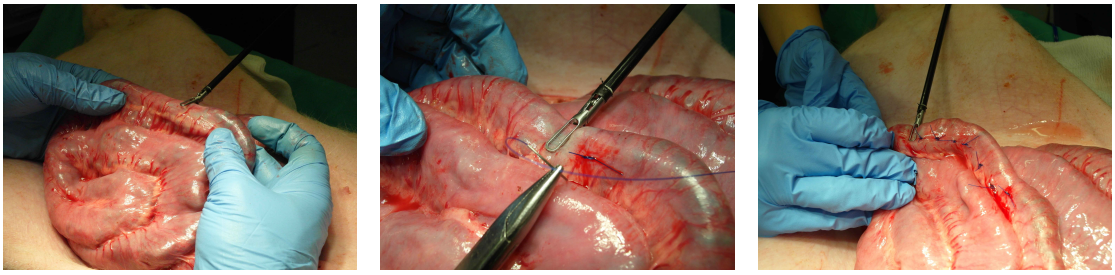

(a) (b) (c)

Figure 3.39: *In-vivo* force grasping procedure; (a) the area to be grasped being placed in the jaws, (b) the grasped section highlighted using sutures above, and (c) multiple grasps and sutures progressing along the length of the colon.

The grasped area was sutured above to mark the test site to allow for easier location after the tests had been completed and to indicate which section of the colon had already been grasped. This experiment was also part of a parallel project in which the grasped samples were subsequently separated and later histologically analysed, hence the need to locate each grasp after the experiment [240].

3.9.3 *In-vivo* Colon Grasping Results

The following results are presented as forces measured along the grasper linkage. This allows direct comparison between the target force and actual force, allowing the grasper's feasibility to be easily assessed. For each set of data the instrumented grasper linkage displacement measurements were converted to jaw angles using the mathematical model (section 3.4). This was chosen over using the displacement values for easier comparison with previous data.

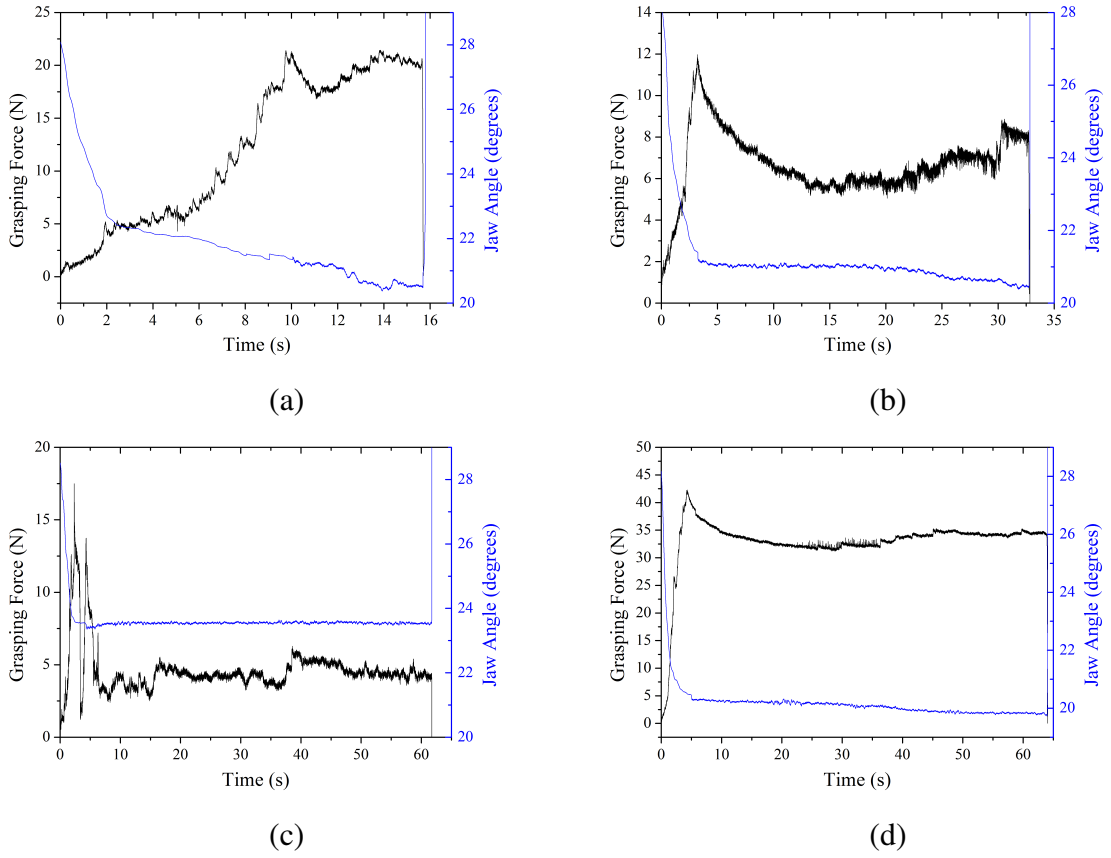

Figure 3.40: Observed *in-vivo* grasping profile characteristics, including (a) a long ramp up to target force (20 N, 5 seconds), (b) an initial relaxation observed but followed by rise (10 N, 30 seconds), (c) a large force spike followed by fluctuations in force (10 N, 60 seconds), and (d) a little relaxation with force fluctuations (50 N, 60 seconds).

When asked to grasp at a particular force the surgeon often found this difficult to perform without aid of the force readout on the program's GUI and as a result the ramp up time could be longer than the actual grasp time (Figure 3.40a). Occasionally relaxation could be observed in some of the grasp profiles, but were usually accompanied by force fluctuations or anomalies where the force rose instead of fell (Figure 3.40b). By asking the surgeon to grasp to a particular force then hold this position, force spikes were seen when trying to steady the grasp (Figure 3.40c). Also due to unknown factors, very little relaxation could be seen in some profiles, possibly due to tremors in the surgeons hands or if the colon moved during the grasp (Figure 3.40d). By observing the grasp angle data, it can be seen that occasional drifting during grasping can lead to a rise in the grasping force (Figure 3.40a), but in other profiles, there are force fluctuations, with a relatively steady angle (Figure 3.40c).

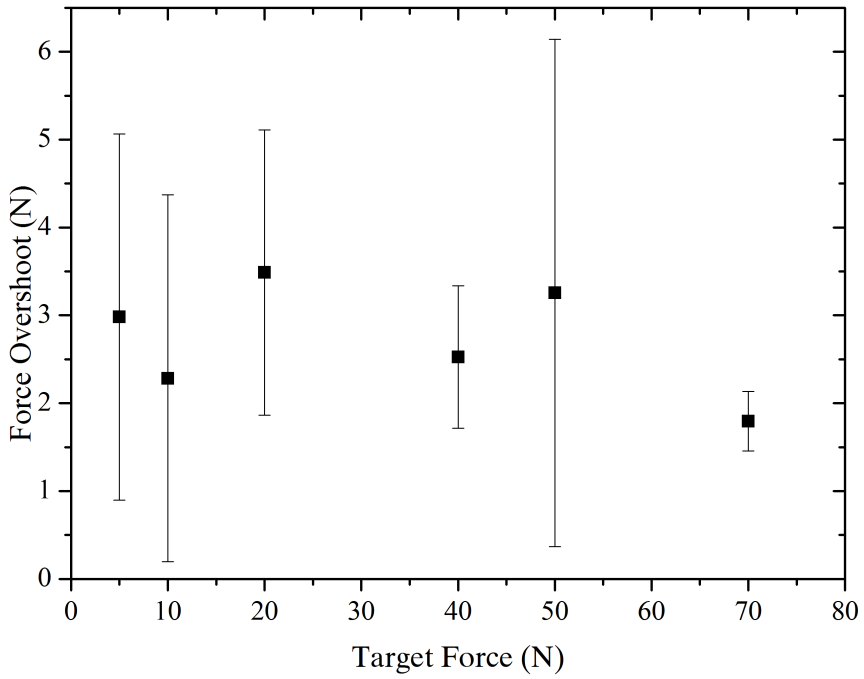

Figure 3.41: Absolute force overshoot during colon grasping with the instrumented grasper.

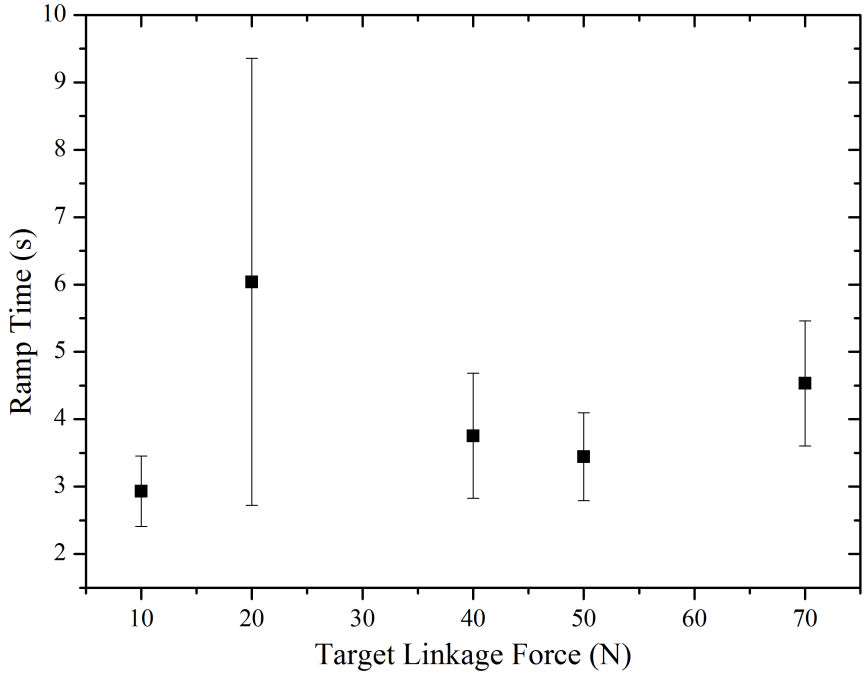

Figure 3.42: The time taken to reach the desired grasping force during colon grasping with the instrumented grasper.

A poor reliability of obtaining repeatable applied forces was seen when grasping manually

(Figure 3.41). The force overshoot seems consistent, with higher forces also subject to larger overshoots, but lower target forces would be more susceptible to high degrees of error.

The time taken to reach the target force for each grasp was also recorded and shown against the desired force (Figure 3.42). The results showed a slight increase from an average of 2.9 seconds up to 4.5 seconds with an increase in force. The large error result from the 20 N grasps is due to a single large result of 9.8 seconds, but by excluding this the average becomes 4.2 seconds.

3.10 Concluding Remarks About the Initial Design

An initial concept for the instrumented grasper has been designed, developed, and used for *in-vivo* testing. The design met the outlined specification (section 3.2), as it was capable of measuring up to 150 N linkage force (1 and 2), the sealed, modular design could be attached without requiring modifications to the grasper or handle (3, 5, 6, and 9), no wires were located at the tip (4 and 8), the data was logged via a computer (7), and the device did not require a power supply to function (10). However there were a number of issues found in the design. During the development, it was noted that the accuracy of the linear potentiometer could affect readings, especially due to the short range needed by the design. This had the potential to cause a large build up of noise in the signal as the contacts became worn over time. During testing there were several problems highlighted. The connecting nuts which joined the handle and shaft to the instrumentation were able to rotate due to the cylindrical design, making it difficult to securely join the parts together. For the instrumented grasper limit test, the maximum force reached for the 30 and 60 seconds grasps were 156.24 N and 166.68 N, with averages of 126.58 N and 146.08 N respectively. At this force it was very difficult to maintain either a constant position or force. It was also noted that after the maximum force tests were completed, the internal struts, which held the connecting nuts against the housing, had deformed and bent allowing the connecting nuts to move linearly. This suggested that if this device was used for prolonged testing in the future, there would an increasing margin of error in displacement measurements. Occasionally the shaft connectors (Figure 3.18) would unhook from the shaft and handle connectors, requiring the instrumentation module to be opened and fixed. From these observations, it was concluded that the design concept was suitable for the required task, but modifications would need to be made for future testing to ensure the design was longer lasting and more reliable. Also from the force grasping results (section 3.9.3), the grasper was shown to be unsuitable for precise force testing. This was due to the difficulties in controlling the force application, particularly at lower forces and over a long period of time, as the measurements were susceptible to a similar level of overshoot, but this was particularly noticeable at lower forces. It was noted that when asked to grasp up to a certain force, the surgeon struggled to reach this *'smoothly'*, as this was difficult to

interpret. For the initial grasps, long ramp up times were seen as the surgeon learnt what each force *'felt'* like. When grasping for long durations (30 and 60 seconds), the surgeon struggled to maintain the force without moving the grasper or hand/finger position. This was most noticeable for higher forces, when the surgeon also experienced more fatigue.

3.11 Redevelopment of the Instrumented Grasper Prototype

3.11.1 Redesigning the Instrumentation Module

The instrumented grasper was redesigned to address the previously highlighted issues (Figure 3.43). The design reduces the number of individual parts required by including both the cone nut and handle threads into the housing, which prevents unwanted rotation during use and makes assembly easier. The internal linear bearing provides smooth motion of the loadcell to prevent it from disconnecting, while supporting the housing and reducing flexing under high forces (Figure 3.44).

Figure 3.43: CAD of the redesigned instrumented grasper prototype, highlighting the location of instrumented module.

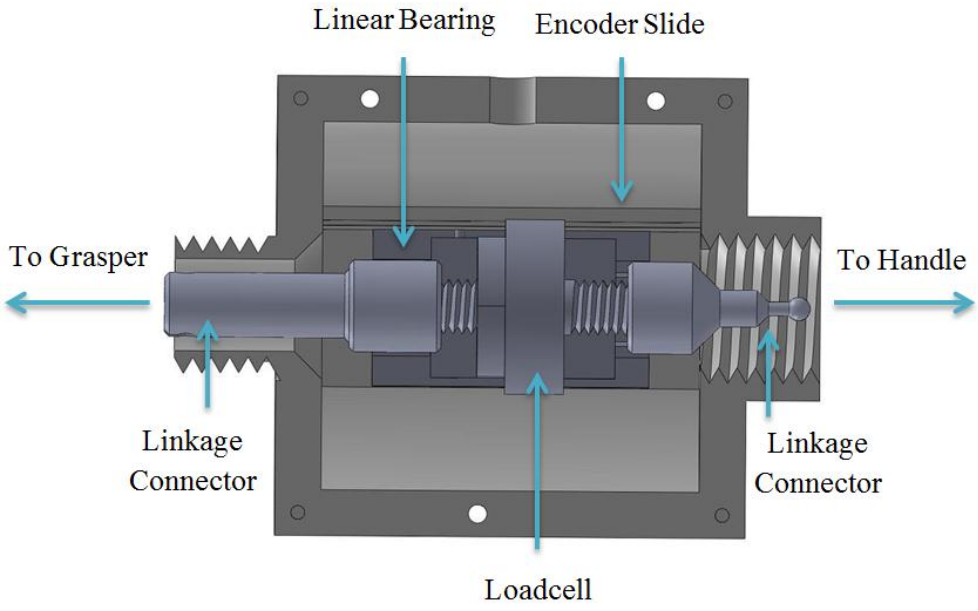

Figure 3.44: CAD of the cross-section of the redesigned instrumented grasper module, highlighting the location of the sensors and connectors.

The design was rapid prototyped using Accura® Xtreme lightweight plastic to reduce the weight of the housing and to allow for faster manufacture if repairs or redesigns are needed.

3.11.2 Instrumented Grasper Hardware

A small, cylindrical loadcell (LCM201-200N, Omegadyne Inc. (Appendix A)) of diameter 19 mm and height 6.4 mm, capable of ± 200 N, was chosen to measure the required tensional force along the inner shaft, while limiting the overall weight of the instrumented grasper and reducing the size of the instrumentation housing. The same amplifier design (DR7DC, RDP Electronics Ltd.) was used to boost the loadcell signal (2 mV/V) and generate a linear output of approximately 0 - 10 V for a 0 - 150 N force range, using a 15 V DC power supply. The loadcell was calibrated for three increasing and decreasing force sweeps with approximate 10 N increments for this range, using the same calibration rig as used previously (Figure 3.19a), with the exact force and voltage readings being taken at each interval.

The resulting line fit equation can determine the relation between applied force and output voltage (Figure 3.45), where F is the force to be calculated, the line gradient is 19.97 ($\pm$0.02), the intercept is -0.68 ($\pm$0.08) and V is the output voltage (0 - 10 V). Again to demonstrate the high accuracy of the loadcell, the R^2 value is included.

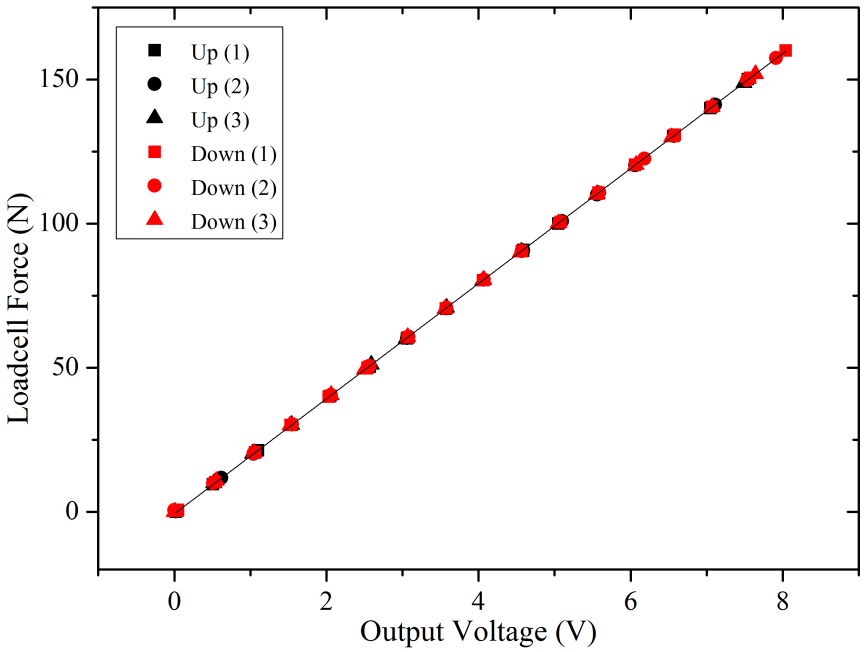

Figure 3.45: Loadcell (LCM201-200N) calibration graph showing three continuous up/down sweeps and linear fit (fit; $F = 19.97V - 0.68 (R^2 = 1.00)$).

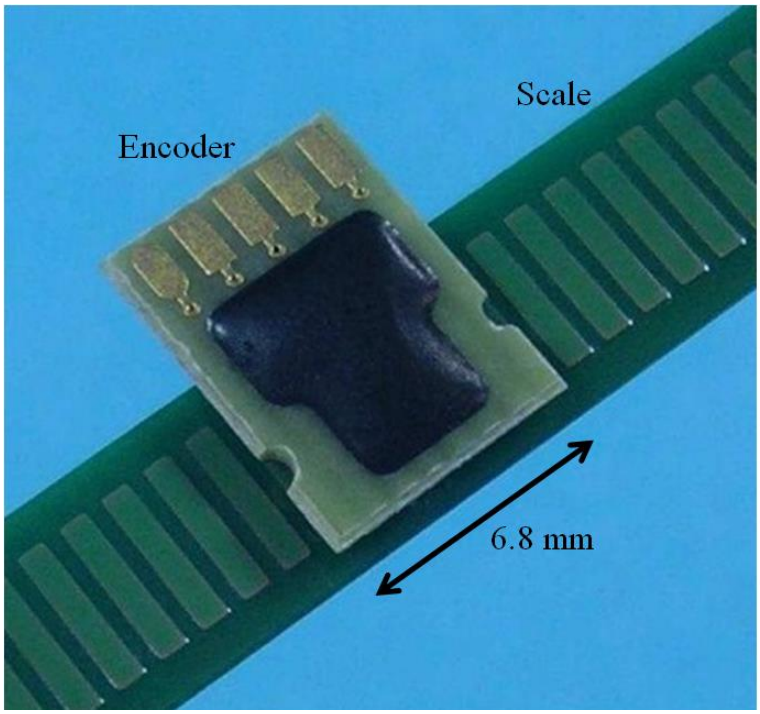

Figure 3.46: Dual-channel miniature linear encoder sensor and scale.

The potentiometer was replaced with a dual-channel miniature linear encoder (ID1101L, Posic (Appendix A)) (Figure 3.46) with a resolution of 75 μm. This was firstly to keep the design compact, and secondly to improve the signal to noise ratio. Over time, the original

potentiometer could potentially produce more noise as the physical contacts are worn. This effect will be greater due to the small grasper linkage range, compared to the full stroke length of the potentiometer. The contactless design of the encoder means there will be no wear, and as a result no degradation over time. The digital output from the encoder also ensured reliable readings giving a longer lasting design.

The encoder is incremental and uses a differential inductive sensing principle whereby the scale is made from an electrically conducting ferromagnetic material and as this moves through the magnetic field (generated by the encoder) it alters the field, causing a varying sinusoidal wave to be detected. Using two detectors (built into the sensor), which are 90° out of phase with each other, the difference in the two sinusoidal signals indicate movement of the scale relative to the sensor. The encoder is digital as it interpolates the analogue sine/cosine signals dividing the scale period and generating a square wave. This design uses a 4 bit interpolation factor to give the 75 μm resolution (the scale period (1.20 mm) divided by the interpolation factor (2^4)). Inductive encoders are robust to contamination compared to other types such as optical and capacitive encoders. The encoder output consisted of three channels. The first two channels output digital signals in quadrature (Figure 3.47) and each step (1 - 4) is 0.075 μm. The third channel outputs a digital signal for each full cycle of the two increment channels to provide a reference and is known as an index pulse. A logic table is used to determine if the position has incremented or decremented (Figure 3.47b). Only one channel can change for each step and the previous channel values are compared to the current values.

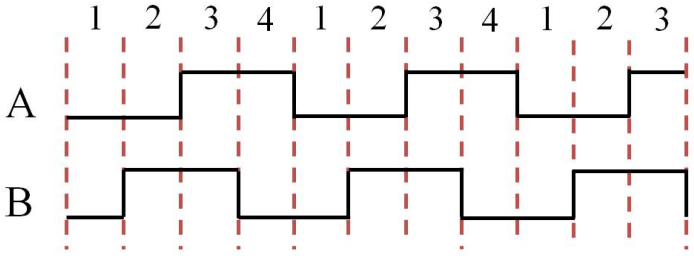

(a)

	A	B
1	0	0
2	0	1
3	1	1
4	1	0

(b)

Figure 3.47: Encoder quadrature output (a) from channel A and B and (b) table used to determine output state.

The same DAQ devise was used as in the previous design, with the sensors located in the instrumented module (Figure 3.48). The three outputs from the encoder were connected to the digital input on the DAQ USB.

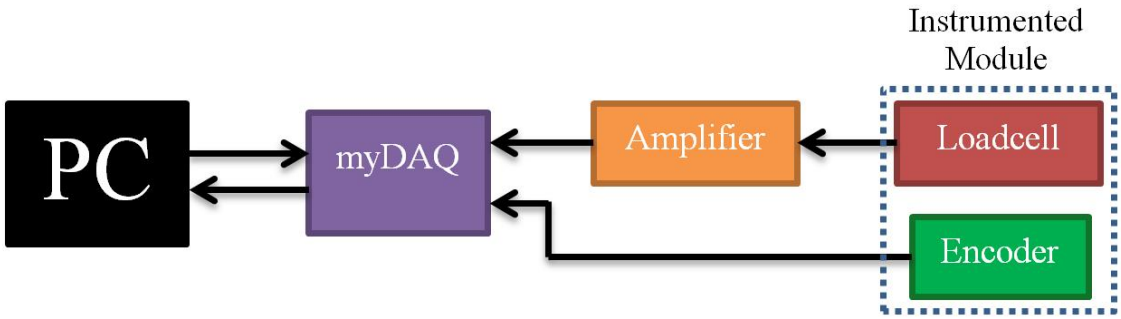

Figure 3.48: Redesigned instrumented grasper system diagram showing the data connections between each hardware device and highlighting the components located in the instrumented module.

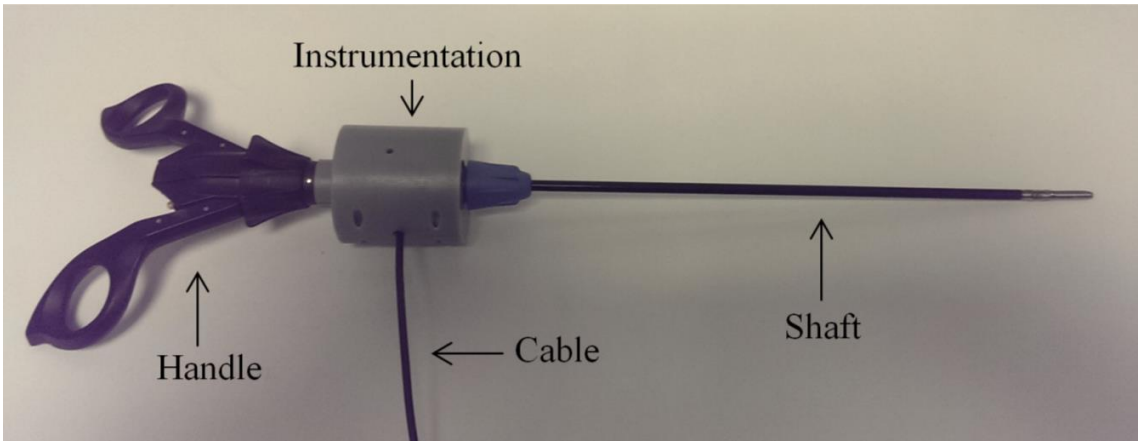

Figure 3.49: The final instrumented grasper redesign, showing the cable, and instrumentation, with the unmodified handle and grasper shaft.

3.11.3 Instrumented Grasper Data-logging Program

The GUI remained the same as the first design (Figure 3.25) with a simple interface allowing for target force and time to be set. A new program was developed to measure the encoder readings (Figure 3.50). Two digital counters were used dependant on each other, i.e. the value would only increment if each channel varied sequentially. A third counter was used to monitor the index pulse and to avoid skipping measurements.

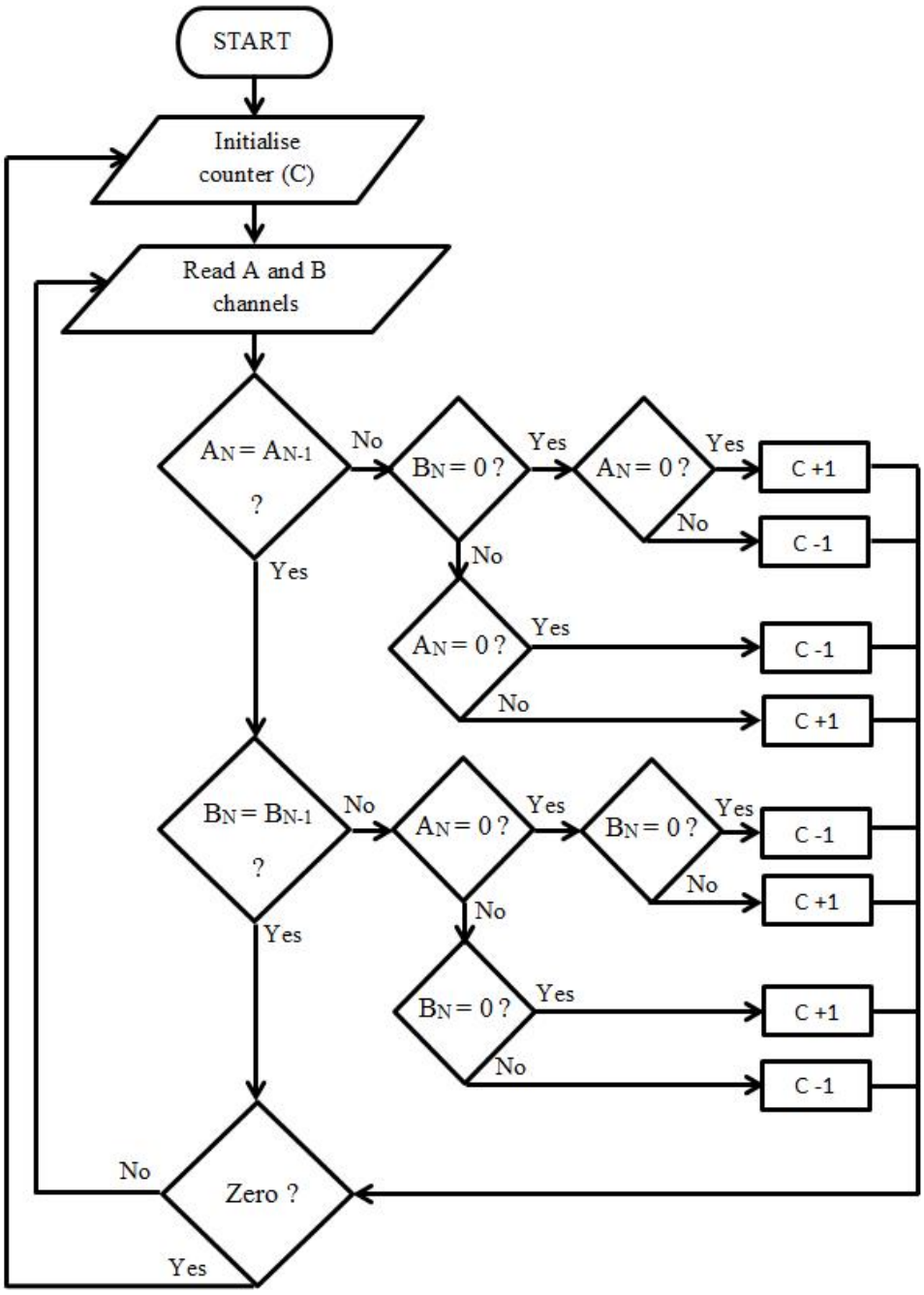

Figure 3.50: Encoder flowchart to calculate positional increment or decrement from channels A and B.

3.11.4 Validation of the Loadcell and Encoder Measurements

The instrumented grasper sensors were validated *in-situ* to ensure the data were accurate and repeatable. Firstly a series of 50 g weight were suspended from the linkage connector and the equivalent force reading was logged, as carried out previously (Figure 3.27). The weights were incremented and decremented from 0 g to 1 kg and each force measurement was

sampled for 3 seconds then averaged, to account for any noise. The weights were incremented and decremented over the full range for three repeats.

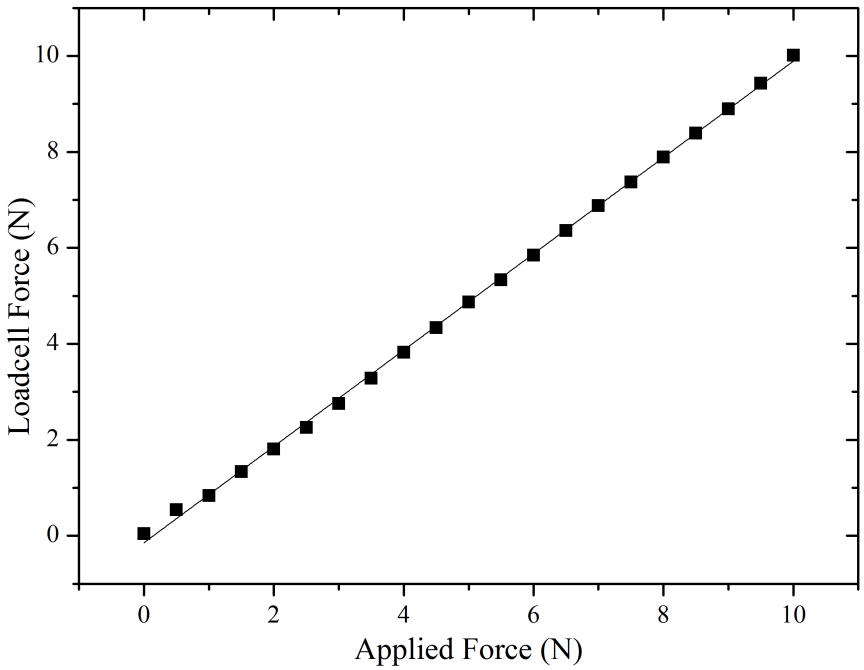

Figure 3.51: Loadcell (LCM201-200) force validation graph for three up/down sweeps with a linear fit (fit; $F_L = 1.00F_A - 0.14 (R^2 = 1.00)$).

The linear fit was used to determine the accuracy of the loadcell (Figure 3.51), where F_L is the loadcell force reading, the line gradient is 1.00 ($\pm$0.01), the intercept is -0.04 ($\pm$0.03) and F_A is the applied force (0 - 10 N). The results show that the loadcell provides readings accurate to 1 DP with a maximum error of 2 % at lower forces.

Using the pre-calibrated laser displacement sensor (accuracy $\pm$0.025 mm), the encoder was moved along the scale using the handle through its full range of motion (0 - 8 mm approximately), as carried out previously (Figure 3.29). At each approximate 1 mm increment the laser position was measured and the reading taken. 3 sweeps of up and down readings were taken of the laser sensor and encoder readings. The linear fit can be used to determine the repeatability of the encoder (Figure 3.30), where D_P is the displacement reading, the line gradient is 1.01 ($\pm$0.01), the intercept is 0.01 ($\pm$0.02) and D_L is the actual displacement (0 - 8 mm). The results show that the encoder readings have a maximum possible error of 2 % for the highest readings, making readings reliable to 1 DP.

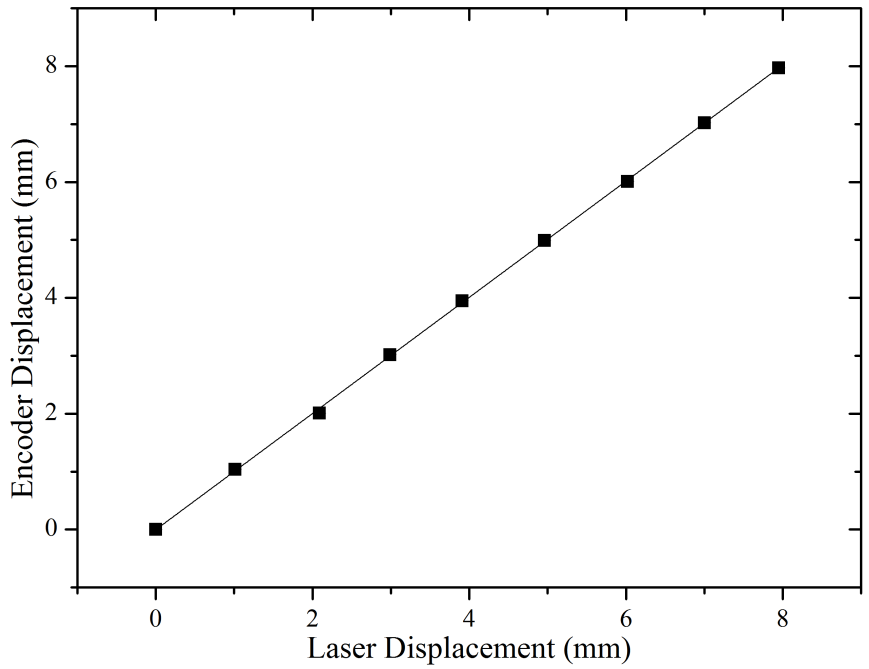

Figure 3.52: Encoder displacement validation graph for three up/down sweeps with a linear fit (fit; $D_E = 1.01D_L - 0.01(R^2 = 1.00)$) (error bars excluded for clarity).

3.12 Concluding Remarks About the Instrumented Grasper Redesign

The instrumented grasper was redesigned for robustness and reliability in future tests. The aluminium panels were removed and the housing connectors were designed as part of the bespoke housing, preventing them from rotating during use. The loadcell and displacement sensor were changed to make the device lighter and easier to use. Even though the loadcell is slightly lower in accuracy than the previous design this can still be considered as negligible for the desired force measurements to be observed [175].

3.13 Conclusion

A mathematical model of the grasper scissor linkage mechanism was developed to estimate the tangential tool-tip forces from the grasper's internal linkage forces. The model highlighted the need to include the linkage displacement in measurements as variations in the grasper jaw opening angle could alter the transmitted force by up to 54 %.

An instrumented grasper has been designed, developed, and used for *in-vivo* testing. The design is a single unit attached to a generic grasper which can be removed quickly and so can potentially be used in future testing with any grasper design, providing it has the appropriate

connectors (Figure 3.3). The instrumented grasper does not change how the grasper functions therefore the surgeon will not need to be specially trained to use it. It can be attached *in-situ*, allowing for multiple tools to be tested with it.

The testing results showed the typical range of *in-vivo* grasping forces for varying abdominal organs and also highlighted a link between average grasping force variation and grasping time variation. The maximum force measured along the linkage was 75.5 N when retracting colon and 38.0 N when manipulating the bowel. However the instrumented grasper proved unreliable when used to grasp at specific forces, particularly at lower forces. Actual forces tended to vary widely but were usually much higher than the target force. Also due to variations in the applied stresses on the grasped tissue, typically from hand tremors or the movement of other organs, true tissue relaxation could not be observed. The grasper was also tested at extreme forces to determine it's capabilities. At these high forces (approximately 150 N along the inner shaft), the internal brackets deformed. Other problems included the housing connectors which rotated during use, and the inner connectors occasionally disconnected. The highlighted issues were addressed in the redesign of the instrumented grasper which focussed on developing a longer lasting device by improving the housing, reducing the weight of components, and replacing the displacement sensor. Even though the loadcell readings were marginally less accurate, the error could be considered negligible for the required grasping forces. This system provides a convenient way to measure surgical task forces, allowing for a greater understanding of how tissue is manipulated *in-vivo*.

Chapter 4

Laparoscopic Grasper Test Rig

4.1 Introduction

The literature review and *in-vivo* data analysis has highlighted the need for an automated test rig to simulate grasping, with greater control and positional accuracy than was possible with the instrumented grasper and *in-vivo* environment. This would provide greater control of the testing environment and increase repeatability of measurements, allowing tissue response to be observed under typical grasping scenarios. Previous research has investigated tissue mechanics by applying a precise strain over a predetermined area and measuring the force relaxation [53]. Other investigations have looked at the retraction forces for varying grasper fenestration geometries, and the designs which produce the least amount of tearing of tissue samples [69]. Both these investigations are typical examples of laboratory based grasper testing but do not provide a realistic comparison to the *in-vivo* conditions found in surgery due to the idealised surfaces use to apply the force. The set-up in this project aims to simulate an idealized surgical grasping scenario, by using test parameters equivalent to those observed *in-vivo* (section 3.8.3). The bespoke rig is required to control a laparoscopic grasper, independent of a user, to provide repeatable test conditions when grasping *ex-vivo* porcine colon samples. Through precise control of grasper jaw position it is possible to investigate and record characteristics such as force relaxation in the grasped tissue samples which can be used to understand the tissue mechanics. Overall the laparoscopic grasper test rig aims to provide a controlled representation of actual *in-vivo* surgery, while allowing for comparable relaxation results and damage observations between *in-vivo* and *ex-vivo*.

4.2 Design Specification for the Test Rig

Before designing the test rig, a list of requirements were derived from the literature review and the *in-vivo* experiments, carried out using the instrumented grasper, to ensure that it will meet the needs identified for both accurate and repeatable experimentation.

1. The design must be able to accurately control the opening and closing of a double action laparoscopic grasper to match the *in-vivo* work and mathematical modelling (section 3.4).

2. From the *in-vivo* work (section 3.8.3) and previous research [175], the maximum applied linkage force observed was 75.5 N and 68.17 N respectively. To ensure all typical grasping circumstances are considered the design must be able to apply a maximum force of 100 N, with less than 5 % overshoot (this would ensure, particularly at lower forces, the overshoot does not exceed 1 N).

3. To match the *in-vivo* grasping test parameters, the rig must be capable of grasping for up to one minute (section 3.9.1).

4. There must be a suitable method of holding the tissue section to be grasped, without inducing unintentional damage to the sample, in order to represent *in-vivo* grasping as close as possible.

5. Due to the number of moving parts, the rig must have safety features to prevent injury to the user. It must also have easy access to the connectors and components in order to remove samples quickly and replace any parts where necessary.

6. There must be a control system which allows the user to change the test variables, such as magnitude of force and length of time a sample is grasped for, via a user interface. The program should give a graphical display of the force, displacement and time data, and save these as a suitable data type. The interface must be user friendly to allow the rig to be operated by non programming users.

7. The applied force must be measured along the grasper shaft so as not to impede the grasper functionality (section 3.3) and allow for direct comparison to previous *in-vivo* work (section 3.7).

8. The necessary parts must be sterilisable due to the biological tissue to be grasped. This includes the grasper mount and connectors, with wipeable surfaces.

4.3 Development of the Initial Test Rig Prototype

4.3.1 Design of the Test Rig Structure

The initial design of the test rig consisted of a simple outer frame on which to mount the grasper, components, and tissue fixtures. The frame was fitted with Perspex® panels to provide a safety barrier between the moving parts and the user. The grasper was orientated in an upright position to allow tissue samples to hang between the grasper jaws, simplifying the tissue mounting and giving greater control over the grasping area. If the grasper was positioned above the tissue, due to the non-homogeneous nature of the tissue, the grasped area could differ each time, which would affect testing repeatability. The design was developed

using SolidWorks Computer Aided Design (CAD) (Figure 4.1). The material used to construct the main frame and mounts was Bosch Rexroth® extruded aluminium bar with a 30 x 30 mm cross sectional profile. A rigid structure could be built quickly and easily as the bar's versatility allows for a simple yet effective modular design. It would also allow for easier future modification if necessary without the need to redesign large sections of the rig, helping to reduce manufacturing time and cost. The grasper mount used an M3 x 0.5 thread to match that of the grasper. Due to the standardized thread on the grasper's shaft, any similar geometry design could be used. The grasper's centrepoint was positioned in-line with a linear actuator for a pure linear motion, and were joined via two bespoke connectors and a loadcell, allowing for a simple method of force transmission and measurement while leaving the actuator and grasper shaft unmodified.

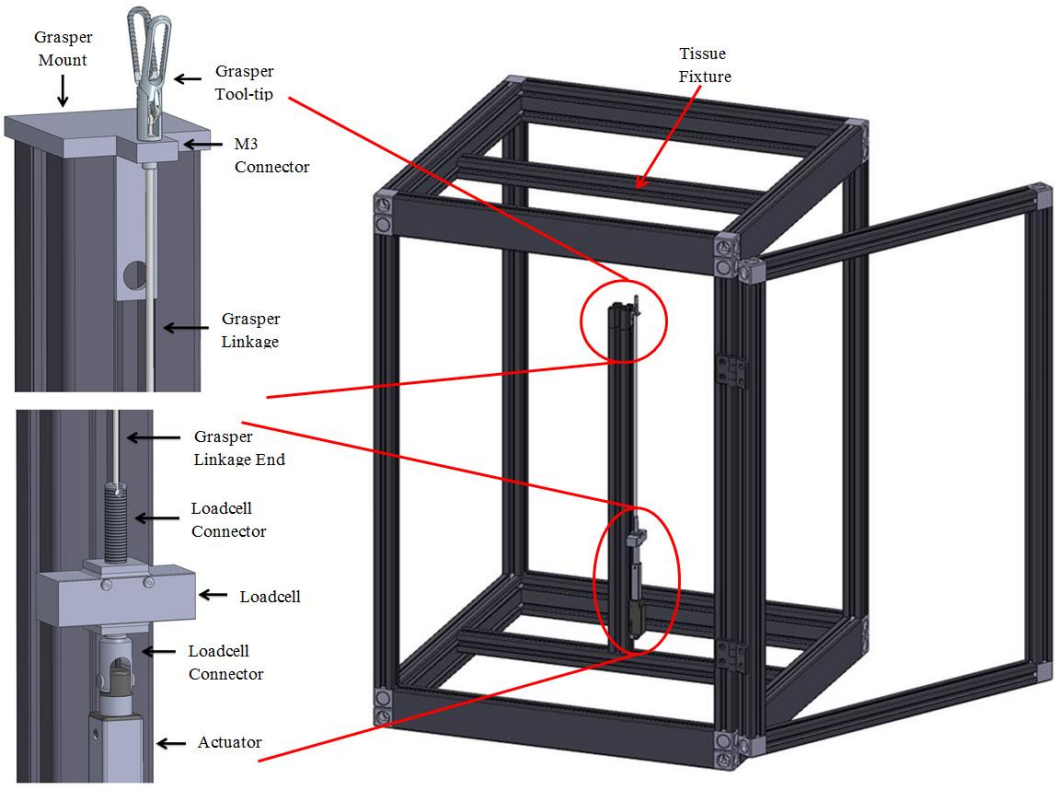

Figure 4.1: CAD of the initial rig prototype showing the location of grasper, loadcell, actuator, and custom made connectors, situated in a frame measuring 360 x 360 x 700 mm.

To transfer the linear movement and force along the grasper shaft, bespoke parts were manufactured from stainless steel to ensure rigidity, and joined the actuator and grasper shaft together via a loadcell. By extending the actuator (Figure 4.2a), the grasper linkage is extended and the jaw mechanism is opened (Figure 4.2b). By retracting the actuator (Figure 4.2c), the grasper jaws are closed. By continuing the actuator retraction a tensional force is applied along the linkage which is measured by the loadcell and is transferred to the

grasper jaws (Figure 4.2d).

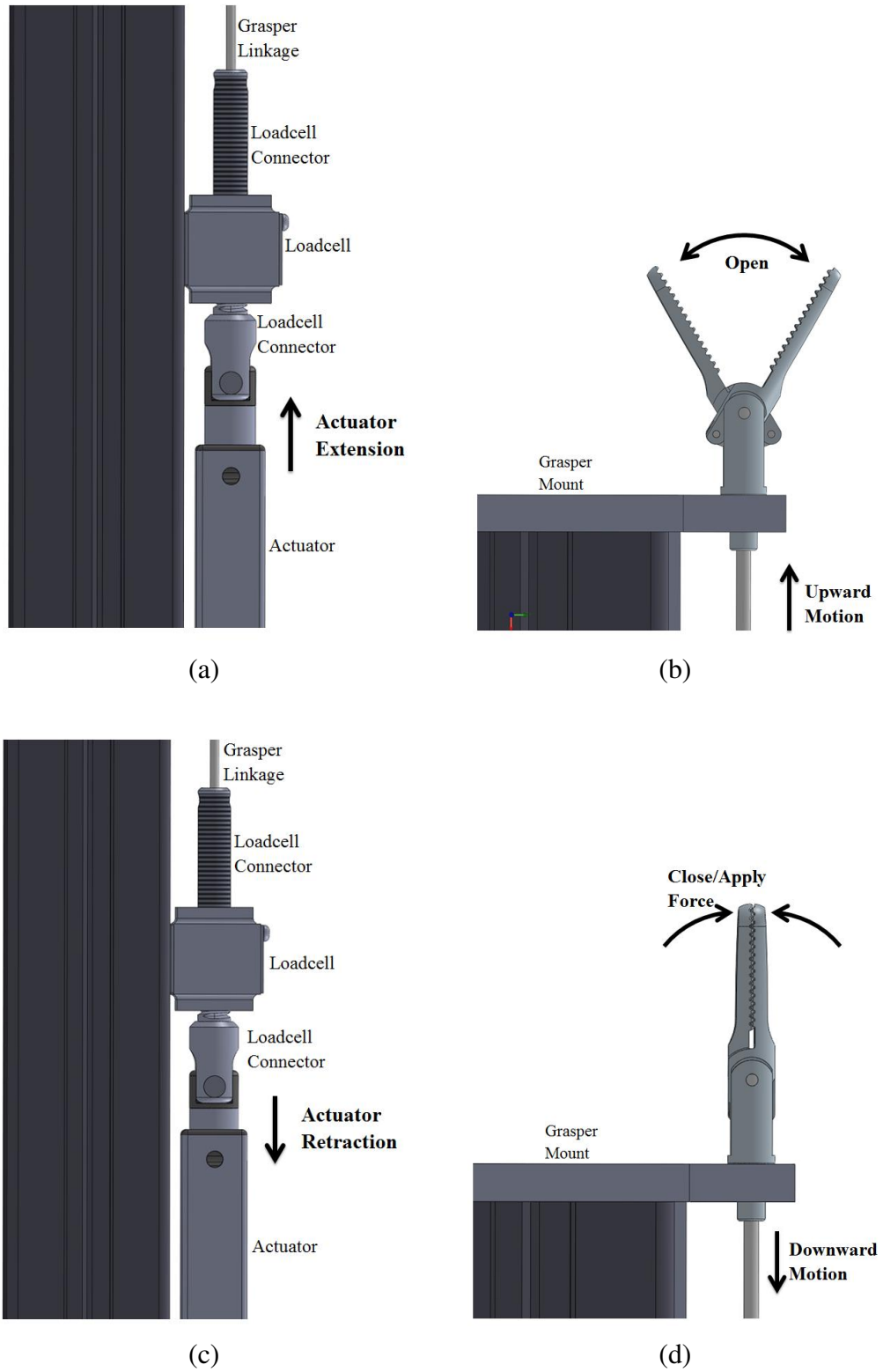

Figure 4.2: Grasping motion control from the actuator to the grasper linkage, then to the jaw; (a) actuator to linkage extension, (b) linkage extension to jaw opening, (c) actuator to linkage retraction, and (d) linkage retraction to jaw closure.

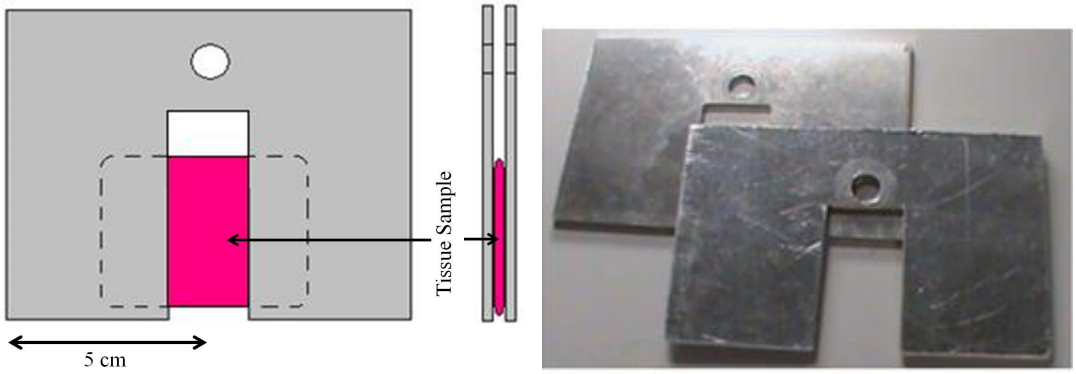

(a) (b)

Figure 4.3: First design of the tissue holder for use in the first rig design; (a) tissue holding method, and (b) manufactured aluminium tissue brackets.

To allow the tissue samples to be changed easily outside the rig, a removable tissue holder was designed. The tissue holder is attached to the frame via the crossbar at the top (Figure 4.1). Several methods were developed to secure the tissue sample in the rig. The first method was manufactured from sheet aluminium (Figure 4.3). The tissue sample is wedged between the two sides of the clamp, with an exposed area to be placed between the grasper jaws. The tissue holder was redesigned due to difficulties encountered while using the tissue holder in preliminary testing, including the tissue slipping down during testing and difficulties with lining up the sample with the jaw. The second used four pins to secure a single walled colon sample, which was subsequently suspended between the grasper jaw's during testing (Figure 4.4). This method ensured the tissue did not slip when held, and the sample could be easily lined up with the jaw, and the individual pins allowed for easier placement of the sample.

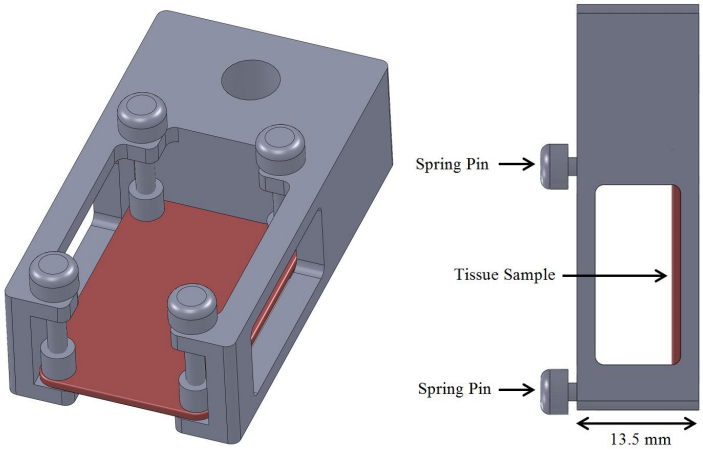

(a) (b)

Figure 4.4: CAD of redesigned tissue holder, showing tissue placement; (a) full design, (b) side profile.

Before the tissue samples are placed in the tissue holders they are prepared. The single wall sample was chosen for testing as this allowed for easier placement in the holder and a more uniform section to be grasped to make measurements as accurate as possible (Figure 4.5).

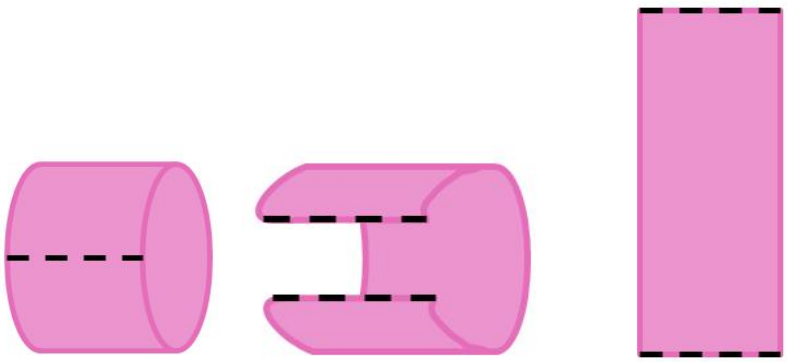

Figure 4.5: Tissue sample preparation procedure before grasping showing (a) initial cylindrical sample and incision line, (b) open cylinder section and (c) final opened sample section to be grasped.

The sample could then be immediately preserved in formaldehyde solution once it had been grasped as no extra sectioning was required. This also allowed the bottom of the tissue sample to be lined up against the grasper jaws.

4.3.2 Hardware Set-up

To provide the motion control of the rig, a micro-linear actuator (Firgelli, L16 (Appendix A)) was chosen over other linear motion devices, such as hydraulics and pneumatics, for the relative high precision and low cost of the devices (Figure 4.6). The magnitude of the maximum force chosen for the measurements was 100 N, as 70 N was demonstrated as the maximum possible from the *in-vivo* work carried out using the Instrumented Grasper (Section 3.8.3). The actuator is capable of producing 200 N force and can extend and retract at a rate of approximately 8 mm/s with 0.5 mm positional accuracy. The actuator has a stroke length of 50 mm, where the maximum travel of the grasper linkage (from a fully open to a closed) is approximately 2.6 mm. It should also be noted that from the previous modelling validation (Section 3.5.1), there was a backlash of 0.13 mm.

Figure 4.6: Firgelli L16 micro actuator used in the first rig prototype.

A controller (Firgelli, LAC (Appendix A)), was used to provide the Proportional Integral Derivative (PID) control of the actuator (Figure 4.7). The controller includes two control potentiometers, P1 and P2 which were used to vary the speed and accuracy respectively, with the accuracy set to its highest and the speed then set to minimise oscillations in the linear motion. Two pins, M+ and M-, provided the varying DC analogue voltage to the actuator, with three pins for the feedback potentiometer, P, P+ and P-. A second connector, + and -, provided the power to the controller, and used a varying voltage, VC, to control the actuator extension and retraction.

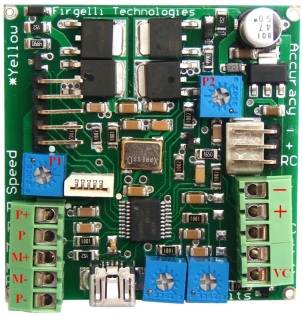

Figure 4.7: Firgelli LAC controller used to provide PID control and measurement of the actuator position.

A linear loadcell (Omega, LCM703-25 (Appendix A)) which can measure compression and tension forces up to 250 N was chosen to measure the force acting along the grasper linkage. The loadcell outputs approximately 2mV/N and includes two M6x1.0 threaded holes at the top and bottom of the device, through which to apply the force. The output voltage from the loadcell was passed through a transducer amplifier (RDP, DR7DC (Appendix A)). This amplified the loadcell voltage while actively reducing the noise. The loadcell was calibrated by placing a similar pre-calibrated loadcell in series and applying a tensional force (Figure 4.8). The calibration rig, with a force accuracy of ± 0.05 N, was used to determine the force/voltage relation equation of the loadcell. As the wheel is rotated clockwise the threaded bar is placed under tension, simultaneously increasing the force applied across each loadcell.

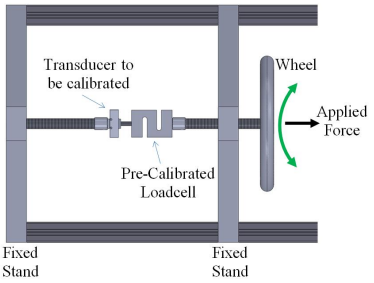

Figure 4.8: Loacell calibration rig showing the loadcell to be calibrated, in series with a pre-calibrated loadcell, both connected to a fixed stand.

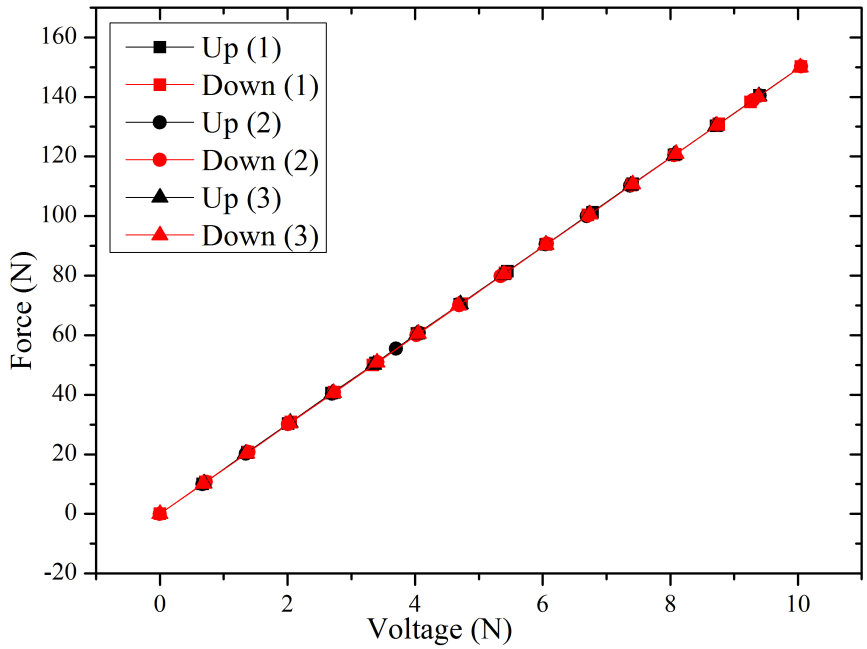

Figure 4.9: LCM703-25 Omega Loadcell calibration graph showing the average of three up/down sweeps and the linear fit (fit; $F = 14.93V - 0.13$).

Voltage readings were taken at each 10 N interval as the force was ramped up from 0 N to 150 N and back down, with 3 repeats. The applied force was plotted against the output voltage to give the force-to-voltage relation equation (Figure 4.9).

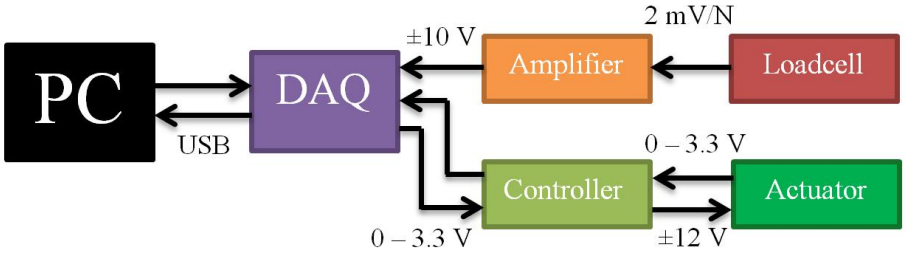

Figure 4.10: The system diagram for the first rig design, showing the data/hardware connections and voltage ranges.

To provide an interface between a Personal Computer (PC) and the rig, a Data Acquisition (DAQ) Universal Serial Bus (USB) device (National Instruments, USB-6009 (Appendix A)) was chosen. This device consists of 8 analogue inputs (14-bit, 48 k Samples/second (S/s)), 2 analogue outputs (12-bit, 150 S/s), 12 digital I/O, 32-bit counter and is compatible with the program development software, LabVIEW. The system diagram shows how each element is connected and how data is passed between them (Figure 4.10).

4.3.3 Control and Data-logging Program

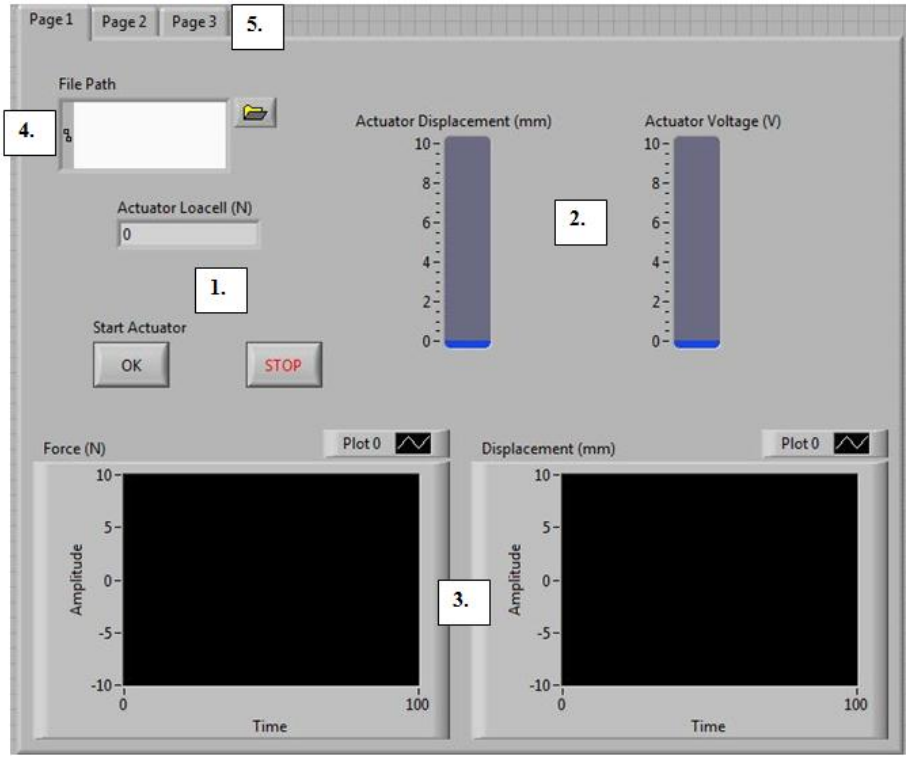

Figure 4.11: The main LabVIEW interface for the initial rig prototype program, highlighting (1) the force and program controls to set the target force, begin executing grasp and stop the program, (2) the actuator demand signal and actual position (used to indicate when the actuator is moving), (3) the output graphs which are updated with the force-time and displacement-time data after each grasp, (4) the file path where data is save after each graph, and (5) the extra tabs used to set the appropriate data connections, calibration data, and debugging the program.

The control program was developed using LabVIEW allowing an accompanying Graphical User Interface (GUI) to be designed (Figure 4.11). The control program runs in the background while the GUI passes the force target and start command from the user to the control program to initiate the grasp, and then the force and displacement data are saved to a spreadsheet and displayed on the interface. The GUI allows the user to set the target force and grasp time before beginning the grasp cycle. Once the target force has been reached by the loadcell, the actuator remains stationary, holding the position, and the grasp timer starts. The program uses a polling structure of controlling the position and force application, whereby the position is advanced and then the force reading is checked (Figure 4.12) (Appendix B).

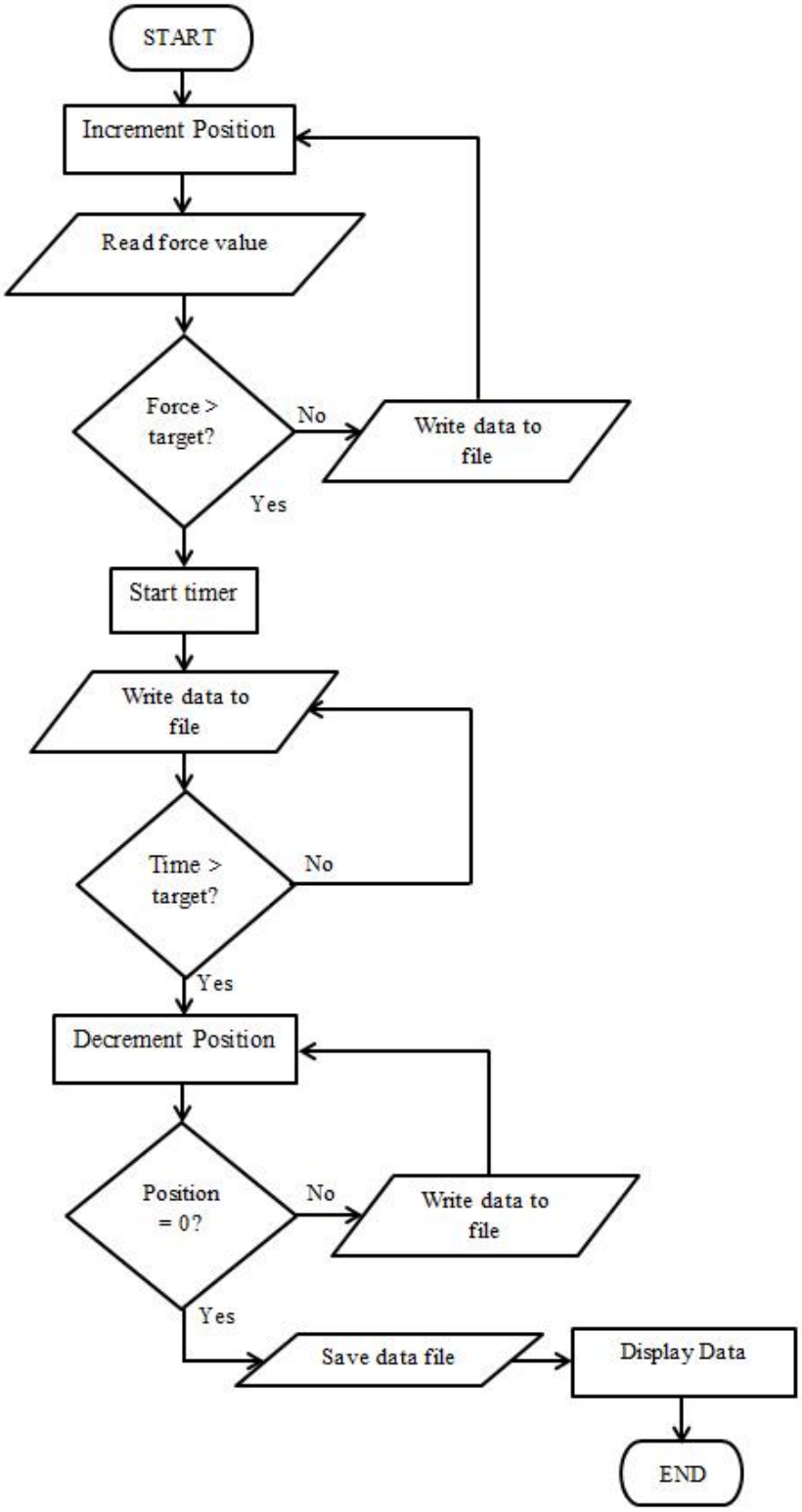

Figure 4.12: Flow chart of the test rig grasp cycle showing actuator position incrementation until desired force is reached, position is held for the preset time, then the actuator is returned to start position and force, position, and time data saved.

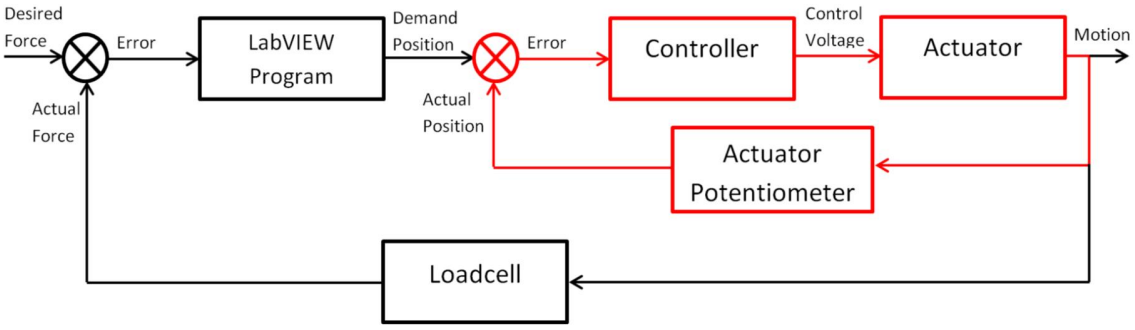

Figure 4.13: Control diagram highlighting the desired force input to the program demand position sent to the controller and converted to a control voltage for the actuator, with the actual position fed back to the controller via the actuator's internal potentiometer, and actual force sent to the LabVIEW program as measured by the loadcell (Changeable sections in black, limited change in red).

4.3.4 Validation of the Measurements and Control System

In order to determine the accuracy and repeatability of the laparoscopic grasper test equipment, the force and position measurements, and control loop were validated. To validate the force readings, weights were suspended, via a pulley, above the loadcell. The weight was incremented from 0 g to 1 kg then back to 0 g, in 50 g steps, with 3 repeats.

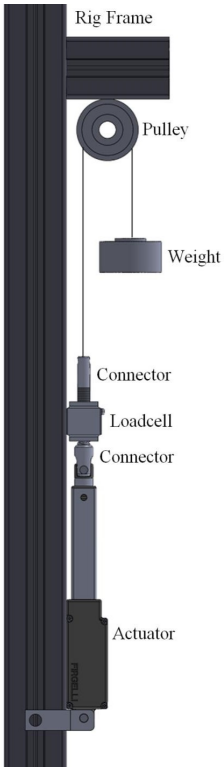

Figure 4.14: The loadcell validation setup for the first rig prototype showing the suspended weight via a pulley, connected to the loadcell.

The force reading was sampled for 3 seconds, then the average was logged (Figure 4.15). The graph shows an approximate 1:1 relation between the applied force and the loadcell readings.

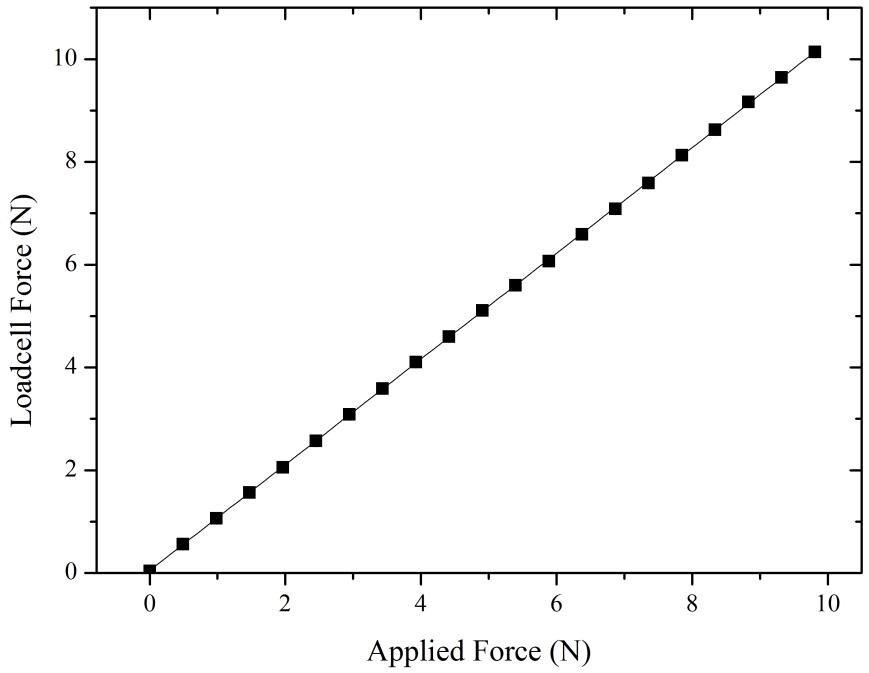

Figure 4.15: LCM703-25 Omega loadcell validation graph showing the average of three up/down sweeps and the linear fit (fit; $F = 1.03V + 0.06$) (error bars excluded for clarity).

The actuator system's (actuator and controller) positional accuracy was validated by incrementing the position demand signal (0 - 3.3 V) until the actuator moved to the next step. This was to show the reliability of the actuator movement. Only the required working range of the grasper (0 - 2.5 mm) was validated (section 3.4.4). Both the demand and actual positions were recorded and plotted for three up and down sweeps (Figure 4.16). The results show that the system has a low positional accuracy of 0.5 mm for the intended application. Due to the small range of movement required, the implications of this impacted on the rig by causing abrupt grasper jaw movements leading to large grasping forces, which were difficult to control and predict. It can also be seen that for each actuator position, there is overlap in the demand values, adding to the unpredictable response of the actuator movement and as a result, the force application. Using the grasper model, the positional accuracy was used to show the jaw angle accuracy as a result. Over 0.5 mm displacement, the jaw angle could vary by up to 15 °. This also means that over the full 2.5 mm extension, there will only be approximately 5 steps to move the jaws from fully open to fully closed highlighting the limited control over the motion and as a result the force application.

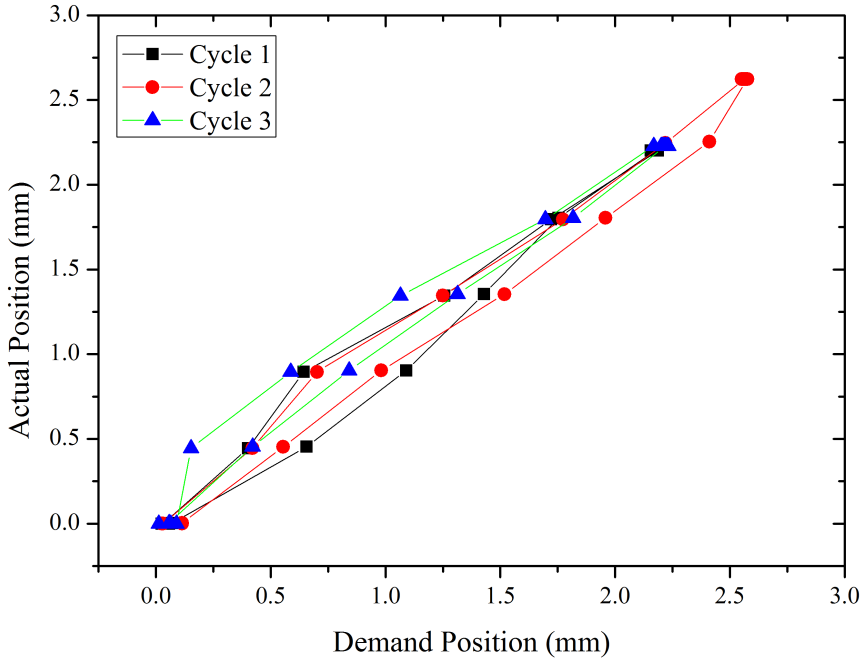

Figure 4.16: Firgelli L16 actuator and controller position calibration graph for three up/down sweeps.

The entire control system was validated using a 5 mm thick sample of silicone with a Young's Modulus of 6.5 kPa as a substitute for tissue (typical values for soft tissue have been shown to range from 1 KPa [101], to 6.7 kPa [96]). The sample of silicone was held in the rig and grasped with ten target forces from 10 to 100 N, each for 5 seconds, with 3 repeats (Figure 4.17).

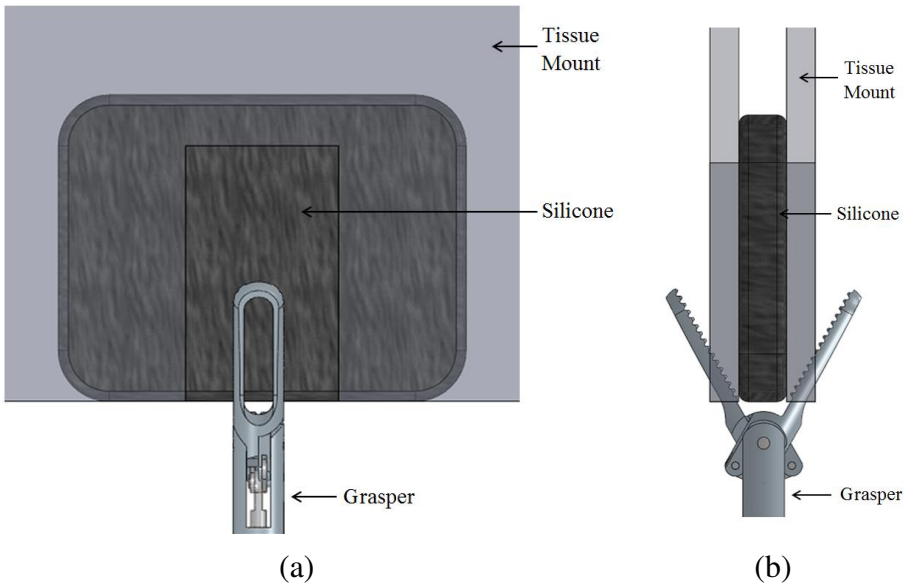

Figure 4.17: System validation set-up with Silicone sample, showing (a) the front view, and (b) the side view.

The ideal requirements for the system would be to achieve the maximum target force without exceeding it. When the system exceeds the maximum target, this is known as overshoot and it should be minimised to give reliable and repeatable control. For this system a suitable overshoot would be no greater than 5 % of the maximum force. This ensures that at the lower forces, the overshoot does not exceed 1 N, as this will provide comparable data for each force target.

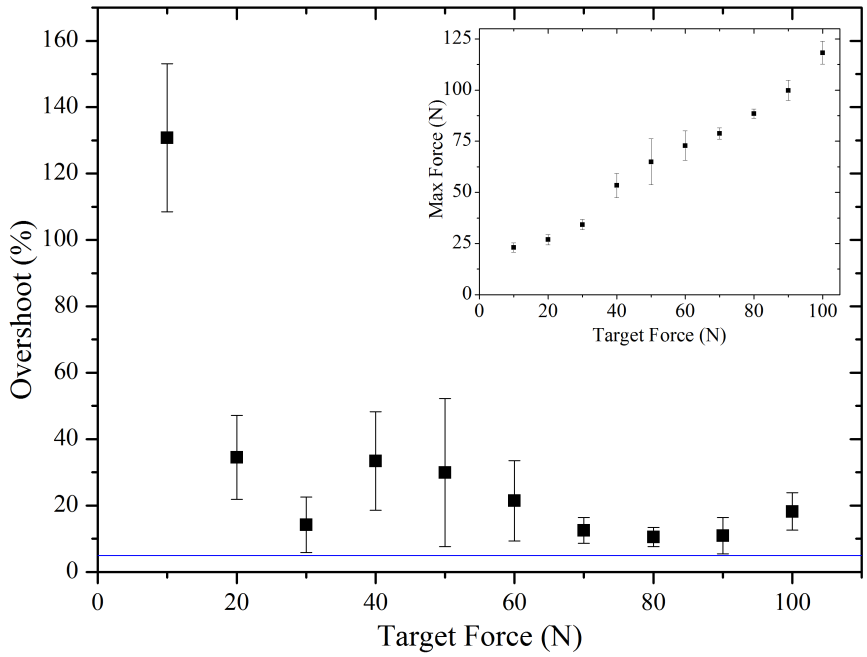

Figure 4.18: The systems control loop force overshoot percentage validation graph (5 % target in blue) (actual forces shown in inset).

The results indicate that the system is not capable of producing grasps with an overshoot of less than 5 %, in particular forces around 10 N have a very large overshoot (Figure 4.18). In general the system cannot provide forces below 20 N, and is not reliable to give repeat grasping forces for each target.

4.4 Concluding Remarks about the Initial Design

The initial test rig prototype was developed from the specification (section 4.2) however even though the linear actuator is capable of the required 100 N maximum force, there is a need for higher positional accuracy to prevent the large force overshoot and improve repeatability. Improvements to the rig rigidity would also improve measurement reliability. Due to the unrepeatable motion control, the rig greatly overshoots the target force, especially for the lower forces, demonstrating that the rig is not suitable for testing at this stage. It was

observed that the rig's mechanical elements (the grasper and actuator brackets) would move during force application. Due to the design of the grasper mount (Figure 4.1), during the force application the grasper would tilt the bracket causing it to pivot. Also the actuator bracket would slide, especially for higher force grasping. This meant that the force application was not truly linear and that the measured displacement of the grasper would be inaccurate. This would affect results as it would not just show tissue relaxation, and would be difficult to distinguish between the two effects. The large variation in grasping forces are due to an instability in the actuator PID controller. This is because the highest positional accuracy from the controller is needed, but because of this the controller often overshoots the position and oscillated about the desired position, but does not reach it. Even a slow actuator speed leads to oscillations. One possible issue would be that the small displacement of the grasper linkage may cause the accuracy of the actuator to become significant. This was highlighted using the grasper model to show the positional control of the actuator and as a result the jaw, showing that for a single actuator *'step'*, the typical jaw movement would be around 15 °. A higher accuracy actuator should improve the force target overshoot of the design. The design will require the component fixtures to be improved through strengthening and improvement of alignments. Also the tissue holder only allows for single layer of sample, whereas a full section would be closer to actual surgery.

4.5 Redevelopment of the Laparoscopic Grasper Test Rig

From the previous design validation and general usage, a number of changes were required in order to meet the specification (section 4.2). These included improving the rigidity of the rig to prevent movement in the actuator and grasper mounts while grasping, as this greatly affected the reliability of the rig, and improving the LabVIEW program to provide an efficient control loop and reduce force overshoot (specification 1, 2, and 6). By redesigning the tissue holder to allow for cylindrical samples this would give a more accurate representation of typical *in-vivo* grasping (specification 4).

4.5.1 Design of the Test Rig Structure

The redesigned rig structure was made from a larger profile (40 x 40 mm) of Bosch Rexroth extruded aluminium bar, and included adjustable feet, to ensure a level set-up, and a door for easy access (Figure 4.19). Perspex panels were used for added safety. The actuator was secured to the base of the rig so that it did not move when applying a force, as the previous design would allow the actuator to gradually slide up the frame, affecting the rig accuracy. The same loadcell linkage connector was used, as in the first rig design to connect the grasper shaft to the loadcell. Another part was manufactured from stainless steel to connect the

loadcell to the new actuator. The grasper mount was integral to the rig frame. This would again add to the rigidity and prevent any unwanted slippage when grasping. The grasper mount was secured through a crossbar in the rig (Figure 4.19).

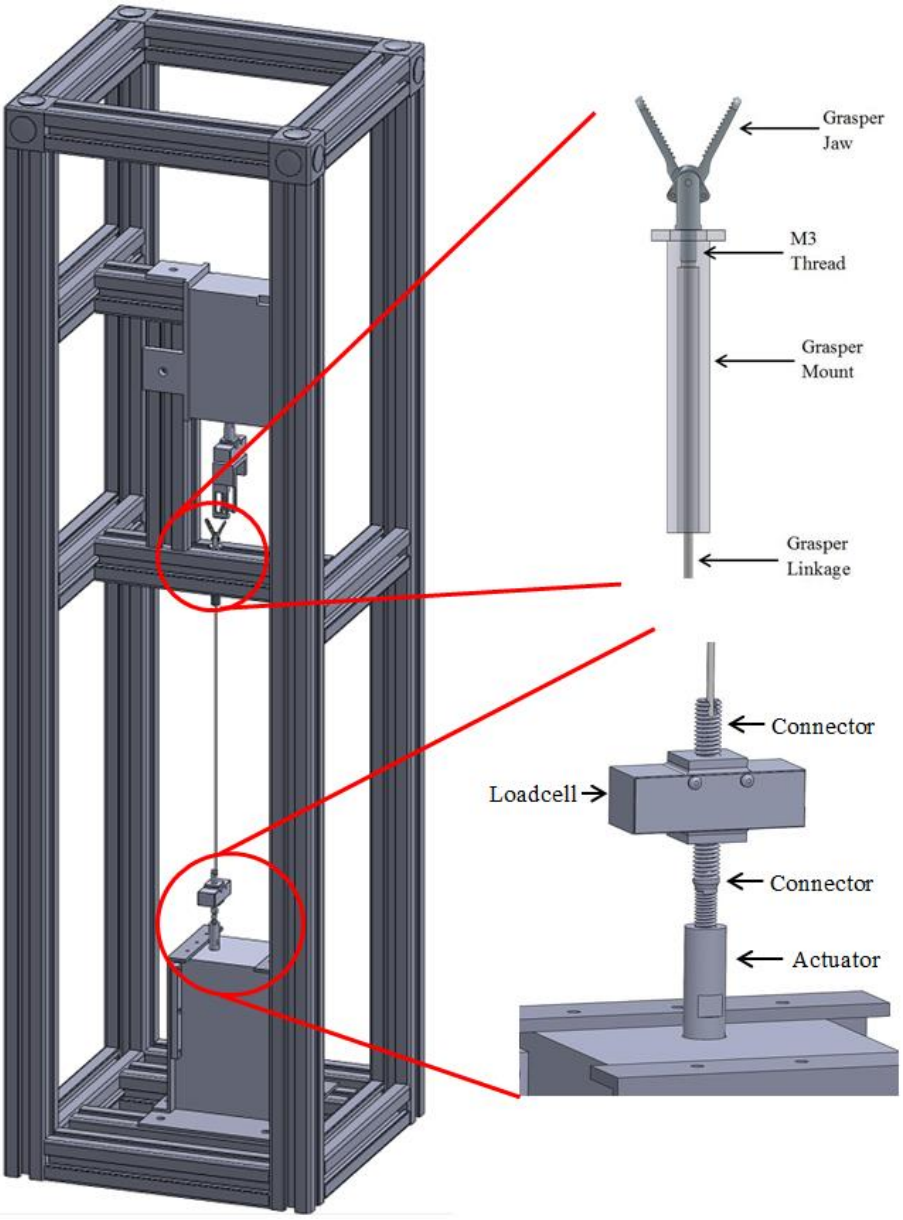

Figure 4.19: The redeveloped rig design showing the modified grasper mount and actuator fittings.

The tissue preparation and holding method were changed to ensure that histological analysis was as accurate as possible and that no other factors would affect these results, so that any damage analysis was true for the applied force and not dependant on the preparation of the sample. Instead of grasping an opened section (Figure 4.20a), the full colon cylinder is grasped (Figure 4.20b), ensuring that the grasped area is not damaged prior to testing. Because the samples are prepared before testing, when using an opened section, each edge

has already been cut, and as a result has cellular damage no matter which way the sample is orientated. When using the full cylinder, the sample can be grasped so that none of the cut areas are being grasped. This improves the accuracy of the histological analysis and keeps the grasp as close as possible to that used in surgery.

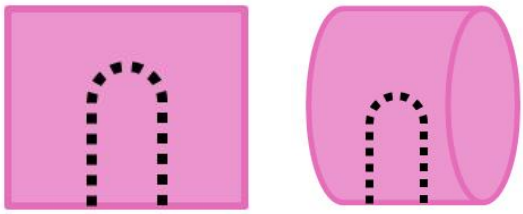

(a) (b)

Figure 4.20: Different tissue grasping methods, showing (a) an opened colon section with grasped area overlapping pre-cut area, and (b) the full cylindrical grasp showing no overlap with cut areas.

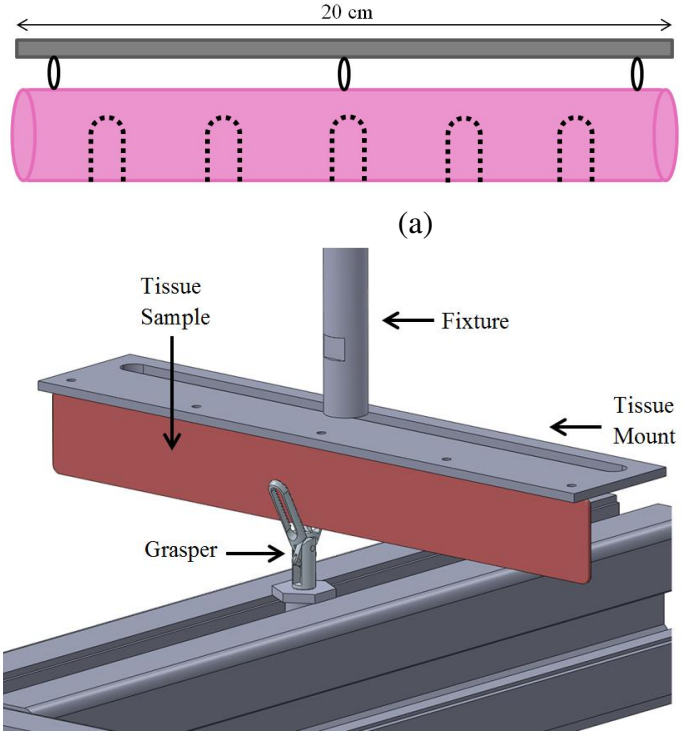

(a)

(b)

Figure 4.21: Redesigned tissue mount; (a) a diagram of the set-up and tissue attachment, with grasped fenestrations, and (b) a CAD model of the new design.

A new tissue mount was manufactured out of aluminium. It allowed a segment of colon to be sutured to it and suspended in the grasper jaws. Between cycles the bracket is moved so that a fresh area of tissue is exposed to the jaws. This removes the chance of unnecessary

damage to the samples when cutting, and allows for cylindrical grasping, which is a more likely scenario in surgery, and ensures the samples are not damaged prior to testing (Figure 4.21).

4.5.2 Hardware Set-up

A higher specification linear actuator (SMAC Inc., LAL95 (Appendix A)) was selected to apply the force along the grasper linkage. The actuator configuration is capable of providing an instant maximum force of 195 N, or a continuous force of 89 N. However the actuator will be able to withstand 100 N for one minute grasps provided the controller is allowed a 2-3 minutes *'cool down'* period between each grasp, as a large current is drawn at higher forces. This meets the stated grasping time requirement (spec 3) of the specification (section 4.2).

The same loadcell has again been used to measure the applied force along the shaft of the grasper and is connect to the PC via the same amplifier and DAQ device (Figure 4.22).

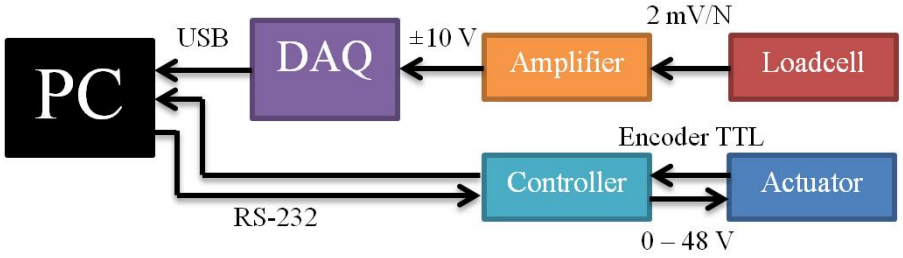

Figure 4.22: System diagram for the redeveloped rig, showing data connections and voltage ranges.

4.5.3 The Design of the LabVIEW Interface

A new LabVIEW program and GUI were developed to provide an improved control interface of the test rig (Figure 4.23). There are 5 possible actions which can be performed. By pressing the *'STOP'* button, commands are sent to the actuator controller to turn the motor off, and then the program is stopped. The *'Set Home'* button sends a command to the controller to deactivate the actuator leaving it free to be moved. A window is then displayed to instruct the user to move the actuator to the desired *'home'* position then press *'OK'*, at which point the controller is instructed to set this position as its start point. This command is used after first starting the program, to open the grasper jaws ready for testing. The *'Zero Loadcell'* button samples readings from the DAQ device for 3 seconds and takes the average of these, then stores this to convert later test readings to give accurate results. This is essential to account for added force on the loadcell from the grasper linkage and connector weight. By pressing the *'Single Test'* button the program begins the test procedure. The *'Abort Test'* button can be pressed at any point during the test procedure to return the actuator to the home

position. This can prevent the rig from damaging the mechanisms or to prevent injury to the user. Finally the *'Save'* button takes the test data and saves this in an excel spreadsheet.

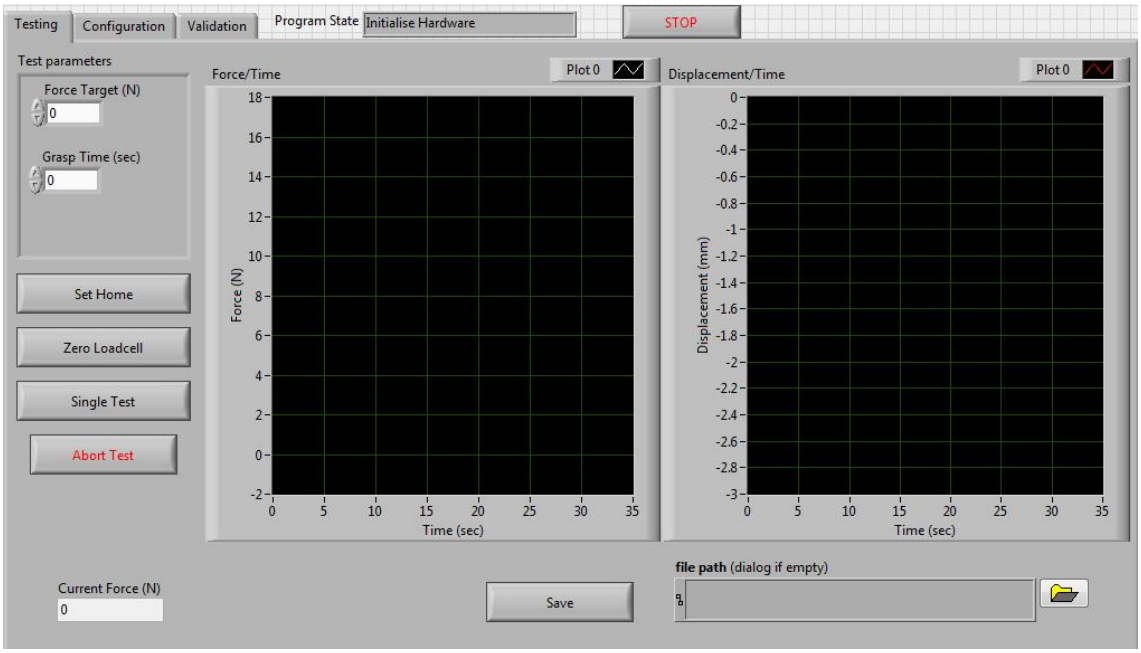

Figure 4.23: Main LabVIEW GUI for redeveloped rig program.

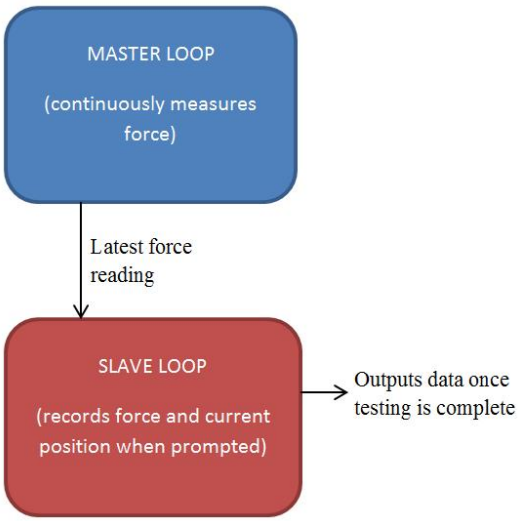

Figure 4.24: The master slave parallel loop setup.

The previous program used a polling method to advance the actuator position and then check the force reading. The new program sets the target speed for the actuator to move at, then sets the end position. Once the desired force target is reached, the actuator is stopped for the desired time, then returned to the start position. If the end position is reached before the target force, the actuator is returned to the start position and an error is displayed, preventing the actuator from damaging itself. The program also uses a master-slave parallel loop with

a notifier, where the master loop is in control and focusses on reading the force signal, then sends notifications to the slave loop which logs the position (Figure 4.24). This ensures quick capture of the force readings so no readings are missed, and the latest reading is acted upon to reduce the degree of force overshoot. Both readings are logged against time to ensure that if readings are missed, the data is still synchronised.

4.5.4 The Actuator Controller Serial Communications

The actuator uses a controller (SMAC Inc., LAC-1 (Appendix A)), which converts the RS-232 serial commands into the desired position and force from the actuator. The controller uses a PID control loop to control the movement of actuator, giving a smooth, stable motion, where the PID constants are sent to the controller via the serial communication before any motion can be performed. The RS-232 serial communication standard (Figure 4.25) uses 10 digital bits to transfer information. This includes a start and stop bit which are set high to ensure devices reading the signal remain synchronised. Transmitting and receiving devices must also use the same Baud rate, which defines the number of bits sent or received per second, typically 9600 bit/s. The remaining eight bits are used to send the data or message by setting them either high or low with the least significant bit sent first.

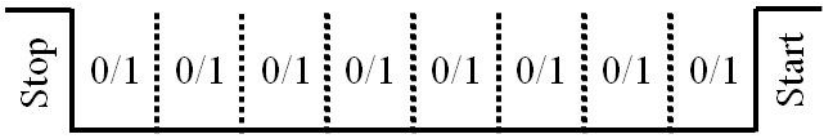

Figure 4.25: The RS-232 serial communication standard.

The SMAC controllers use a Baud rate of 9600 bit/s and signals are sent using the American Standard Code for Information Interchange (ASCII) which converts the alphabet, numbers and other characters, such as space, carriage return or punctuation marks into 8 bit binary numbers (Figure 4.26).

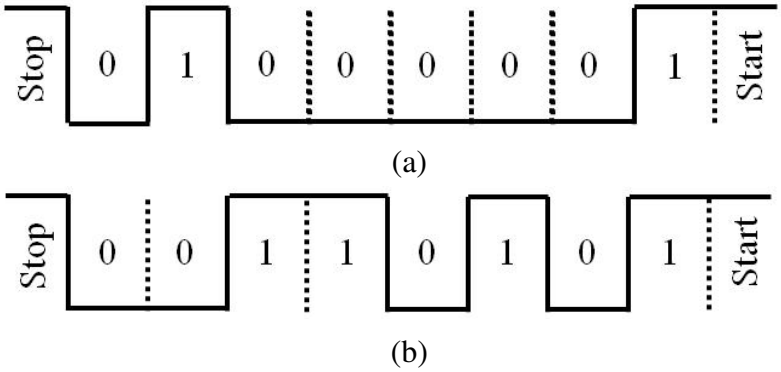

Figure 4.26: ASCII characters binary serial signal examples; (a) the letter A (binary value 65), (b) the number 5 (binary value 53).

Two LabVIEW sub-programs were designed to read and write values from the controller. This used a string generator which took the commands and values (if necessary) and created a string of information which is then passed through the PC's serial port using the inbuilt LabVIEW component. Once received by the controller, the same message would be *'echoed'* back to the PC which could then be read and checked against the sent message to ensure it was correct. If any data was requested, this would subsequently follow the echoed message. The controller uses a termination character (carriage return) to indicate the end of the message, which can be removed from the replies, and the result can be converted into numerical values.

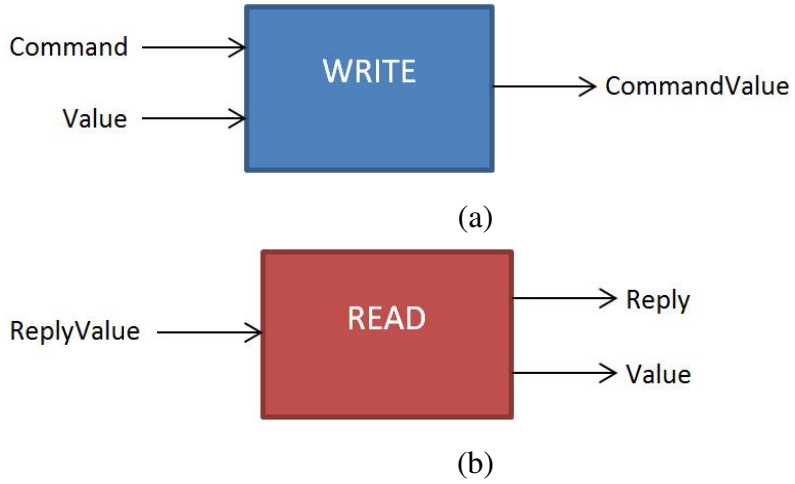

Figure 4.27: The program system for (a) generating the write commands and (b) reading the returned replies.

Command	ASCII	Definition
Motor ON	MN	Used to turn the actuator on.
Motor OFF	MF	Used to turn the actuator off.
Set Velocity	SVn	Sets the target velocity 'n' of the actuator.
Define Home	DH	Sets the current position to home.
Tell Position	TP	Returns the current absolute encoder count.
Go Home	GH	Moves the actuator to the home position.

Table 4.1: Typical commands used to control the actuator sent to the controller via RS-232 from the PC (7.6.5).

For each command sent, there must be a short delay of approximately 100 ms to ensure the controller has received it fully. To improve the efficiency, the LabVIEW read and write VIs use the echoed string check as an indicator that the controller has received the command, and does not act until this has occurred. Instead of waiting for the desired time, the program

acts immediately, ensuring the system responds as quickly as possible. This is also another reason for not setting each individual position of the actuator, allowing the velocity control to determine when to move.

4.5.5 The LabVIEW State Machine Structure and Control

The program implements a queued state machine which removes unnecessary processor demand between grasp cycles as the program will wait until it receives a command. This also contributed to a neater wiring diagram, allowing minor alterations to be performed easily. This provides a more modular programming approach, enabling modifications to be made more easily and quickly than in the previous linear program. Rather than incrementing individual positions, the actuator velocity and desired end position are set to give a smoother motion. On starting, the different actuator configuration parameters (describing positional limits, resolution, etc.) are sent to the actuator controller, and the loadcell is zeroed. This ensures that the program is able to communicate with the hardware and will indicate any errors immediately. The program then sits in the *'Listen'* state until a user input is specified via the GUI (Figure 4.28).

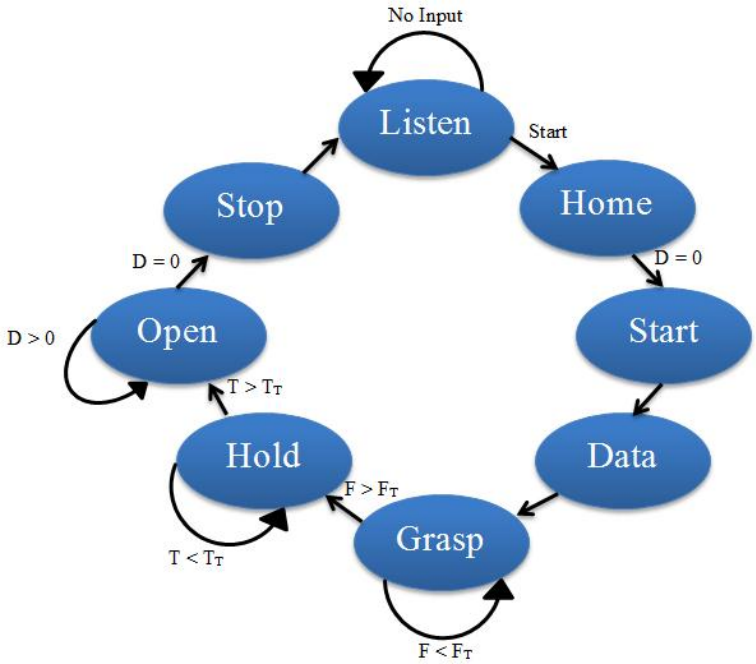

Figure 4.28: State diagram of the redesigned rig's program test procedure, where D is displacement, F is current force, F_T is force target, T is current time and T_T is time target .

When the test procedure is started the program moves to the HOME state, where the controller sends the actuator to the home position to ensure all tests begin at the same point. Once at the home position (i.e. displacement is 0), the program moves to the START state,

which sets the desired speed at which the actuator is to move, and sets the end position target before entering the DATA state. Here the program starts recording data with the DAQ device and then the actuator is told to move. Note that even with the velocity and end target set, the actuator will not move until told to do so. Once these initial procedures have been performed, the program enters the GRASP state where the program continuously logs the data from the loadcell, while measuring the position of the actuator until the loadcell reading passes the desired target (which has been set by the user). Once the force target is reached the program enters the HOLD state, at which point the actuators velocity is set to zero, ensuring it remains stationary for the desired time, during which time the force is still continuously measured from the loadcell. Once the target time has been reached, the program moves to the OPEN state where the actuator is sent *'home'* and the position and force logged until it reaches the start point (i.e. displacement is 0). Here the program moves to the STOP state where the DAQ device is stopped and the program is instructed to return to the LISTEN state.

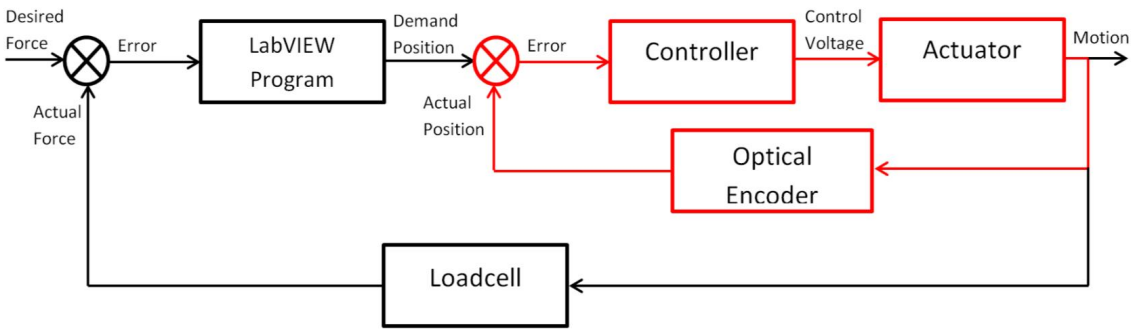

Figure 4.29: Control diagram highlighting desired force input to LabVIEW program demand position sent to the controller and converted to a control voltage for the actuator, with the actual position fed back to the controller via the actuator's internal optical encoder and actual force sent to the LabVIEW program as measured by the loadcell (Changeable sections in black, limited change in red).

The degree of overshoot is determined by a number of factors which affect the control loop (Figure 4.29). The PID settings are preconfigured by the manufacturer to provide minimal overshoot and a smooth motion within the current limits of the actuator. Controls such as the speed of the actuator, the sample rate, and efficiency of the program can be optimised to give the best performance and are discussed later in this chapter.

4.5.6 Validation of the Actuator Positon

To determine the repeatability and accuracy of the rig, the position and control loop were tested. To provide a true position measurement, a micro-laser linear displacement sensor (LM-10, (Appendix A), with positional accuracy of 5 μm, was used to measure the position of the actuator rod. The laser sensor was secured above the actuator and loadcell (Figure 4.31).

The loadcell was included when validating the position to validate the full assembly of the design.

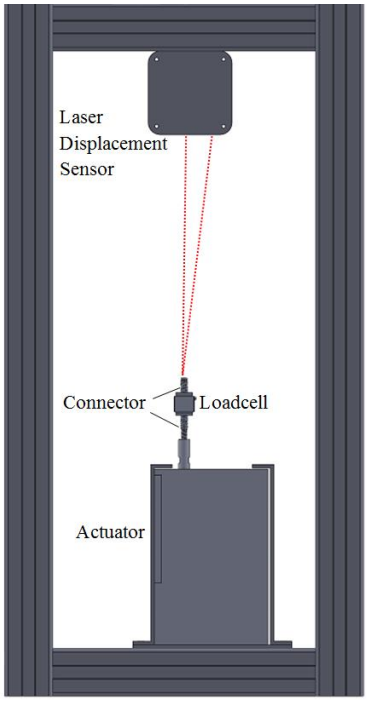

Figure 4.30: Redesigned rig displacement validation set-up with actuator, loacell and laser sensor.

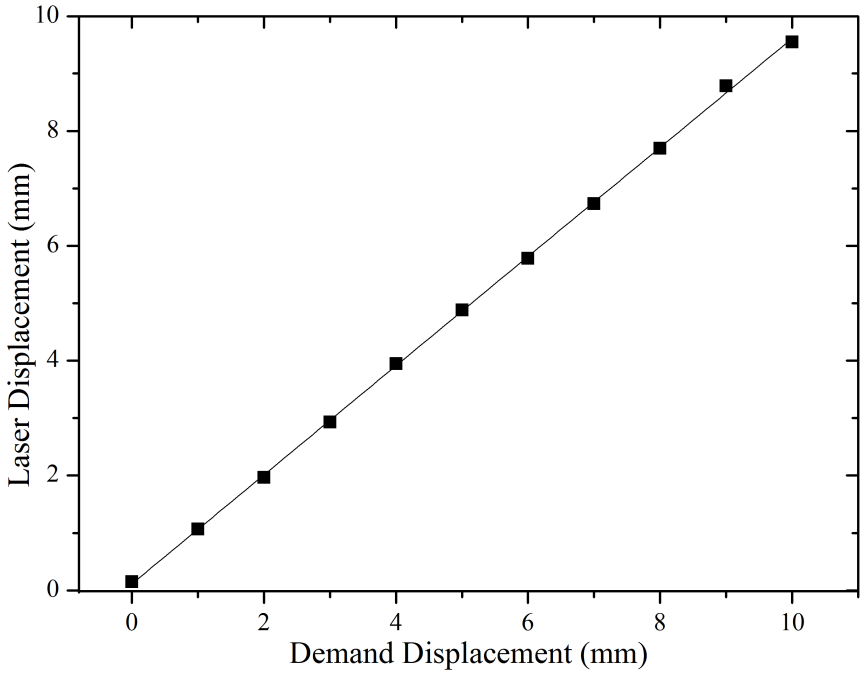

Figure 4.31: Redesigned rig SMAC actuator position validation graph for 3 up/down sweeps with linear fit (fit; $F = 0.95V + 0.11$).

The actuator was passed through the full range and the laser reading was logged against the actual encoder position for 3 up and down sweeps. The results show accurate and repeatable position measurements from the actuator (Figure 4.31). This ensures a smooth closing motion of the grasper jaws due to the higher positional resolution of the actuator rod (improved from 0.5 mm to 0.005 mm).

4.5.7 The Optimisation of the Control Loop

As discussed previously, the factors which affect the control of the system can be optimised to run reliably and also give the fastest grasping rate with repeatable limited overshoot of less than 5 % (specification 2 (section 4.2)). One factor affecting the control of the system is the sample rate. A fast sample rate ensures that data is captured quickly, allowing the program to respond faster as the force passes the target, reducing the overshoot. However if the system runs too fast the time between readings can become inconsistent. By limiting this variation in time measurements an optimum sample rate can be found. The desired sample rate was reduced by 100 Hz from 1 kHz to determine the fastest actual sample rate. The time between samples was logged for 3 grasping cycles and the standard deviation was calculated. The fastest possible sample rate was 500 Hz (Figure 4.32). At this point the standard deviation was 0.03, showing little deviation in time between samples.

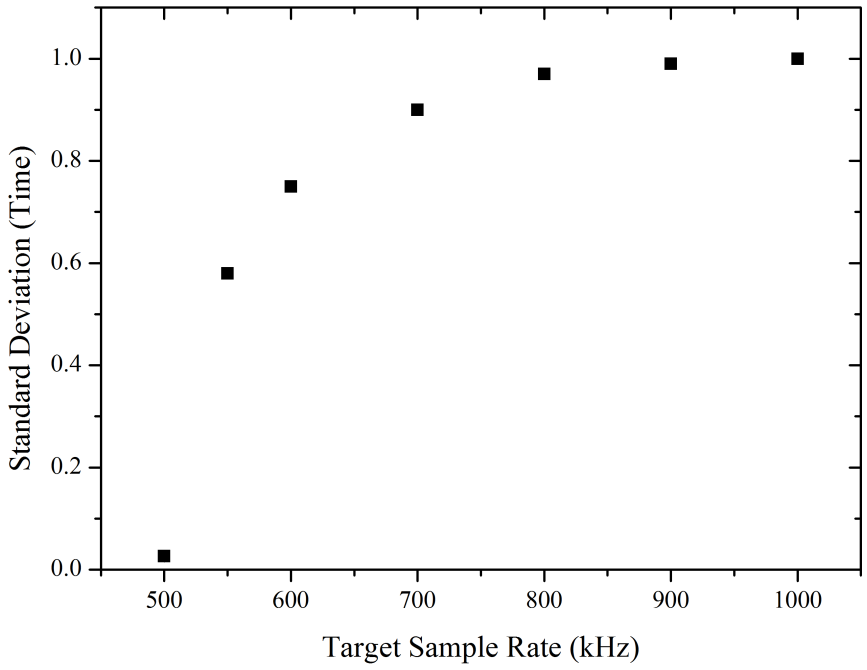

Figure 4.32: Redesigned rig control loop sample rate validation graph.

A sample of Sorbothane (DURO 40) with a Young's modulus similar to soft tissue (approximately 1.70 MPa), was grasped at 10 N for five seconds for a range of actuator

speeds to ensure the 5 % target is not exceeded for the minimum force. A fresh sample was used for each grasp to ensure that the mechanical properties were consistent. The Sorbothane is a uniform viscoelastic material with known properties which is used to determine the rigs capabilities. From the previous *in-vivo* work (section 3.8.3) the average grasping speed during the force application was shown to range from 0.3 mm/s up to 3.0 mm/s, with average values lying between 0.5 mm/s and 2 mm/s, therefore the higher end of this range will be tested first to see if there is an optimum maximum speed. The approach speed of the actuator was varied from 1.5 mm/s up to 3.5 mm/s in 0.5 mm/s increments. The force overshoot was logged over 5 repeats. A speed of 2.5 mm/s provided the fastest response, while keeping the overshoot below 5% (Figure 4.33).

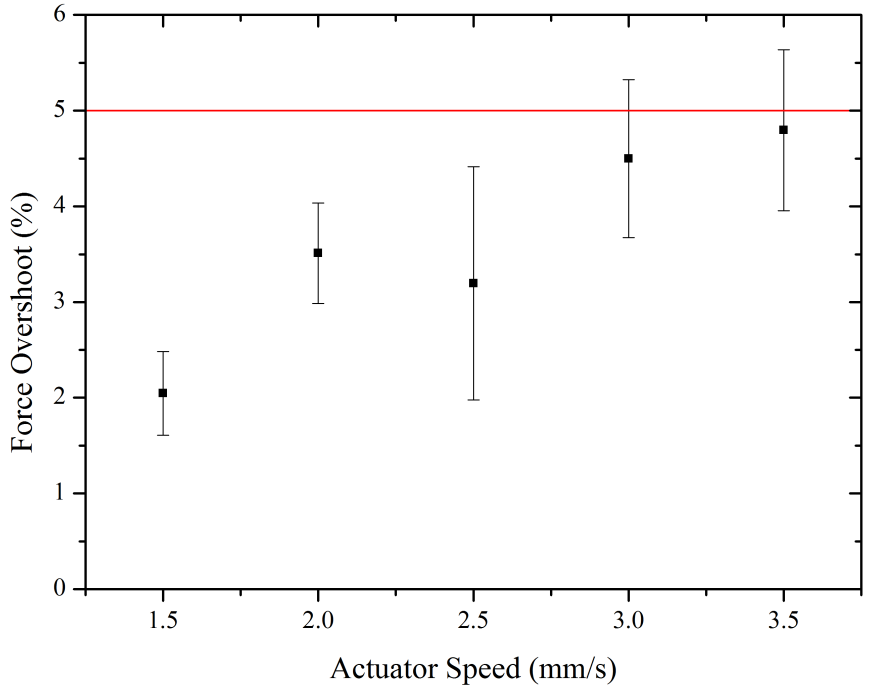

Figure 4.33: Redesigned rig control loop actuator speed validation graph for 5 repeats, with standard deviation (5% threshold indicated by red line).

To establish the abilities of the rig, a sample of Sorbothane (DURO 40) was grasped for 5 seconds with target forces from 10 N to 100N with 10 N increments, using the previous actuator speed result of 2.5 mm/s. The Sorbothane provided a uniform material on which to test. Due to the larger standard deviation for the 2.5 mm/s actuator speed (Figure 4.33), the force overshoot was logged for 10 repeats to ensure the grasping does not exceed the 5 % target overshoot. This test aimed to show how the control system performed over the full grasping force range. For 10 N to 30 N the overshoot is less that 1 N (Figure 4.34). Above this force the overshoot is maintained to between 1-2% which is negligible when compared to the maximum forces being applied [175].

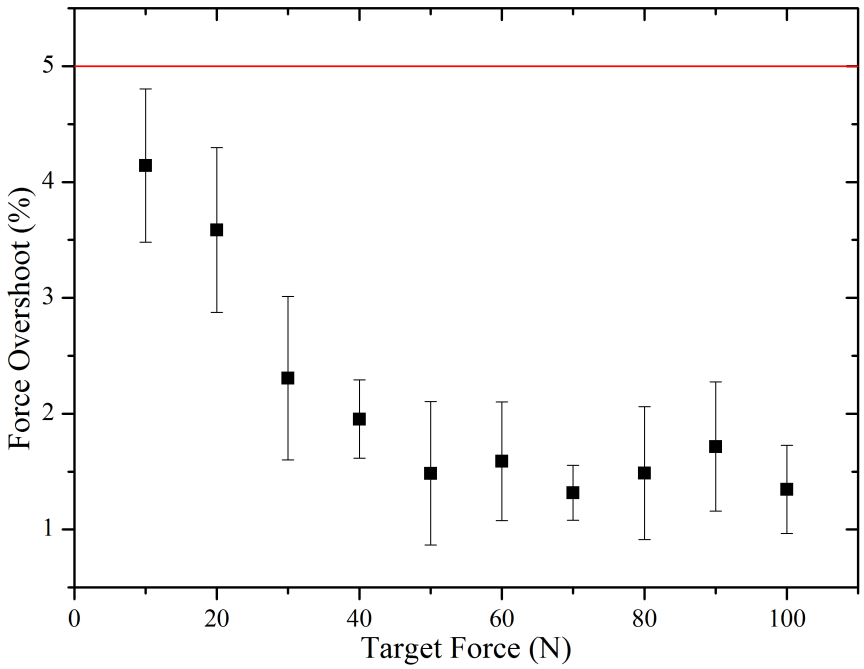

Figure 4.34: Redesigned rig control loop overshoot validation graph for 10 repeats with standard deviation (5% threshold indicated by red line).

The validation results showed that the system control can reliably provide grasping forces with an overshoot of less than 5%, and are repeatable over numerous grasps.

4.6 Concluding Remarks about the Final Design

The improved test rig design has allowed for increased precision of grasping forces with linkage force overshoot limited to less than 5 % for lower forces ($<$ 30 N), and under 3% for higher linkage forces (30 – 100 N). This has been achieved by integrating a high precision (± 5 μm) positional accuracy actuator and improved control loop utilising parallel processing to ensure the rig responds as quickly as possible. Redesigns to the rig structure have added rigidity to ensure the set-up does not flex during testing, giving high repeatability and reliable results. Finally changes to the tissue holder have allowed for the test set-up to give a closer representation of typical *in-vivo* surgery and limited tissue damage to the grasp site.

4.7 Conclusion

A laparoscopic grasper test rig was developed to meet the specification (section 4.2), which it met in the following ways. The rig is able to accurately control the grasping of a double action laparoscopic grasper and apply a linkage force range of 10 to 100 N, for up to

one minute, with a limit overshoot of less than 5 %. The force and displacement are measured along the grasper shaft (resolution 0.005 mm), to match previous *in-vivo* work (section 3.3). The redesigned set-up used a higher specification actuator system to achieve this, with an improved LabVIEW program which allowed for faster data capture. The tissue holder allows for cylindrical grasping of the colon, to simulate as close as possible to *in-vivo* surgery without inducing excessive tissue damage to the grasped area. Suitable safety measures were implemented into the design in the form of a door on the front of the rig, which can be closed during testing, a reminder in the program to close this door before executing a test, and an *'abort'* button integrated in the program to open the grasper if anything should happen. The LabVIEW program also allowed the user to vary the applied grasping force and time, displaying the force and displacement data after each grasp. The rig is manufactured using aluminium and stainless steel parts which can be sterilised, as well as being disassembled for thorough cleaning.

Chapter 5

Ex-vivo Tissue Damage Investigation

5.1 Introduction

The *ex-vivo* tissue testing work involved in the first instance, the development of the tissue tester followed by the analysis of the mechanics of tissue. Supporting histology enabled the extent of damage to be determined after the tests, and it is this information which is integrated into an intelligent grasper, which is subsequently described in chapter 6. By fitting the five element Wiechert model (section 2.3.2) to the tissue time response data, this can indicate how the magnitude of applied force affects the tissue response. From this the tissue mechanics can be understood. This method gives direct and quantitative measures of tissue mechanical properties, to be linked to clinical measures of damage which have been qualitatively assessed by histology. The mechanical measures allow a fast and convenient means of identifying tissue damage, with the potential for real-time intraoperative use.

5.2 Laboratory Setup for *Ex-vivo* Tissue Testing

A reusable, short, fenestrated, atraumatic grasper (part no. 101–48020, Surgical Innovations Ltd.), with a 5 mm shaft diameter and length of 305 mm was used for the *ex-vivo* testing to match the previous work carried out *in-vivo* (section 3.7). The sample used was a cylindrical length of porcine tissue, of approximately 20 cm. Due to the variation in width, thickness and texture of the porcine colon over the full length, and the availability of the tissue, the samples taken for each test were between the rectum and descending colon. This ensured that the measurements taken were over the same area. Similarly due to the limited colon length, there is one repeat at each force for each colon. It is first prepared by flushing the sample with tap water to remove any debris. While flushing the sample before testing may alter how realistic the test is (in surgical procedures, the colon may or may not have residual debris after being prepared), a clean sample gives higher repeatability of measurements and keeps the samples consistent. Colon samples were suspended between the grasper jaws via the tissue mount (Figure 5.1).

To match the *in-vivo* work, the full fenestrated area of the grasper is used to perform the grasp. Between each grasp cycle the sample was moved along by approximately 3 cm to give appropriate space between to separate after testing, without inducing damage to the grasped

area (Figure 5.2). The full length of the sample was used, with typically around 5 - 6 grasps performed.

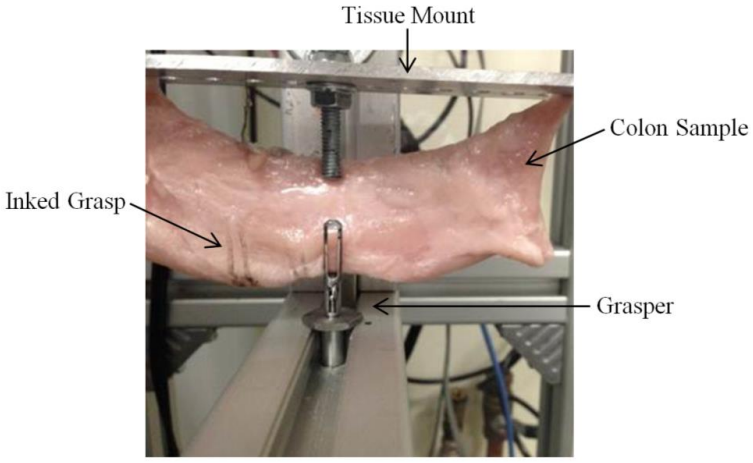

Figure 5.1: *Ex-vivo* colon tissue grasping in the laparoscopic grasper test rig.

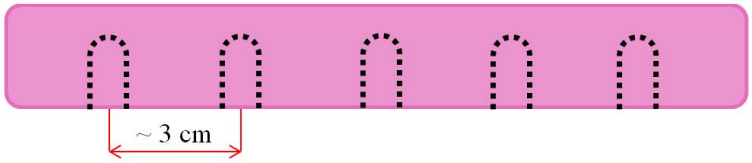

Figure 5.2: *Ex-vivo* colon tissue sample spacing between grasped areas to provide space to separate samples without inducing extra damage.

The actuator begins retracting (1), until the grasper comes into contact with the tissue (2) and then continues until the desired force reading is measured along the shaft (Figure 5.3). At this point the grasper position is maintained for the desired grasping time (3), and the force readings are logged. After this time the tissue sample is released by the grasper (4), the actuator is returned to the open position (5), and the data saved.

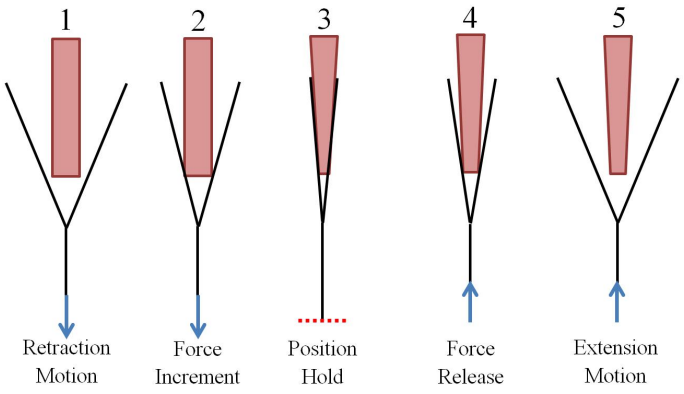

Figure 5.3: *Ex-vivo* grasping cycle for the laparoscopic grasper test rig, showing the linkage retraction (1), force incrementing (2), position maintenance (3), sample release (4), and the actuator extension cycle (5).

5.3 Data Analysis Methodology

For each grasp a summary measure, termed *'force relaxation'*, was used. This is defined as the difference between the maximum and minimum force over the grasp time before releasing the grasp, denoted by ΔF (Figure 5.4).

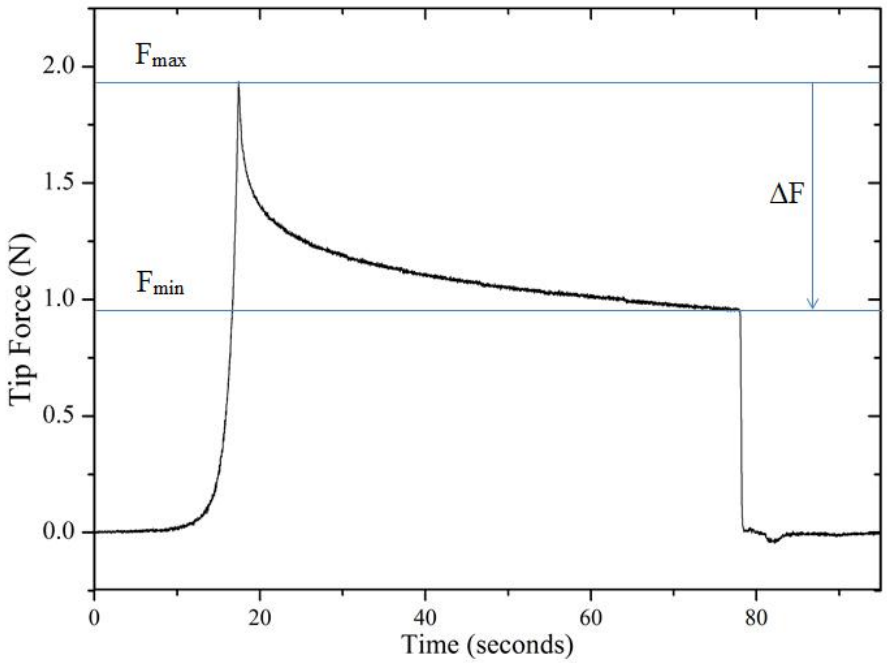

Figure 5.4: A typical response showing the method of determining the change in force, ΔF, over the grasping time, from the maximum, F_{max}, to the minimum force, F_{min}.

The resulting relaxation profile can be compared to the previously discussed model responses (Figure 2.22) (section 2.3.2). For a step strain test, the Maxwell and Kelvin models show a similar profile, where the force shows a sudden increase, followed by an exponential decay. For the Maxwell model, this decays to zero, unlike the response shown in this work. The Kelvin model shows a similar response, where the force decays to a set point. However the response in this work suggests that a more complex model is needed for the very fast initial decay, followed by a slower relaxation.

For each result the tool-tip force was plotted against the jaw angle to show the hysteresis in the grasp (Figure 5.5). This hysteresis, termed *'work done'*, is the amount of energy dissipated by the grasper on the tissue sample, and is found from the integration of the encapsulated area of the force/displacement curve.

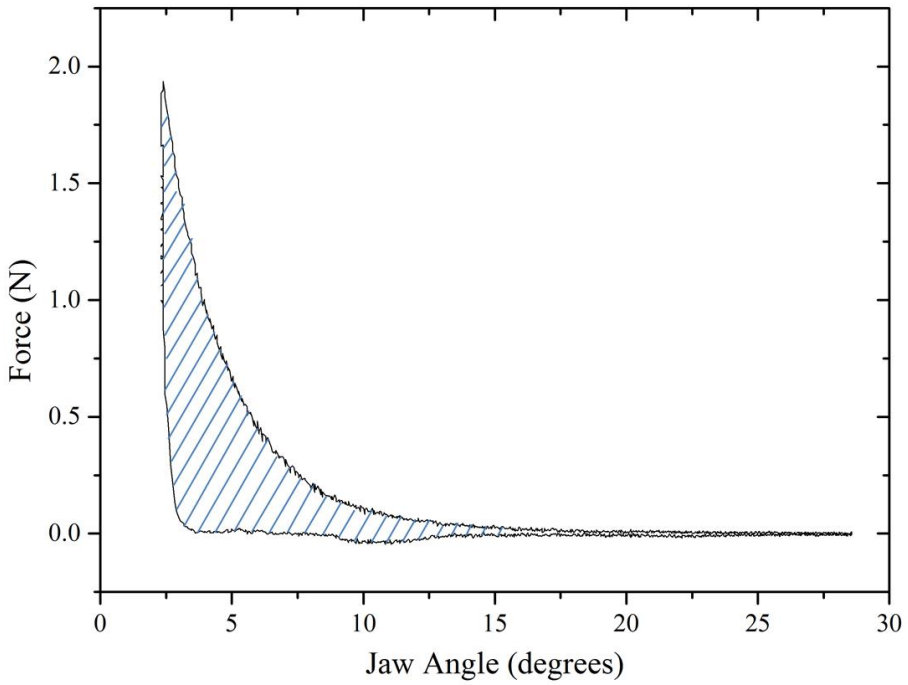

Figure 5.5: A typical response showing the method of determining the work done by the tissue during the grasp as the encapsulated area (blue) when tip force and angular displacement are plotted together.

The work done by the grasper on the tissue shows the energy dissipated, which could be converted in a number of ways. These potentially include a small amount of heat, which would radiate to the surrounding tissue, the breaking of chemical bonds in the tissue structures, and possibly the potential energy stored in the tissue which would show as the tissue relaxes after being grasped. Observing this parameter will show how the tissue responds to an increase in energy rather than just input force.

5.4 Tissue Mechanics Investigation

This investigation aims to establish if and how the the mechanical properties of porcine tissue may change for increasing grasping forces. This study aims to identify key points through a detailed investigation, by focussing on the force range 0 - 100 N and show detail of the tissue relaxation response. By analysing the mechanical response of the tissue, a higher number of test results can be analysed in a faster time than is possible when using other measures of damage. The MATLAB program was written and developed by Zahra Ehteshami [241], to extract the model parameters from the relaxation curve. Data analysis of these parameters was performed by myself, along with the interpretation of the data.

5.4.1 Tissue Mechanics Methodology

The cylindrical porcine tissue samples were grasped using the full fenestrated grasper surface at forces from 5 to 100 N linkage force with 5 N increments. The tissue was grasped for 60 seconds to give the higher repeatable relaxation characteristics. The small force increment will highlight areas of interest where the tissue mechanics may change.

As discussed in the literature review (Section 2.3.2) an effective model for representing the tissue relaxation is the five element Wiechert model (Figure 5.6). The model uses the five parameters (E1, E2, E0, η1, η2) as two Maxwell models (spring and dashpot) in series with a single spring element to characterise the relaxation [113]. The five element model is used above other combinations as this gives the lowest error between the fit and actual data compared to other combinations, but with the lowest complexity. When compared to the Kelvin model, the Wiechert has 2 viscous element, resulting in 2 time constants and can represent a more complex response, with a fast initial drop in force, followed by a slower relaxation. Higher element models could also be used to describe tissue relaxation, but typically does not noticeably reduce the fit error, but will increase the complexity.

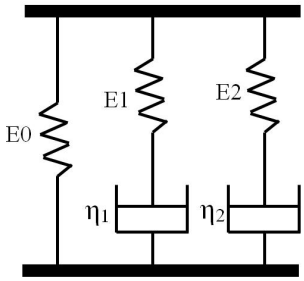

Figure 5.6: The five element Wiechert viscoelastic model for soft tissue analysis.

The equation of the model shows the two time dependant elements and single elastic element (Equation 5.1).

$$E(t) = E_1 e^{-t/\tau_1} + E_2 e^{-t/\tau_2} + E_0 \tag{5.1}$$

From E_i and η_i for each spring and damper combination, the relative time coefficients can be found (Equation 5.2).

$$\tau_i = \eta_i / E_i \tag{5.2}$$

The model has been previously implemented in MATLAB [241], to determine the five parameters using the Least Squares method. For this method, initial parameters need to be determined and are found using a basic three element model, Kelvin model (Figure 5.7), and determining the half-life response of this. The parameters are found from this response and

input in the five element model as an initial starting point. This improves the reliability of the fit, compared to starting without initial values which could lead to more iterations needed, or a solution not being found.

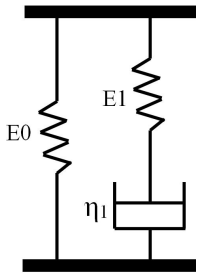

Figure 5.7: The three element Kelvin viscoelastic model for soft tissue analysis.

For each result the model was fitted against the relaxation curve (F_{max} to F_{min}) and the parameters calculated (Figure 5.8). The typical fit was generally close ($< 1\%$ error) to the tissue response data (Figure 5.8a), although the higher force data typically had a noisy signal (from the actuator motors), but the fit still followed closely, as indicated by the smoothed signal (Figure 5.8b). Alongside these measurements, the samples were also photographed to observe any correlation between the tissue modelling characteristics and visual differences in the tissue. This could provide an instant method of determining tissue changes or trauma, instead of using previous methods which require a long analysis period.

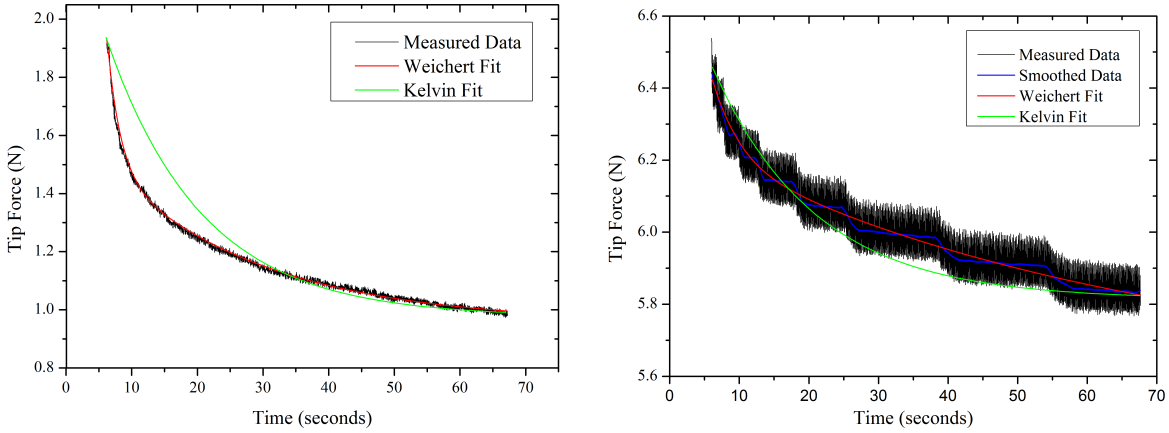

(a) (b)

Figure 5.8: Model characteristic graph, showing (a) the force relaxation (black), the Wiechert model fit (red), and the Kelvin model fit (green) for a low noise signal, and (b) force relaxation (black), Wiechert model fit (red), the Kelvin model fit (green), and smoothed data (blue) for a noisy signal.

The single spring element E_0 describes the initial instant relaxation observed in the response curve, demonstrating the tissues elastic response, as this has no viscous element,

and hence no time coefficient. The spring-dashpot combinations, E_1, η_1 and E_2, η_2 represent the middle and final stage of relaxation. Typically E_1 should be greater than E_2 as the middle stage still exhibits elastic behaviour, but with an increasingly apparent viscous component. Also η_2 should be greater than η_1 leading to a greater time constant τ_2 which is the remaining component of relaxation over the final stage of the response.

5.4.2 Tissue Mechanics Results

Tip forces were calculated and used to plot the data against, to give a closer representation of the forces applied at the tissue tool interface. Observations of the force relaxation (Figure 5.9) shows a clear trend, as the force increases so does the amount of relaxation occurring in the sample, up to a minimum of 2.11 N tip force. From here to 2.55 N tip force, there is a sharp decline in the amount of relaxation observed in the sample, suggesting a critical point in tissue grasping where the mechanics dramatically change.

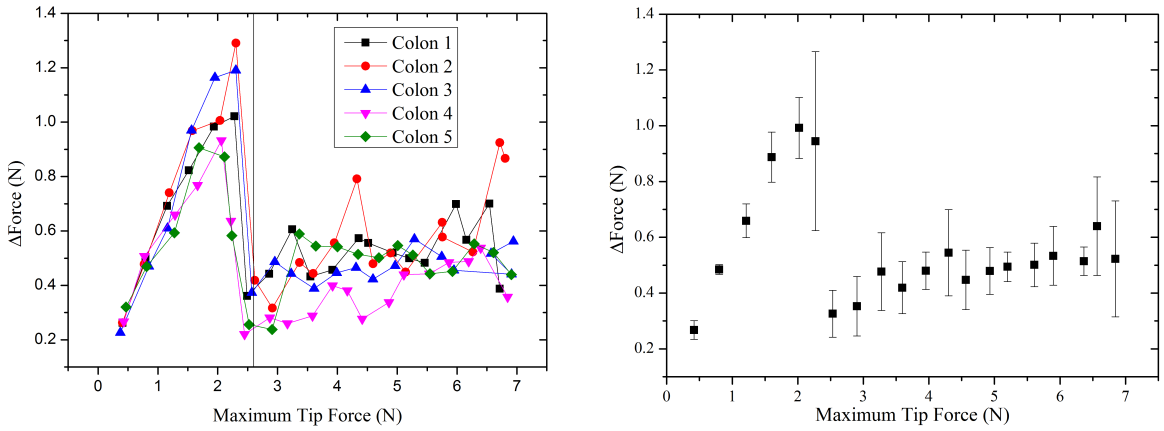

(a) (b)

Figure 5.9: The tissue relaxation (ΔF) for the 60 seconds grasps, of (a) the 5 different colons over the full tip force range (proposed threshold of 2.55 N shown), and (b) the repeatability of results (the mean relaxation for each tip force).

Using the normalised relaxation values (Figure 5.10), this critical force is emphasised, and highlights that this does not occur again at higher tip forces. There is a single point at which the response of the sample changes, and from this point the relative relaxation in the tissue increments again with an increasing force. Also note the points from colon 4 and 5 which lie along this decline, suggesting that the breakdown in the tissue progressively decreases and not in one single sudden drop. This suggests that the change in the tissue structure is not an instant effect, such as the tissue cells bursting, but is a gradual transition, such as pushing an increasing amount of fluid out of the tissue and away from the grasp site. This higher threshold will therefore be used as this is the minimum value beyond which all data exhibit a

force relaxation of less than 20%.

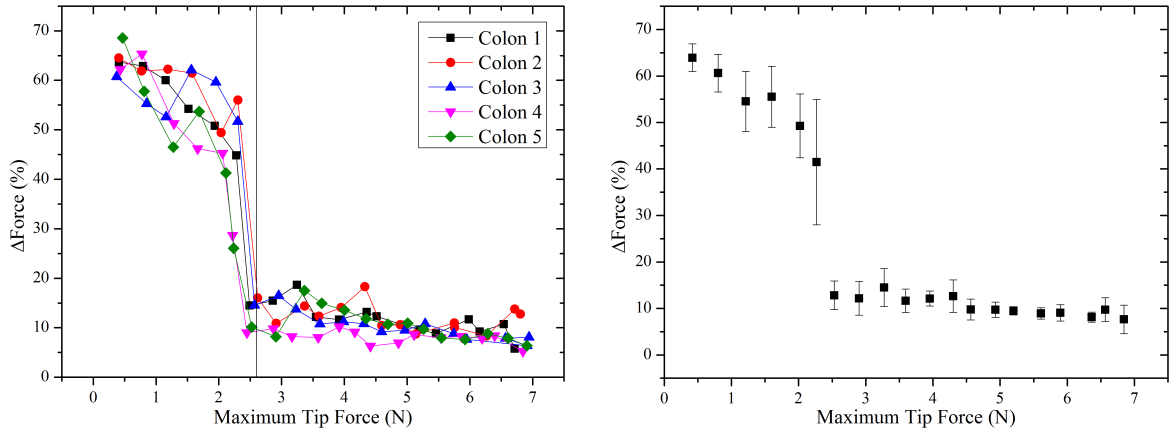

(a) (b)

Figure 5.10: The normalised tissue relaxation ($\Delta F\%$) for the 60 seconds grasps, of (a) the 5 different colons over the full tip force range (proposed threshold of 2.55 N shown)), and (b) the repeatability of results (the mean relaxation percentage for each tip force).

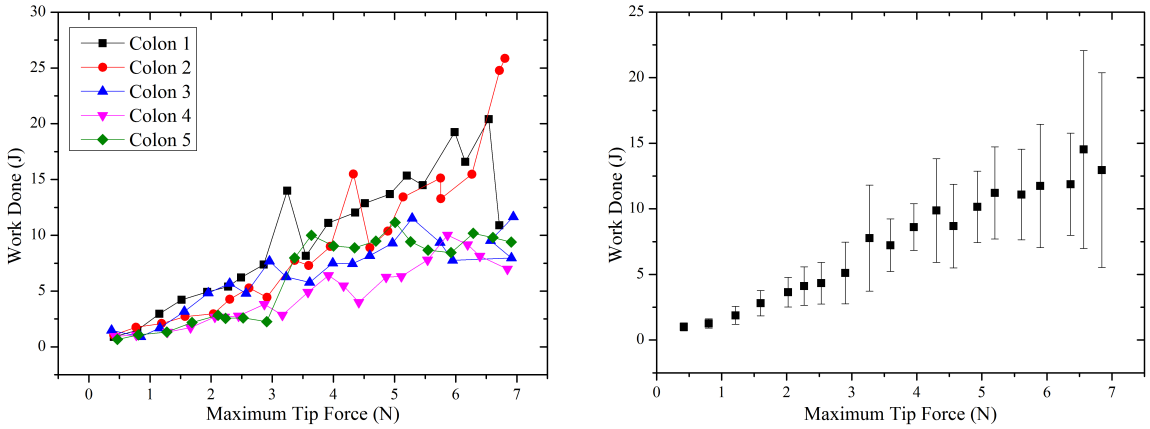

(a) (b)

Figure 5.11: The work done for the 60 seconds grasps, of (a) the 5 different colons over the full tip force range, and (b) the repeatability of results (the mean work for each tip force).

The work was plotted against the maximum tip force (Figure 5.11) and results show that as the applied force increases the work increases, which is to be expected, however past the critical point the response becomes more variable and it is difficult to infer any further information from this. Also the same breakdown in response is not seen in the work data. For increasing tip forces, the work increases, approximately linearly. Because the work is a measurement of the energy dissipated by the grasper into the tissue, when compared to the percentage of force relaxation results (Figure 5.10) these results suggest that as the amount

of energy put into the tissue is increased, the mechanism for energy conversion changes from potential/elastic energy to another (possibly heat, or chemical changes).

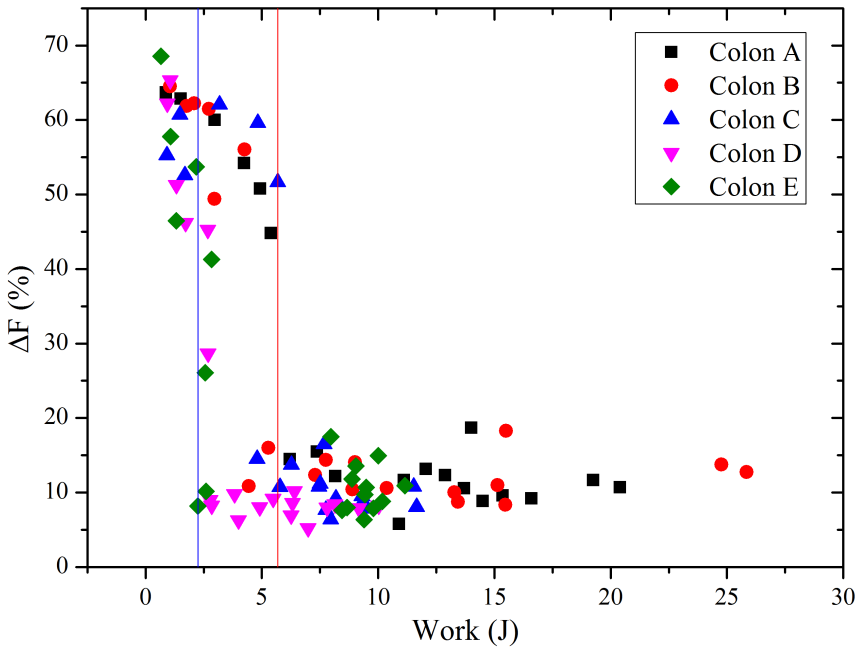

Figure 5.12: The work done by the tissue, plotted against the normalised tissue relaxation ΔF% to indicate the work damage threshold of 5.68 J (red).

The work was then plotted against ΔF% to investigate if there is relation between the work done by the tissue, and the observed relaxation, i.e. how the tissue responds to an increase in grasping energy (Figure 5.12). The results indicate a clear upper threshold (5.68 J), beyond which all levels of work give a value of ΔF% of less than 20%, suggesting that this level of work crushes the tissue layers beyond their limit, where the cell cannot relax any further. Also this highlights how there seems to be an apparent change in how the energy is transferred. Instead of converting the energy into elastic energy, the mechanism seems to change, possibly by releasing heat, or by breaking chemical bonds in the tissue cells. There is a transitional state between 2.25 and 5.68 J where differences in tissue thickness and the composition of the different layers will determine at which point the structure breaks down. Therefore the upper limit will be used to indicate a threshold as beyond this, all samples were affected. From these results, two different thresholds have been established indicating the change in the tissue mechanics. This has been investigated further using the Wiechert modelling (Figure 5.13).

To analyse how the tissue response characteristics are changed over the grasping range, the resulting response parameters have been plotted against the tip force (Figure 5.13). The results from this build on the analysis from the force relaxation data, and the work data, by attempting to show how the tissue response characteristics change, and potentially highlight

which mechanisms change in the transfer of energy.

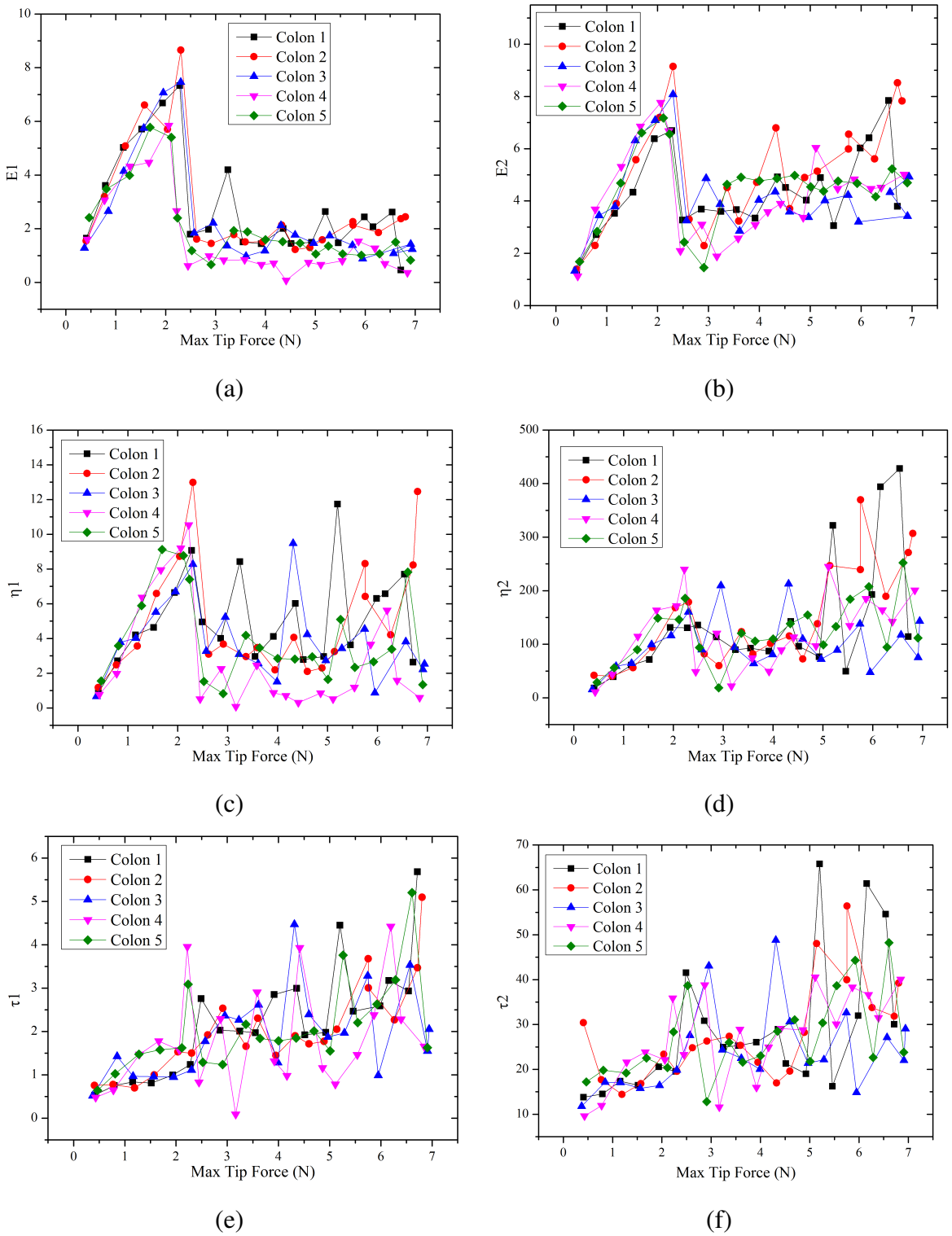

Figure 5.13: The results of the Wiechert modelling parameters plotted for each of the five different colons, over the full force range for each parameter (a) $E1$, (b) $E2$, (c) $\eta 1$, (d) $\eta 2$, (e) $\tau 1$, and (f) $\tau 2$.

The values for η_1 show a similar critical point where the viscosity increases as the applied force is increased, and then suddenly drops. This suggests that by increasing the applied force, the cell structure becomes more rigid [109] until the critical point where the structure is ruptured, the cells are no longer held together and there is little resistance against the grasper. Similarly with η_2 up to the critical point the viscosity is increasing, suggesting the cell structures are responding by becoming more rigid. Pass the critical force, the cells are no longer held together, as with the histology results (Figure 5.30a), and the effective viscosity drops. However in this case, as the force increases, there are points where the viscosity rises again, suggesting that deeper layers of the tissue are also responding to the applied force (Figure 5.27b). Using the values of E_1, E_2 and η_1, η_2 respectively (Figure 5.13), the time response, τ_1 and τ_2 were calculated (Equation 5.2). The results of the time constants τ_1 and τ_2 similarly show an increase up to the threshold of 2.11 N where beyond this the results are varied and difficult to predict. As with the viscosity results, this could be due to the break down of the tissue structures and unique for each sample.

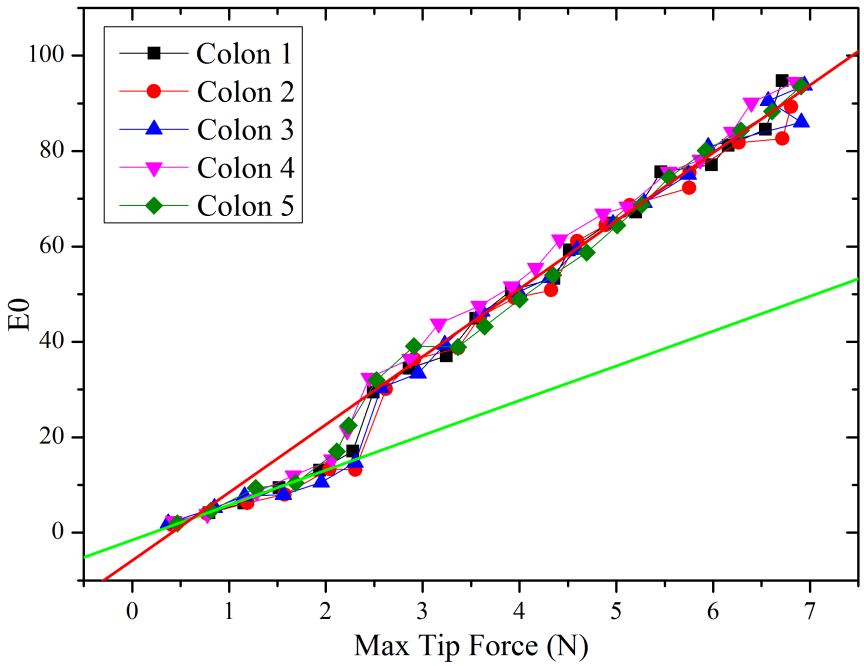

Figure 5.14: The results of the Wiechert modelling plotted for each of the five different colons, over the full force range for $E0$.

The results of E_0 show that the relative stiffness of the tissue increases as the applied force is increased, showing that the tissue is becoming increasingly rigid in response to grasping. However there is a jump at the critical force suggesting that due to the drop in viscosity in other structures the remaining tissue layers become increasingly rigid to counteract this. This also supports the observations of the work analysis in that the energy dissipation mechanism

changes beyond the threshold. This is highlighted in the difference between the initial stiffness gradient of E_0 and the gradient beyond the threshold, showing the inherent change in the tissue's characteristics.

Observations of the tissue samples immediately after grasping showed that for increasing forces, the depth and visibility of the grasper fenestration indentation increases. A typical control sample (Figure 5.15a) shows the undulating surface profile of the porcine colon tissue, with a similar result for the 0.41 N grasp (Figure 5.15b) showing no visible signs of trauma or fenestration indentations.

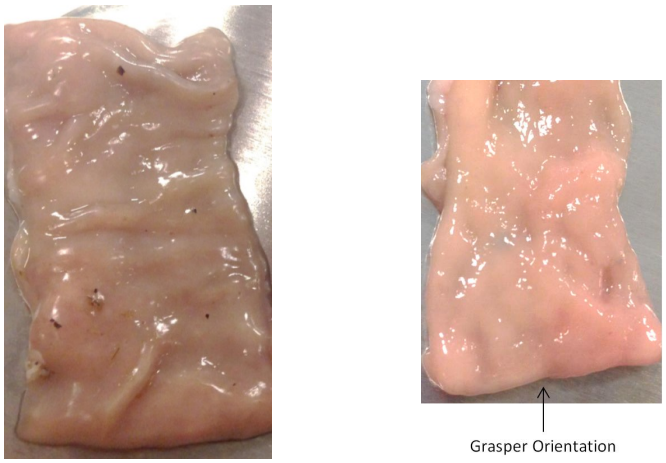

(a) (b)

Figure 5.15: Porcine tissue sample images, showing (a) the control sample surface with typical undulations, and (b) a 0.41 N grasped section showing no signs of trauma.

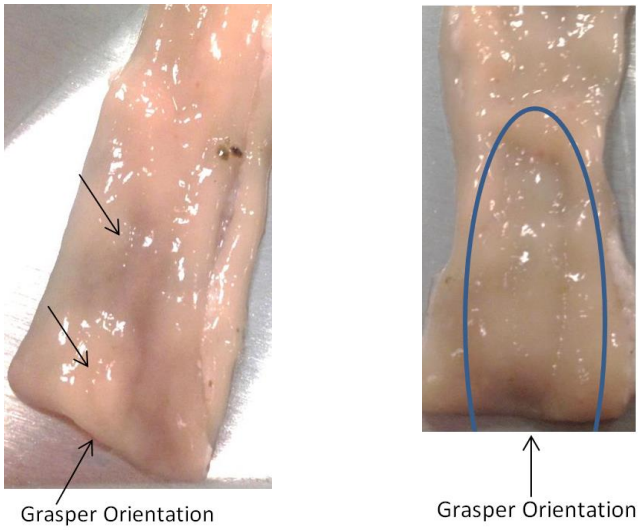

(a) (b)

Figure 5.16: Porcine tissue sample images, showing (a) a 0.84 N grasped section with slight fenestration indentations, and (b) a 1.62 N grasped section again with signs of grasper fenestration indentations.

For the 0.84 N sample (Figure 5.16a) slight fenestration indentations can be seen, and similarly with a higher grasping force of 1.62 N, the same degree of indentation can be seen.

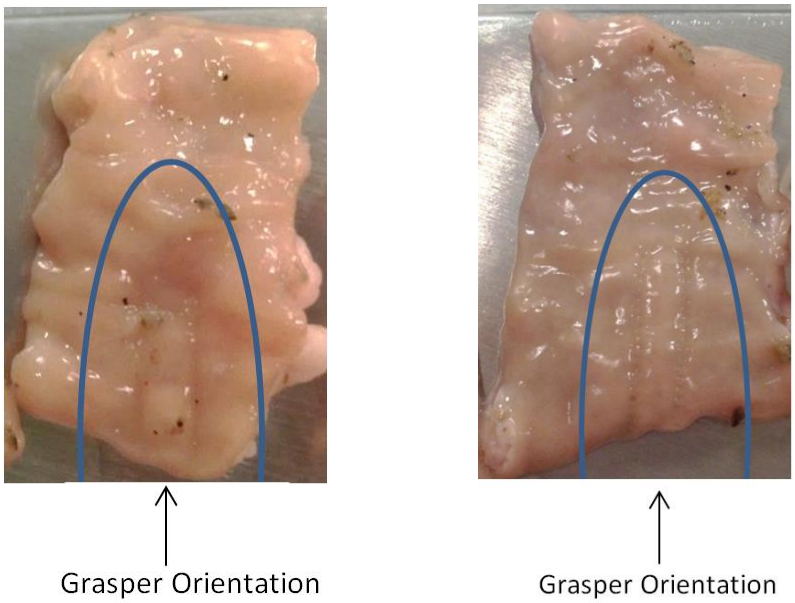

Figure 5.17: Porcine tissue sample images showing (a) a 5.55 N grasped section with clear deep fenestration indentations, and (b) a 6.95 N grasped section again with pronounced grasper fenestration indentations.

For a grasping force of 5.55 N (Figure 5.17a) up to 6.95 N (Figure 5.17b) there are clear and deep indentations from the grasper fenestrations. Below 5.55 N it is difficult to distinguish between samples based on indentations alone.

5.5 Histology Damage Investigation

The histological investigation was used to highlight cellular damage, where the cell layers are disrupted or compressed. The rig was used to grasp the colon samples, which were then stored in a formaldehyde solution and processed. The processing was performed by Jenifer Barrie, a surgeon working in collaboration with this project. This involved her setting, staining, and cutting the samples, which were then photographed. The damage analysis and grading were performed by myself, after receiving these images.

5.5.1 Histology Testing Methodology

A typical colon sample is comprised of five mains layers (Figure 5.18). The outer layer is the longitudinal muscle which runs along the length of the colon held in place with connective tissue which surround the whole colon. The circular

muscle layer wraps around the colon, providing the main motion during peristalsis (although this is also assisted by the longitudinal muscles). The submucosa is a layer of connective tissue which provides support to the mucosa layer, and also secures this to the muscle layer. The mucosa layer comes into contact with digested food in the intestinal lumen. There is also occasionally a thin layer of connective tissue which surrounds internal viscera, but damage and removal to this is not severe enough to cause concern, and is therefore not used as a measure of damage.

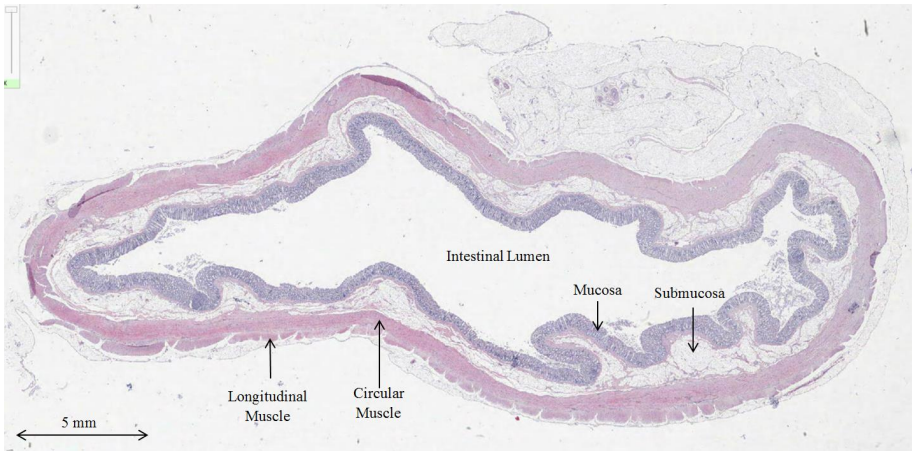

Figure 5.18: A cross section of a histological tissue sample of porcine colon for 3.00 N grasping force over 5 seconds, highlighting the mucosa, submucosa, circular muscle, and longitudinal muscle, typically surrounded by connective tissue.

Testing was performed on five different cylindrical porcine colon specimens (A - E). The linkage force targets were 10, 20, 40, 70 and 100 N (chosen to give a spread of measurements and the maximum 100 N), with grasping times of 5 and 60 seconds to simulate a quick manipulation grasp, and a longer retraction grasp. By ensuring that the response has reached a steady state (equilibrium) gives for a higher repeatability of measurements, which has been investigated between the 5 and 60 second grasps. One colon (E) was used for both 5 and 60 second tests. Due to the long processing time for the histological analysis, specific forces were chosen to link to the previous *in-vivo* analysis linkage forces (section 3.8.3). 10 and 20 N relate to the lowest and average observed during the bowel run manipulation tests. 40 N relates to the approximate maximum bowel run force and the lowest colon grasp force. 70 N was observed as the approximate maximum colon grasping force, and finally 100 N was used as an absolute limit which was physically possible, to account for all potential values. Before each grasp the grasper fenestrations were coated with a thin layer of Indian ink to highlight the area which had been grasped, as with the *in-vivo* work. Indian ink was used as it does not affect the chemistry of the sample, survives the histological tissue processing and can be used to identify the grasped area in histological analysis. A control sample for each colon was also preserved, using an ungrasped section, to highlight what the structure

would look like unaffected and show any pre-existing abnormalities. After each test was performed, the sample was placed in a falcon tube of formaldehyde solution to preserve the tissue for histological analysis. The samples were then rehydrated and stained using Haematoxylin and Eosin to highlight the cell architecture, and to emphasise physical tissue damage. The samples were then sliced to give the cross section so any damage could be observed (Figure 5.19 and 5.20) [240].

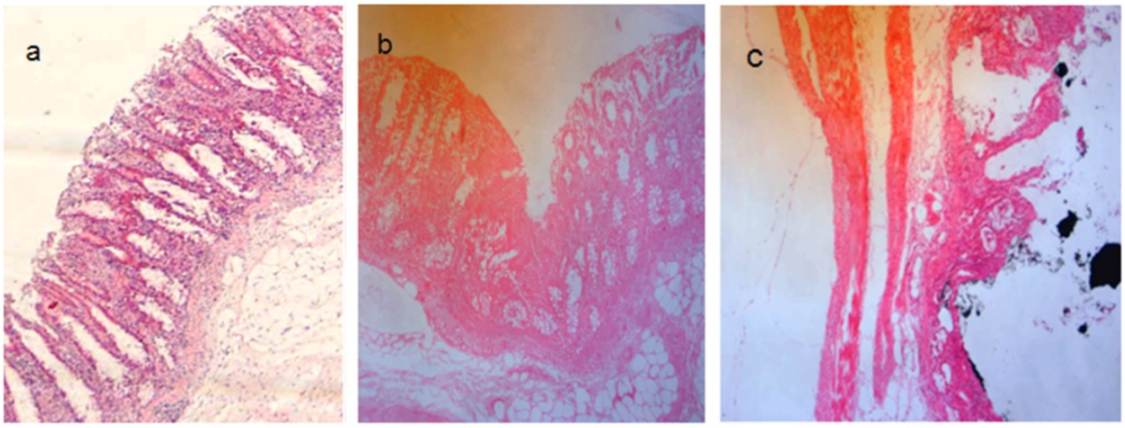

Figure 5.19: Examples of histological damage for single layer tissue grasping, showing (a) a control area of the mesocolon, (b) a grasped section of mesocolon with mild damage, and (c) severe mesocolon damage with areas missing or severely crushed [240].

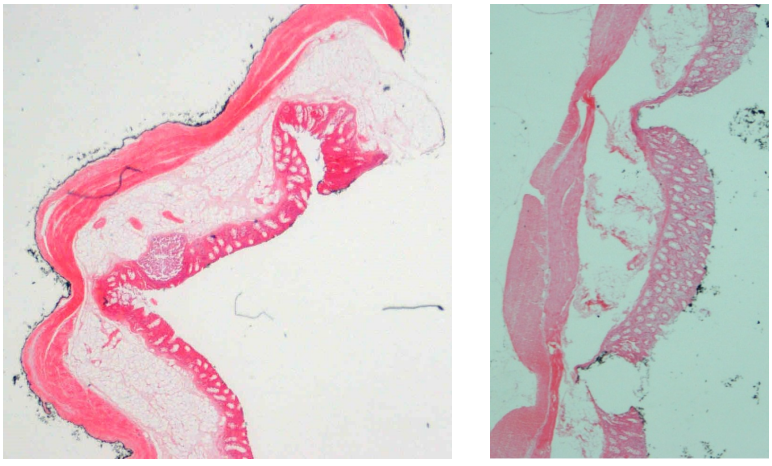

(a) (b)

Figure 5.20: Examples of damage across a single layer porcine colon grasp, showing (a) crushed section where grasper made contact, (b) severe damage with removal of part of the mesocolon where grasper made contact [240].

5.5.2 Mechanical Modelling Results with Supporting Histology

The force measurements were converted to the tool-tip values using the previously developed model (Section 3.4) to give an estimate of the forces occurring at the tissue tool interface. The ΔF values were then plotted against the maximum applied tip forces for 5 seconds (Figure 5.21a) and 60 seconds grasp time (Figure 5.22a).

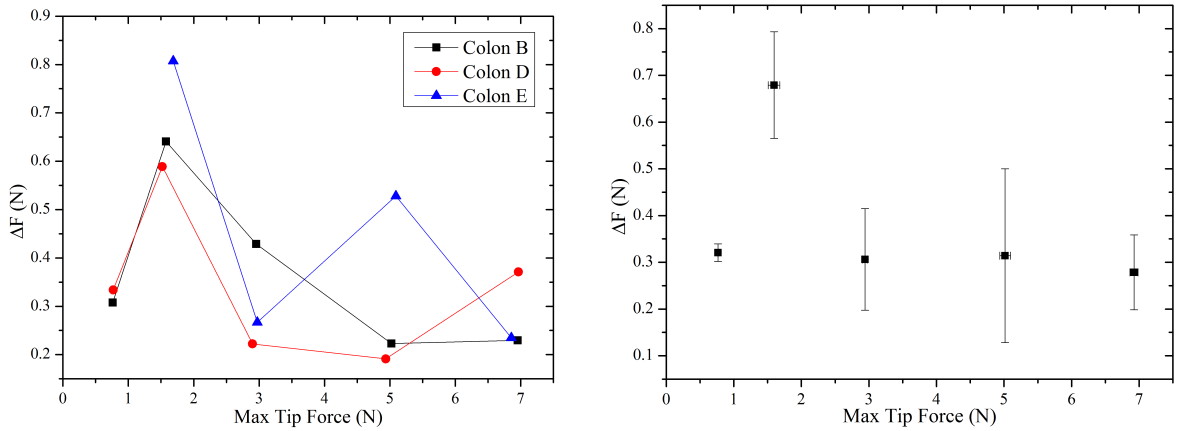

(a) (b)

Figure 5.21: The force relaxation, ΔF, plotted against the maximum applied tip force for the 5 seconds grasps, for (a) individual colon sample trends, and (b) the mean and standard deviation at each force.

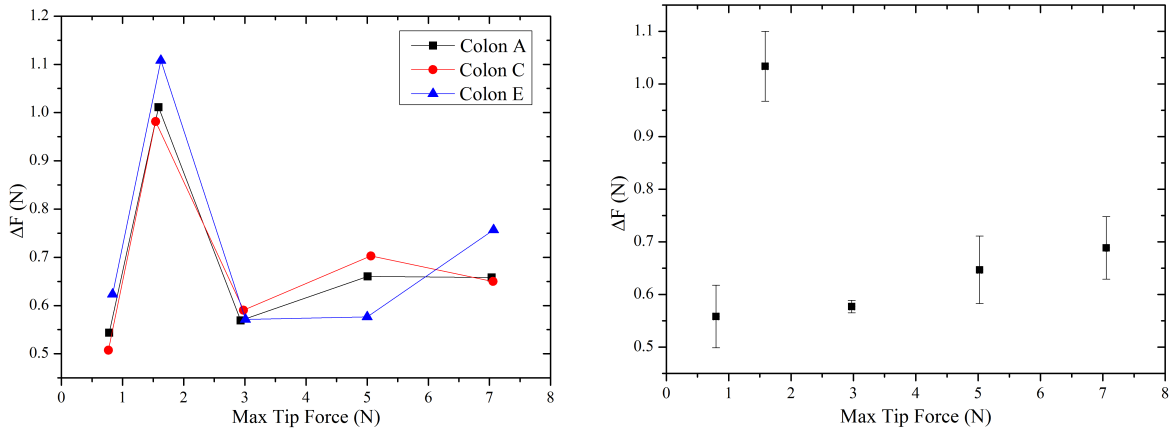

(a) (b)

Figure 5.22: The force relaxation, ΔF, plotted against the maximum applied tip force for the 60 seconds grasps, for (a) individual colon sample trends, and (b) the mean and standard deviation at each force.

There is a higher repeatability for the 60 seconds grasps over the five seconds grasps. For the lowest applied force, there is relatively little relaxation compared to the second force. This

shows the highest force relaxation. Beyond this point the amount of relaxation is relatively small. This could link to disruption to the tissue layers. The force relaxation was normalised against the maximum applied force for each grasp to show the percentage of force relaxation and give a clearer representation. These were then plotted against the maximum tip force values for 5 (Figure 5.23a) and 60 seconds (Figure 5.24a).

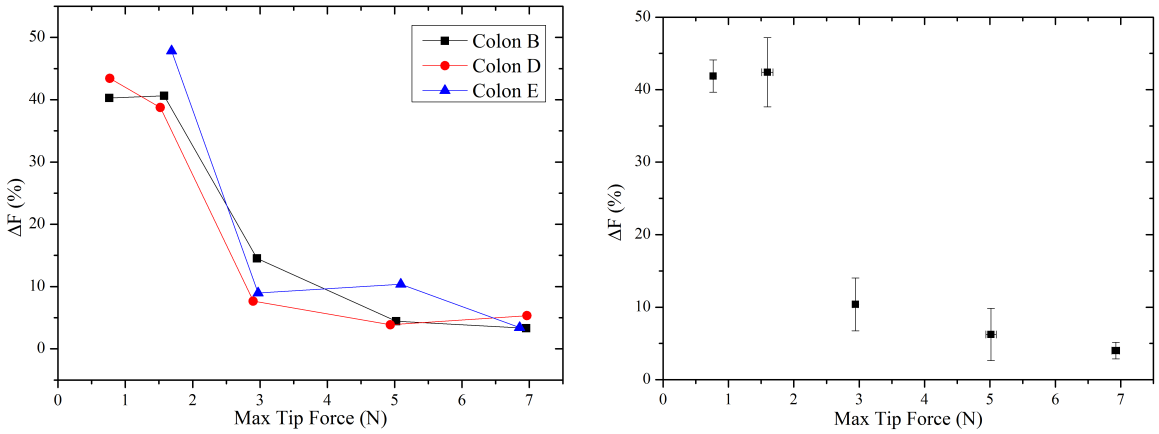

(a) (b)

Figure 5.23: The normalised force relaxation, ΔF%, plotted against the maximum applied tip force for the 5 seconds grasps, for (a) individual colon sample trends, and (b) the mean and standard deviation at each force.

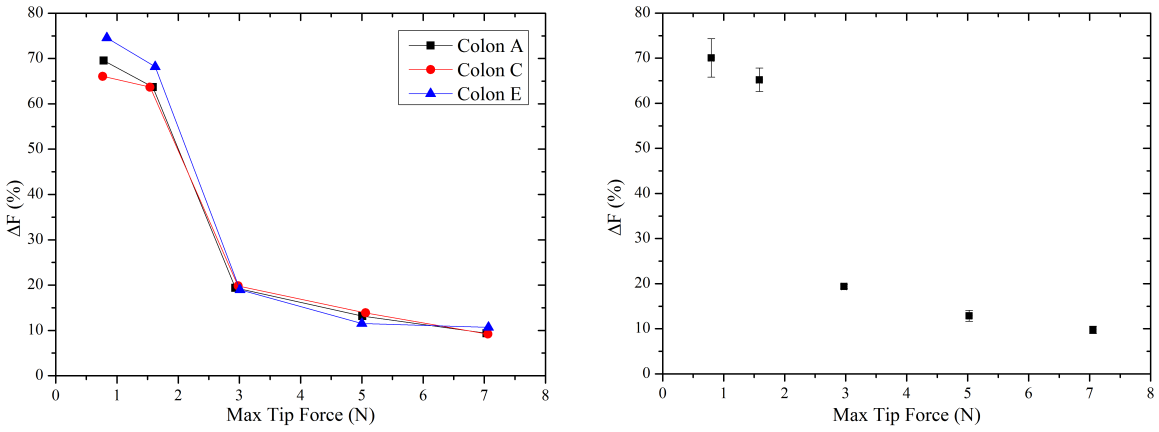

(a) (b)

Figure 5.24: The normalised force relaxation, ΔF%, plotted against the maximum applied tip force for the 60 seconds grasps, for (a) individual colon sample trends, and (b) the mean and standard deviation at each force.

Again a higher repeatability can be seen for the 60 seconds grasps. It is apparent that beyond the second applied force, the percentage of force relaxation observed drops suddenly, suggesting that an excessive amount of compression is placed over the sample, so little

additional relaxation can occur. Each value of work was plotted against the maximum applied tip force for five (Figure 5.25a) and 60 seconds (Figure 5.25b).

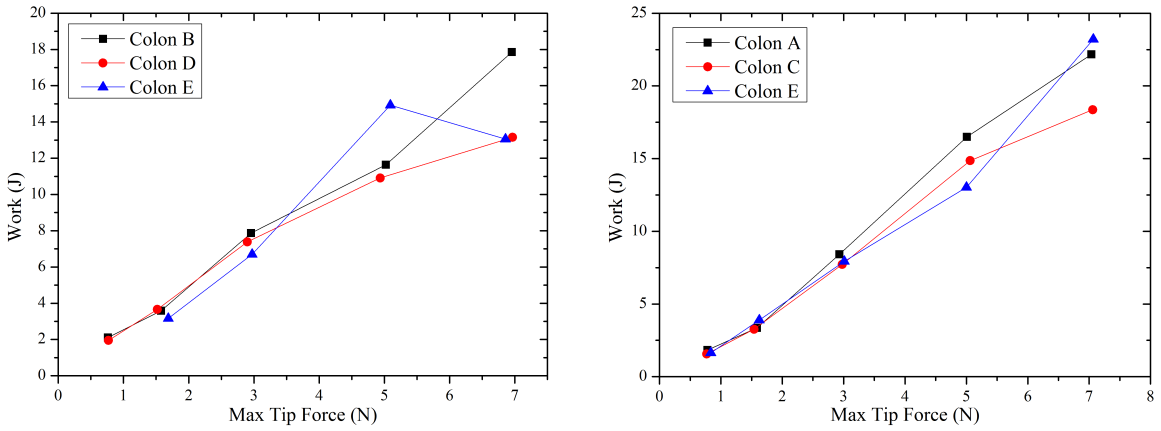

(a) (b)

Figure 5.25: The work done by the tissue, plotted against the maximum applied tip force for (a) the 5 seconds grasps, and (b) the 60 second grasp.

Once again there is a higher repeatability of results for the longer grasps, but also beyond the third force target, the repeatability drops suggesting that the the relaxation in the tissue structures is a reliable measurement until excessive compression is applied, disrupting the tissue layer structures. Exactly how these layers are disrupted will affect the response and will vary with each test, leading to poor repeatability. The ΔF% measurements have been investigated as a function of the work done by the tissue (Figure 5.26b). Time does not affect ΔF% beyond work threshold, as outlined in the previous investigation. Below this point less relaxation is observed in tissue.

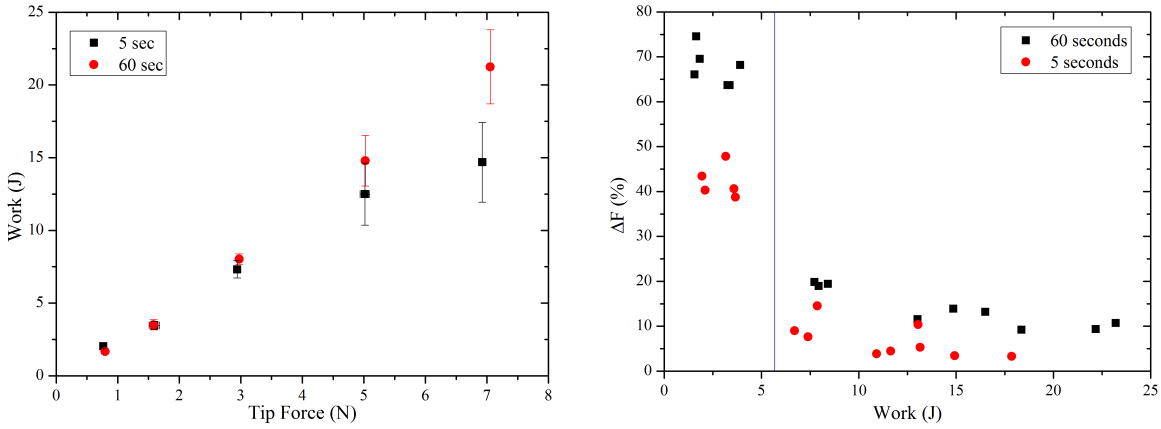

(a) (b)

Figure 5.26: The work done by the 5 and 60 second grasps; (a) plotted against maximum tip force, with average and standard deviation, and (b) plotted against ΔF%.

Each test sample from colon E was processed [240], ready for slicing and photographing. A number of sample images were not collected due to the poor outcome of the histology processing. Also 1 repeat of the 10 N, 5 second grasp was not collected due to the limited length of the porcine colon, E.

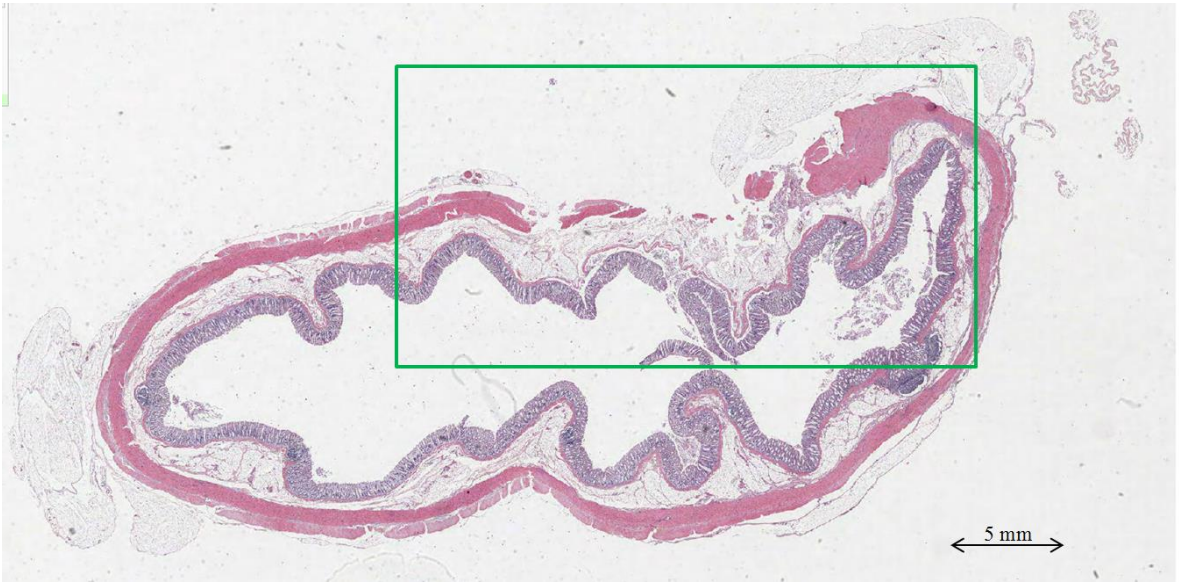

(a)

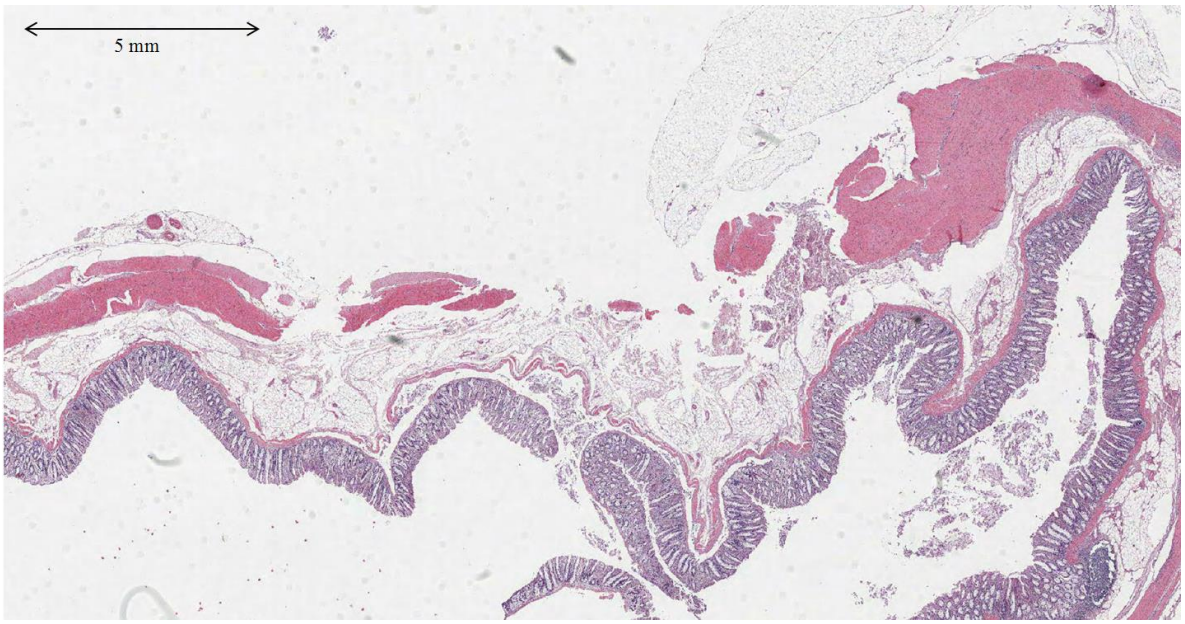

(b)

Figure 5.27: A histology sample image of the 6.95 N, 5 seconds grasp, showing (a) the full cross sectional area, with trauma site highlighted in green, and (b) a higher magnification image of the trauma site showing full damage to longitudinal and circular muscle, with minor damage to the submucosa.

It can be seen from the 6.95 N (5 seconds) histology image (Figure 5.27a) that at this

force, damage is induced in the longitudinal and circular muscle layers, with encroaching trauma to the submucosal layer (Figure 5.27b). It can be inferred that this degree of damage, at least, would also occur in the 6.95 N (60 seconds) grasp.

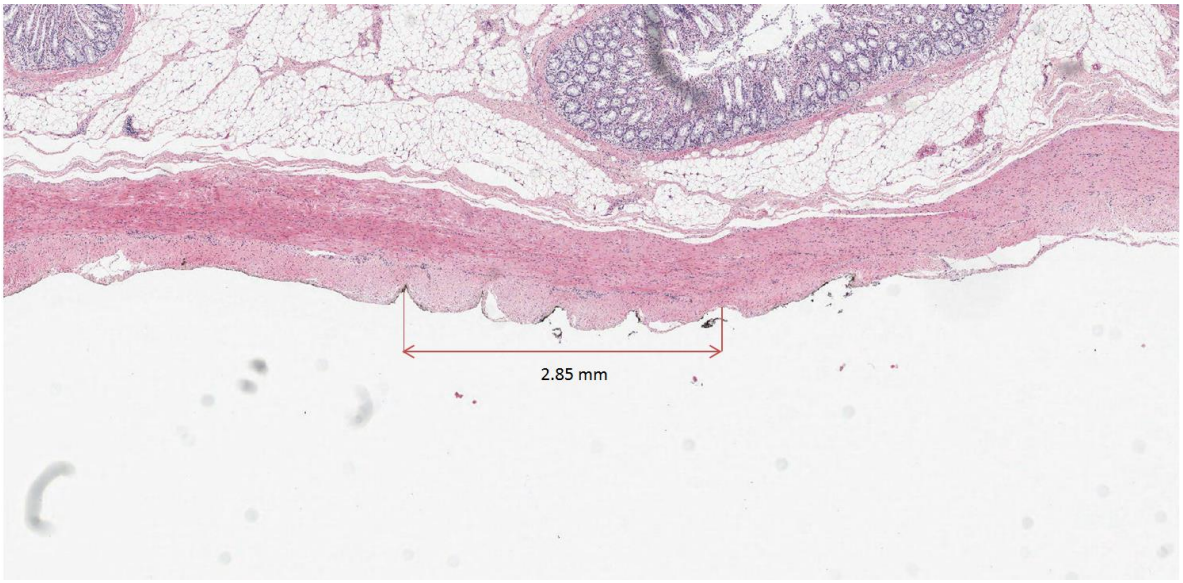

(a)

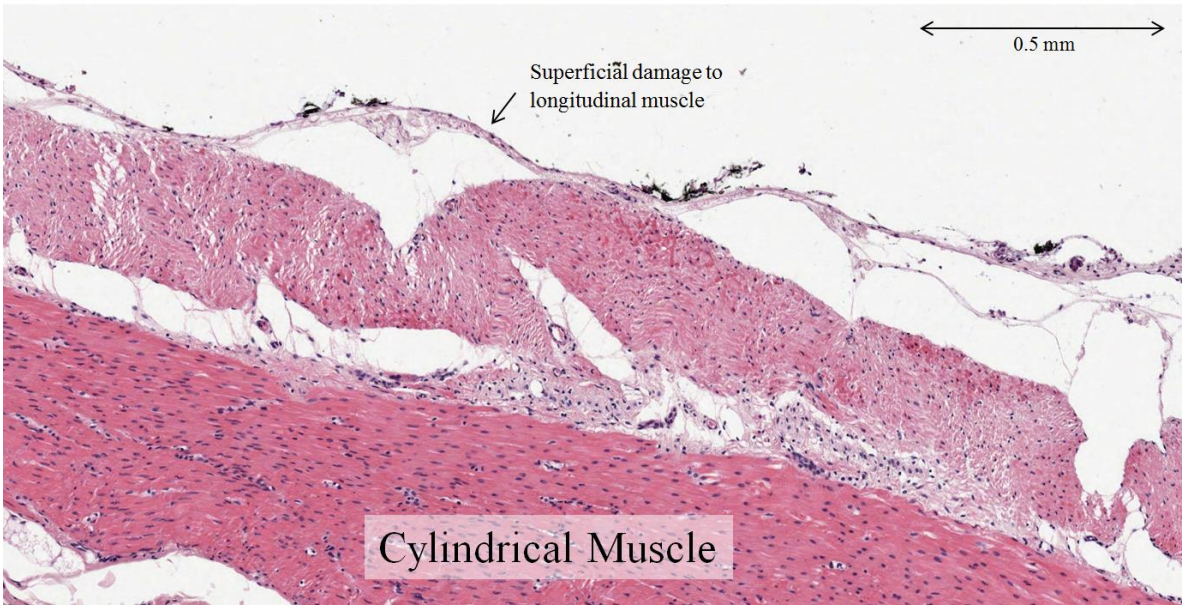

(b)

Figure 5.28: A histology sample image of the 5.09 N, 5 seconds grasp, showing (a) the inked fenestration indentations, and (b) distruptions to the longitudinal muscle.

There are possible indentations from the grasper fenestrations seen, following signs of Indian ink for the 5.09 N grasping over 5 seconds (Figure 5.28a). Over the full indented section (2.85 mm) there are 4 distinct indentation spaces, which give an average spacing of 0.72 mm. The fenestration spacing as measure on the grasper is 0.86 mm spacing. Although

this is not the same, it is of the same order of magnitude. The histological tissue processing would likely affect this, and the sample has likely been unintentionally reshaped when manipulated. Due to the presence of the Indian ink, it is possible to deduce that the indentations are made by the grasper fenestrations, and that this has been made more prominent by the force at which the tissue has been grasped, and is not seen elsewhere.

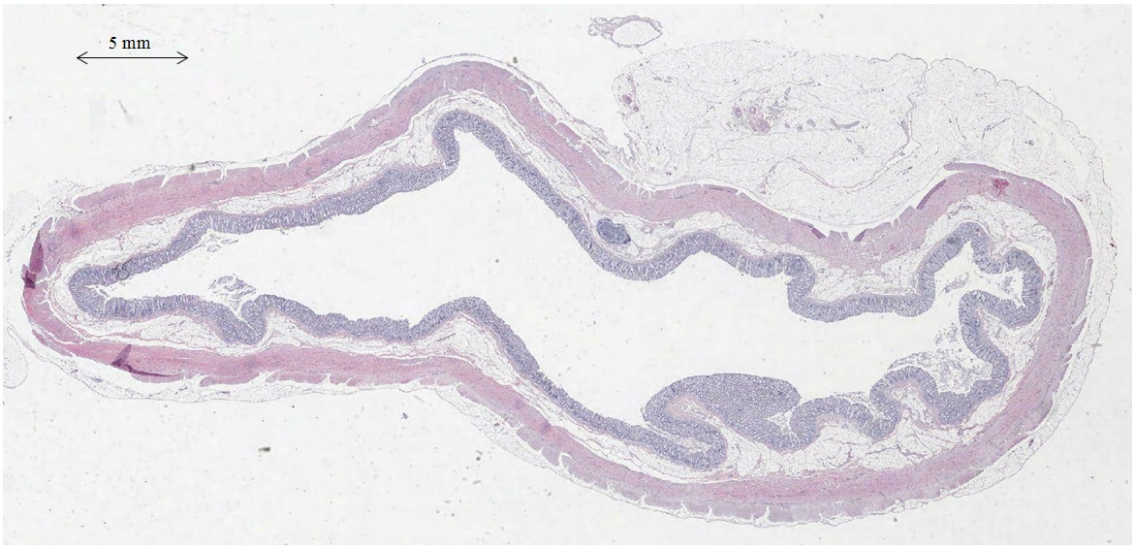

Figure 5.29: The full cross section of a 3.00 N grasp over 5 seconds showing no evidence of Indian ink and no clear indication of damage due to grasping.

For the 3.00 N grasping, little evidence could be seen of trauma for the 5 second duration, including a lack of Indian ink. This is most likely similar to the previous discrepancy whereby the cross section has missed the grasped area so nothing can be seen. For the 60 seconds grasp there are slight traces of the ink, and potentially showing slight agitation to the top layer of the longitudinal muscle layer (Figure 5.30a). On the opposing side to the ink (inferring that this site was also grasped by the opposing jaw) there is evidence that the typical layer of connective tissue, which usually covers the longitudinal muscle has been removed (Figure 5.30b).

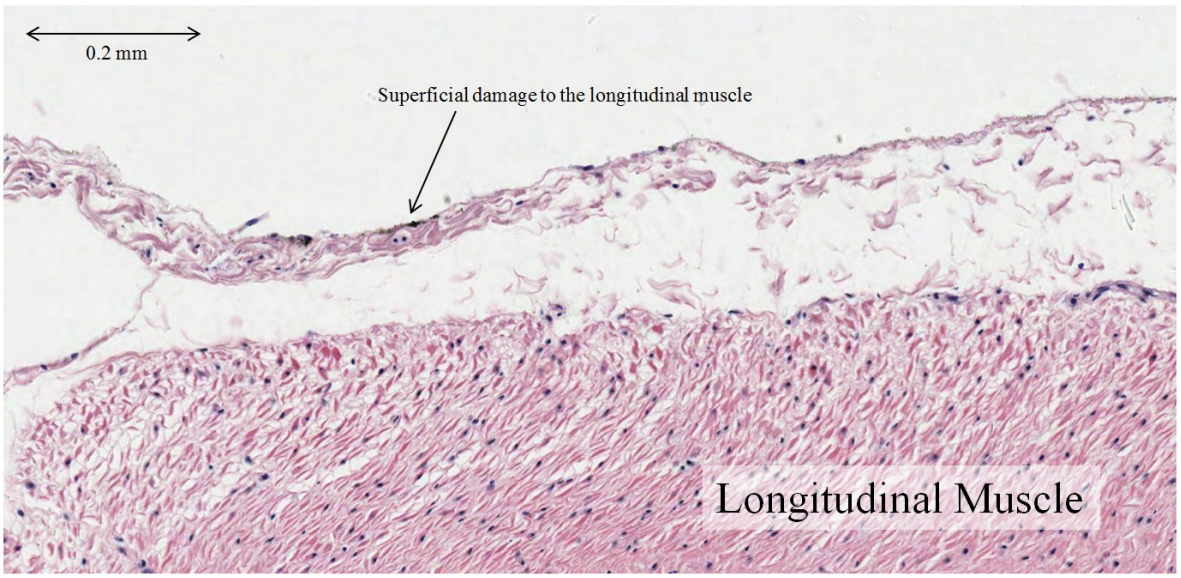

(a)

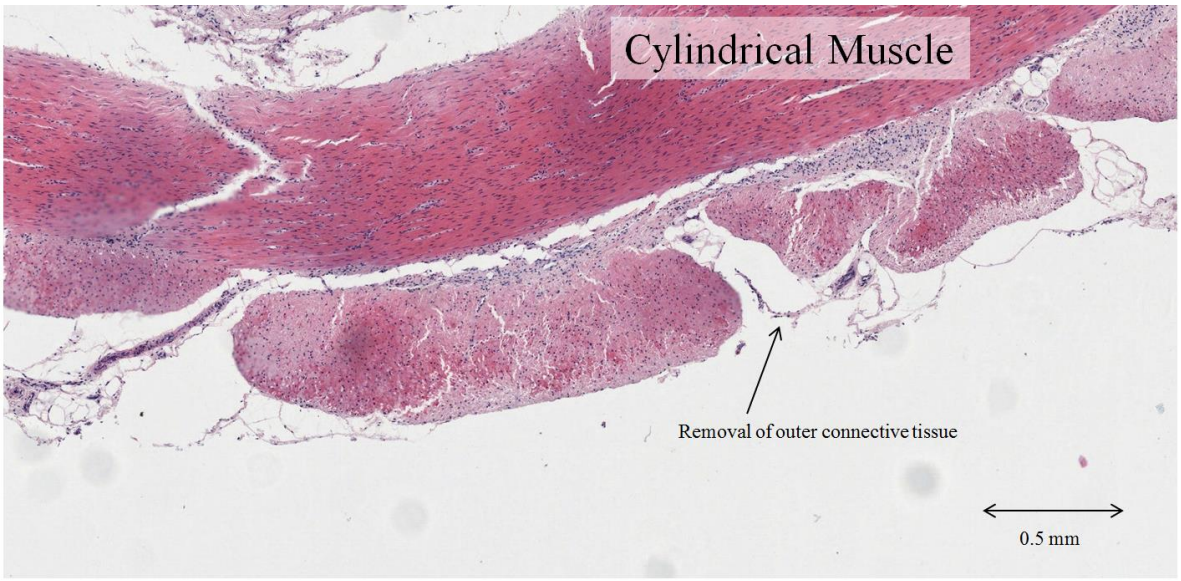

(b)

Figure 5.30: A histology sample image of the 3.00 N, 60 seconds grasp, showing (a) some trace of Indian ink on the top layer of longitudinal muscle, which appears to have been agitated, and (b) the removal of the connective tissue on the opposing side to the ink.

For the 0.84 N grasps with a 5 second duration, there initally appears to be a large amount of trauma (Figure 5.31a). However this is likely to be an unfortunate result of the sample processing, and not indicative of the induced damage. Due to this level of damage not occurring at the higher forces, and traces of the Indian ink found elsewhere (Figure 5.31b), this *'damage'* can be ignored. I can be noted however, that the connective tissue which has signs of ink, shows little damage, especially to the muscle and mucosa layers.

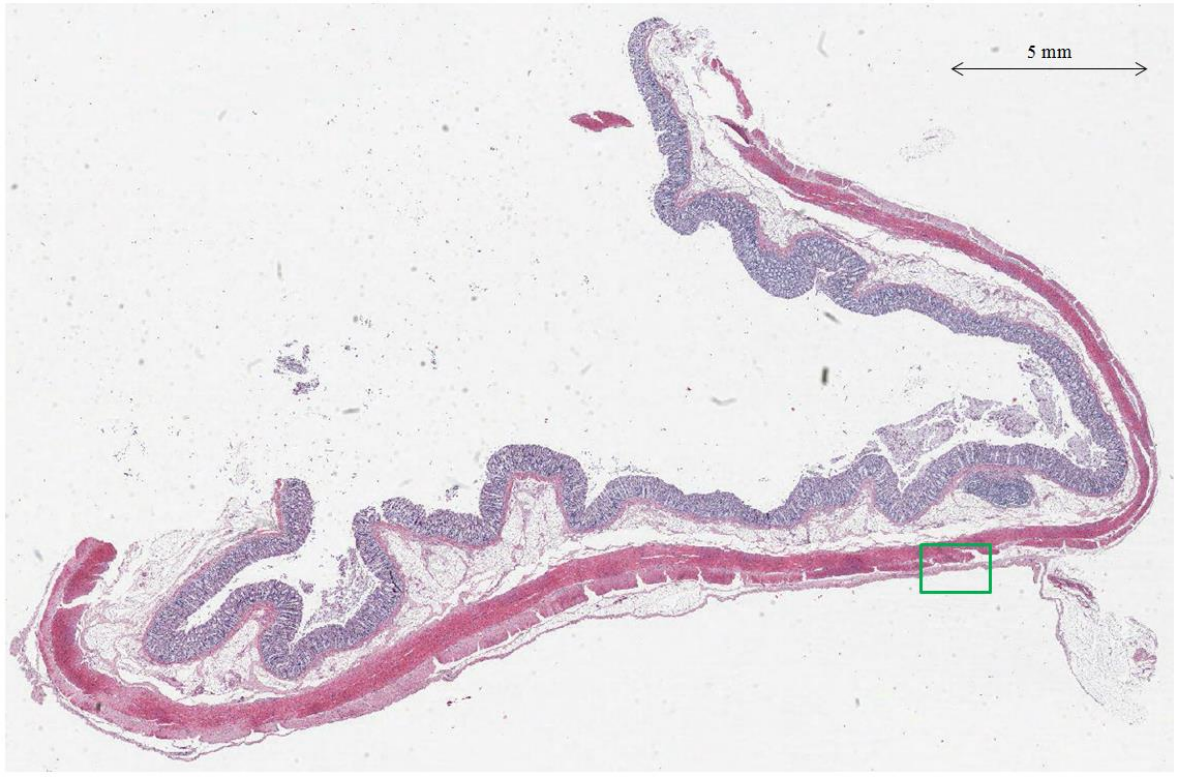

(a)

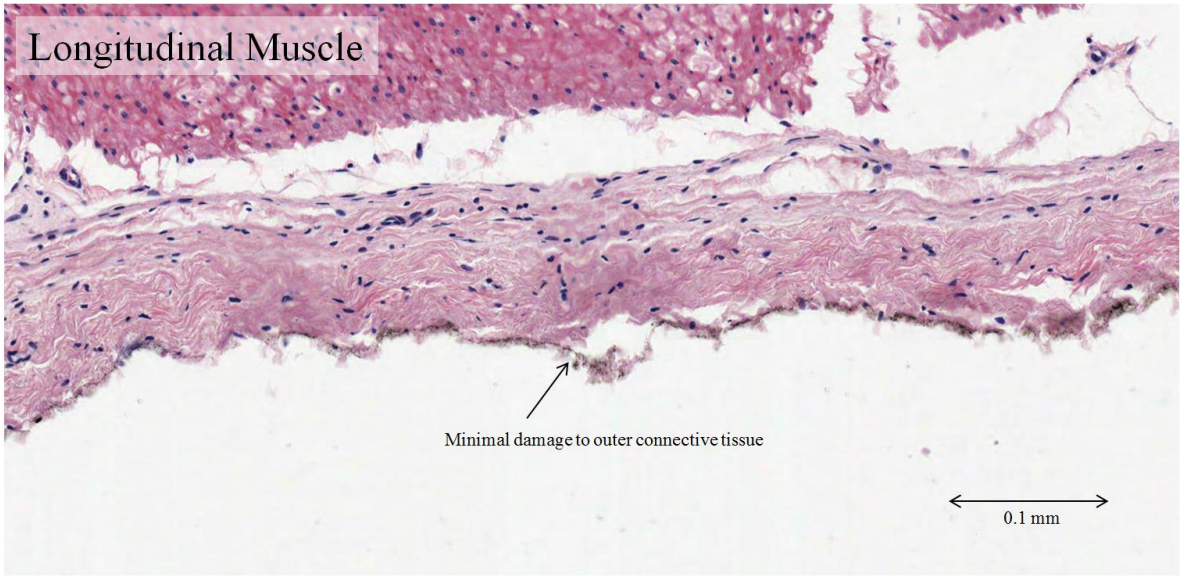

(b)

Figure 5.31: A histology sample image of the 0.84 N, 5 second grasp, showing (a) the full cross sectional area, with the inked site highlighted in green, and (b) the grasped connective tissue showing negligible damage.

From the histological analysis, a table has been generated to show the available histological samples and indicate the damage severity of each.

Tip Force (N)	Colon E (5 s)	ΔF %	Colon E (60 s)	ΔF %
0.84	–	–	✓	74.54
1.62	✗	47.82	✗	68.20
3.00	✓	8.98	✓	18.98
5.09	✓	10.37	✓	11.54
6.95	✓	3.43	✗	10.71

Table 5.1: Table of histological samples shown against relaxation and colour coded to show histological damage, with green (no visible damage), orange (superficial distruption/compression), red (severe damage), and grey (inconclusive).

The results show a significant difference in tissue damage between the 0.84 N grasping force of little or no damage for a 60 second grasp, to the 6.95 N grasping force with destruction of both muscle layers and damage to the submucosa for a 5 second grasp. It has been inferred that for a shorter grasping time at 10 N there would be a similar result of no damage to the tissue layers, also for the a longer grasping time at 100 N there would be a similar severe level of damage to the tissue layers. For the 3.00 N grasping over 60 seconds, slight disruption was observed of the top layer of longitudinal muscle, and for the 5.09 N grasping over 5 seconds, severe indentations were witnessed to this layer.

5.6 Conclusion

Ex-vivo porcine colon tissue testing was performed using the previously developed test rig (section 4). For each colon used, only one repeat for each force could be performed due to the limited length of tissue samples. Samples were grasped and the tissue response mechanics were investigated, to develop a faster method of tissue analysis and to give direct quantitative measures of damage. Samples were also grasped and then preserved for histological analysis to investigate damage on a cellular scale, to support findings from the mechanical investigation. Analysis of the force data highlighted a critical force point beyond which the relaxation in the tissue drops. This characteristic was also shown in the mechanical analysis, using a fitted Wiechert model against the force relaxation responses to show the variation in the mechanical properties of the tissue. This also showed how the modelled viscosity and elasticity of the tissue changed as the force is increased. Over the critical force range 2.11 - 2.55 N (25 - 35 N linkage force) the viscosity of the tissue drops significantly. Similarly the tissue mechanics were investigate as a function of the work done, highlighting another threshold of 5.68 J. The duration of grasping was also considered and showed that beyond this threshold the response showed no clear difference between 5 and 60 second grasps.

This range covers forces and work typically used in *in-vivo* manipulations (section 3.8.3), indicating that surgeons are generally likely to disrupt the mechanical behaviour and as a result increase the likelihood that the tissue will perforate. From observations of images of the tissue surface immediately after grasping, it is not clear how the tissue has been affected, and is difficult to distinguish between varying grasp forces, except for much higher forces 5.55 - 6.95 N (80 – 100 N linkage force). These findings represent a novel approach to tissue damage quantification by using a typical laparoscopic tool with which to apply the force. Observation of the histology analysis highlighted the degrees of damage induced in tissue samples over the applied force range 0 - 6.95 N (0 - 100 N linkage force). Low tip forces, around 0.84 N, showed no damage to any of the tissue layers, including the outer layer of connective tissue. As the force was increased to around 3.00 N, slight disruptions could be seen in the surface of the longitudinal muscle relating to the mechanical changes observed previously. At 5.09 N there were clear signs of damage where the grasper fenestrations made significant indentations in the longitudinal muscle. At 6.95 N there was substantial tissue damage where the longitudinal and circular muscle had been completely destroyed and the submucosal layer has been exposed. These threshold have been tabulated (Table 5.2), allowing for comparison to measured data.

Threshold Damage Type	**Threshold**	**Description**
Mechanical Force	2.55 N	The applied tip force beyond which the mechanical response of the tissue breaks down.
Tissue Work	5.68 J	Amount of work done by the tissue, above which the mechanical response of the tissue breaks down.
Histology	5.55 N	The applied tip force beyond which the tissue layers are destroyed.

Table 5.2: The observed thresholds from *ex-vivo* tissue analysis.

These tests have shown the difficulties in using histological analysis as a means of determining tissue damage. These include the subjective nature when observing the samples, but also the inconsistency with sample processing, and the often low yield (Table 5.1).

Chapter 6

Intelligent Grasper Damage Prediction

6.1 Introduction

As indicated in the literature review (section 2.4.2), previous research has investigated multi Degrees Of Freedom (DOF) grasper designs to measure *in-vivo* surgical task parameters such as grasping and retracting forces, as well as handle positions [160]. The data (typically grasping, retraction and tip force, handle motion, and shaft rotation) for each surgeon (trainee or expert) is then compared to other users performances to give an indication of surgical skill. The work has not then been used to investigated tissue damage caused during particular tasks. Other investigations have aimed to measure the amount of trauma caused to tissue samples (liver, colon, etc) by varying the structure used to compress tissue, which relates to grasper geometry and fenestration design [53]. However this work has not been linked to *in-vivo* measurements. Investigations into *in-vivo* tissue characterisation involved the use of a Motorized Endoscopic Grasper (MEG) to control the force applied by a laparoscopic grasper, and measure the tissue response. However this work focusses solely on measuring the tissue properties and does not quantify this against typical grasping, as the device removes the ability to perform natural grasping [100]. Previous work carried out in this project has investigated the typical grasping forces found in surgery (section 3.8.3), which have then advised *ex-vivo* testing methodologies to show how those grasping forces can induce tissue damage to porcine colon samples (section 5).

Drawing from the previous findings (chapter 5), this chapter aims to develop an algorithm to predict the level of tissue damage caused during *in-vivo* surgical grasping, based on the grasping force and work done, allowing for analysis of grasping data to help reduce or prevent iatrogenic tissue damage. The algorithm can be used post-operatively, on data already collected, and in real-time, but the implementation of the algorithm differs slightly for both these applications. Combining this damage algorithm with the previously designed Instrumented Grasper provides the basis of the Intelligent Grasper.

6.2 Development of the Tissue Damage Algorithm

To develop the algorithm, firstly a system diagram was drawn to highlight the desired inputs and outputs (Figure 6.1). The algorithm will use inputs from the force-time and

displacement-time data along with the thresholds previously found from *ex-vivo* porcine tissue testing (section 5). The mechanical threshold force (2.55 N tip force) relates to the critical point at which the tissue resistance breaks down found from the mechanical modelling, the work threshold (5.68 J) is found from the hysteresis graph and indicated the damage caused from work done by the tissue, and the structural threshold (5.55 N tip forces) is found from the histological analysis where significant damage is done to the tissue layers.

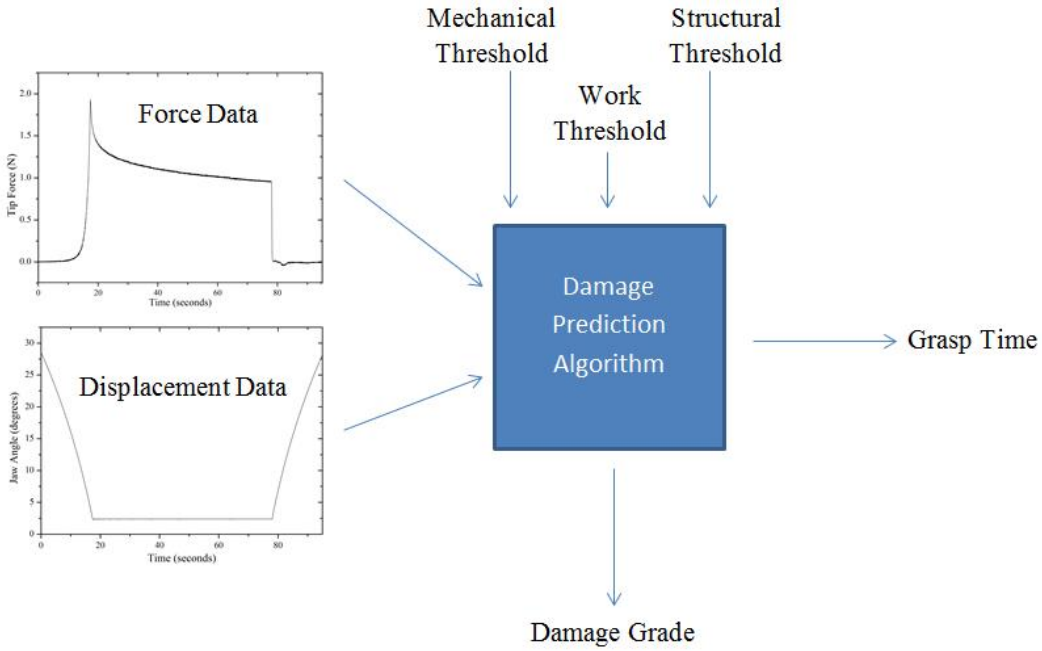

Figure 6.1: The damage predication algorithm, which uses force and displacement data from the instrumented grasper, along with pre-determined thresholds, to give the grasping duration and a predicted damage grade.

Using the system diagram (Figure 6.1), *in-vivo* manipulation data was observed to understand the typical force and displacement profiles. This ensured that regardless of the measurements from the instrumented grasper, the algorithm would still be able to process the data and output the required characteristics. For example if the force were to fluctuate above and below a damage threshold, the algorithm should be able to determine to total time above this threshold, instead of just one instance. From this the algorithm was developed in the following steps.

Step 1. Negative grasping forces are removed or ignored. This is due to the grasper jaws being opened to their maximum, causing a compressive force to act across the instrumentation loadcell, and is not indicative of a grasp taking place, therefore it can be dismissed.

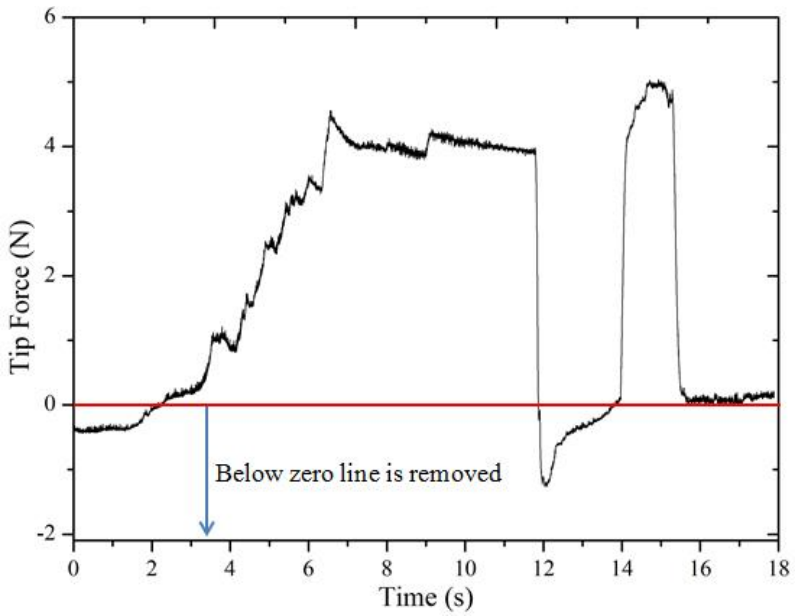

Figure 6.2: *In-vivo* force-time data with zeroed line (red).

Step 2. Any *'empty'* grasp data is removed or ignored. An *'empty'* grasp is observed when the user applies a grasping force (i.e. closes the grasper jaws) with nothing placed inside the jaws. This causes a grasping force to register even though tissue has not been grasped. By observing the jaw angle, forces which are applied when the jaws are fully closed, measuring 0.1 degrees or less (0.1 used to take noise into account), are not being applied to tissue and therefore can be dismissed.

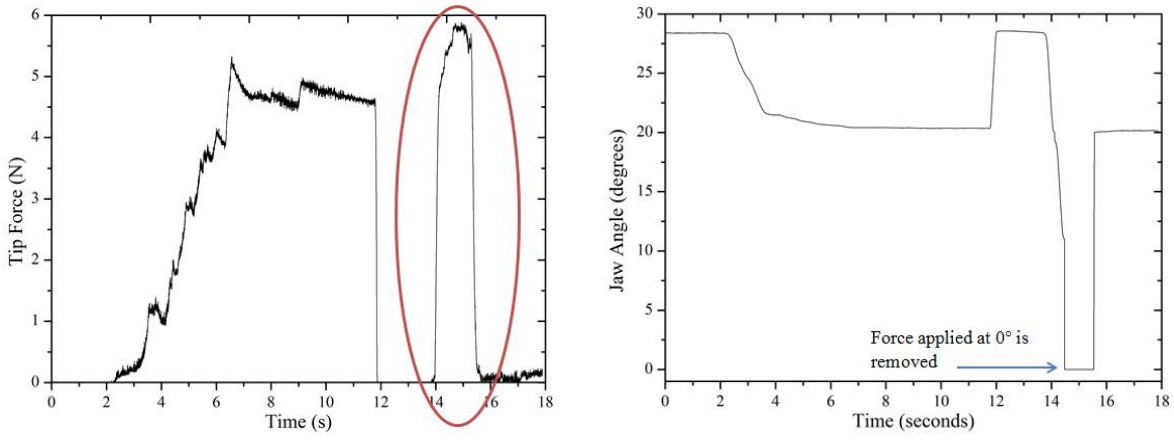

Figure 6.3: *In-vivo* grasping data, of (a) the force data, and (b) the angle data, highlighting empty grasping.

Step 3. From the remaining data the total grasp time is calculated. To represent the data clearly, the results are compared to the time spent grasping, rather than against the whole

procedure length. This is shown as both the time value and as a percentage of the overall grasping time. This ensures that the time between grasping does not affect the results, as this does not affect the tissue damage. Also the surgeon's performance can be compared to others.

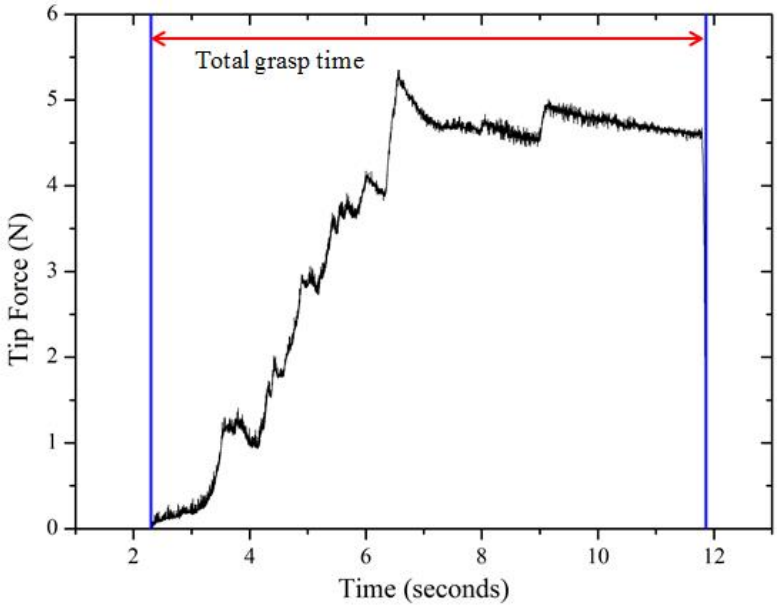

Figure 6.4: *In-vivo* force data highlighting grasping time (blue).

Step 4. The work done can be found by plotting the force against the displacement for the total grasp time. The hysteresis can then indicate the work done (Figure 6.5).

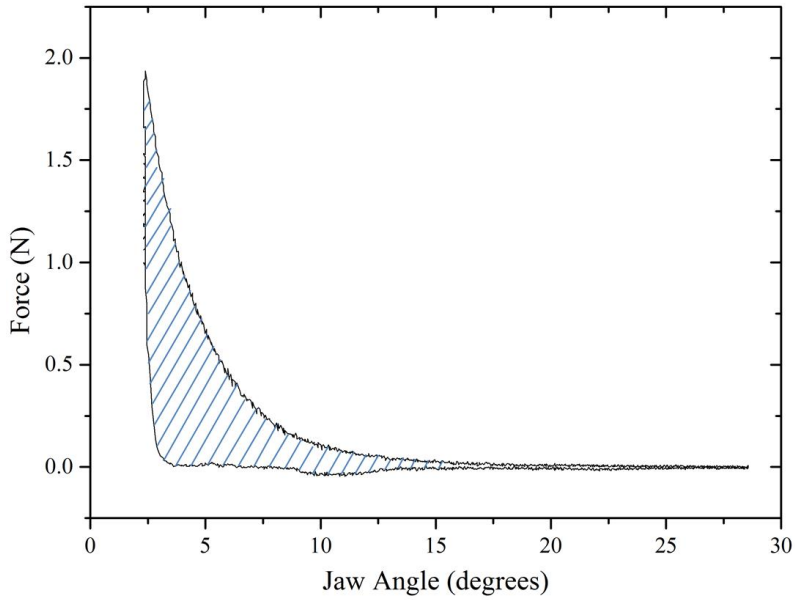

Figure 6.5: The force-displacement graph showing the hysteresis (work) from the encapsulated area (blue).

The time, and subsequently the percentage of time spent above the threshold is determined. If during a grasp the force fluctuates above and below the threshold, only time above this is counted.

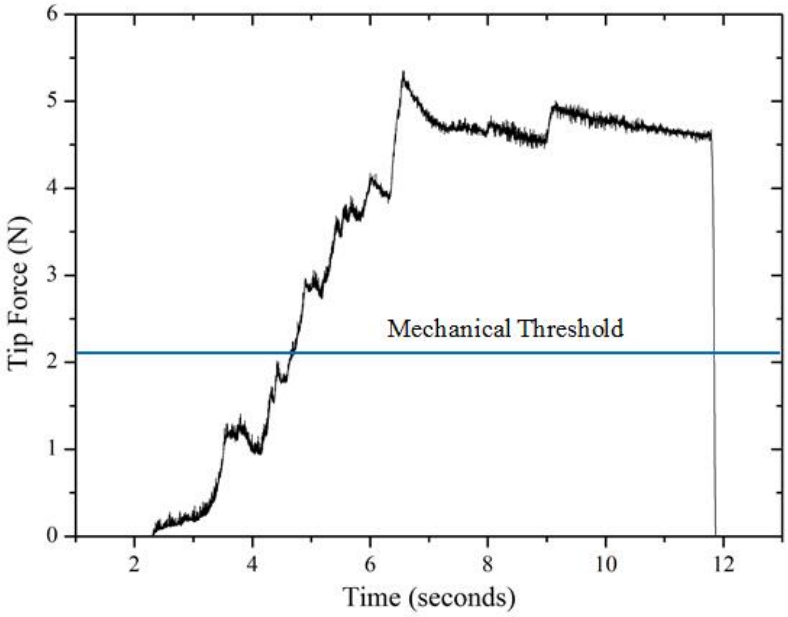

Figure 6.6: *In-vivo* force data highlighting first threshold (blue).

Step 5. As with the above step, the time and percentage of time spent above the threshold is determined taking into consideration any force fluctuations above and below the threshold.

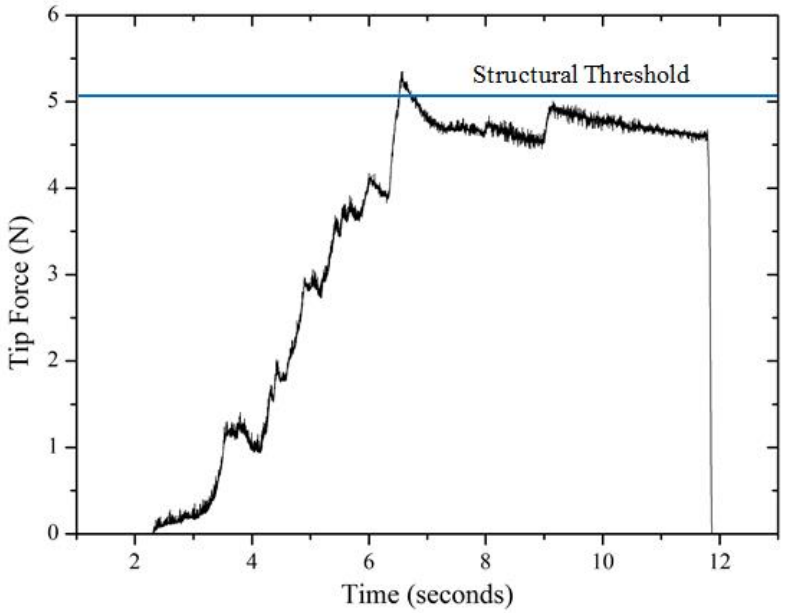

Figure 6.7: *In-vivo* force-time data highlighting second threshold (blue).

Once the grasping durations have been determined, the damage grade is given. From the *ex-vivo* tissue mechanics investigation (section 5) a table has been derived to determine the grade of tissue damage, based on the applied tip force and work done by the tissue (Table 6.1).

Threshold Damage Type	Threshold	Description
Mechanical Force (Force too high) (Mechanical Damage)	2.55 N	The applied tip force beyond which the mechanical response of the tissue breaks down.
Tissue Work (Work too high) (Mechanical Damage)	5.68 J	Amount of work done by the tissue, above which the mechanical response of the tissue breaks down.
Structural (Force too high) (Cellular Damage)	5.55 N	The applied tip force beyond which the tissue layers are destroyed.

Table 6.1: The observed thresholds from *ex-vivo* tissue analysis.

6.3 Implementation of the Tissue Damage Algorithm

The steps developed above have been implemented for post-op analysis and real-time data capture to allow the damage grading to be performed in training scenarios (post-operatively) and potential surgical use (real-time).

6.3.1 Post-operative Analysis of Tissue Damage

A MATLAB script has been written using the above steps and table (Appendix B). This measures the necessary data, and then gives the user a grade of damage. The benefits of this method is that the whole data can be instantly analysed and an overall grading given. This was developed using the data found from the *ex-vivo* testing (section 5), which has then been used on the *in-vivo* data. Using the previously collected *in-vivo* data (section 3.7) for the colon manipulations and grasping, a grading level has been given. This highlights what would have been shown if the Intelligent Grasper were used.

The results of the *in-vivo* damage grading show that when performing fast manipulation tasks, such as the bowel run, there is minimal force applied to the tissue to ensure efficient motions (Table 6.2). This results in a relatively low potential for damage to occur, and hence typically low gradings given for each run. Out of the 5 bowel runs performed, 3 exerted a force higher than the first threshold. For the colon retraction grasps there was typically mild damage seen except for one grasp (Colon 3) where it exceeded all thresholds.

Task Name	Grasp Time (s)	Mechanical Threshold	Structural Threshold	Work Threshold	Predicted Grade
Colon 1	32.8	Above	Below	Above	Mechanical Damage
Colon 2	31.2	Above	Below	Above	Mechanical Damage
Colon 3	32.1	Above	Above	Above	Mechanical Damage & Cellular Damage
Colon 4	32.1	Above	Below	Above	Mechanical Damage
Bowel Run 1	14.2	Above	Below	Below	Mechanical Damage
Bowel Run 2	19.0	Below	Below	Below	Little/No damage
Bowel Run 3	27.0	Above	Below	Below	Mechanical Damage
Bowel Run 4	18.3	Above	Below	Below	Mechanical Damage
Bowel Run 5	32.3	Below	Below	Below	Little/No damage

Table 6.2: Colon manipulation damage grading results showing the total grasping time, and if the grasp was over the force and work threshold, with resulting damage grade.

6.3.2 Real-time Analysis of Tissue Damage

The damage algorithm was also implemented in LabVIEW (Figure 6.8) to work in parallel with previous instrumented grasper code (section 3.11.3). The benefits of this method are that the user could be immediately alerted to an excessive force, potentially avoiding any serious complications.

While logging the data, grasping time and times above the relative thresholds, light outputs are used to indicate in real-time to the user that they are exceeding the forces which have been shown to induce damage. Working in parallel to this is the work calculations (Figure 6.9). Due to the fact that the work must be calculated from the full profile of the grasp, the work damage is not output until after each grasp. The program waits until the grasp has started (the force is above 0.1 N) then records the tip force and a jaw angle until the force returns to 0.1 N. At this point the work is calculated, using the trapezoid rule for the ramp up and down profiles, then subtracting the ramp down from the ramp up to give the final work and comparing to the threshold.

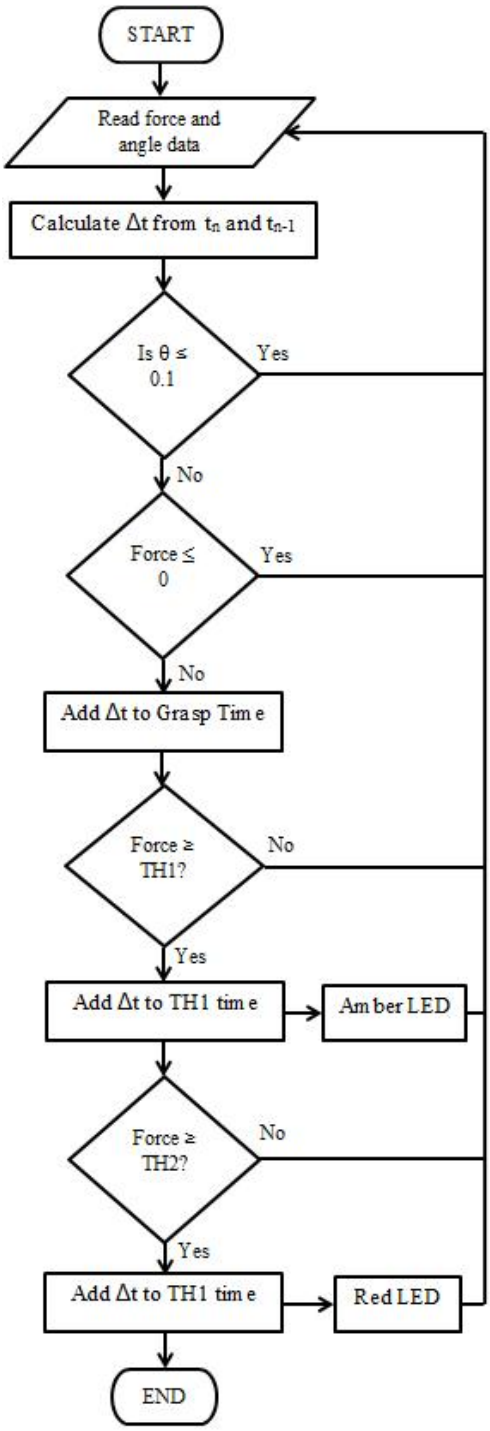

Figure 6.8: A flowcode diagram of the intelligent grasper implementation in LabVIEW, where TH1 and TH2 are threshold 1 and 2 respectively.

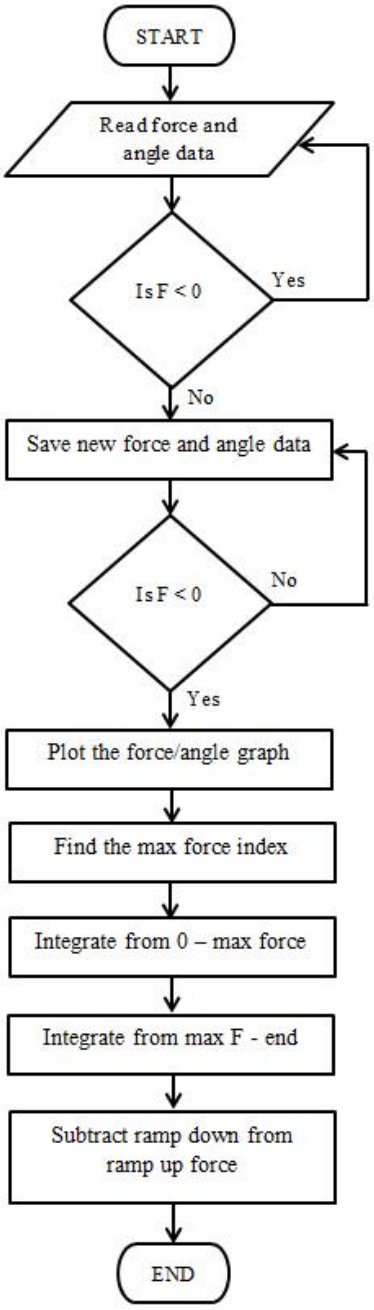

Figure 6.9: A flowcode diagram of the intelligent grasper work calculation implementation in LabVIEW.

6.4 Conclusion

Using previously acquired *ex-vivo* data, a damage prediction algorithm has been developed to provide the user with a grade of damage, using force and displacement data. This has be implemented for both a post-operative and real-time system, using MATLAB and LabVIEW respectively. The post-operative methods gives the user feedback over the whole procedure, whereas the real-time method allows an instant indication of potential damage. This chapter

demonstrates the concept of the intelligent grasper using previously acquired *ex-vivo* data to apply to *in-vivo* measurements. This work offers a novel approach to monitoring *in-vivo* surgical tasks, as instead of providing the user with arbitrary values of grasping, they are given a grade of damage. The results showed that the algorithm gives an increased severity grade as the applied force rises. For quick surgical manipulation tasks a minimal force is typically used to ensure efficient motion, leading to little predicted damage.

Chapter 7

Discussion

This discussion explores the key contributions of this work and its context in this field of research. The development of the laparoscopic grasper instrumentation is discussed, which provides an *'easy-to-use'* means of measuring *in-vivo* grasping forces as close to actual surgery as possible. The measured *in-vivo* tasks have been compared to other research results. The development of an *ex-vivo* tissue testing rig, used to simulate/replicate the grasping action in typical laparoscopic surgery, has been discussed alongside other *ex-vivo* tissue testing set-ups. Observations of the changes to tissue response under varying grasping parameters have been discussed, interpreted, and compared to previous work. Finally the use of the mechanical response data of tissue as a measure of damage, is compared to other methods, along with the intelligent grasper concept as a whole.

7.1 Measuring *In-vivo* Manipulation and Grasping

The instrumented grasper design (Chapter 3) uses a sensor module located between the grasper shaft and handle. Unlike the BlueDRAGON [170], the instrumentation consists of both a loadcell, to measure force, and a potentiometer to account for the linkage displacement. As highlighted by the mechanical model of the grasper (section 3.4), the relation between the applied linkage force and tip force is not linear, but dependant on the jaw angle (which can be determined by the linkage displacement). The research carried out with the BlueDRAGON only looks to investigate the motions performed by the surgeon, and therefore the tip forces and tissue-tool interactions were not considered, but future work may require the need to include displacement measurements to fully understand the tissue-tool interface. The BlueDRAGON design incorporates 7 Degrees Of Freedom (DOF) providing a higher degree of detail of surgical manipulations than the instrumented grasper. The 7 DOF are a translation along axis x, y, and z, rotation about x, y, and z, and a grasping motion. But this design is not modular and it's size means that it would not be suitable for actual surgical procedures and repeated use *in-vivo*. The instrumented grasper design has aimed to provide a concept which could be used to monitor actual surgery while limiting the restriction on the surgeon, and allowing multiple tools to be attached. Another instrumented grasper design is the Motorized Endoscopic Grasper (MEG) [183], which aims to measure *in-vivo* tissue response characteristics. This design takes a different approach than the instrumented grasper from this project in that the force application is performed with a motor, instead of a surgeon

(section 2.4.3). However this is still susceptible to hand tremors and does not allow for a natural grasp.

Measurements taken from both the instrumented grasper and BlueDRAGON have been compared (Figure 7.1) and show the viability of the instrumented grasper, highlighting similar grasping profiles. As only the linkage force is available from the BlueDRAGON, the linkage measurements from this work are shown, before these have been converted to tip forces. The instrumented grasper was used to measure *in-vivo* surgical grasping forces for different tasks, including running the bowel, and grasping then retracting different abdominal organs. When running the bowel, the surgeon was asked to perform 10 grasps (5 for each hand), while the force data were logged (Figure 7.1a). The maximum applied shaft force was measured at 35.21 N with a grasp duration of 3.64 $\pm$1.42 seconds. A similar investigation was performed by researchers using the BlueDRAGON [175], with 20 grasps in total (10 per hand), showing a maximum shaft force under 25 N and grasp time of 2.29 $\pm$1.65 seconds; 10 grasps (5 per hand) is shown for comparison (Figure 7.1b).

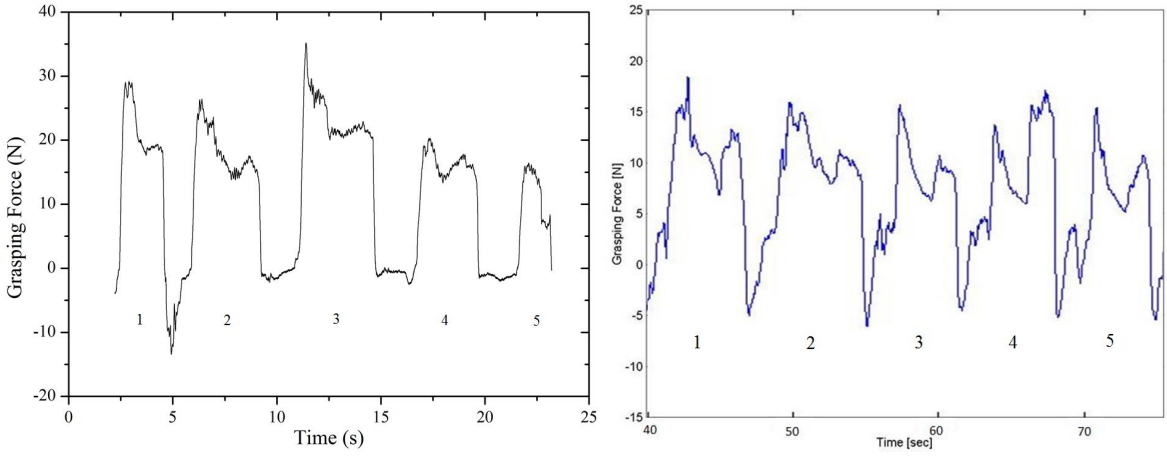

(a) (b)

Figure 7.1: The linkage force grasping profile of a single surgical grasper when running the bowel, showing (a) 5 grasps using the instrumented grasper, (b) 5 grasp section (from 10 grasps) for the BlueDRAGON [170].

There is close agreement between the measured data from this work and the BlueDRAGON, providing confidence in the accuracy of the measurements. However as both sets of data are from the linkage measurements, the actual grasping tip forces may differ in reality, due to the non-linear relation between the shaft and tip. Given that the comparison is of the grasping profile and the results are of a similar magnitude, this can be overlooked. The force profile for the individual grasps from each graph are similar in shape, suggesting that the peak forces and grasp duration are characteristic of the individual performing the grasps. These graphs generally show an initial peak when the force is applied, with some relaxation (either from the tissue or surgeon's grasp), followed by a slight increase in force again at the end of the grasp,

suggesting that the user ensures the tissue is held securely when reaching with the other hand; seen in profile 3 (Figure 7.1a). This profile is not always the case for some grasps where the peak force may come at the end, from either the surgeon readjusting or overcompensating the grasp force when moving the tissue; seen in profile 4 (Figure 7.1b).

Other grasping tasks, involving manipulation of abdominal organs, have been performed in this work and the BlueDRAGON. Using the instrumented grasper, a surgeon was asked to grasp different abdominal organs and retract for 30 seconds, as if to move the organ to gain access behind, as would be done in surgery. The BlueDRAGON was also used to pass the stomach behind the oesophagus. Results from these tests indicated a maximum applied shaft force of 75.53 N (57.81 $\pm$ 13.40 N average) was applied to the colon by the instrumented grasper, and a maximum shaft force of 68.17 N by the BlueDRAGON, showing a large variance in possible grasping forces. The retraction testing performed with the instrumented grasper however, shows grasping forces for a larger range of abdominal organs, and therefore provides a broader overview of typical forces in abdominal surgery, instead of just two tasks from the BlueDRAGON [175].

The MEG has also been used to grasp organs *in-vivo* to measure tissue properties [128]. However grasping performed using the MEG are not entirely comparable because the grasp force is controlled and predefined. These readings are highly susceptible to hand tremors, or the effect of other organs moving during grasping. Slight vibrations in the stress strain curves could affect the repeatability and reliability of results.

Overall the instrumented grasper has allowed for typical *in-vivo* grasping characteristics to be analysed. Although measurements from the MEG highlight tissue characteristics, and the BlueDRAGON have shown full tool kinetic parameters of manipulation tasks, the instrumented grasper has highlighted the applied grasping forces for typical *in-vivo* tasks, over a larger range of abdominal organs. It also provided information directly relevant to the configuration of the grasper, which advised the development of the grasper tissue testing rig.

7.2 Simulated *Ex-vivo* Tissue Grasping

Informed by the *in-vivo* grasping characteristics, a tissue grasping test rig was developed, capable of grasping tissue up to 100 N, up to a duration of 60 seconds, to simulate *in-vivo* grasping in an *ex-vivo* laboratory set-up. Other research systems have been developed to investigate tissue properties, varying from this project by using a cylindrical indenter [88], or an idealised grasper surface [53]. One research group developed an indenter based system to apply a force to the sample (up to 44.5 N), over a known area (7 mm^2), and measure the tissue response (Figure 2.15). This set up does not accurately simulate *in-vivo* surgical grasping as an indenter is used to apply the force instead of a surgical tool, meaning features such as the grasper teeth or pressure profile are not considered. Also the set-up only uses a

relatively low load to measure the tissue properties rather than using the high forces at which damage may be caused [88]. The indenter differs from a grasper jaw in that the pressure distribution across the indenter surface should be approximately constant, but for grasper jaws the pressure increases exponentially the nearer the tissue is to the hinge. Similarly a different section of the grasper could be used (e.g. the end third, or full area) again affecting the pressure distribution.

Other research has developed a test set up for the optimisation of grasper fenestration designs [53]. This focusses on the retraction capabilities of different fenestration designs, but again does not simulate typical *in-vivo* grasping, as the fenestrated surfaces apply the force to the tissue in parallel rather than a typical grasping wedge [53]. It does allow for retraction investigations on porcine colon, and investigates the effect of increasing the size, spacing and overall design of grasping surfaces. This shows that increasing the height of fenestrations can reduce the grasp force needed to successfully retract, while changes to the profile showed similar results. To apply the grasping force a compression mechanism is used in the form of a spring which would vary the applied load with the change in tissue thickness, between tests (Figure 2.16). Finally the force is applied longitudinally (along the colon sample), which is not a typical orientation of grasping. The test set-up described in this project, grasps a cylindrical sample of tissue perpendicular to the actual sample, as would be done *in-vivo*. This method was discussed previously and was dismissed for two main reasons; firstly that this does not replicate typical *in-vivo* grasping, where the muscle layer orientation would differ, possibly affecting results, and secondly that the area being grasped is likely to already be damaged due to cutting the sample (Figure 4.20).

Unlike these methods, the test set up described in this thesis uses a laparoscopic grasper to apply the force to the tissue, allowing for *in-vivo* grasping forces to be replicated in a controlled laboratory set up, providing direct comparison between the *in-vivo* and *ex-vivo* applied forces. However due to the pressure distribution of the jaws, which can vary with tissue thickness and how the tissue is grasped, it is difficult to compare to different grasper types. This could be done however by varying the grasper geometry to create an idealised surface, but would not provide an accurate *in-vivo* representation. Also by calculating the surface area of the grasper, the applied pressure could be determined and compared, but this may prove complex from both the grasper fenestration geometry, and also the non-homogeneous nature of tissue.

While there are many variations of tissue testing rigs investigating tissue characteristics, tissue damage, or optimisation of tool design, the set-up described in this project allows for commonly used laparoscopic graspers to be controlled, to grasp *ex-vivo* porcine tissue, providing a closer comparison to *in-vivo* testing.

7.3 Characterising the Mechanical Response of Tissue

From the testing performed in the tissue grasping rig a drastic change in the tissue relaxation response was observed for increasing tip forces (Chapter 5). From this two critical thresholds were determined, beyond which the mechanical response of the tissue alters markedly (Figure 7.2). These were investigated to further understand how the response was affected.

Zone A highlights the force and work regions where the relaxation gradually reduces as the respective force and work increases. Zone B shows the transition stage where the response falls rapidly. Zone C shows the zone beyond which the tissue relaxation remains below 20 %.

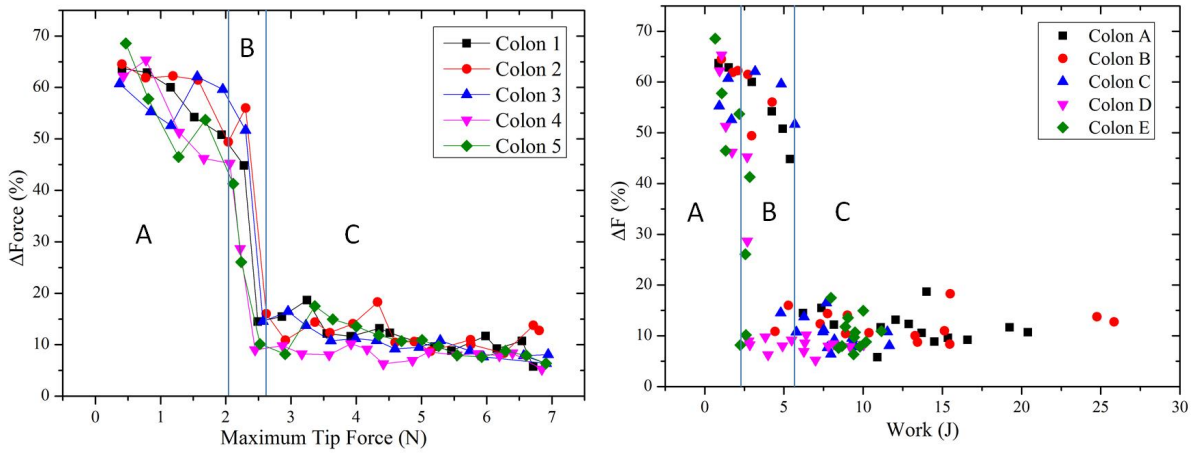

(a) (b)

Figure 7.2: The force relaxation $\Delta F\%$, plotted against, (a) the maximum tip force, and (b) the work done by the grasper on the tissue, showing zones A, B and C which correspond to the normal response, the transition stage, and the damage region, respectively.

Considering the previous Wiechert model (Figure 5.6), firstly for zone A, as the applied tip force increases, the response shows that the tissue appears to stiffen. The E_0 parameter increases linearly as the tip force is increased (Figure 5.14). This could be as a result of the extracellular fluid, which surrounds tissue cells, being forced out (Figure 7.3a). Similarly the viscosity of the response increases, possibly as a result of there being less extracellular fluid, or the increased pressure on the cells causing an increase in viscosity (Figure 7.3c). There have been a number of investigations into the behaviour of bodily fluids, many of which are believed to be non-Newtonian. Generally fluids such as blood or synovial fluid are believed to exhibit stress-thinning properties, whereby an increase in stress results in a reduced viscosity [105]. These results suggest otherwise, that in fact stress-thickening is observed, which could be logically explained by the protein chains, often found in cells, becoming compacted under

stress and therefore restricting the flow [105]. These compacted proteins would also account for the increase in elastic response of the E_1 and E_2 parameters. Another alternative is that the excess fluid is pushed out, and therefore less is present to contribute to the mechanical response. To fully understand the nature of these individual fluids, they would need to be isolated, and confined in order to measure the stress responses accurately.

Due to the low number of samples which fall in the transition region in zone B (in between states), it is difficult to fully determine the transitional phase in the mechanical response. It is understood that due to the non-homogeneous nature of tissue, a number of factors will affect when the mechanical response will dramatically change [92]. These factors include the water content, fat layers, age of samples, exposure length to air, etc. To account for this breakdown, a number of ideas have been considered. Firstly as described previously, by applying a force, the extracellular fluid is pushed away. Once there is virtually no fluid left it is no longer present to contribute to the response, and all the force is applied to the cells (Figure 7.3b), likely contributing to the sudden increase in E_0. Secondly by applying too great a force to the cell, this may cause them to rupture (Figure 7.3d), releasing the cellular fluid, and resulting in the drop in the visco elastic parameters η_1 and η_2, and also the drop in the elastic parameters E_1 and E_2, accompanied by the gradient change in E_0. Likely it is a combination of these effects to give the overall relaxation response. Also as highlighted previously, from observation of the work applied to the tissue, the energy dissipation mechanism appears to change. Below the threshold the energy is dissipated through the relaxation of the tissue, but beyond the threshold this changes. Likely there are a number of contributing factors, including heat loss and the breaking of chemical bonds in the cells.

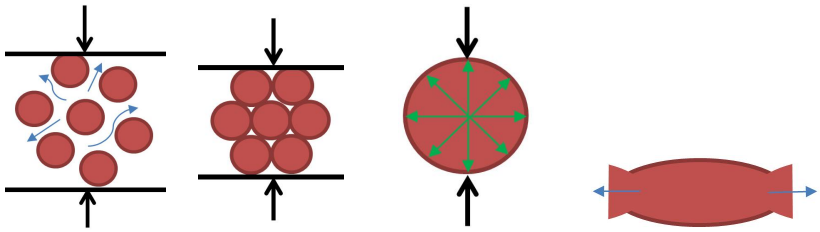

Figure 7.3: Cell response schematics, showing (a) extracellular fluid motion with applied pressure, (b) little remaining extracellular fluid with pressure applied to cells, (c) the force applied to individual cells with internal pressure, and (d) a ruptured cell showing cytoplasm flow.

Beyond the threshold, into zone C, the tissue is likely to be increasingly damaged. At the upper limit of the applied force and work, the histology shows the destruction of the muscle layers, but with the submucosa and mucosa remaining. Previous studies have investigated the difference in structure between the longitudinal and circular muscle, and the submucosa and mucosa, showing that the latter two are mostly comprised of collagen fibres, orientated

to form a strong mesh or lattice (Figure 7.4a) [94]. This promotes a strong structure with a high elastic response, which likely provides the largest contribution to the parameter E_0. This suggests that the submucosa and mucosa would be more resilient to damage, as is supported by the histology results (Figure 7.4b). Similarly from the work analysis, the different tissue layers could have a varied way of dissipating energy.

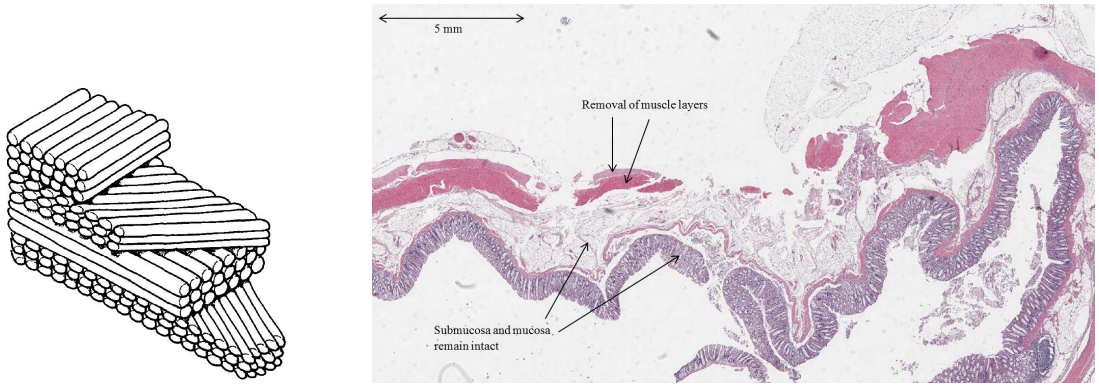

(a) (b)

Figure 7.4: The structure of the submucosa and mucosa, highlighting (a) the collagen fibre orientation and layering, and (b) the histological analysis of the 6.95 N grasp showing the damaged muscle layers and intact mucosa layers.

It should be noted however, that this may be a result of how the colon is grasper, with the jaws only making contact with muscle layers. This could be investigated further by opening the colon samples before grasping, and then observing the histological damage. If a larger amount of the mucosa and submucosa are left intact, this would suggest they are less susceptible to damage. However in this project this has not been investigated as it would not naturally occur in typical MIS.

7.4 Damage Grading Using Mechanical Response Data

From the previous analysis of the mechanical changes in tissue, this was investigated as a potential method to link mechanical measures with clinical indications of damage, to provide real-time feedback to the surgeon. This has been compared to other investigations of tissue damage and analysis.

Perforation forces of large pig bowel and human small bowel were investigated. The force was applied direct to the tissue surface, with a system to measure the electrical continuity between each side of device. This indicates when both sides touch, to show tissue perforation [2]. This however does not show damage which occurs before perforation, which can still be of serious concern. The results showed that for large bowel (Figure 2.25), the average perforation force was 13.5$\pm$3.7 N (using a 1.5 mm hemisphere indenter), with a minimum

force needed to perforate the tissue was approximately 8 N, greater than the maximum grasping tip force, 4.9 N, found in this research, suggesting that typical grasping forces will not lead to perforation, supporting the results from this work. However the surface area and geometry differs from the grasper which will affect the different pressures, and therefore may not provide an entirely accurate comparison. This provides the closest method of using grasping force measurements as a way of determining tissue damage. Other research investigations have aimed to measure tissue damage from measuring the concentration of 4 serums/chemicals (C-reactive protein, granulocyte-elastase, interleukin-6, and interleukin-10) typically found in blood [138]. While these typically showed a general increase after surgery, samples were taken at 6 hours, 1 day and 2 days after surgery, and in the case of C-reactive protein, the greatest increase was seen on the second day. There is therefore a long time constant associated with this form of measurement and analysis. It is unclear if measurable changes could be observed at the same time scales used in this study. With regards to the degree of damage, the greater the levels typically the higher the degree of damage, although this would be unique for each individual, even with a baseline established, and would be difficult to impartially interpret. Another investigation used image analysis to measure the colour variation of grasped liver (Figure 2.26) [100]. The image pixels over the tissue surface are compared to a colour chart to determine the degree of damage. Applied stresses of 0, 60, 120, 180 and 240 kPa were used, where these readings had been previously found from *in-vivo* testing with the BlueDRAGON. This method shows an alternative non intrusive method of determining if the tissue has been damaged, with a clear variation of colour over the range of applied forces. This however would take time for bruise to develop (approximately 3 hours), again limiting the efficiency of diagnosing damage. Also the colour identification may differ between individuals, and be susceptible to lighting, picture quality, etc, whereas this work has shown repeatable results for 5 different colons.

Another method used in this project is the observations of the work threshold which has been shown to pick up additional data which would otherwise not be considered (Figure 7.5). While all the data points above both thresholds exhibit a force relaxation of less than 20%, there are still two points below which are classed as '*safe*'. This is likely due to the unpredictable nature of the tissue samples, and may occur because they had different amounts of each tissue layer.

Even though the force and work are determined from the same data response, the work is calculated using the displacement of the jaw angle, but as this is very difficult to predetermine, both measures are needed. The work shows how the tissue response changes to an increase in the energy put into the system. This has previously not been used to measure grasping quality and would be virtually impossible for a surgeon to monitor. Therefore providing this as feedback would be crucial.

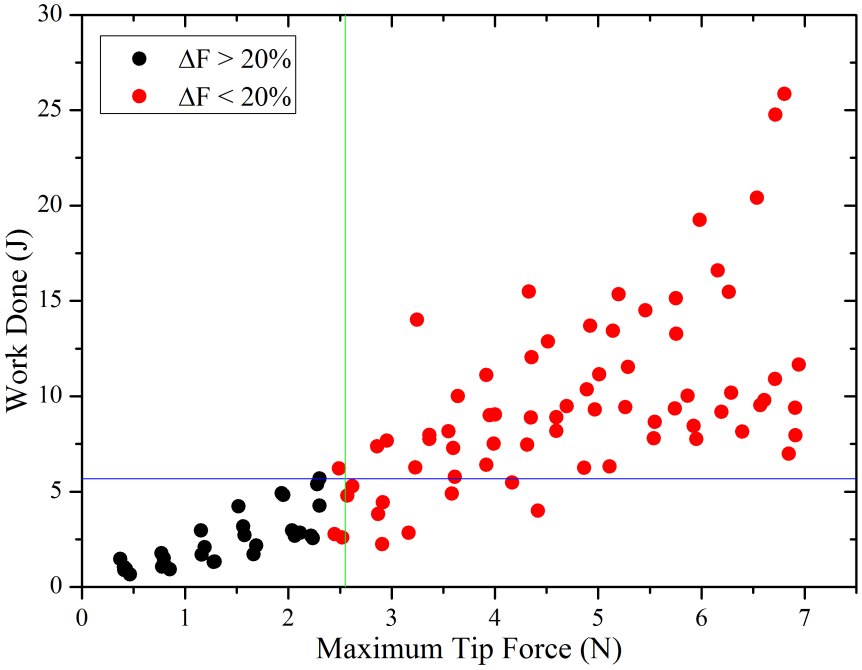

Figure 7.5: Tissue relaxation plotted against work and maximum tip force; Force threshold 2.55 N (green line), work threshold 5.68 J (blue line), high relaxation >20% (black), and low relaxation <20% (red).

A number of methods have been developed to try and quantify tissue damage, with investigations into the cell mechanics providing deeper understanding of the results. The methods presented in this work allow for a real-time update of damage, compared to other which require time to either allow the damage to develop, or to analyses blood samples. Previous work suggests the need for a real-time damage measure which is presented in the form of the Intelligent Grasper. Alongside the force measurements, the work done by the grasper on the tissue has also shown a damage threshold. Without this threshold it would be possible to miss data which would show as damaged (Figure 7.5). Ultimately the typical measures are difficult to interpret, and often subjective, but using mechanical measures are only suitable when a closer link has been shown with clinical measures.

7.5 Final Conclusions

7.5.1 Overall Conclusions

Overall the project was a success, as the concept of an Intelligent Grasper has been demonstrated for potential use as a training aid to surgeons, or for *in-vivo* use to highlight the potential of damage being caused. The findings in the changes in tissue mechanical response are particularly interesting, specifically that this occurs at forces commonly used *in-vivo*.

Given more time more histology samples would be collected, particularly focussing on the *'transition zone'*, to observe what is happening here on a cellular level. Also validation of the Intelligent Grasper prediction, by taking it both *in-vivo* and in an *ex-vivo* set-up. Finally investigation of the grasper mechanics using multiple graspers to understand if any dynamic frictional losses affect grasping, providing a more detailed model. If the project was restarted, it would investigate alternative methods of quantifying tissue damage, perhaps observing samples under a microscope to show the cellular response after grasping. This would then contribute to the tissue mechanics discussion, and improve the understanding of the threshold breakdown.

During the project there were a number of dismissed methodologies, which are outlined in the following paragraph. The surface topography was investigated using a laser scanner as a potential means of measuring damage. Firstly this was very difficult to scan using a laser, due to the wet nature of fresh tissue samples. The samples could not be dried out as this could greatly affect the response of the tissue. Using post-test drying and surface treatment proved unreliable. Alongside this, non-tissue samples were scanned to try develop a surface topology damage grading. This also proved difficult due to the undulating nature of the tissue surface, resulting in huge disparities in indentation measurements. Due to both aspects of this methodology proving immensely difficult and unreliable, this was not used. Mesocolon analysis alongside the colon grasping was initially investigated, however it was difficult to source, and the porcine model structure of the mesocolon differs greatly from that of the human model, and therefore was believed to not provide a relative analysis.

7.5.2 Practical Significance in Surgery

The Intelligent Grasper is beneficial to surgeons both for *in-vivo* surgery, post operatively and for training purposes. It can inform the surgeon of the potential damage induced in the the tissue from real-time grasping, without preventing excessive grasping in the case of an emergency. The combination of *ex-vivo* tissue mechanics and histological analysis can provide the surgeon with a damage grading. This is not simply numerical information, but an indication of if potential damage has been inflicted, and therefore does not require any further interpretation of the results by the surgeon. The program alerts the surgeon, but does not restrict the grasper as in serious situations it will be of higher importance to make sure an immediate problem is fixed than to prevent potential damage. By indicating the likelihood that severe damage has occurred, post operative care resources can be used more efficiently, and reduce the chance of problems occurring after surgery and symptoms being overlooked. As discussed previously, the system provides a damage grading, which can be found after collecting the data, not just during the procedure. For those with a higher number of damaging grasps, a more thorough observation can be give during the recovery

process. It is also a useful aid to trainee surgeons to improve their rate of learning by alerting them to when excessive force is being applied. If the trainee were to use the Intelligent Grasper with a laparoscopic training device, as they perform various tasks, the system would alert them, indicating that either the grasp force or work was too high. Through repetition with the Intelligent Grasper, while also learning how to perform the task, the surgeon would have a greater understanding of the grasping characteristics which cause damage, and more importantly how this feels to the user.

7.5.3 Project Inspiration

Inspiration for this project came from investigating the difficulties that surgeons face when using laparoscopic tools to perform complex procedures, often leading to excessive forces being used to manipulate delicate tissues, and potentially leading to severe damage. This becomes of even greater concern when laparoscopic techniques are used to resect cancerous tissue. Damage to the delicate membranes surrounding the tissue can rupture, and leak cancer cells into the abdominal cavity, greatly increasing the chance of recurrence. This has lead to the need for the surgeon to understand the damage caused during laparoscopic grasping. To date, a number of devices have aimed to measure grasping data, but this work goes on to provide the surgeon with a damage grading so that there would be no additional need to interpret the data. Allowing still for laparoscopic surgery to be performed quickly, and efficiently while providing the surgeon with added confidence that any major tissue damage will be detected. This work adds to the previous work, and provides a better link between mechanical and clinical measures of damage. However there is still work to be done in better understanding what happens to the tissue during grasping.

7.6 Future Recommendations

As a continuation of this work, a number of future directions have been outlined in the following sections.

7.6.1 Assessment of Retraction Forces

The addition of a retraction module would allow for further investigations into the characteristic use of graspers *in-vivo*. Initial investigations into appropriate components has highlighted typical *'donut'* loadcells as suitable for a retraction module, due to the hole through the centre, down which the grasper shaft could be passed. With this in mind, the bespoke design of a retraction module has been developed (Figure 7.6).

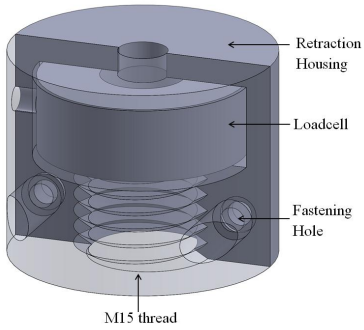

Figure 7.6: Retraction module design, highlighting the location of the *'donut'* loadcell and housing, comprising of the M15 thread, holes to secure and the inner space through which to pass the grasper shaft.

The grasper shaft would be inserted through the device with the shaft bottom secured against the loadcell when tightened, replacing the previously used cone-nut (Figure 7.7).

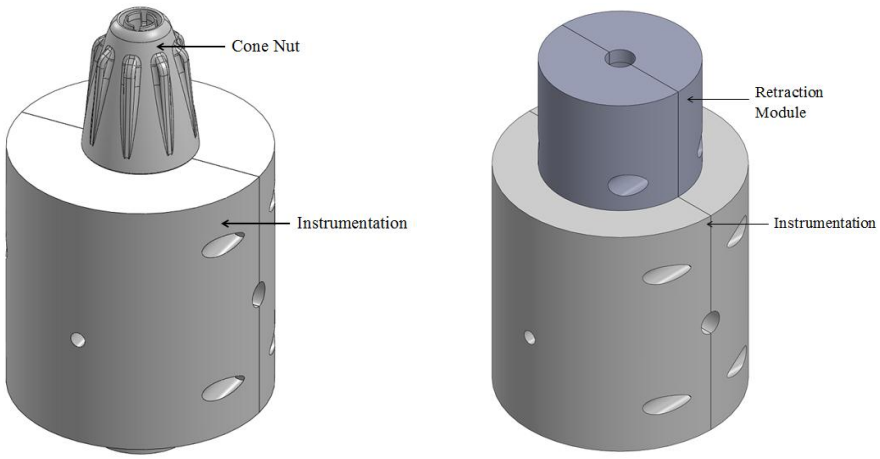

Figure 7.7: The original grasper instrumentation, with (a) the location of the cone-nut, and (b) the location of the retraction module.

The output from the loadcell can be passed through a similar amplifier as previously used, with this then being logged using a program via the DAQ USB device. The retraction module would need to be used alongside the previously developed instrumentation as the grasping force would affect the force acting along the shaft and, as a result, the measured retraction force. By subtracting the current grasping force acting along the shaft, from the measured retraction force, the actual retraction can be measured.

From this, additional sensors could be incorporated into the design to develop a fully defined, 7 DOF system (x, y, and z axis translation and rotation, and grasping), which considers all possible motions made. This would require modification to the instrumentation, and the focus should still be on the key design features; allowing for *'natural'* grasping, and

a modular design which can be removed and placed on another grasper. This would enhance the previous *in-vivo* data and add to further understanding tissue manipulation.

7.6.2 Tissue Mechanics Transition Investigation

Using the tissue testing rig, or similar, the transitional phase of the tissue response could be investigated to determine what factors are dependant on this change. This would include determining how variations in the proportions of each layer affect the change, either by isolating each layer, or performing numerous repeats. By looking at the different layers individually, the mechanical model could be developed further allowing for increased predictability in the damage grading.

Accompanying this data with further histological analysis would give a more informed view of how the tissue responds and why its mechanical characteristics change here. Also by investigating alternative methods to histology, the energy conversion change could be found i.e. by monitoring the residual heat in the tissue, or by changes in the chemical structures to isolate each mechanic.

From this there would be potential to highlight other thresholds where changes occur in the tissue, such as the breakdown of the mucosa and submucosal layers. This would likely occur at much greater forces, larger than those typically witnessed in surgery, but would help to further understand the tissue characteristics, and allow for increased predictability in the tissue response.

This would lead to a greater understanding of the behaviour of biological structures, aiding surgeons and manufacturers in future surgical developments.

7.6.3 Understanding and Improving the Grasper Mechanism

Using the previously developed mathematical model on other grasper geometries, the variation in different aspects of the grasper designs can be investigated to show how changes in the scale of a scissor grasper can affect the overall force transmission.

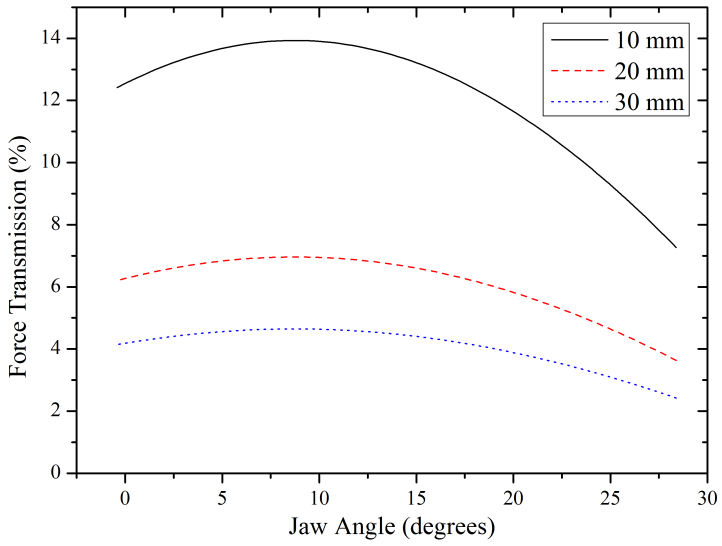

Figure 7.8: The force transmission percentage model in a double action laparoscopic grasper, with matching geometries and different jaw length (10, 20 and 30 mm).

It can be seen that there is a radial relation between the input and tip force for varying jaw lengths (Figure 7.8). Other parameters to be considered are the internal linkages, and how the ratio between these can vary results. Finally, investigation into frictional losses in the grasper, both for static and dynamic motions would provide a greater understanding of the grasper efficiency.

7.6.4 Grasper Manufacturing Standard

Using both the grasper modelling and the test rig, various designs of grasper could be investigated to show what design criteria give higher grasping pressures, and a better force transmission efficiency and linearity. This could be combined into a performance indicator, or grading of the tool used to compare various design types, which would then advise manufacturers as to how changes in the design may effect the performance overall. By providing surgeons with this additional information, they can make a more informed choice of tool, leading to improved performance in surgery.

7.6.5 Integration into Robotic Surgery

As there is currently no haptic feedback to the surgeon when performing robotic surgery, by incorporating sensors into the grasping mechanics, the damage prediction model could be used. Similar testing would need to be performed using typical robotic graspers, or if the tissue model had been further developed into a general model, simply the geometry of the grasper would be needed. This would then allow the tip forces/pressures to be determined

and the appropriate thresholds to be found. Then if the surgeon grasps tissue beyond this he would be alerted to excessive forces. This would reduce the need to relearn surgical tasks with often *'complex'* designs, and instead could be used immediately.

References

[1] M. Voort, E.A.M. Heijnsdijk, and D.J. Gouma. Bowel injury as a complication of laparoscopy. *British Journal of Surgery*, 91(10):1253–1258, 2004.

[2] E.A.M. Heijnsdijk, M. Voort, H. Visser, J. Dankelman, and D.J. Gouma. Inter- and intraindividual variabilities of perforation forces of human and pig bowel tissue. *Surgical Endoscopy And Other Interventional Techniques*, 17(12):1923–1926, 2003.

[3] Surgical Innovations Ltd. "private communication". 2014.

[4] A.G. Harrell and B.T. Heniford. Minimally invasive abdominal surgery: lux et veritas past, present, and future. *The American Journal of Surgery*, 190(2):239–243, 2005.

[5] A.E. Blackmore, M.T.C. Wong, and C.L. Tang. Evolution of laparoscopy in colorectal surgery: An evidence based review. *World Journal Gastroenterology*, 20(17):4926–4933, 2014.

[6] B. Jacobson and A. Murray. *Medical Devices: Use and Safety*. Churchill Livingstone, 2007.

[7] A. Arezzo. The past, the present, and the future of minimally invasive therapy in laparoscopic surgery: A review and speculative outlook. *Minimally Invasive Therapy and Allied Technologies*, pages 1–8, 2014.

[8] C.R. Tracy, J.D. Raman, J.A. Cadeddu, and A. Rane. Laparoendoscopic single-site surgery in urology: where have we been and where are we heading? *Nature Clinical Practice Urology*, 5(10):561–568, 2008.

[9] P. Culmer, J. Barrie, R. Hewson, M. Levesley, M. Mon-Williams, D. Jayne, and A. Neville. Reviewing the technological challenges associated with the development of a laparoscopic palpation device. *The International Journal of Medical Robotics and Computer Assisted Surgery*, 8(2):146–159, 2012.

[10] S. Kumar, R.G. Wilson, S.J. Nixon, and I.M.C. Macintyre. Chronic pain after laparoscopic and open mesh repair of groin hernia. *British Journal of Surgery*, 89(11):1476–1479, 2002.

[11] J.R. Eriksen. Pain and convalescence following laparoscopic ventral hernia repair. *Dan Med Bull*, 58(12):15, 2011.

[12] C.N. Gutt, T. Oniu, P. Schemmer, A. Mehrabi, and M.W. Bchler. Fewer adhesions induced by laparoscopic surgery? *Surgical Endoscopy And Other Interventional Techniques*, 18(6):898–906, 2004.

[13] C.L. Garrard, R.H. Clements, L. Nanney, J.M. Davidson, and W.O. Richards. Adhesion formation is reduced after laparoscopic surgery. *Surgical Endoscopy*, 13(1):10–13, 1999.

[14] H.G. Stassen, J. Dankelman, K.A. Grimbergen, and D.W. Meijer. Man-machine aspects of minimally invasive surgery. *Annual Reviews in Control*, 25:111–122, 2001.

[15] R.M. Verteuil, R.A. Hernndez, and L. Vale. Economic evaluation of laparoscopic surgery for colorectal cancer. *International Journal of Technology Assessment in Health Care*, 23(4):464–472, 2007.

[16] H.G. Stassen, J. Dankelman, and C.A. Grimbergen. Open versus minimally invasive surgery: a man-machine system approach. *Transactions of the Institute of Measurement and Control*, 21(4-5):151–162, 1999.

[17] M.S. Lasser and R. Ghavamian. Surgical complications of laparoscopic urological surgery. *Arab Journal of Urology*, 10(1):81–88, 2012.

[18] B. Deml, T. Ortmaier, and U. Seibold. The touch and feel in minimally invasive surgery. *Haptic Audio Visual Environments and their Applications*, page 6 pp., 2005.

[19] D.D. Marucci, A.J. Shakeshaft, J.A. Cartmill, M.R. Cox, S.G. Adams, and C.J. Martin. Grasper trauma during laparoscopic cholecystectomy. *Australian and New Zealand Journal of Surgery*, 70(8):578–581, 2000.

[20] S. Rodrigues, T. Horeman, J. Dankelman, J. Dobbelsteen, and J.W. Jansen. Suturing intraabdominal organs: when do we cause tissue damage? *Surgical Endoscopy*, 26(4):1005–1009, 2011.

[21] D.R. Seils. A comprehensive methodology for assessing biomechanical risks associated with hand tool use: Applied to laparoscopic surgical instruments. *Connecticut Graduate School*, page 99, 2012.

[22] A.L. Trejos, R.V. Patel, and M.D. Naish. Force sensing and its application in minimally invasive surgery and therapy: a survey. *Proceedings of the Institution of Mechanical Engineers, Part C: Journal of Mechanical Engineering Science*, 224(7):1435–1454, 2010.

[23] T. Ichihara, M. Takada, S. Fukumoto, T. Yasuda, and Y. Kuroda. A novel technique of finger-assisted laparoscopic surgery. *The American Journal of Surgery*, 187(2):285–287, 2004.

[24] J. Dankelman, J.J. Dobbelsteen, and P. Breedveld. Current technology on minimally invasive surgery and interventional techniques. *Instrumentation Control and Automation (ICA), 2011 2nd International Conference on*, pages 12–15, 2011.

[25] A. Wedmid, E. Llukani, and D.I. Lee. Future perspectives in robotic surgery. *BJU International*, 108(6b):1028–1036, 2011.

[26] E.J. Hanly and M.A. Talamini. Robotic abdominal surgery. *The American Journal of Surgery*, 188(4):19–26, 2004.

[27] K.C. Curley. An overview of the current state and uses of surgical robots. *Operative Techniques in General Surgery*, 7(4):155–164, 2005.

[28] C. Freschi, V. Ferrari, F. Melfi, M. Ferrari, F. Mosca, and A. Cuschieri. Technical review of the da vinci surgical telemanipulator. *The International Journal of Medical Robotics and Computer Assisted Surgery*, 9(4):396–406, 2013.

[29] P.J. Johnson, D.E. Schmidt, and U. Duvvuri. Output control of da vinci surgical system's surgical graspers. *Journal of Surgical Research*, 186(1):56–62, 2014.

[30] P. Gomes. Surgical robotics: Reviewing the past, analysing the present, imagining the future. *Robotics and Computer-Integrated Manufacturing*, 27(2):261–266, 2011.

[31] R. Richa, P. Poignet, and L. Chao. Deformable motion tracking of the heart surface. *International Conference on Intelligent Robots and Systems*, pages 3997–4003, 2008.

[32] J.F. Noguera and A. Cuadrado. Notes, manos, sils and other new laparoendoscopic techniques. *World Journal of Gastrointestinal Endoscopy*, 4(6):212–217, 2012.

[33] S. Stylianos, L. Nichols, N. Ventura, L. Malvezzi, C. Knight, and C. Burnweit. The all-in-one appendectomy: quick, scarless, and less costly. *Journal of Pediatric Surgery*, 46(12):2336–2341, 2011.

[34] S.R. Markar, A. Karthikesalingam, S. Thrumurthy, L. Muirhead, J. Kinross, and P. Paraskeva. Single-incision laparoscopic surgery (sils) vs. conventional multiport cholecystectomy: systematic review and meta-analysis. *Surgical Endoscopy*, 26(5):1205–1213, 2012.

[35] E. Lambaudie, F. Cannone, M. Bannier, M. Buttarelli, and G. Houvenaeghel. Laparoscopic extraperitoneal aortic dissection: does single-port surgery offer the same possibilities as conventional laparoscopy? *Surgical Endoscopy*, 26(7):1920–1923, 2012.

[36] J.P. Arroyo, L.A. Martin-del Campo, and G. Torres-Villalobos. Single-incision laparoscopic cholecystectomy: Is it a plausible alternative to the traditional four-port laparoscopic approach? *Minimally Invasive Surgery*, 2012:9, 2012.

[37] Y.M. Zhou, L.P. Wu, Y.F. Zhao, D.H. Xu, and B. Li. Single-incision versus conventional laparoscopy for colorectal disease: A meta-analysis. *Digestive Diseases and Sciences*, pages 1–10, 2012.

[38] T.C. Tsai, V. Lin, S.D. Chung, C.H. Ho, F.S. Jaw, and H.C. Tai. Ergonomic and geometric tricks of laparoendoscopic single-site surgery (less) by using conventional laparoscopic instruments. *Surgical Endoscopy*, pages 1–7, 2012.

[39] L. Maggiori, S. Gaujoux, E. Tribillon, F. Bretagnol, and Y. Panis. Single-incision laparoscopy for colorectal resection: a systematic review and meta-analysis of more than a thousand procedures. *Colorectal Disease*, 14(10):e643–e654, 2012.

[40] U. Bracale, P. Melillo, F. Lazzara, J. Andreuccetti, C. Stabilini, F. Corcione, and G. Pignata. Single-access laparoscopic rectal resection versus the multiport technique: A retrospective study with cost analysis. *Surgical Innovation*, 2014.

[41] P.P. Rao, P.P. Rao, and S. Bhagwat. Single-incision laparoscopic surgery - current status and controversies. *Minimal Access Surgery*, 7(1):6 – 16, 2011.

[42] K.M. Reavis and W.S. Melvin. Advanced endoscopic technologies. *Surgical Endoscopy*, 22(6):1533–1546, 2008.

[43] S. Bergman and W.S. Melvin. Natural orifice translumenal endoscopic surgery. *Surgical Clinics of North America*, 88(5):1131–1148, 2008.

[44] R. Reilink, A.M.L. Kappers, S. Stramigioli, and S. Misra. Evaluation of robotically controlled advanced endoscopic instruments. *The International Journal of Medical Robotics and Computer Assisted Surgery*, 9(2):240–246, 2013.

[45] C. Fan, D. Dodou, and P. Breedveld. Review of manual control methods for handheld maneuverable instruments. *Minimally Invasive Therapy and Allied Technologies*, 22(3):127–135, 2012.

[46] S. Bona, M. Molteni, and M. Montorsi. Minilaparoscopic colorectal resections: Technical note. *Minimally Invasive Surgery*, 2012, 2012.

[47] M.M. Tiwari, J.F. Reynoso, A.C. Lehman, A.W. Tsang, S.M. Farritor, and D. Oleynikov. In vivo miniature robots for natural orifice surgery: State of the art and future perspectives. *World Journal of Gastrointestinal Surgery*, 2(6):217–23, 2010.

[48] M.E. Rentschler, S.R. Platt, K.R. Berg, J. Dumpert, D. Oleynikov, and S.M. Farritor. Miniature in-vivo robots for remote and harsh environments. *Information Technology in Biomedicine*, 12(1):66–75, 2008.

[49] C. Bergeles and G. Yang. From passive tool holders to microsurgeons: Safer, smaller, smarter surgical robots. *Biomedical Engineering*, (99):1–1, 2013.

[50] M.C. Carrozza, A. Arena, D. Accoto, A. Menciassi, and P. Dario. A sma-actuated miniature pressure regulator for a miniature robot for colonoscopy. *Sensors and Actuators A: Physical*, 105(2):119–131, 2003.

[51] P. Dario and C.A. Mosse. Review of locomotion techniques for robotic colonoscopy. *Robotics and Automation, 2003. Proceedings. ICRA '03. IEEE International Conference on*, 1:1086–1091 vol.1, 2003.

[52] B. Behkam and M. Sitti. Design methodology for biomimetic propulsion of miniature swimming robots. *Journal of Dynamic Systems, Measurement, and Control*, 128(1):36–43, 2005.

[53] H. Visser. Grasping safely: Instruments for bowel manipulation investigated. *Mechanical Maritime and Materials Engineering*, page 140, 2003.

[54] The top 30 european manufacturers of laparoscopic instruments, devices and accessories, 2010.

[55] K.T. Boer, J.L. Herder, W. Sjoerdsma, D.W. Meijer, D.J. Gouma, and H.G. Stassen. Sensitivity of laparoscopic dissectors. *Surgical Endoscopy*, 13(9):869–873, 1999.

[56] K.A. Ball. *Endoscopic surgery*. Mosby, 1997.

[57] E.A.M. Heijnsdijk, H. Visser, J. Dankelman, and D.J. Gouma. Slip and damage properties of jaws of laparoscopic graspers. *Surgical Endoscopy And Other Interventional Techniques*, 18(6):974–979, 2004.

[58] A. Bonakdar, M. Molavi, J. Dargahi, and R. Bhat. Grasping contact analysis of tissues with semi-cylindrical teeth grasper for minimally invasive surgery applications. *ASME 2007 Summer Bioengineering Conference*, pages 689–90, 2007.

[59] E.P. Putten, J. Dobbelsteen, R. Goossens, J. Jakimowicz, and J. Dankelman. Effect of laparoscopic grasper force transmission ratio on grasp control. *Surgical Endoscopy*, 23(4):818, 2009.

[60] S.M. Sukthankar and N.P. Reddy. Towards force feedback in laparoscopic surgical tools. *Engineering in Medicine and Biology Society, 1994. Engineering Advances: New Opportunities for Biomedical Engineers. Proceedings of the 16th Annual International Conference of the IEEE*, page 1041, 1994.

[61] E.P. Putten, J.J. Dobbelsteen, R.H.M. Goossens, J.J. Jakimowicz, and J. Dankelman. Force feedback requirements for efficient laparoscopic grasp control. *Ergonomics*, 52(9):1055 – 1066, 2009.

[62] T. Dohi, R. Kikinis, T. Hu, A. Castellanos, G. Tholey, and J. Desai. *Real-Time Haptic Feedback in Laparoscopic Tools for Use in Gastro-Intestinal Surgery*, volume 2488 of *Lecture Notes in Computer Science*, pages 66–74. Springer Berlin / Heidelberg, 2002.

[63] J. Dobbelsteen, R. Lee, M. Noorden, and J. Dankelman. Indirect measurement of pinch and pull forces at the shaft of laparoscopic graspers. *Medical and Biological Engineering and Computing*, 50(3):215–221, 2012.

[64] A. Sie and T.M. Kowalewski. Quantifying forces at the tool-tissue interface of a surgical laparoscopic grasper. *Journal of Medical Devices*, 7(3):030913(1–2), 2013.

[65] W. Sjoerdsma, J.L. Herder, M.J. Horward, A. Jansen, J.J.G. Bannenberg, and C.A. Grimbergen. Force transmission of laparoscopic grasping instruments. *Minimally Invasive Therapy and Allied Technologies*, 6(4):274–278, 1997.

[66] E.A.M. Heijnsdijk, A. Pasdeloup, J. Dankelman, and D.J. Gouma. The optimal mechanical efficiency of laparoscopic forceps. *Surgical Endoscopy And Other Interventional Techniques*, 18(12):1766–1770, 2004.

[67] T. Yang, L. Xiong, J. Zhang, L. Yang, W. Huang, J. Zhou, J. Liu, Y. Su, C.K. Chui, C.L. Teo, and S. Chang. Modeling cutting force of laparoscopic scissors. *Biomedical Engineering and Informatics*, 4:1764–1768, 2010.

[68] F. Amato, M. Carbone, C. Cosentino, A. Merola, M. Morelli, and F. Zullo. A versatile mechatronic tool for minimally invasive surgery. *Biomedical Robotics and Biomechatronics*, page 192, 2006.

[69] A.W. Brown, S.I. Brown, D. McLean, Z. Wang, and A. Cuschieri. Impact of fenestrations and surface profiling on the holding of tissue by parallel occlusion laparoscopic graspers. *Surgical Endoscopy*, 28(4):1277–1283, 2014.

[70] D.D. Marucci, J.A. Cartmill, W.R. Walsh, and C.J. Martin. Patterns of failure at the instrument-tissue interface. *Journal of Surgical Research*, 93(1):16–20, 2000.

[71] A. Bonakdar, J. Dargahi, and R. Bhat. Investigations on the grasping contact analysis of biological tissues with applications in minimally invasive surgery. *American Journal of Applied Sciences*, 4(12):1016–23, 2007.

[72] J.A. Cartmill, A.J. Shakeshaft, W.R. Walsh, and C.J. Martin. High pressures are generated at the tip of laparoscopic graspers. *Australian and New Zealand Journal of Surgery*, 69(2):127–130, 1999.

[73] V. Gupta, N.P. Reddy, and P. Batur. Forces in surgical tools: comparison between laparoscopic and surgical forceps. *Engineering in Medicine and Biology Society*, 1:223, 1996.

[74] J. Bos, E. Doornebosch, J.G. Engbers, O. Nyhuis, and D. Dodou. Methods for reducing peak pressure in laparoscopic grasping. *Journal of Engineering in Medicine*, 227(12):1292–1300, 2013.

[75] S. Kota, K.J. Lu, Z. Kreiner, B. Trease, J. Arenas, and J. Geiger. Design and application of compliant mechanisms for surgical tools. *Journal of Biomechanical Engineering*, 127(6):981–989, 2005. 10.1115/1.2056561.

[76] R. Ohshima, T. Takayama, T. Omata, T. Ohya, K. Kojima, K. Takase, and N. Tanaka. Assemblable three fingered five-dof hand for laparoscopic surgery. *Robotics and Automation*, pages 3896–3901, 2008.

[77] A. Mirbagheri and F. Farahmand. A triple-jaw actuated and sensorized instrument for grasping large organs during minimally invasive robotic surgery. *The International Journal of Medical Robotics and Computer Assisted Surgery*, 9(1):83–93, 2013.

[78] T. Takayama, T. Omata, R. Oshima, M. Osaki, H. Miyamoto, K. Kojima, K. Takase, and N. Tanaka. Assemblable tools for laparoscopic surgery. *Micro-NanoMechatronics and Human Science*, pages 59–64, 2010.

[79] H. Yamashita, N. Hata, M. Hashizume, and T. Dohi. Handheld laparoscopic forceps manipulator using multi-slider linkage mechanisms. *Medical Image Computing and Computer-Assisted Intervention*, 3217:121–128, 2004.

[80] M.I. Frecker, K.M. Powell, and R. Haluck. Design of a multifunctional compliant instrument for minimally invasive surgery. *Journal of Biomechanical Engineering*, 127(6):990–993, 2005. 10.1115/1.2056560.

[81] M.I. Frecker, J. Schadler, R.S. Haluck, K. Culkar, and R. Dziedzic. Laparoscopic multifunctional instruments: Design and testing of initial prototypes. *Journal of the Society of Laparoendoscopic Surgeons*, 9(1):105–112, 2005.

[82] D.D. Marucci, J.A. Cartmill, C.J. Martin, and W.R. Walsh. A compliant tip reduces the peak pressure of laparoscopic graspers. *ANZ Journal of Surgery*, 72(7):476–478, 2002.

[83] J.H. Low, I.D. Martinez, and C.H. Yeow. Customizable soft pneumatic chamber-gripper devices for delicate surgical manipulation. *Journal of Medical Devices*, 2014.

[84] M.A. Veelen, D.W. Meijer, R.H.M. Goossens, and C.J. Snijders. New ergonomic design criteria for handles of laparoscopic dissection forceps. *Journal of Laparoendoscopic and Advanced Surgical Techniques*, 11(1):17–26, 2001.

[85] V. Boncheva, S.A. Bonney, S.E. Brooks, M. Tangney, G. O'Sullivan, A. Mirnezami, and B.A. Guinn. New targets for the immunotherapy of colon cancer-does reactive disease hold the answer? *Cancer Gene Ther*, 20(3):157–168, 2013.

[86] E. Samur, M. Sedef, C. Basdogan, L. Avtan, and O. Duzgun. A robotic indenter for minimally invasive measurement and characterization of soft tissue response. *Medical Image Analysis*, 11(4):361–373, 2007.

[87] V. Colombo, M.R. Correro, R. Riener, F.E. Weber, and L.M. Gallo. Design, construction and validation of a computer controlled system for functional loading of soft tissue. *Medical Engineering and Physics*, 33(6):677–683, 2011.

[88] J. Rosen, J.D. Brown, S. De, M. Sinanan, and B. Hannaford. Biomechanical properties of abdominal organs in vivo and postmortem under compression loads. *Journal of Biomechanical Engineering*, 130(2):021020, 2008.

[89] G.A. Holzapfel and R.W. Ogden. *Mechanics of Biological Tissue*. Springer, 2005.

[90] I. Brouwer, J. Ustin, L. Bentley, A. Sherman, N. Dhruv, and F. Tendick. Measuring in vivo animal soft tissue properties for haptic modeling in surgical simulation. *Medicine Meets Virtual Reality*, pages 69 – 74, 2001.

[91] J.M. Schwartz, M. Denninger, D. Rancourt, C. Moisan, and D. Laurendeau. Modelling liver tissue properties using a non-linear visco-elastic model for surgery simulation. *Medical Image Analysis*, 9(Copyright 2005, IEE):103–112, 2005.

[92] S.C. Cowin and S.B. Doty. *Tissue mechanics*. Springer, New York, 2007. 2006932976 Stephen C. Cowin, Stephen B. Doty. ill. ; 26 cm. Includes bibliographical references and index.

[93] R. Raghupathy and V.H. Barocas. A closed-form structural model of planar fibrous tissue mechanics. *Journal of Biomechanics*, 42(Copyright 2009, The Institution of Engineering and Technology):1424–8, 2009.

[94] H.J. Thomson, A. Busuttil, M.A. Eastwood, A.N. Smith, and R.A. Elton. The submucosa of the human colon. *Journal of Ultrastructure and Molecular Structure Research*, 96(13):22–30, 1986.

[95] R.Q. Erkamp, P. Wiggins, A.R. Skovoraoda, S.Y. Emelianov, and M. O'Donnell. Measuring the elastic modulus of small tissue samples. *Ultrasonic Imaging*, 20(1):17–28, 1998.

[96] A. Samani, J. Bishop, C. Luginbuhl, and D.B. Plewes. Measuring the elastic modulus of ex vivo small tissue samples. *Physics in Medicine and Biology*, 48(14):2183, 2003.

[97] C. Sumi, A. Suzuki, and K. Nakayama. Estimation of shear modulus distribution in soft tissue from strain distribution. *Biomedical Engineering, IEEE Transactions on*, 42(2):193–202, 1995.

[98] J.R. McLaughlin, N. Zhang, and A. Manduca. Calculating tissue shear modulus and pressure by 2d log-elastographic methods. *Inverse Problems*, 26(8):085007, 2010.

[99] S. Bourgouin, T. Bge, C. Masson, P.J. Arnoux, J. Mancini, S. Garcia, C. Brunet, and S. Berdah. Biomechanical characterisation of fresh and cadaverous human small intestine: applications for abdominal trauma. *Medical and Biological Engineering and Computing*, 50(12):1279–1288, 2012.

[100] S. De, J. Rosen, A. Dagan, B. Hannaford, P. Swanson, and Mika Sinanan. Assessment of tissue damage due to mechanical stresses. *The International Journal of Robotics Research*, 26(11-12):1159, 2007.

[101] K. Comley and N.A. Fleck. A micromechanical model for the young's modulus of adipose tissue. *International Journal of Solids and Structures*, 47(21):2982–2990, 2010.

[102] S. Cheng, E.C. Clarke, and L.E. Bilston. The effects of preconditioning strain on measured tissue properties. *Journal of Biomechanics*, 42(9):1360–1362, 2009. doi: 10.1016/j.jbiomech.2009.03.023.

[103] C.V.C. Bouten, R.G.M. Breuls, E.A.G. Peeters, C.W.J. Oomens, and F.P.T. Baaijens. In vitro models to study compressive strain-induced muscle cell damage. *Biorheology*, 40:383–388, 2003.

[104] Y.N. Wang, C.V.C. Bouten, D.A. Lee, and D.L. Bader. Compression-induced damage in a muscle cell model in vitro. *Proceedings of the Institution of Mechanical Engineers, Part H: Journal of Engineering in Medicine*, 219(1):1–12, 2005.

[105] Y.C. Fung. *Biomechanics - Mechanical properties of living tissues*. Springer-Verlag, New York, NY, USA, 1981.

[106] J.L. Katz. Hard tissue as a composite material - i. bounds on the elastic behavior. *Journal of Biomechanics*, 4(5):455–473, 1971.

[107] B. Ji and H. Gao. Elastic properties of nanocomposite structure of bone. *Composites Science and Technology*, 66(9):1212–1218, 2006.

[108] W.C. Oliver and G.M. Pharr. Measurement of hardness and elastic modulus by instrumented indentation: Advances in understanding and refinements to methodology. *Journal of Materials Research*, 19(01):3–20, 2004.

[109] G. Forgacs, R.A. Foty, Y. Shafrir, and M.S. Steinberg. Viscoelastic properties of living embryonic tissues: a quantitative study. *Biophysical Journal*, 74(5):2227–2234, 1998.

[110] B.K. Tay, K. Jung, and M.A. Srinivasan. In vivo mechanical behavior of intra-abdominal organs. *IEEE Transactions on Biomedical Engineering*, 53(Copyright 2006, The Institution of Engineering and Technology):2129–38, 2006.

[111] N.B. Narayanan, A. Bonakdar, J. Dargahi, M. Packirisamy, and R. Bhat. Design and analysis of a micromachined piezoelectric sensor for measuring the viscoelastic properties of tissues in minimally invasive surgery. *Smart Materials and Structures*, 15(6):1684, 2006.

[112] L.A. Taber. *Nonlinear theory of elasticity: applications in biomechanics*. World Scientific, 2004.

[113] X. Wang, C. Natali, M. Beccani, M. Kern, P. Valdastri, and M. Rentschler. Novel medical wired palpation device: A validation study of material properties. *Solid-State Sensors, Actuators and Microsystems*, pages 1653–1658, 2013.

[114] S. Meghezi, F. Couet, P. Chevallier, and D. Mantovani. Effects of a pseudophysiological environment on the elastic and viscoelastic properties of collagen gels. *International Journal of Biomaterials*, 2012:9, 2012.

[115] P. Provenzano, R. Lakes, T. Keenan, and R. Vanderby Jr. Nonlinear ligament viscoelasticity. *Annals of Biomedical Engineering*, 29(10):908–914, 2001.

[116] Y.J. Lim, D. Deo, T.P. Singh, D.B. Jones, and S. De. In situ measurement and modeling of biomechanical response of human cadaveric soft tissues for physics-based surgical simulation. *Surgical Endoscopy*, 23(6):1298–1307, 2009.

[117] C. Bellini, P. Glass, M. Sitti, and E.S. Di Martino. Biaxial mechanical modeling of the small intestine. *Journal of the Mechanical Behavior of Biomedical Materials*, 4(8):1727–1740, 2011.

[118] H.D. Hoeg, A.B. Slatkin, J.W. Burdick, and W.S. Grundfest. Biomechanical modeling of the small intestine as required for the design and operation of a robotic endoscope. *IEEE International Conference on Robotics and Automation, 2000*, 2:1599–1606, 2000.

[119] M. Higa, Y. Luo, T. Okuyama, Y. Shiraishi, H. Liu, T. Yambe, T. Takagi, R. Magjarevic, and J.H. Nagel. *In vivo measurements and constitutive modeling of colon tissue*, volume 14 of *IFMBE Proceedings*, pages 3186–3189. Springer Berlin Heidelberg, 2007.

[120] A. Nava, E. Mazza, M. Furrer, P. Villiger, and W.H. Reinhart. In vivo mechanical characterization of human liver. *Medical Image Analysis*, 12(2):203–216, 2008.

[121] Y. Qiao, E. Pan, S.S. Chakravarthula, F. Han, J. Liang, and S. Gudlavalleti. Measurement of mechanical properties of rectal wall. *Journal of Materials Science: Materials in Medicine*, 16(2):183–188, 2005.

[122] D.C. Lin, E.K. Dimitriadis, and F. Horkay. Robust strategies for automated afm force curve analysis—i. non-adhesive indentation of soft, inhomogeneous materials. *Journal of Biomechanical Engineering*, 129(3):430–440, 2007.

[123] D. Schwenninger, S. Schumann, and J. Guttmann. In vivo characterization of mechanical tissue properties of internal organs using endoscopic microscopy and inverse finite element analysis. *Journal of Biomechanics*, 44(3):487–493, 2011.

[124] X. Li, G. Wang, L. Huang, and G. Zhang. Young's modulus extraction methods for soft tissue from ultrasound measurement system. *Instrumentation Science and Technology*, 34:393–404, 2006.

[125] A.L. Weisenhorn, M. Khorsandi, S. Kasas, V. Gotzos, and H.J. Butt. Deformation and height anomaly of soft surfaces studied with an afm. *Nanotechnology*, 4(2):106, 1993.

[126] J.Z. Wu, R.G. Dong, and A.W. Schopper. Analysis of effects of friction on the deformation behavior of soft tissues in unconfined compression tests. *Journal of Biomechanics*, 37(1):147–155, 2004.

[127] B.D. Hoffman, G. Massiera, K.M. van Citters, and J.C. Crocker. The consensus mechanics of cultured mammalian cells. *Proceedings of the National Academy of Sciences*, 103(27):10259–10264, 2006.

[128] J.D. Brown, J. Rosen, Y.S. Kim, L. Chang, M.N. Sinanan, and B. Hannaford. In-vivo and in-situ compressive properties of porcine abdominal soft tissues. *Medicine Meets Virtual Reality*, 11:26–32, 2003.

[129] C. Gao and H. Gregersen. Biomechanical and morphological properties in rat large intestine. *Journal of Biomechanics*, 33(9):1089–1097, 2000.

[130] D.P. Sokolis, I.K. Orfanidis, and M. Peroulis. Biomechanical testing and material characterization for the rat large intestine: regional dependence of material parameters. *Physiological Measurement*, 32(12):1969, 2011.

[131] S.E. Cross, Y.S. Jin, J. Rao, and J.K. Gimzewski. Nanomechanical analysis of cells from cancer patients. *Nat Nano*, 2(12):780–783, 2007. 10.1038/nnano.2007.388.

[132] J. Cinats, D.C. Reid, and J.B. Haddow. A biomechanical evaluation of sorbothane. *Clinical Orthopaedics and Related Research*, 222:281–288, 1985.

[133] H.A. Mansy, J.R. Grahe, and R.H. Sandler. Elastic properties of synthetic materials for soft tissue modeling. *Physics in Medicine and Biology*, 53(8):2115, 2008.

[134] I. Ionescu, J.E. Guilkey, M. Berzins, R.M. Kirby, and J.A. Weiss. Simulation of soft tissue failure using the material point method. *Journal of Biomechanical Engineering*, 128(6):917–924, 2006.

[135] P. Schrenk, R. Woisetschlger, R. Rieger, and W. Wayand. Mechanism, management, and prevention of laparoscopic bowel injuries. *Gastrointestinal Endoscopy*, 43(6):572–574, 1996.

[136] S. De. The grasper-tissue interface in minimally invasive surgery : stress and acute indicators of injury. *PhD Thesis*, 2008.

[137] N. Famaey, E. Verbeken, S. Vinckier, B. Willaert, P. Herijgers, and J.V. Sloten. In vivo soft tissue damage assessment for applications in surgery. *Medical Engineering and Physics*, 32(5):437, 2010.

[138] U. Hildebrandt, K. Kessler, T. Plusczyk, G. Pistorius, B. Vollmar, and M.D. Menger. Comparison of surgical stress between laparoscopic and open colonic resections. *Surgical Endoscopy*, 17(2):242–246, 2003.

[139] M.S.R. Jakeways, V. Mitchell, I.A. Hashim, S.J.D. Chadwick, A. Shenkin, C.J. Green, and F. Carli. Metabolic and inflammatory responses after open or laparoscopic cholecystectomy. *British Journal of Surgery*, 81(1):127–131, 1994.

[140] S.S.G. Yadav and R.V. Krishnaiah. Haptic science and technology. *International Journal of Computer Engineering and Applications*, 2(1-3):8, 2013.

[141] C.R. Wagner, N. Stylopoulos, P.G. Jackson, and R.D. Howe. The benefit of force feedback in surgery: Examination of blunt dissection. *Presence: Teleoperators and Virtual Environments*, 16(3):252–262, 2007.

[142] R.S. Dahiya, G. Metta, M. Valle, and G. Sandini. Tactile sensing - from humans to humanoids. *Robotics*, 26(1):1–20, 2010.

[143] J. Tegin. Tactile sensing in intelligent robotic manipulationa review. *Industrial Robot: An International Journal*, 32(1):64–70, 2005.

[144] P. Puangmali, K. Althoefer, L.D. Seneviratne, D. Murphy, and P. Dasgupta. State-of-the-art in force and tactile sensing for minimally invasive surgery. *IEEE Sensors Journal*, 8:371–81, 2008.

[145] D.H. Kim, S. Wang, H. Keum, R. Ghaffari, Y.S. Kim, H. Tao, B. Panilaitis, M. Li, Z. Kang, F. Omenetto, Y. Huang, and J.A. Rogers. Thin, flexible sensors and actuators as instrumented surgical sutures for targeted wound monitoring and therapy. *Small*, 8(21):3263–3268, 2012.

[146] A.H. Gosline, V. Arabagi, A. Kassam, and P.E. Dupont. Achieving biocompatibility in soft sensors for surgical robots. *The Hamlyn Symposium on Medical Robotics*, pages 5–6, 2013.

[147] X. Hui, L. Hongbin, L. Shan, L.D. Seneviratne, and K. Althoefer. Fiber optics tactile array probe for tissue palpation during minimally invasive surgery. *Intelligent Robots and Systems (IROS)*, pages 2539–2544, 2013.

[148] M.Y. Cheng, C.L. Lin, and Y.J. Yang. Tactile and shear stress sensing array using capacitive mechanisms with floating electrodes. *Micro Electro Mechanical Systems (MEMS), 2010 IEEE 23rd International Conference on*, pages 228–231, 2010.

[149] C.G. Li and J.J. Shen. Design and analysis of a tactile sensor used in minimally invasive surgery. *Advanced Intelligent Mechatronics (AIM)*, pages 1454–1457, 2013.

[150] D. Zbyszewski, A. Bhaumik, K. Althoefer, and L.D. Seneviratne. Tactile sensing using a novel air cushion sensor: A feasibility study. *Intelligent Robots and Systems*, pages 41–46, 2008.

[151] D. Zbyszewski, P. Polygerinos, L.D. Seneviratne, and K. Althoefer. A novel mri compatible air-cushion tactile sensor for minimally invasive surgery. *Intelligent Robots and Systems*, pages 2647–2652, 2009.

[152] P.J. Codd, A. Veaceslav, A.H. Gosline, and P.E. Dupont. Novel pressure-sensing skin for detecting impending tissue damage during neuroendoscopy. *Journal of Neurosurgery: Pediatrics*, 13(1):114–121, 2014.

[153] R.S. Dahiya, A. Adami, M. Valle, L. Lorenzelli, and G. Metta. Cmos implementation of posfet tactile sensing arrays with on chip readout. *Sensor Technologies and Applications*, pages 80–83, 2010.

[154] R.S. Dahiya, L. Lorenzelli, G. Metta, and M. Valle. Posfet devices based tactile sensing arrays. *Circuits and Systems*, pages 893–896, 2010.

[155] M.Y. Cheng, C.M. Tsao, Y.Z. Lai, and Y.J. Yang. The development of a highly twistable tactile sensing array with stretchable helical electrodes. *Sensors and Actuators A: Physical*, In Press, Corrected Proof, 2011.

[156] F.L. Hammond, R.K. Kramer, W. Qian, R.D. Howe, and R.J. Wood. Soft tactile sensor arrays for micromanipulation. *International Conference on Intelligent Robots and Systems (IROS)*, pages 25–32, 2012.

[157] F.L. Hammond, R.K. Kramer, W. Qian, R.D. Howe, and R.J. Wood. Soft tactile sensor arrays for force feedback in micromanipulation. *Sensors Journal*, 14(5):1443–1452, 2014.

[158] A.L. Trejos, S. Jayaraman, R. Patel, M. Naish, and C. Schlachta. Force sensing in natural orifice transluminal endoscopic surgery. *Surgical Endoscopy*, 25(1):186–192, 2010.

[159] S.K. Prasad, M. Kitagawa, G.S. Fischer, J. Zand, M.A. Talamini, R.H. Taylor, and A.M. Okamura. *A Modular 2-DOF Force-Sensing Instrument For Laparoscopic Surgery*, volume 2878 of *Lecture Notes in Computer Science*, chapter 35, pages 279–286. Springer Berlin Heidelberg, 2003.

[160] G. Tholey, A. Pillarisetti, W. Green, and J.P. Desai. Design, development, and testing of an automated laparoscopic grasper with 3-d force measurement capability. *Medical Simulation International Symposium*, pages 38–48, 2004.

[161] G. Tholey and J.P. Desai. A modular, automated laparoscopic grasper with three-dimensional force measurement capability. *2007 IEEE International Conference on Robotics and Automation, 10-14 April 2007*, page 6 pp., 2007.

[162] N. Zemiti, G. Morel, T. Ortmaier, and N. Bonnet. Mechatronic design of a new robot for force control in minimally invasive surgery. *Mechatronics*, 12(2):143–153, 2007.

[163] G.B. Hanna, T. Drew, G. Arnold, M. Fakhry, and A. Cuschieri. Development of force measurement system for clinical use in minimal access surgery. *Surgical Endoscopy*, 22(2):467–471, 2008.

[164] J.L. Herder, M.J. Horward, and W. Sjoerdsma. A laparoscopic grasper with force perception. *Minimally Invasive Therapy and Allied Technologies*, 6(4):279–286, 1997.

[165] G.S. Fischer, T. Akinbiyi, S. Saha, J. Zand, M. Talamini, M. Marohn, and R. Taylor. Ischemia and force sensing surgical instruments for augmenting available surgeon information. *Biomedical Robotics and Biomechatronics*, page 1030, 2006.

[166] P. Dubois, Q. Thommen, and A.C. Jambon. In vivo measurement of surgical gestures. *IEEE Transactions on Biomedical Engineering*, 49(Copyright 2002, IEE):49–54, 2002.

[167] H. Visser, E.A.M. Heijnsdijk, J.L. Herder, and P.V. Pistecky. Forces and displacements in colon surgery. *Surgical Endoscopy And Other Interventional Techniques*, 16(10):14263–1430, 2002.

[168] K. Vakili, M.S. Flander, T.R. Sepp, M. Corral, J.D. Diaz, A. Slocum, and G.S.L. Teo. Design and testing of a pressure sensing laparoscopic grasper. *Design of Medical Devices*, 2011.

[169] M.J.H. Lum, D. Trimble, J. Rosen, K. Fodero, H.H. King, G. Sankaranarayanan, J. Dosher, R. Leuschke, B. Martin-Anderson, M.N. Sinanan, and B. Hannaford. Multidisciplinary approach for developing a new minimally invasive surgical robotic system. *Biomedical Robotics and Biomechatronics*, page 841, 2006.

[170] J. Rosen, J.D. Brown, L. Chang, M.N. Sinanan, and B. Hannaford. Generalized approach for modeling minimally invasive surgery as a stochastic process using a discrete markov model. *Biomedical Engineering, IEEE Transactions on*, 53(3):399, 2006.

[171] N. Sgambelluri, G. Valenza, M. Ferro, G. Pioggia, E.P. Scilingo, D. Rossi, and A. Bicchi. An artificial neural network approach for haptic discrimination in minimally invasive surgery. *The 16th IEEE International Symposium on Robot and Human interactive Communication*, pages 25–30, 2007.

[172] J. Rosen, M. Barreca, L. Chang, B. Hannaford, and M. Sinanan. The blue dragon-a system for monitoring the kinematics and the dynamics of endoscopic tools in minimally invasive surgery for objective laparoscopic skill assessment. *Medicine Meets Virtual Reality*, pages 412–416, 2002.

[173] E. Petter, M. Biehl, and J.U. Meyer. Vibrotactile palpation instrument for use in minimal invasive surgery. *Engineering in Medicine and Biology Society*, vol.1:179–80, 1997.

[174] M. Ottermo. Virtual palpation gripper. *Engineering Cybernetics*, PhD:115, 2006.

[175] J.D. Brown, J. Rosen, L. Chang, M.N. Sinanan, and B. Hannaford. Quantifying surgeon grasping mechanics in laparoscopy using the blue dragon system. *Medicine Meets Virtual Reality*, 12:34–36, 2004.

[176] J. Rosen, B. Hannaford, M.P. MacFarlane, and M.N. Sinanan. Force controlled and teleoperated endoscopic grasper for minimally invasive surgery-experimental performance evaluation. *IEEE Transactions on Biomedical Engineering*, 46(10):1212–21, 1999.

[177] M. Tavakoli, R.V. Patel, and M. Moallem. Bilateral control of a teleoperator for soft tissue palpation: Design and experiments. *International Conference on Robotics and Automation*, 2006:3280–3285, 2006.

[178] D.A. Kontarinis, J.S. Son, W. Peine, and R.D. Howe. A tactile shape sensing and display system for teleoperated manipulation. *Robotics and Automation*, 1:641–646, 1995.

[179] K. Tadano and K. Kawashima. Development of 4-dofs forceps with force sensing using pneumatic servo system. *Robotics and Automation, 2006. ICRA 2006. Proceedings 2006 IEEE International Conference on*, page 2250, 2006.

[180] G. Tholey and J.P. Desai. A compact and modular laparoscopic grasper with tridirectional force measurement capability. *Journal of Medical Devices*, 2(3):031001, 2008.

[181] A.L. Trejos, A.C. Lyle, A. Escoto, M.D. Naish, and R.V. Patel. Force/position-based modular system for minimally invasive surgery. *IEEE International Conference on Robotics and Automation*, pages 3660–3665, 2010.

[182] J.D. Brown. In-vivo and postmortem biomechanics of abdominal organs under compressive loads: Experimental approach in a laparoscopic surgery setup. *PhD Thesis*, 2003.

[183] J.D. Brown, J. Rosen, M. Moreyra, M. Sinanan, and B. Hannaford. Computer-controlled motorized endoscopic grasper for in-vivo measurements of soft tissue biomechanical characteristics. *Medicine Meets Virtual Reality*, 10(2):71–73, 2003.

[184] M.M. Dalvand, B. Shirinzadeh, A.H. Shamdani, J. Smith, and Y. Zhong. An actuated force feedback-enabled laparoscopic instrument for robotic-assisted surgery. *The International Journal of Medical Robotics and Computer Assisted Surgery*, 10(1):11–21, 2014.

[185] H. Yussof, M. Ohka, A.R. Omar, and M.A. Ayub. Determination of object stiffness control parameters in robot manipulation using a prototype optical three-axis tactile sensor. *Sensors*, pages 992–995, 2008.

[186] F. Xie, J. A., and Z. Hao. A novel piezoelectric device with dual functions of studying biological soft tissues. *Biomedical Engineering and Informatics (BMEI)*, 4:2360–2364, 2011.

[187] A. Stekelenburg, C.W.J. Oomens, G.J. Strijkers, L. de Graaf, D.L. Bader, and K. Nicolay. A new mr-compatible loading device to study in vivo muscle damage development in rats due to compressive loading. *Medical Engineering and Physics*, 28(4):331–338, 2006.

[188] K. Ikuta, T. Kato, H. Ooe, and S. Ando. 'surgery recorder system' for recording position and force of forceps during laparoscopic surgery. *Advanced intelligent mechatronics, 2007 IEEE/ASME international conference on*, page 1, 2007.

[189] K.U. Kyung, S.W. Son, G.H. Yang, and D.S. Kwon. How to effectively display surface properties using an integrated tactile display system. *IEEE International Conference on Robotics and Automation*, 2005:1761–1766, 2005.

[190] K. Deng and E.T. Enikov. Design and development of a pulsed electromagnetic micro-actuator for 3d virtual tactile displays. *Mechatronics*, 20(4):503–509, 2010.

[191] C.R. Wagner, S.J. Lederman, and R.D. Howe. A tactile shape display using rc servomotors. *Haptic Interfaces for Virtual Environment and Teleoperator Systems*, pages 354–355, 2002.

[192] K. Fukuyama, N. Takahashi, Z. Feng, and H. Sawada. Tactile display using the vibration of sma wires and the evaluation of perceived sensations. *Human System Interactions*, pages 685–690, 2009.

[193] R.D. Howe, D.A. Kontarinis, and W.J. Peine. Shape memory alloy actuator controller design for tactile displays. *Proceedings of 1995 34th IEEE Conference on Decision and Control, 13-15 Dec. 1995*, vol.4:3540–4, 1995.

[194] K.A. Kaczmarek, K. Nammi, A.K. Agarwal, M.E. Tyler, S.J. Haase, and D.J. Beebe. Polarity effect in electrovibration for tactile display. *Biomedical Engineering*, 53(10):2047–2054, 2006.

[195] C. Li, H. Yao, J. Xu, Y. Zhang, and B. Kuang. A plate tuning fork shaped tactile display using elastic waves. *Haptic interfaces for virtual environment and teleoperator systems, 2008. haptics 2008. symposium on*, pages 375–376, 2008.

[196] M. Oyarzabal, M. Nakatani, and R.D. Howe. Vibration enhances geometry perception with tactile shape displays. *Haptic Interfaces for Virtual Environment and Teleoperator Systems*, pages 44–49, 2007.

[197] M. Zhou and C.G.L. Cao. Vibrotactile feedback improves laparoscopic palpation skills. *Human Factors and Ergonomics Society Annual Meeting*, 2:738–742, 2009.

[198] K.U. Kyung and J.S. Park. Ubi-pen: Development of a compact tactile display module and its application to a haptic stylus. *Haptic Interfaces for Virtual Environment and Teleoperator Systems*, pages 109–114, 2007.

[199] C. Wottawa, R.E. Fan, C.E. Lewis, B. Jordan, M.O. Culjat, W.S. Grundfest, and E.P. Dutson. Laparoscopic grasper with an integrated tactile feedback system. *Complex Medical Engineering*, pages 1–5, 2009.

[200] T. Hu, A.E. Castellanos, G. Tholey, and J.P. Desai. Real-time haptic feedback in laparoscopic tools for use in gastro-intestinal surgery. *Medical Image Computing and Computer-Assisted Intervention*, pages 66–74, 2002.

[201] A. Hamam, M. Eid, and A. El Saddik. Effect of kinesthetic and tactile haptic feedback on the quality of experience of edutainment applications. *Multimedia Tools and Applications*, pages 1–18, 2012.

[202] S. Payandeh and T. Li. Toward new designs of haptic devices for minimally invasive surgery. *International Congress Series*, 1256(0):775–781, 2003.

[203] S. Schostek, M.O. Schurr, and G.F. Buess. Review on aspects of artificial tactile feedback in laparoscopic surgery. *Medical Engineering and Physics*, 31:887–98, 2009.

[204] H. Chen, W. Wu, H. Sun, and P.A. Heng. Dynamic touch-enabled virtual palpation. *Computer Animation and Virtual Worlds*, 18(The Institution of Engineering and Technology):339–48, 2007.

[205] M. Cheng, J. Passenger, O. Salvado, S. Riek, S. Ourselin, and M. Watson. Pneumatic haptic interface fuzzy controller for simulation of abdominal palpations during colonoscopy. *EuroHaptics conference, 2009 and Symposium on Haptic Interfaces for Virtual Environment and Teleoperator Systems. World Haptics 2009. Third Joint*, pages 250–255, 2009.

[206] M. Lazeroms, A. Haye, W. Sjoerdsma, W. Schreurs, W. Jongkind, G. Honderd, and C. Grimbergen. A hydraulic forceps with force-feedback for use in minimally invasive surgery. *Mechatronics*, 6(4):437–446, 1996.

[207] R.D. Howe, W.J. Peine, D.A. Kantarinis, and J.S. Son. Remote palpation technology. *IEEE Engineering in Medicine and Biology Magazine*, 14:318–323, 1995.

[208] T. Alja'afreh. Controlling force variations during soft-tissue grasping. *Proceedings of the Institution of Mechanical Engineers, Part H: Journal of Engineering in Medicine*, 223(6):749, 2009.

[209] M. Tavakoli, R.V. Patel, and M. Moallem. A force reflective master-slave system for minimally invasive surgery. *Intelligent Robots and Systems*, 4:3077, 2003.

[210] J.C. Gwilliam, Z. Pezzementi, E. Jantho, A.M. Okamura, and S. Hsiao. Human vs. robotic tactile sensing: Detecting lumps in soft tissue. *IEEE Haptics Symposium*, pages 21–28, 2010.

[211] K. Houston, A. Sieber, C. Eder, O. Tonet, A. Menciassi, and P. Dario. Novel haptic tool and input device for real time bilateral biomanipulation addressing endoscopic surgery. *Engineering in Medicine and Biology*, pages 198–201, 2007.

[212] G. Tholey, J.P. Desai, and A.E. Castellanos. *Evaluating the Role of Vision and Force Feedback in Minimally Invasive Surgery: New Automated Laparoscopic Grasper and A Case Study*, volume 2878 of *Lecture Notes in Computer Science*, pages 198–205. Springer Berlin / Heidelberg, 2003.

[213] G. Tholey and J.P. Desai. Design and development of a general purpose 7 dof haptic device. *Haptic Interfaces for Virtual Environment and Teleoperator Systems*, pages 95–101, 2006.

[214] G. Tholey and J.P. Desai. A general-purpose 7 dof haptic device: Applications toward robot-assisted surgery. *Mechatronics, IEEE/ASME Transactions on*, 12(6):662–669, 2007.

[215] S.M. Sukthankar and N.P. Reddy. *Force feedback issues in minimally invasive surgery*. Interactive Technology and the New Paradigm for Healthcare. 1995.

[216] E.P. Putten, M. Hajian, R. Goossens, J. Dobbelsteen, and J. Jakimowicz. A laparoscopic grasper handle with integrated augmented tactile feedback, designed for training grasp control. *Haptics: Generating and Perceiving Tangible Sensations*, vol.2:243–50, 2010.

[217] A. Spiers, S. Baillie, T. Pipe, and R. Persad. Experimentally driven design of a palpating gripper with minimally invasive surgery considerations. *Haptics Symposium (HAPTICS)*, pages 261–266, 2012.

[218] E.P. Putten, M.C.J. Berben, R.H.M. Goossens, J.J. Jakimowicz, and J. Dankelman. The opinion and experience of surgeons with laparoscopic bowel grasper haptics. *Biomedical Science and Engineering*, 3:422–429, 2010.

[219] J. Kim, B. Ahn, Y. Kim, and J. Kim. Inclusion detection with haptic-palpation system for medical telediagnosis. *Engineering in Medicine and Biology Society*, pages 4595–4598, 2009.

[220] S.M. Khadem, S. Behzadipour, M. Boroushaki, F. Farahmand, and M. Tavakoli. Design and implementation of an emotional learning controller for force control of a robotic laparoscopic instrument. *2014*, 1(3):168–181, 2014.

[221] M. Beccani, C. Di Natali, M.E. Rentschler, and P. Valdastri. Wireless tissue palpation: Proof of concept for a single degree of freedom. *IEEE International Conference on Robotics and Automation*, pages 711–717, 2013.

[222] M. Beccani, C. Natali, M. Rentschler, and P. Valdastri. Uniaxial wireless tissue palpation device for minimally invasive surgery. *Journal of Medical Devices*, 7(2):1–3, 2013. 10.1115/1.4024331.

[223] S. Payandeh. Force propagation models in laparoscopic tools and trainers. *Engineering in Medicine and Biology Society*, 3:957, 1997.

[224] K.S. Lehmann, C. Holmer, S. Gillen, J. Grne, U. Zurbuchen, J.P. Ritz, and H.J. Buhr. Suitability of a virtual reality simulator for laparoscopic skills assessment in a surgical training course. *International Journal of Colorectal Disease*, 28(4):563–571, 2012.

[225] J. Rosen, B. Hannaford, C.G. Richards, and M.N. Sinanan. Markov modeling of minimally invasive surgery based on tool/tissue interaction and force/torque signatures for evaluating surgical skills. *Biomedical Engineering, IEEE Transactions on*, 48(5):579, 2001.

[226] A.L. Trejos, R.V. Patel, R.A. Malthaner, and C.M. Schlachta. Development of force-based metrics for skills assessment in minimally invasive surgery. *Surgical Endoscopy*, pages 1–14, 2014.

[227] C.R. Wottawa, J.R. Cohen, R.E. Fan, J.W. Bisley, M.O. Culjat, W.S. Grundfest, and E.P. Dutson. The role of tactile feedback in grip force during laparoscopic training tasks. *Surgical Endoscopy*, 27(4):1111–1118, 2013.

[228] J. Slieker, H. Theeuwes, G. Rooijen, J. Lange, and G.J. Kleinrensink. Training in laparoscopic colorectal surgery: a new educational model using specially embalmed human anatomical specimen. *Surgical Endoscopy*, pages 1–6, 2012.

[229] R.E. Willis, P.P. Gomez, S.J. Ivatury, H.S. Mitra, and K.R. Van Sickle. Virtual reality simulators: Valuable surgical skills trainers or video games? *Journal of Surgical Education*, 2014.

[230] T. Horeman, J. Dankelman, F.W. Jansen, and J.J. Dobbelsteen. Assessment of laparoscopic skills based on force and motion parameters. *Biomedical Engineering, IEEE Transactions on*, 61(3):805–813, 2014.

[231] P.A. Shields. A novel electronic laparoscopic training device. *Seymour and Esther Padnos School of Engineering and Computing*, Masters of Science in Engineering with Biomedical Emphasis:77, 2012.

[232] P. Empel, L. Rijssen, J. Commandeur, M. Verdam, J. Huirne, F. Scheele, H.J. Bonjer, and W.J. Meijerink. Validation of a new box trainer-related tracking device: the trendo. *Surgical Endoscopy*, pages 1–7, 2012.

[233] T. Horeman, S. Rodrigues, F.W. Jansen, J. Dankelman, and J. Dobbelsteen. Force measurement platform for training and assessment of laparoscopic skills. *Surgical Endoscopy*, 24(12):3102–3108, 2010.

[234] S.Y. Kim, K.U. Kyung, J. Park, and D.S. Kwon. Real-time area-based haptic rendering and the augmented tactile display device for a palpation simulator. *Advanced Robotics*, 21(Compendex):961–981, 2007.

[235] S. Gillen, J. Grne, F. Kndgen, P. Wolf, M. Meyer, H. Friess, H.J. Buhr, J.P Ritz, H. Feussner, and K. Lehmann. Educational and training aspects of new surgical techniques: experience with the endoscopiclaparoscopic interdisciplinary training entity (elite) model in training for a natural orifice translumenal endoscopic surgery (notes) approach to appendectomy. *Surgical Endoscopy*, pages 1–7, 2012.

[236] C. Loukas, N. Nikiteas, D. Schizas, V. Lahanas, and E. Georgiou. A head-to-head comparison between virtual reality and physical reality simulation training for basic skills acquisition. *Surgical Endoscopy*, pages 1–9, 2012.

[237] A.J. Debes, R. Aggarwal, I. Balasundaram, and M.B. Jacobsen. A tale of two trainers: virtual reality versus a video trainer for acquisition of basic laparoscopic skills. *The American Journal of Surgery*, 199(6):840–845, 2010.

[238] P. Lamata, E.J. Gomez, F.L. Hernandez, A.O. Pastor, F.M. Sanchez-Margallo, and F. del Pozo Guerrero. Understanding perceptual boundaries in laparoscopic surgery. *IEEE Transactions on Biomedical Engineering*, 55(Compendex):866–873, 2008.

[239] A.V. Bartrol, R. Wegenkittl, A. Knig, and E. Grller. Nonlinear virtual colon unfolding. *Proceedings of the conference on Visualization'01*, pages 411–420, 2001.

[240] J. Barrie. "private communication". *University of Leeds, UK*, 2014.

[241] Z. Ehteshami. "private communication". *University of Leeds, UK*, 2014.

Appendix A

3.0 CONNECTIONS

3.1 Connections General

Transducer, supply and output connections are made by 4 x 4 way screw-clamp terminals as shown in Fig 1.

To reverse output polarity, reverse signal hi/signal lo. Voltage output is between Volts Out and common, current output is between current out and common.

WARNING: INCORRECT SUPPLY CONNECTION, E.G. CONNECTING SUPPLY WIRE TO OUTPUT (O/P) MAY DAMAGE THE UNIT AND INVALIDATE THE WARRANTY.

Fig. 1 Connections

1	Excitation Hi
2	Excitation Lo
3	Signal Hi
4	Signal Lo
5	Screen
6	R. Cal com
7	R. Cal
8	CAL
9	Volts Out
10	Common
11	Common
12	Current Out
13	Supply +
14	Supply -
15	Screen
16	N/C

3.2 Internal Controls

To access internal controls the front part of the DR7DC case needs to be removed. To do this, use a small screw driver to gently press in the clips behind terminal 1-4 and 13-16. At the same time pull forward the front of the case. The front of the case and pcb assembly should now slide forward.

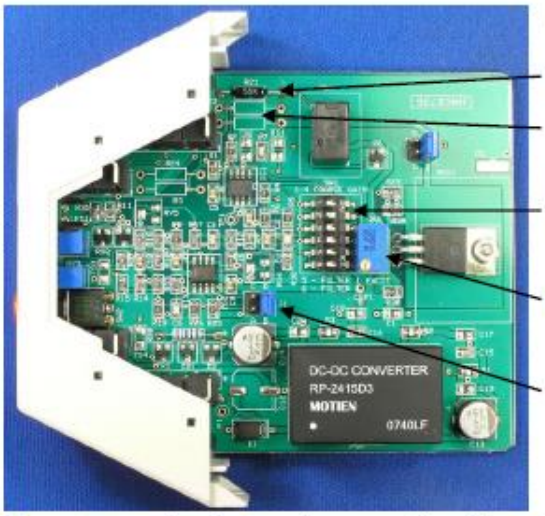

Fig. 2 Internal Controls

Shunt Calibration Resistor

Bridge Completion Resistors (section 3.5)

1-4 Coarse Gain (section 4.5)
5-6 Bandwidth/Noise filter (section 4.7)

Transducer excitation (section 4.2)

4-20mA Offset Link J1 (section 4.8)

To put case back together, gently slide pcb assembly into case guide slots. Ensure pcb earth pad CG1 is lined up with the earth clip inside the case, and push back until the front of the case clicks back into place.

3.3 Transducer connections

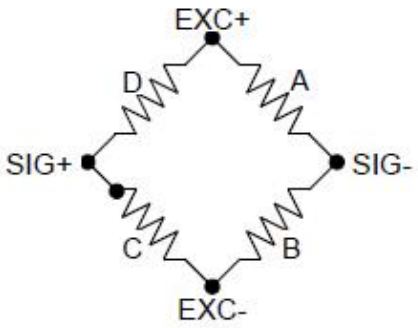

Before connecting the transducer, check the excitation voltage.

Applying an excitation voltage that is too high may destroy the transducer

3.4 Full bridge Strain Gauge Transducer

Transducer connector details are as shown in Fig. 1. (Section 3.1)

3.5 1/4 or 1/2 bridge transducer connections

For 1/4 bridge transducers, 3 bridge completion resistors are required. The active gauge should be fitted on arm 'C' and the bridge completion resistors in arms D, A & B.

For 1/2 bridge systems, the active gauges should be C and D, and 2 completion resistors are required.

The bridge completion resistors should be high stability, the same resistance as the active gauge and may be fitted either in the transducer connector, or in the designated position on the DR7DC PCB. This requires removal of the PCB from the case.

R22 replaces bridge arm D, R23 replaces bridge arm A, R24 replaces bridge arm B

Note: Mounting these resistors in the instrument is a compromise. To reduce temperature and long lead effects, completion resistors should preferably be mounted at the transducer and be of close tolerance and low t.c., e.g. 0.1%, 15 ppm..

3.6 Potentiometric Transducers

Select R24 value to drop at least 1.5V. For example, with an excitation of say 10V and a potentiometer resistance of 500 ohms and R24 value of 100 Ohms, the voltage drop across R24 = 10V / (500+100) X 100 = 1.7V.

This raises terminal 4 to within the common mode voltage range of the amplifier.

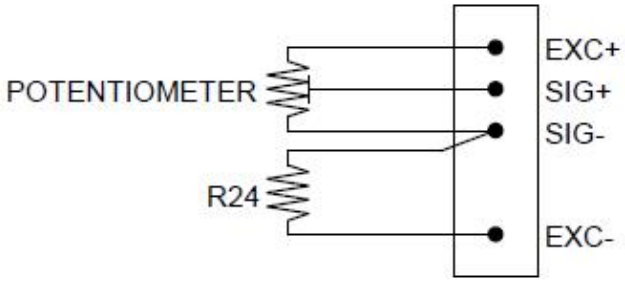

Input signal = 10-1.7 = 8.3V so use the lowest gain range for ±10V output. For lower output voltage or 4-20mA output, use lower excitation, e.g. 5V.

R24 can be added either in the location on the PCB, or more easily into the transducer screw terminals, between pin 4 (sig LO) and pin 2 (EXC LO).

MINIATURE LOW-PROFILE TENSION LINKS
LOW PROFILE 19 mm (0.75") TO 25 mm (1") HEIGHT
STANDARD AND METRIC MODELS

Tension/Compression
Calibrated in Tension
10 lb to 1000 lb
5 kg to 500 kgf

1 Newton = 0.2248 lb
1 daNewton = 10 Newtons
1 lb = 454 g
1 t = 1000 kgf = 2204 lb

STANDARD
LC703-25,
shown actual size.

METRIC
LCM703-150,
shown actual size.

LC703/LCM703 Series

NIST RoHS
Standard

- **Low Profile**
- **High Accuracy**
- **Rugged Industrial Design**

LC703-100, enlarged view.

The LC703/LCM703 Series comprises economical universal (tension/compression) load cells with a low profile. Ranges above 100 lb are stainless steel; ranges below 100 lb are aluminum. The low profile and rugged design make LC703 and LCM703 suitable for many industrial applications, including robotics, automated weighing systems, and batch-process control systems.

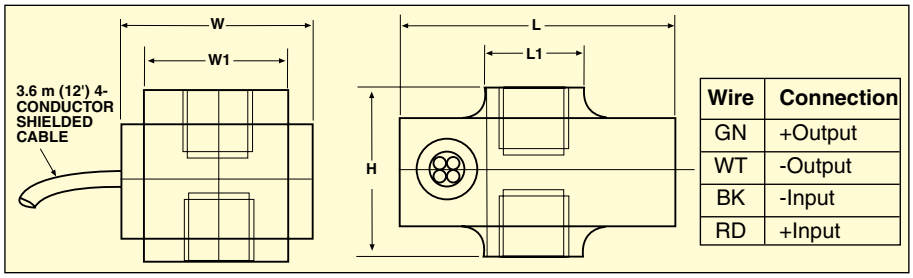

Wire	Connection
GN	+Output
WT	-Output
BK	-Input
RD	+Input

Dimensions: mm (inch)

CAPACITY	L (MAX)	L1	W	W1	H	THREAD
10 lb	38 (1.50)	14 (0.56)	14 (0.54)	9.5 (0.38)	19 (0.75)	10-32 x 0.20
5 kgf						M5 x 0.8-6H
25 to 100 lb	41 (1.62)	14 (0.56)	17 (0.66)	13 (0.50)	19 (0.75)	¼-28 x 0.23
10 to 50 kgf						M6 x 1.00-6H
150 to 1K lb	44 (1.75)	14 (0.56)	24 (0.93)	19 (0.75)	25 (1.0)	⅜-24 x 0.38
75 to 500 kgf						M10 x 1.5-6H

SPECIFICATIONS

Excitation: 10 Vdc (15V max)
Output: 2 mV/V nominal
5-Point Calibration:
0%, 50%, 100%, 50%, 0%
Linearity:
10 to 100 lb: ±0.15%
>100 lb: ±0.10 FSO
5 to 50 kgf: ±0.15%
75 to 500 kgf: ±0.10%
Hysteresis:
10 to 100 lb: ±0.15%
>100 lb: ±0.10 FSO
5 to 50 kgf: ±0.15%
75 to 500 kgf: ±0.10%
Repeatability: ±0.05%
Zero Balance: ±1.0% FSO
Operating Temp Range:
-40 to 82°C (-40 to 180°F)
Compensated Temp Range:
16 to 71°C (60 to 160°F)
Thermal Effects:
Zero: ±0.005% FSO/°F
Span: ±0.005%% FSO/°F
Protection Class: IP54
Safe Overload: 150% of capacity
Ultimate Overload: 300% of capacity
Output Resistance: 350 ±10 Ω
Input Resistance: 360 Ω minimum
Full Scale Deflection: 0.003" nominal
Construction:
≤100 lb: Aluminum
>100 lb: 17-4 PH stainless steel
≤50 kg: Aluminum
>50 kg: 17-4 PH stainless steel
Electrical: 3.6 m (12') shielded 4-conductor PVC cable

Features

- Carbon element
- Red, orange, green, amber and white LED colors
- Center detent option
- Assortment of resistance tapers
- Various travel lengths
- Various lever sizes

BOURNS® PRO AUDIO

PTL Series Slide Potentiometer w/LED

Electrical Characteristics

Standard Resistance Range
..... 1K ohms to 1 megohm
Standard Resistance Tolerance... ±20 %
End Resistance
20 mm Travel..... 10 ohms max.
30 mm Travel..... 20 ohms max.
45 mm Travel..... 20 ohms max.
60 mm Travel..... 30 ohms max.
Insulation Resistance @ 250 VDC
..... 100 megohms min.
Dielectric Withstanding Voltage
..... 300 VAC
Standard Taper..... Linear, Audio
Power Rating - Linear
20 mm Travel..... 0.05 watt
30 mm Travel..... 0.1 watt
45 mm Travel..... 0.125 watt
60 mm Travel..... 0.2 watt
Power Rating - Audio
20 mm Travel..... 0.025 watt
30 mm Travel..... 0.05 watt
45 mm Travel..... 0.06 watt
60 mm Travel..... 0.1 watt
Slider Noise ..... 200 mV max.

Environmental Characteristics

Operational Life ..... 15,000 cycles
TR Shift ..... ±15 %
Operating Temperature Range
..... -10 °C to +55 °C
Resistance to Solder Heat..... ±5 %

Mechanical Characteristics

Mechanical Travel..... Length ±0.5 mm
Operating Force ..... 30 gf to 250 gf
Center Detent Force..... 20 gf to 200 gf
Stop Strength ..... 5 kgf min.
Shaft Axial Force ..... 5 kgf min.
Shaft Wobble.. 2(2 x L/20) mm p-p max.
Soldering Condition
Manual .....300 °C ±5 °C for 3 sec.
Wave .....260 °C ±5 °C for 5 sec.
Wash .....Not recommended

Product Dimensions

20 mm Length of Travel

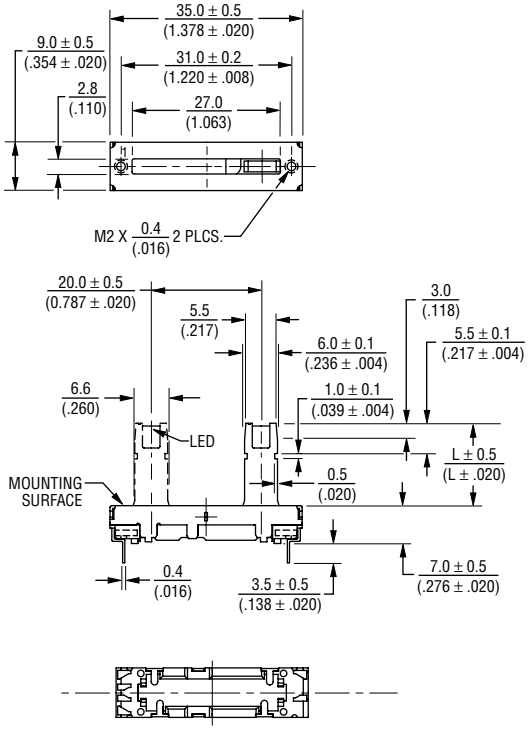

DIMENSIONS: MM / (INCHES)

Lever Length
10.0 (.394)
15.0 (.591)
19.0 (.748)

Mounting Hole Detail

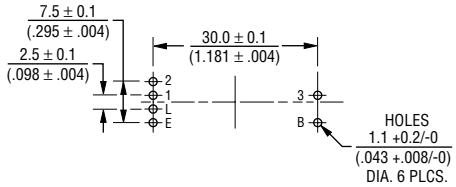

Standard Resistance Table

Resistance (Ohms)	Resistance Code
1,000	102
2,000	202
5,000	502
10,000	103
20,000	203
50,000	503
100,000	104
200,000	204
500,000	504
1,000,000	105

Schematic

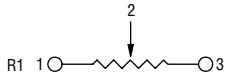

*RoHS Directive 2002/95/EC Jan 27, 2003 including Annex.
Specifications are subject to change without notice.
Customers should verify actual device performance in their specific applications.

Technical Sales

(866) 531-6285
orders@ni.com

Requirements and Compatibility | Ordering Information | Detailed Specifications
For user manuals and dimensional drawings, visit the product page resources tab on ni.com.

Last Revised: 2013-07-10 09:55:53.0

Low-Cost, Bus-Powered Multifunction DAQ for USB

12- or 14-Bit, Up to 48 kS/s, 8 Analog Inputs

- 8 analog inputs at 12 or 14 bits, up to 48 kS/s
- 2 analog outputs at 12 bits, software-timed
- 12 TTL/CMOS digital I/O lines
- One 32-bit, 5 MHz counter
- Digital triggering
- Bus-powered
- 1-year warranty

Overview

With recent bandwidth improvements and new innovations from National Instruments, USB has evolved into a core bus of choice for measurement applications. The NI USB-6008 and USB-6009 are low-cost DAQ devices with easy screw connectivity and a small form factor. With plug-and-play USB connectivity, these devices are simple enough for quick measurements but versatile enough for more complex measurement applications.

Back to Top

Requirements and Compatibility

OS Information

- Mac OS X
- Windows 2000/XP
- Windows 7
- Windows CE
- Windows Mobile
- Windows Vista 32-bit
- Windows Vista 64-bit

Driver Information

- NI-DAQmx
- NI-DAQmx Base

Software Compatibility

- ANSI C/C++
- LabVIEW
- LabWindows/CVI
- Measurement Studio
- SignalExpress
- Visual Basic .NET
- Visual C#

Back to Top

Comparison Tables

Product	Analog Inputs	Input Resolution	Max Sampling Rate (kS/s)	Analog Outputs	Output Resolution	Output Rate (Hz)	Digital I/O Lines	32-Bit Counter	Triggering
USB-6008	8 single-ended/4 differential	12	10	2	12	150	12	1	Digital
USB-6009	8 single-ended/4 differential	14	48	2	12	150	12	1	Digital

Back to Top

LM10 SERIES
Micro Laser Sensor

* Original NAiS Sensor

Displacement Sensing with Analog Output

CE Marked
Conforming to EMC Directive

High-precision measurements, comparative output function

Comparative output function (Intensity/displacement) gives this high-precision device the feel of a photoelectric sensor.

In addition to conventional analog output, the LM10 also comes with ON/OFF control output (single or window comparator) as a standard function. This gives the LM10 the feel of a photoelectric sensor, yet it still offers the "micro-spotting" and "high precision" that only come with a laser sensor.

• Setting modes and types of ON/OFF control

Type	Standard mode	Intensity mode
Window comparator	Displacement control (triple output)	No mode setting
Single comparator	Displacement control (double output)	Intensity control (double output)

Displacement control: ON/OFF control on the basis of distance measurement.
Intensity control: ON/OFF control on the basis of received light level.

• Measurement principle of the LM10 (optical triangulation)

Part of the light rays which come from the target object by means of diffuse reflection produce a light spot on the position sensing device (PSD). This light spot varies depending on the displacement of the target object. By measuring the fluctuations in the light spot, the LM10 can measure the displacement of the target object.

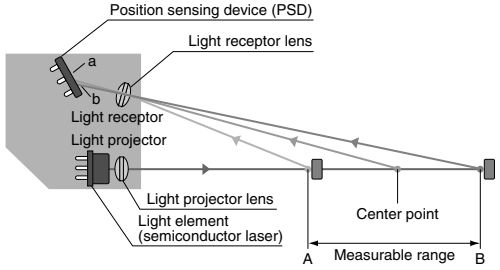

New circuitry lowers costs.

Incorporates our own unique built-in single-channel IC.

The LM10 uses the first single-channel IC (patent pending) ever produced in the industry,* which reduces the dual-channel processing requirement of conventional products to a single channel. Building the arithmetic circuits into the IC has made it possible to reduce costs.

• As of November 1996.

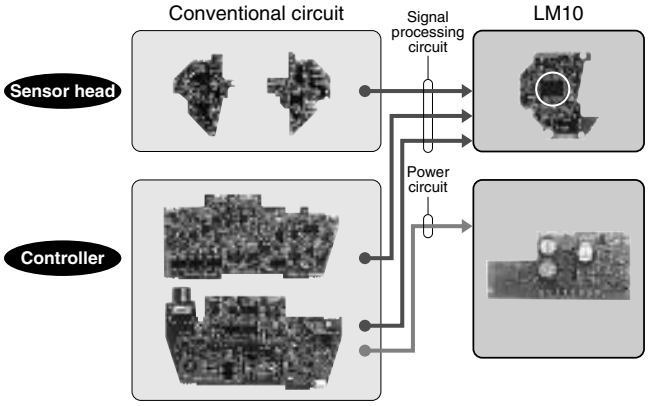

19 mm (0.75") DIAMETER SUBMINIATURE TENSION OR COMPRESSION LOAD CELLS

STANDARD AND METRIC MODELS

Tension/Compression
Calibrated in Tension
0-25 lb to 0-300 lb
0-100 to 0-500 N

1 Newton = 0.2248 lb
1 daNewton = 10 Newtons
1 lb = 454 g
1 t = 1000 kg = 2204 lb

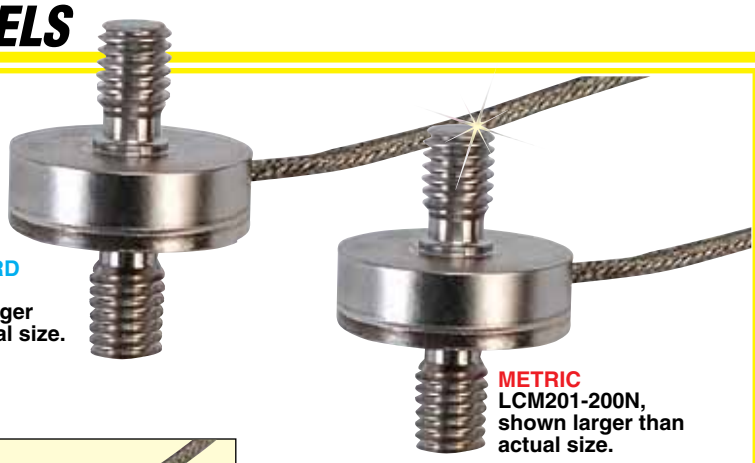

STANDARD
LC201-50, shown larger than actual size.

METRIC
LCM201-200N, shown larger than actual size.

LC201/LCM201 Series

NIST RoHS
Standard

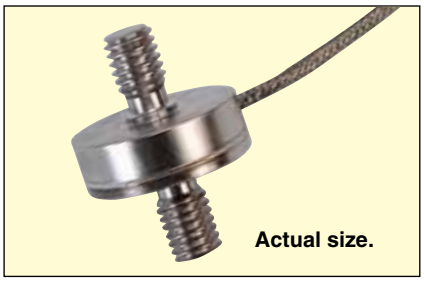

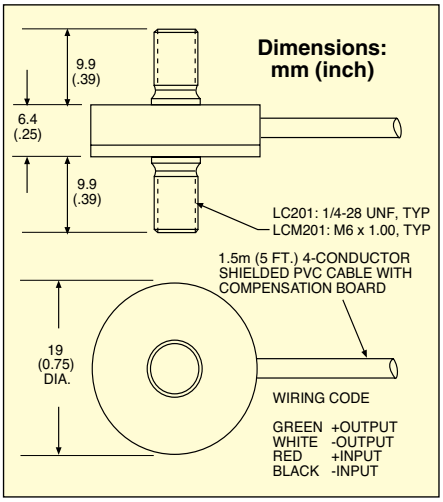

- **Subminiature Package for Robotic Applications, 19 mm (0.75") Diameter**
- **Dual Mounting Studs for Easy Installation**
- **5-Point Calibration Provided**

Thermal Effects:
Zero: 0.018% FSO/°C
Span: 0.018% FSO/°C
Safe Overload: 150% of capacity
Ultimate Overload: 300% of capacity
Input Resistance: 360 Ω minimum
Output Resistance: 350 ±10 Ω
Construction: Stainless steel
Electrical: 1.5 m (5') 4-conductor shielded cable with compensation board

OMEGA's LC201/LCM201 Series subminiature load cells are designed for the demanding environment of industrial automation and robotics. With a diameter of only 19 mm (0.75") and all stainless steel construction, they can fit into small systems. They deliver high accuracy and long-term reliability in a subminiature package.

STANDARD MODELS

To Order

CAPACITY lb	CAPACITY N	MODEL NO.	COMPATIBLE METERS*	ROD END
25	111	**LC201-25**	DP41-S, DP25B-S	**REC-014F**
50	222	**LC201-50**	DP41-S, DP25B-S	**REC-014F**
75	334	**LC201-75**	DP41-S, DP25B-S	**REC-014F**
100	445	**LC201-100**	DP41-S, DP25B-S	**REC-014F**
300	1334	**LC201-300**	DP41-S, DP25B-S	**REC-014F**

METRIC MODELS

CAPACITY N	CAPACITY lb	MODEL NO.	COMPATIBLE METERS*	ROD END
100	22	**LCM201-100N**	DP41-S, DP25B-S	**MREC-M6F**
200	45	**LCM201-200N**	DP41-S, DP25B-S	**MREC-M6F**
300	67	**LCM201-300N**	DP41-S, DP25B-S	**MREC-M6F**
500	112	**LCM201-500N**	DP41-S, DP25B-S	**MREC-M6F**

Comes complete with 5-point NIST traceable calibration and 59 kΩ shunt data.

** Visit us online for compatible meters. DPiS meter suitable for one direction measurement only.*

***Ordering Examples: LC201-25,** 25 lb capacity subminiature universal load cell.*
***LCM201-500N,** 500 N capacity subminiature universal load cell.*

SPECIFICATIONS

Excitation: 10 Vdc, 15 Vdc max
Output: 2 mV/V nominal
Accuracy: ±1.0% FSO linearity, hysteresis, repeatability combined
5-Point Calibration (in Tension): 0%, 50%, 100%, 50%, 0%
Zero Balance: ±2% FSO
Operating Temp Range: -54 to 121°C (-65 to 250°F)
Compensated Temp Range: 16 to 71°C (60 to 160°F)
Protection Class: IP54

ID1101L
Dual Channel
Linear Encoder Kit

Product data

Features

- Highly miniaturized linear encoder
- Differential inductive sensing principle
- Insensitive to magnetic interference fields
- Robust against oil, water, dust, particles
- Ultra-thin encoder and scale (total < 2 mm)
- Optional with cable, connector and holder

Applications

- Linear actuators
- Industrial / laboratory / office automation
- X-Y stages
- Pick & Place assembly equipment
- High-speed motion control
- Mechatronics applications

Key Specifications

Output format.....A and B in quadrature
Resolution.....down to 0.3 um
Maximum speed .....up to 40 m/s
Airgap .....up to 0.7 mm
Supply.....5 V, 12 mA
Temperature .....0 – 100℃

Description

The ID1101L incremental encoder kit consists of an encoder and a linear scale (Fig. 1). The encoder is an integrated circuit in a PCB housing. It provides incremental A and B output signals in quadrature (Fig. 2). The linear scale is a PCB with passive copper strips. Table 1 allows to configure two possible orientations of encoder vs. scale.

Resolution, maximum speed and airgap
The resolution and the maximum speed of the encoder are programmed ex-factory. The resolution depends on a filter setting that limits the maximum speed of the encoder vs. the scale. The resolution also depends on the maximum distance between the encoder and the scale. Tables 2 and 3 allow the configuration of resolution and maximum speed for a certain maximum air-gap.

Scales
Scales with different dimensions and period lengths are available (Fig. 4) and are selected in Table 4. The scale may be mounted on any substrate, using an edge for accurate positioning in front of the encoder.

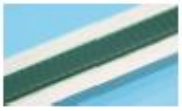

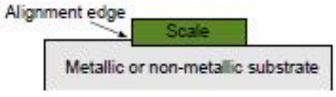

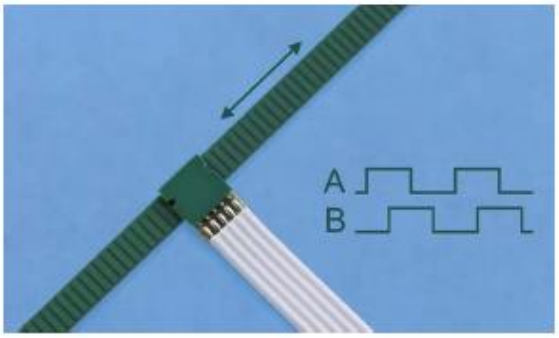

Encoder holders
Different encoder holder options are available and can be selected in Table 5.
The encoder holder **type A0** (Fig. 5) may be mounted on any substrate using 4 screw-holes. It has a strain relief for the cable.

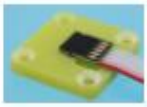

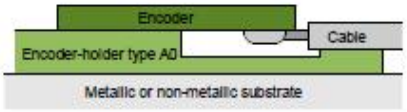

The encoder holder **type B0** (Fig. 3) may be mounted on any substrate. Use half-holes on encoder PCB housing and alignment pins for accurate positioning.

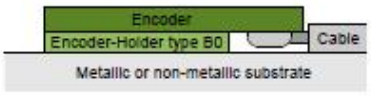

The encoder without holder may be mounted on non-metallic substrates. Use half-holes on encoder housing and alignment pins for accurate positioning.

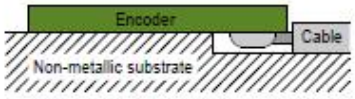

Encoder cable and connector
The encoder is supplied with a flat cable of pitch 1.27 mm and a connector (Fig. 6). The cable length and the connector type are selected in Tables 5 and 6.

3D models of encoder, holders and scales
STEP and IGES 3D models available on www.posic.com.

Miniature Linear Motion Series · L16

Firgelli Technologies' unique line of Miniature Linear Actuators enables a new generation of motion-enabled product designs, with capabilities that have never before been combined in a device of this size. These linear actuators are a superior alternative to designing your own push/pull mechanisms.

The L16 actuators are complete, self contained linear motion devices with position feedback for sophisticated position control capabilities, or end of stroke limit switches for simple two position automation. Driving them couldn't be easier, simply apply a DC voltage to extend the actuator, and reverse the polarity to retract it. Several gear ratio's are available to give you varied speed/force configurations.

L16 Specifications

Gearing Option	35:1	63:1	150:1
Peak Power Point	50N @16mm/s	75N @10mm/s	175N @4mm/s
Peak Efficiency Point	24N @24mm/s	38N @15mm/s	75N @7mm/s
Max Speed (no load)	32mm/s	20mm/s	8mm/s
Max Force (lifted)	50N	100N	200N
Back Drive Force	31N	46N	102N
Stroke Option	50mm	100mm	140mm
Mass	56g	74g	84g
Positional Accuracy	0.3mm	0.4mm	0.5mm
Max Side Load (extended)	40N	30N	20N
Feedback Potentiometer	9kΩ±30%	18kΩ±30%	25kΩ±30%
Electrical Stroke	48mm	98mm	138mm
Input Voltage	0-15 VDC. Rated at 12VDC.		
Stall Current	650mA @ 12V		
Operating Temperature	-10°C to +50°C		
Lifetime @ Peak Eff. Pt.	20,000 strokes, 20% Duty Cycle		
Audible Noise	57dB @ 45cm		
Ingress Protection	IP-54		
Mechanical Backlash	0.2mm		
Limit Switches	Max. Current Leakage: 8uA		

Basis of Operation

The L16 is designed to push or pull a load along its full stroke length. The speed of travel is determined by the load applied. (See the Load Curves). When power is removed the actuator will hold its position, unless the applied load exceeds the backdrive force. Stalling the actuator for short periods will not cause damage, however repeated stalling will shorten the life of the actuator.

Ordering

Small quantity orders can be placed directly online at www.firgelli.com. Each actuator ships with two mounting brackets and #8-32 mounting hardware. The cable length is approximately 300mm and connector is a 0.1" pitch female socket connector.

Applications

- → **Robotics**
- → **Consumer appliances**
- → **Toys**
- → **RC vehicles**
- → **Automotive**
- → **Industrial Automation**

Firgelli Technologies Inc.
1550 Mileva Lane
Victoria, BC V8N 2V5
Canada
1 (206) 347-9684 *phone*
1 (888) 225-9198 *toll-free*
1 (206) 347-9684 *fax*
sales@firgelli.com
www.firgelli.com

LAC • Firgelli Linear Actuator Control Board

The Linear Actuator Control Board is a stand-alone closed-loop control board specifically designed for Firgelli actuators. The LAC greatly simplifies designs by saving the development time, cost, and processor overhead associated with direct motor control. As little as 1 digital or analog output is required for position control. Supported input signals include USB, Voltage, Current, RC Servo, and PWM. Firgelli's motor control IC uses a software based algorithm to optimize position and speed control. This makes the LAC compatible with a wide range of actuators, using only the default settings. Firgelli's Advanced Configuration Program allows full customization of actuator response. A stall detection feature provides a great increase in actuator life for applications that may briefly exceed the rated force.

The LAC can be operated as both an interface board, or as a stand alone controller with the addition of an external potentiometer and power supply.

(Accessory kit and housing sold separately)

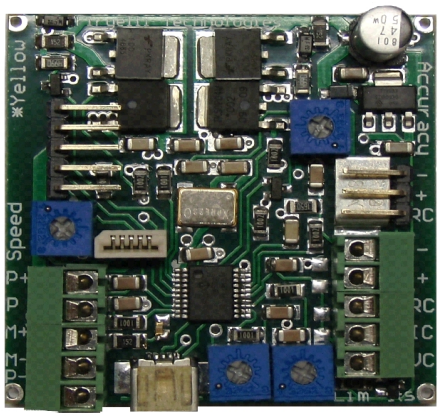

Specifications

Control input modes	**Digital: USB, RC Servo, 1 kHz PWM** **Analog: 0–3.3 V, 4–20 mA**
Controller	**10-bit Dual Sample Rate Quasi PD**
Compatible actuators	**PQ12 Actuators with position feedback, 6 or 12 volts** **L12–P Actuators with position feedback, 6 or 12 volts** **L16-P Actuators with position feedback, 6 or 12 volts** **Larger Actuators with position feedback, 12 volts, 24 volts**
Dimensions	**50 mm x 50 mm** (excluding battery holder)
Power	**5–24 VDC, 4 Amps peak current at 10% duty cycle**
Operating environment	**–10 to +70°C at 10–80% relative humidity**

Operation

When the CIB is powered up, it will repeatedly scan for an input signal that is valid under any of the five supported interface modes (see reverse for External Connections Detail illustration). When a valid signal is first detected, the actuator will self-configure to the corresponding interface mode, and all other interface modes and input leads are disabled until the actuator is next powered on. The sensitivity or accuracy of the actuator control algorithm can be set by adjusting the "Accuracy" trim potentiometer. Turning clockwise will allow the actuator to move in smaller increments and be more accurate. However, due to the differences in actuator types this may cause jittery or unstable behaviour. If this occurs, consider using the USB configuration program to more finely tune the controller for your application. Each time a control potentiometer is adjusted, power must be cycled to the LAC board prior to the new settings taking effect. Adjusting the "Speed" potentiometer will set the maximum actuator speed. The two "Limits" potentiometers allow user settable digital limit switches. These set the minimum and maximum acceptable positions. Control inputs that exceed these limits will cause the actuator to position to the limit.

Firgelli Technologies Inc.
1550 Mileva Lane
Victoria, BC V8N 2V5
Canada

1 (206) 347-9684 *phone*
1 (888) 225-9198 *toll-free*
1 (206) 347-9684 *fax*

sales@firgelli.com
www.firgelli.com

Rotary Motion (LAR series only)

An assembly comprising a rotary DC motor, magnetic encoder and gearbox is carried by the piston to rotate the rod. The rod is mounted to the piston in a rotary bearing. The rod and gearbox shaft are connected using a flexible coupling. To locate a home position for the rotary axis, the actuator rod carries a flag. This flag is sensed by a reflective proximity switch and is identified as the coarse index.

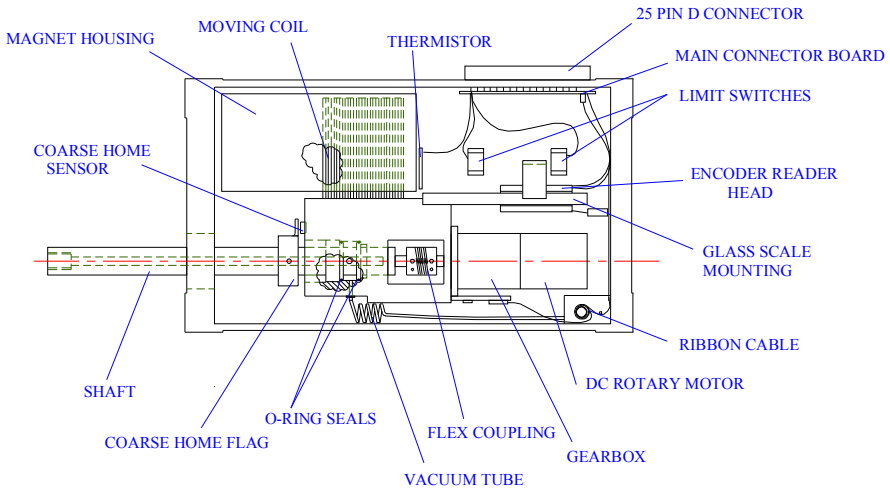

Fig 1. Actuator Components (LAR30-15 shown)

SMAC equipment required to run a system

Linear Actuator only:	**Linear / Rotary Actuator:**
LAL series actuator	LAR series actuator
LAC – 1 Controller	LAC – 25 controller
LAH-LO(D)-03 Cable	LAH-RT(D)-03 cable

Other equipment required

RS232 cable and connector (appendix page 1)
Laptop PC or text editor to construct program (see setup instructions)
26 pin I/O connector for Input/ Output channels
Either 24 Volt D.C., 4 Amp Power supply (30, 37, 50 series)
Or 48 Volt D.C., 4 Amp Power supply (90, 300 series)

PID values for SMAC Actuators

Note: These are starting values only, they may need to be adjusted for different load values or actuator orientations. Values should work with both LAC-25 and LAC-1

For 0.5µ and 0.1µ, reduce all values by a factor of 5 (e.g. SG25 becomes SG5)

Linear Encoder	Actuator	Proportional (SG)	Integral (SI)	Derivative (SD)	Integral Limit (IL)
1µ	**LA*20**	50	80	600	5000
5µ	**LA*20**	100	200	1200	5000
1µ	**LAL30 / LAR30**	50	100	600	5000
5µ	**LAL30 / LAR30**	100	200	1200	5000
1µ	**LAL37 / LAR37**	50	100	600	5000
5µ	**LAL37 / LAR37**	100	200	1200	5000
1µ	**LAL55 / LAR55**	50	150	600	5000
5µ	**LAL55 / LAR55**	100	300	1600	5000
1µ	**LAL90 / LAR90**	50	100	600	5000
5µ	**LAL90 / LAR90**	100	200	1200	5000
1µ	**LAL90-50**	50	100	600	5000
5µ	**LAL90-50**	100	200	1200	5000
1µ	**Grippers**	40	100	500	5000
5µ	**LAL300**	100	300	1500	2000
Rotary					
Standard	**LAR 30/37/55**	150	200	1500	5000
1Nm	**LAR90**	20	200	300	1500
Direct Drive	**LAR20/34/55**	50	300	250	3000

It will also be necessary to program the following values. These values are nominal and can be changed to suit the motion profile as required during the program.

Command	Mnemonic	Value
Derivative Sampling Frequency	**FR**	**1**
Integration Limit	**IL**	**5000**
Phase	**PH**	**0**
Sampling rate of integral	**RI**	**1**
Set Acceleration	**SA**	**1000**
Set Velocity	**SV**	**30000**
Set torque	**SQ**	**32767**
Set Servo speed	**SS**	**2**
Set following error	**SE**	**16383**

These values can be displayed at any time by typing the **TK** (tell constants) command. Note that changing the **SS** command will alter the **SV** and **SA** values produced, as these are dependent on the clock speed.

1. Introduction

The LAC-1 is a one axis stand-alone integrated controller / driver, with input / output (I/O) capabilities, designed primarily for the control of DC brush type motors or actuators with it's integrated driver.

The LAC-1 implements a mnemonic type command instruction set via a standard RS-232 serial communications interface. These commands can be executed directly or used to create command macros which are stored in the onboard nonvolatile RAM (NVRAM).

The LAC-1 can interface to the real world via the onboard DC motor driver, a quadrature type encoder interface, 8 channels of HCT TTL digital input and 8 channels of HCT TTL type digital output, with additional TTL inputs serving for limit, home and fault functions, 4 channels of 10-bit analog to digital (A/D) conversion (1 of which is reserved for monitoring amplifier output current), and an RS-232 serial communications link. A proprietary RS-422 interface is provided for I/O expansion modules.

1.1 Specifications

Description	Stand-Alone 1 Axis Servo Motor Controller / Driver
Operating Modes	Position, Velocity, Torque
Filter Algorithm	PID
Max. Servo Loop Rate	200 µS
Trajectory Generator	Trapezoidal
Servo Position Feedback	Incremental Encoder with Index
Output (Standard)	PWM Motor Drive, 3 Amps Cont. and 6 Amps Peak at 50 VDC Max.
PWM Frequency	Approximately 19.531 KHz
Encoder and Index Input	Single-ended or Differential
Encoder Supply Voltage	5 VDC
Encoder Input Voltage	5.5 VDC Max., -0.1 VDC Min.
Encoder Count Rate	2 Million Quadrature Counts per Second
Position Range	32 Bits
Velocity Range	32 Bits
Acceleration Range	32 Bits
General Purpose Digital I/O	8 HCT TTL Inputs, 8 HCT TTL Outputs
Dedicated Digital Inputs	Limit+, Limit-, Home and Fault, all TTL
Analog Inputs	4 Channels With 10-Bit Resolution, 3 are user accessible
Expansion I/O	Optional Expansion to 64 I/O
Communication Interface	RS-232 Serial Interface, Adjustable Baud Rate, 8 Bits, 1 Stop Bit, No Parity, XON/XOFF Handshake
Supply Voltage	+11 To +50 VDC
Motor Voltage	+12 To +48 VDC
Dimensions	Approximately 5.0" Long by 3.3" Wide by 1.1" Thick
Weight	Approximately 1 Lb.

Table 1. Specifications.

8. Index

Appendix B

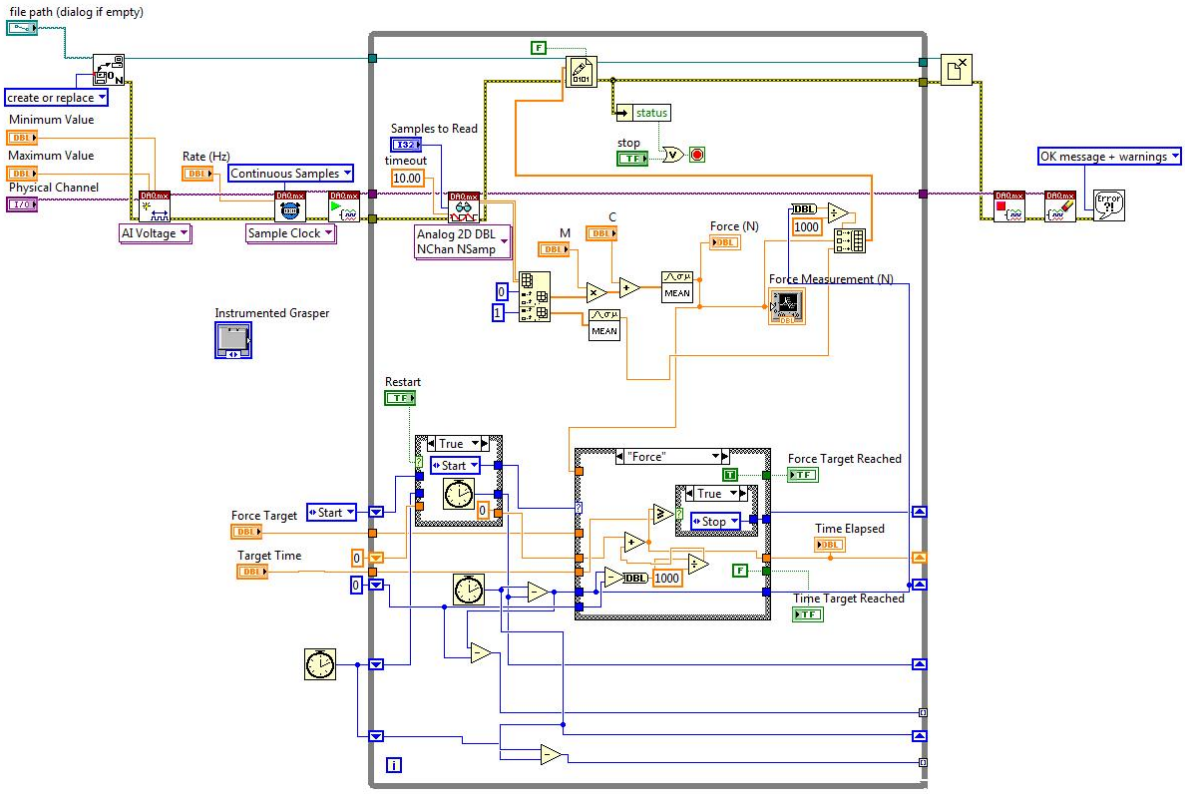

Figure 7.9: Instrumented Grasper VI.

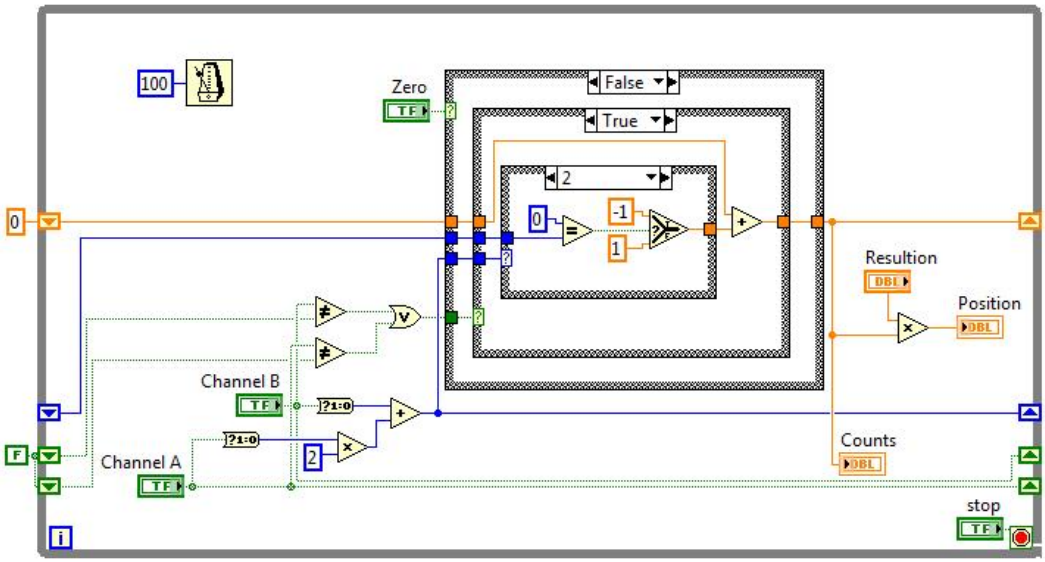

Figure 7.10: Linear encoder VI.

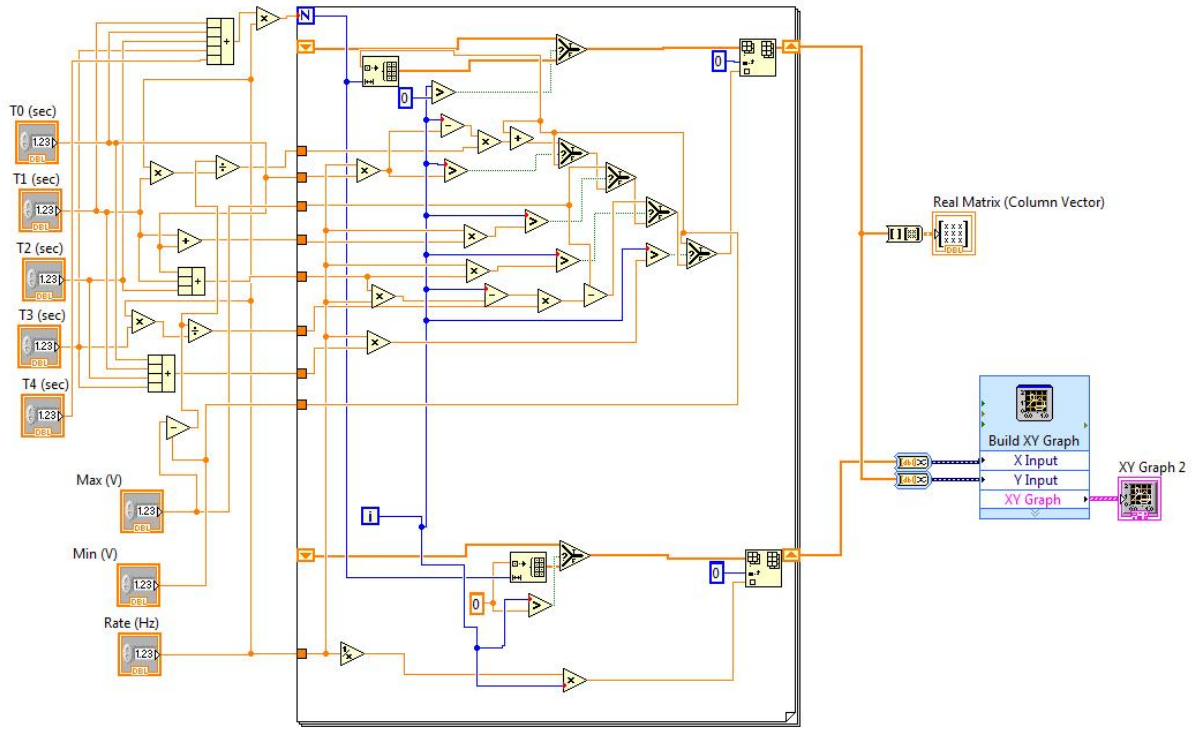

Figure 7.11: Initial rig program waveform generator.

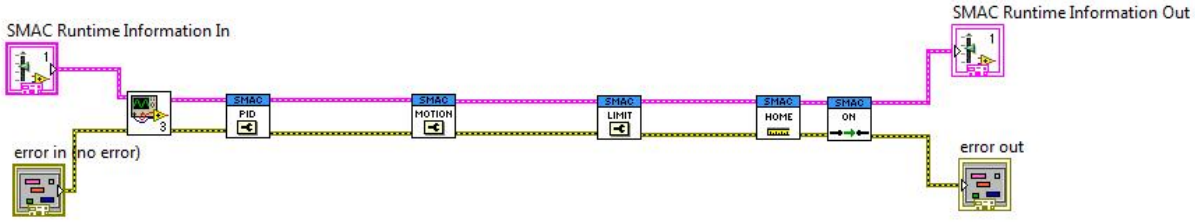

Figure 7.12: Rig program VI - actuator setup.

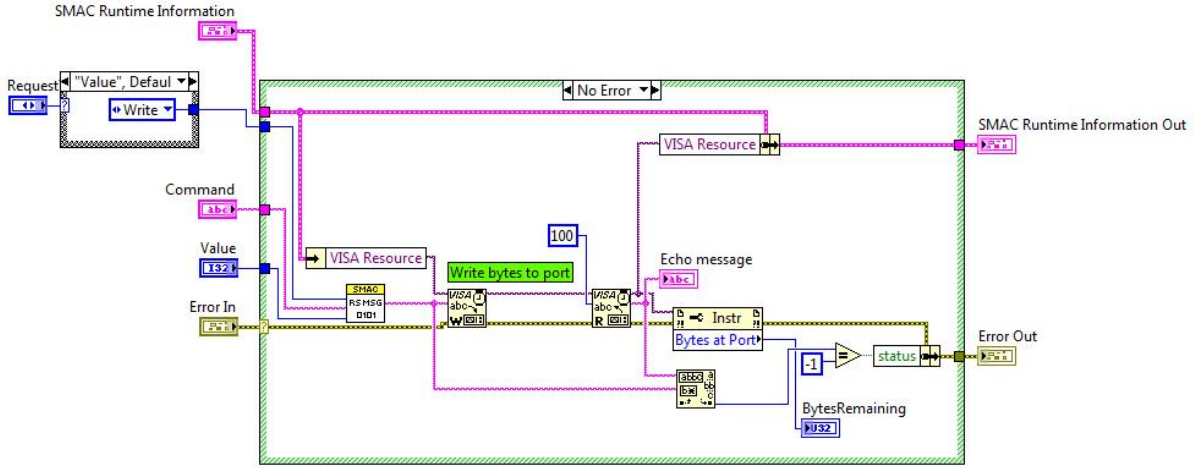

Figure 7.13: Rig program VI - actuator write.

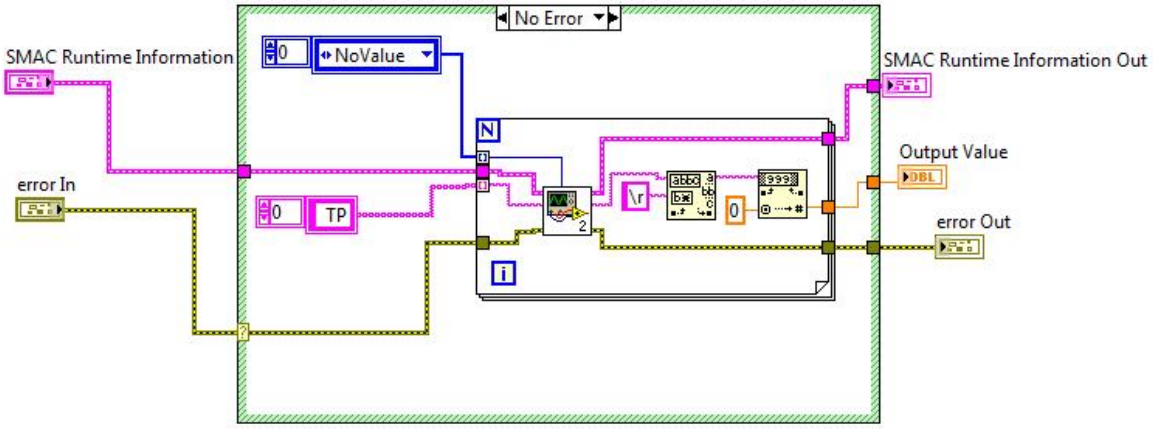

Figure 7.14: Rig program VI - actuator read.

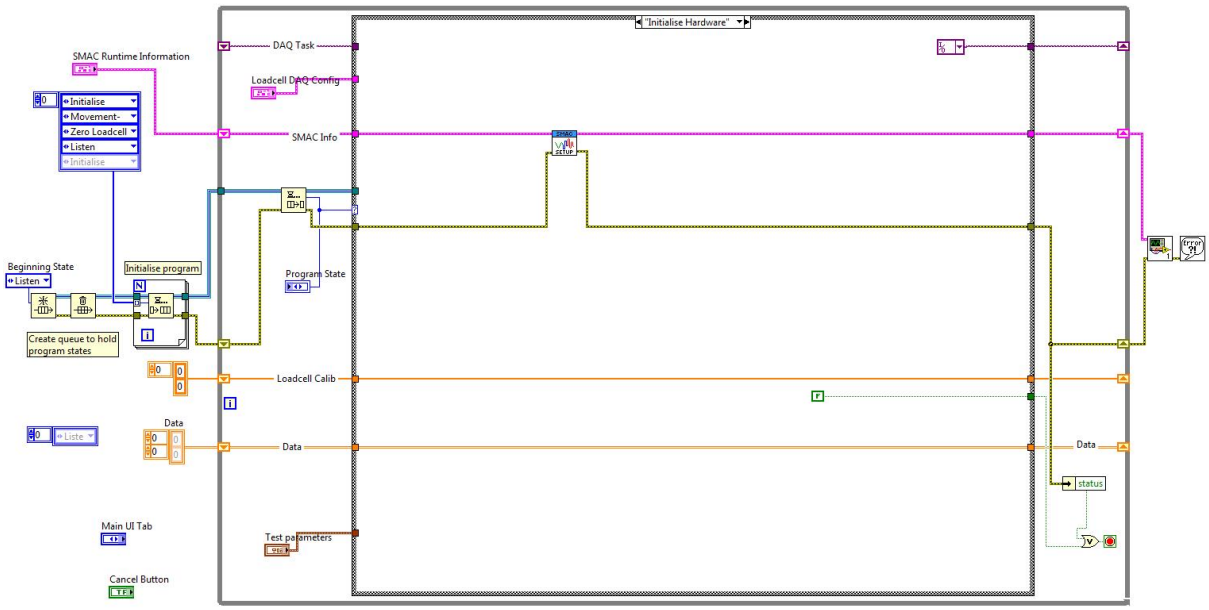

Figure 7.15: Rig program VI - program initialise.

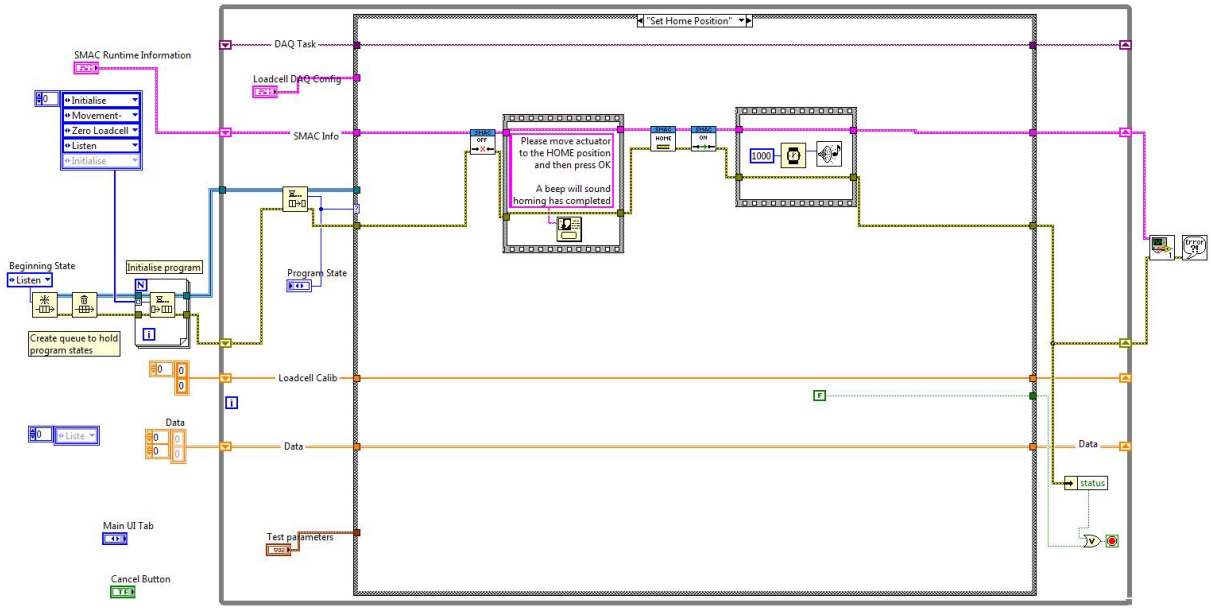

Figure 7.16: Rig program VI - set actuator home.

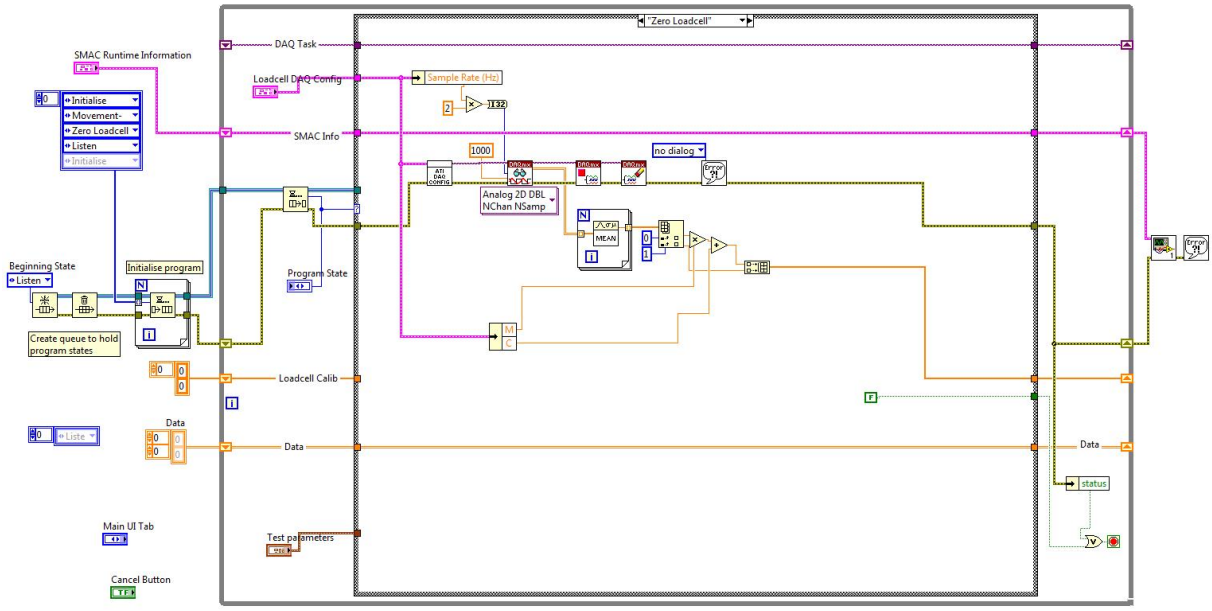

Figure 7.17: Rig program VI - zero loadcell.

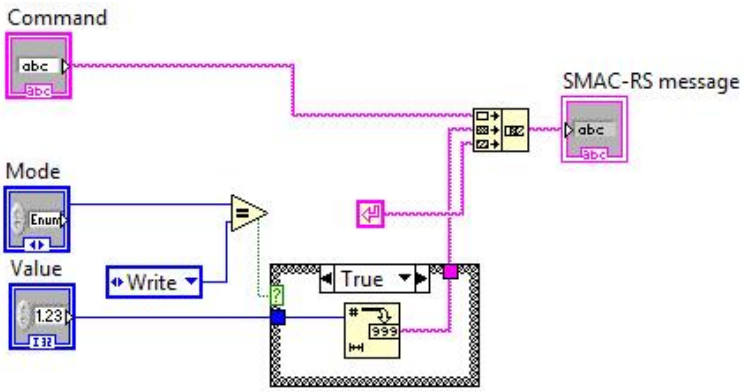

Figure 7.18: Rig program VI - RS-232 string generator.

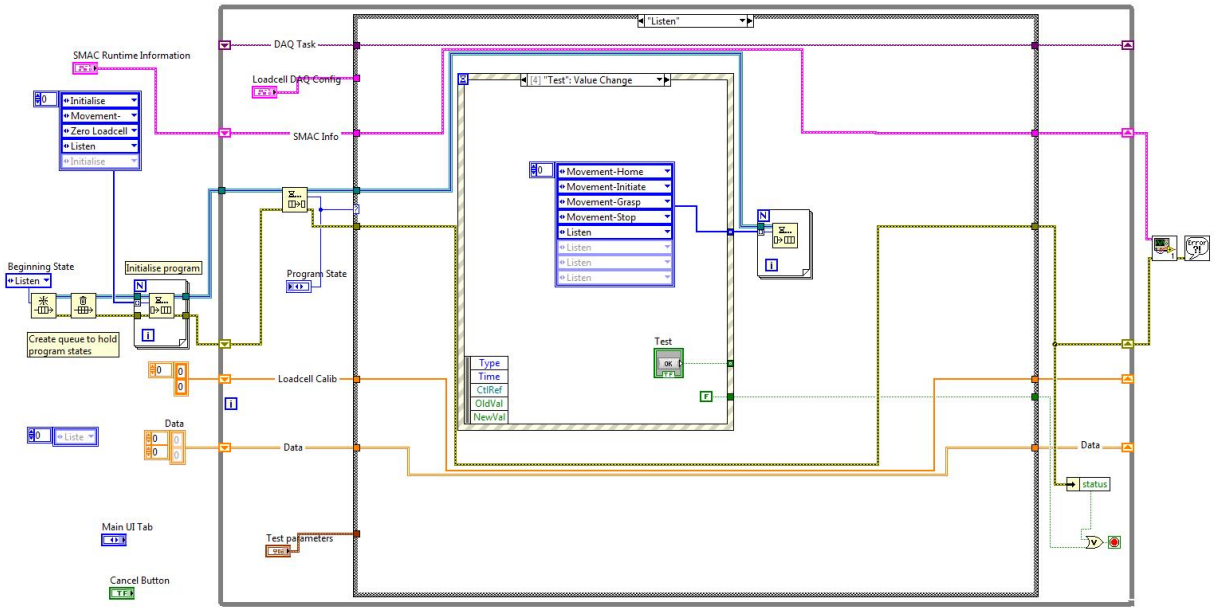

Figure 7.19: Rig program VI - listen state.

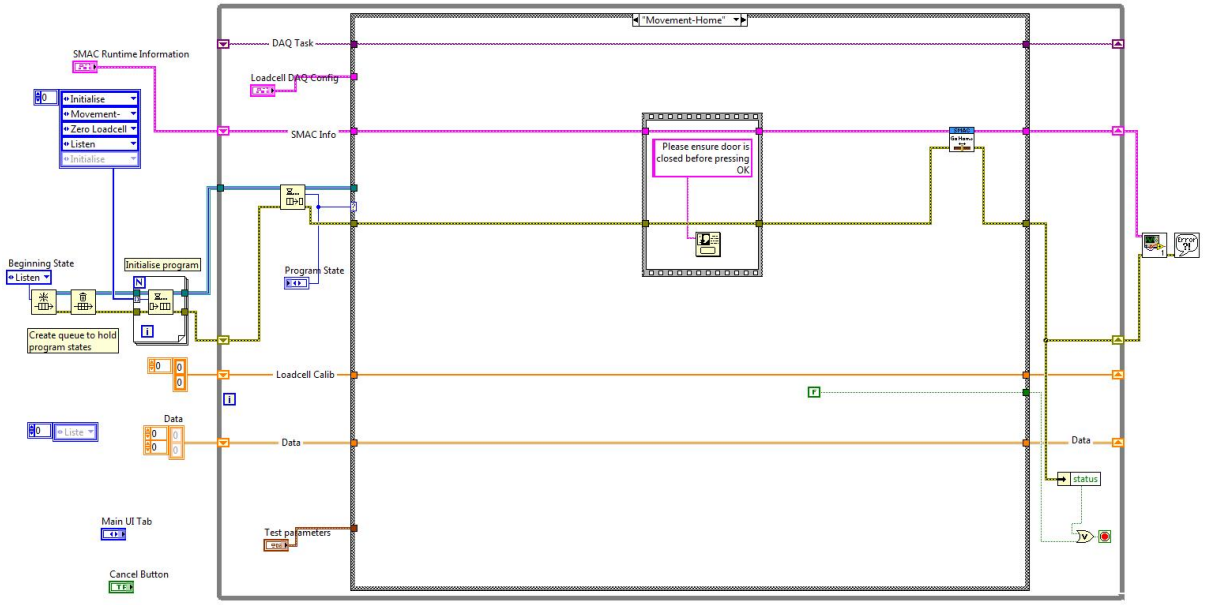

Figure 7.20: Rig program VI - movement home state.

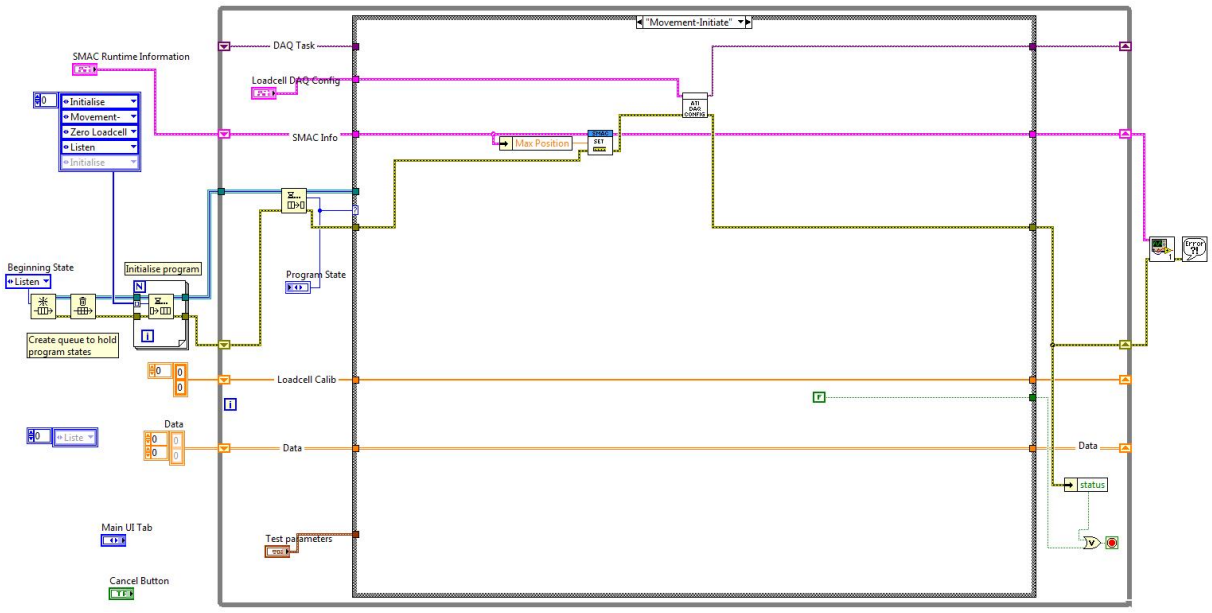

Figure 7.21: Rig program VI - movement initiate state.

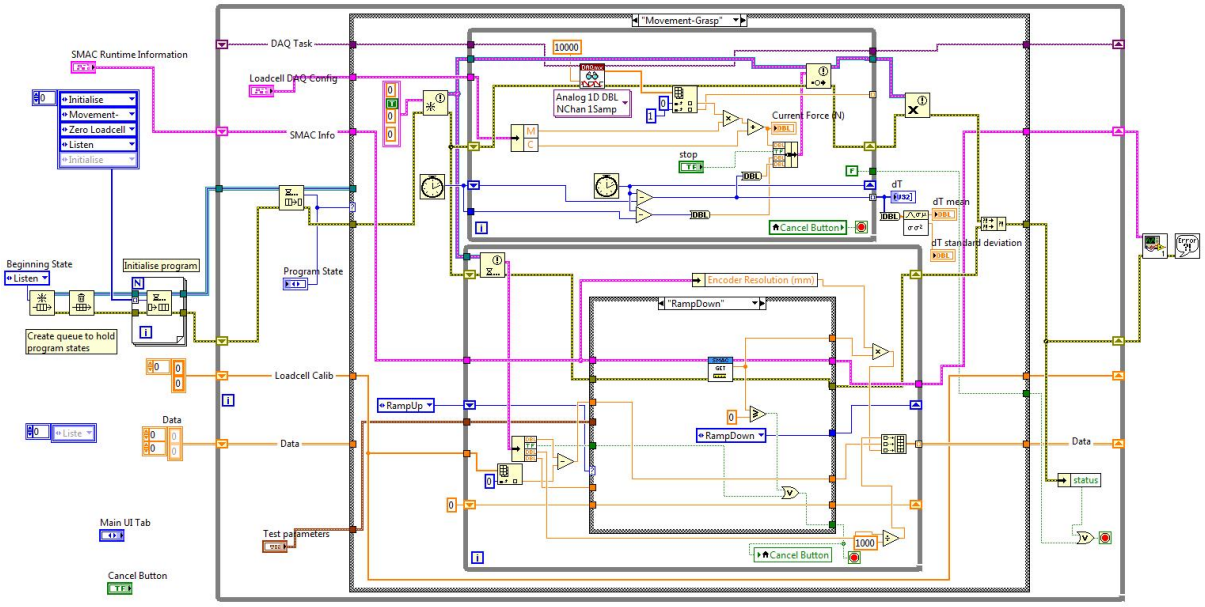

Figure 7.22: Rig program VI - movement grasp state.

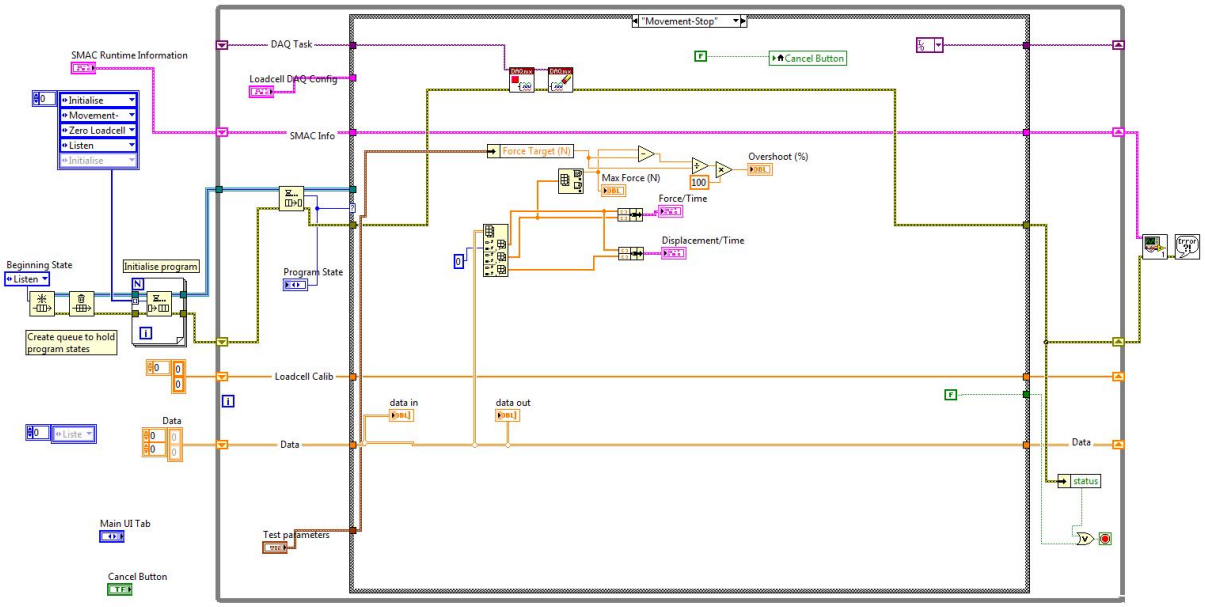

Figure 7.23: Rig program VI - movement stop state.

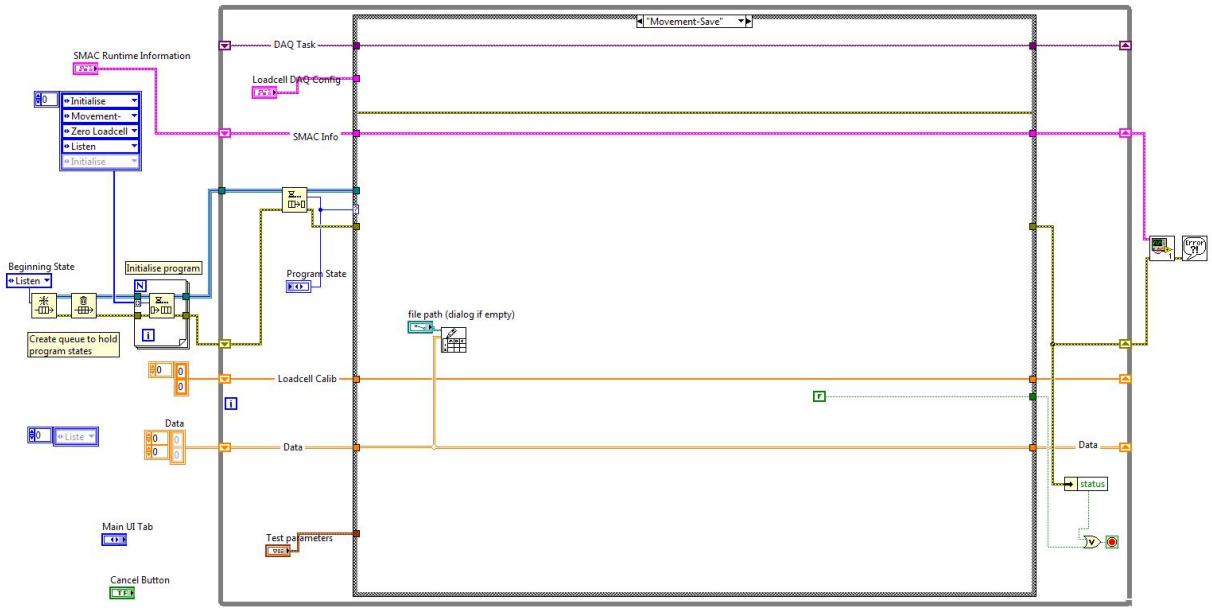

Figure 7.24: Rig program VI - data save state.

```
function [Fout, OT] = TipForceSingle(Fin, LD, lj)

% Define grasper stucture

c = 0.00377;       %Length of linkage 'c' (m)
d = 0.0032;       %Length of linkage 'd' (m)
f0 = 0.00375;    % Minmum length of f (m)

A0 = 21.8;     % offset from normal of grasper (degrees)



% Calculate

    f = LD+f0;
    theta = acosd((d^2 - f^2 - c^2)/(-2*f*c));
    OT = theta - A0;

    alpha1 = asind((c*sind(theta))/d);
    alpha2 = theta+alpha1-90;

    % calculate force out
    Fout = ((c * Fin * cosd(alpha1)*cosd(alpha2))/(2 * lj));

end
```

Figure 7.25: MATLAB code of mathematical grasper model.

```
Data = xlsread(filename);   %Read in data from excell file to array

Time = Data(:,1);                   %Extract time data
Force = Data(:,2);                  %Extract force data
Disp = Data(:,3);                   %Extract displacement data

M = length(Force);
[Fmax, IF] = max(Force);            %Find index of maximum force value

ID=M-IT;

DispFLIP = Disp(end:-1:1);          %Flip displacement to find first max value
ForceFLIP = Force(end:-1:1);        %Flip force to match displacement indices

FupFLIP = ForceFLIP(ID:end);        %Split force array - up
DupFLIP = DispFLIP(ID:end);         %Split disp array - up

Fup = FupFLIP(end:-1:1);            %Flip arrays (otherwise WD will show as negative)
Fup = max(Fup,0);                   %Remove negative values
Dup = DupFLIP(end:-1:1);            %Flip arrays (otherwise WD will show as negative)

Fdown = ForceFLIP(1:ID);            %Split force array - down
Fdown = max(Fdown,0);               %Remove negative values
Ddown = DispFLIP(1:ID);             %Split disp array - down

WDup = trapz(Dup, Fup);             %Calculate area under top curve
WDdown = trapz(Ddown, Fdown);       %Calculate area under bottom curve

WD = (WDup-WDdown);                 %Calculate final work done
```

Figure 7.26: MATLAB code of work damage algorithm.

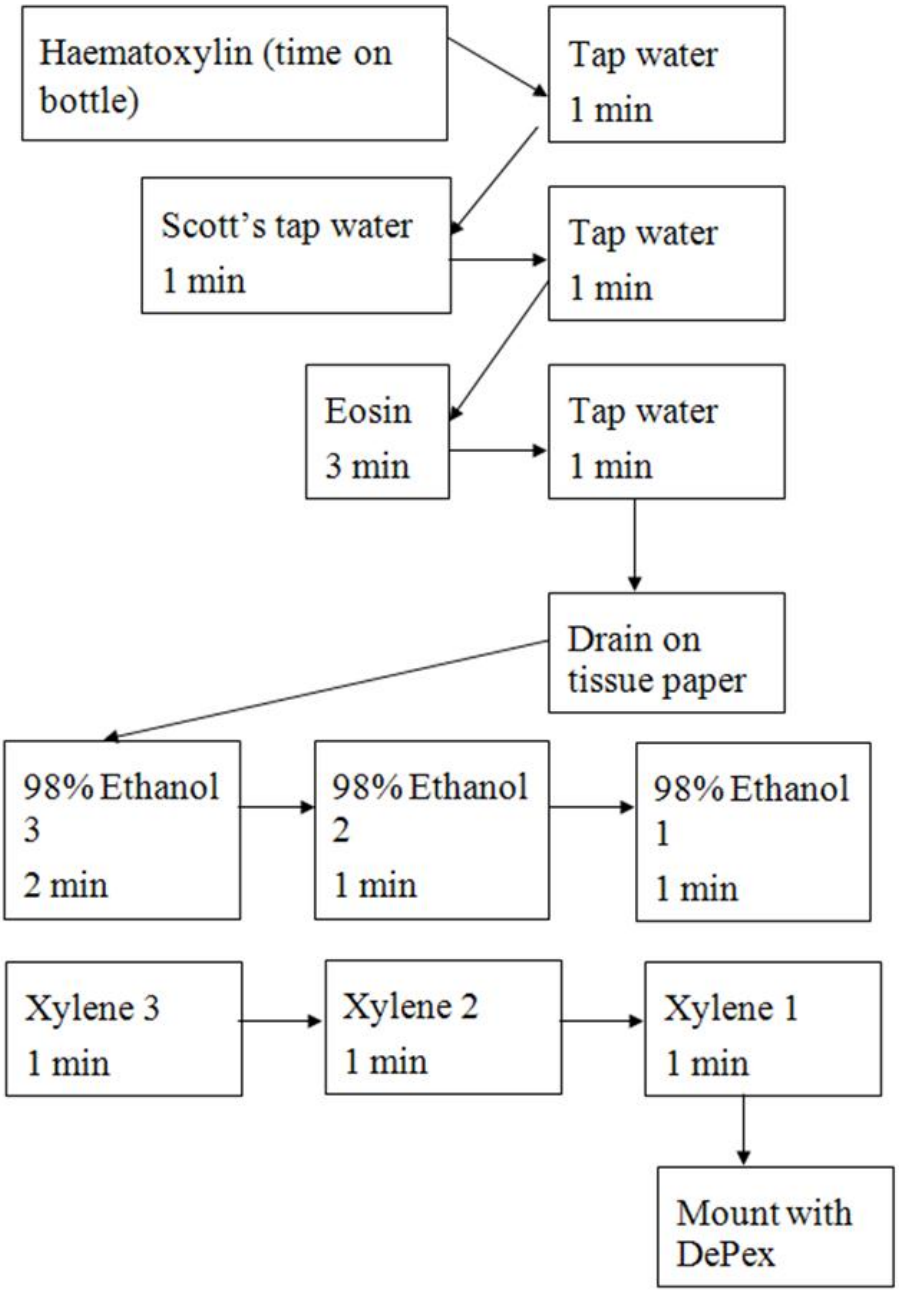

Figure 7.27: Staining protocol for tissue samples [240].

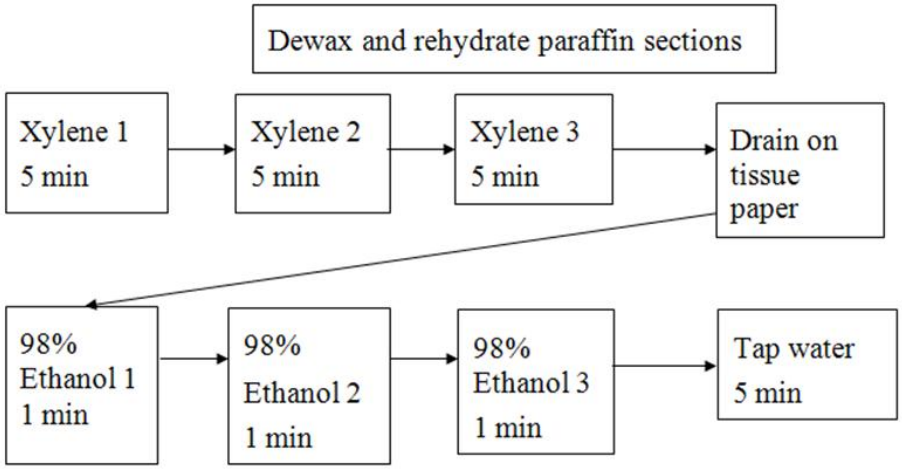

Figure 7.28: Histological protocol for tissue sample preparation [240].